Jamal Y. Sheikh-Ahmad

Machining of Polymer Composites

Springer

Machining of Polymer Composites

Jamal Y. Sheikh-Ahmad

Machining of Polymer Composites

Springer

Jamal Y. Sheikh-Ahmad
The Petroleum Institute
Department of Mechanical Engineering
Abu Dhabi
United Arab Emirates

ISBN 978-0-387-35539-9 e-ISBN 978-0-387-68619-6
DOI:10.1007/978-0-387-68619-6
Library of Congress Control Number: 2008932279

Printed on acid-free paper

9 8 7 6 5 4 3 2 1

springer.com

This work is dedicated to my family, who stood by my side all the time: my wife Manal and my children Iman, Sahar, Abdurrahman, and Ayah.

Preface

The idea for writing a book on machining fiber-reinforced polymer (FRP) composites came about during the time I taught a graduate course on the subject at Wichita State University. Preparing lecture notes and material for the course was and still is a laborious and painstaking task because of the lack of complete books and references on the subject. The machining of FRP composites is a relatively new practice, and unlike the well-established practices of metal machining, it is still in the development stages. Despite the fact that ample research work has been published in the past three decades, there exists no single source that provides a comprehensive treatment of the subject from fundamental and practical points of view. Therefore, a need for such a book exists, and this current book is perhaps the first compilation of its kind on the subject.

This book addresses both the theoretical foundation and practical aspects of machining FRP composites. A brief introduction to composite materials is provided in Chap. 1. This is necessary to familiarize readers who are new to the subject with the terminology, technology, and manufacturing aspects of polymer composites. The section on properties of composites at the end of this chapter is very brief and by no means is a fair treatment of this very complicated subject. Its inclusion is necessary for completeness, so that the reader would appreciate the complexity of the subject. Chapter 2 provides a brief synopsis of machining kinematics. This treatment is necessary for anyone who intends to engage in machining studies, whether it is for metals or composites. Chapter 3 covers the fundamental concept of mechanics of chip formation from the experimental and analytical perspectives. Much of the techniques discussed in this chapter have been imported from established metal machining tradition. A case in point is the application of single shear plane theory to the orthogonal machining of fiber-reinforced composites. Therefore, great effort is spent in explaining the similarities and contrasts between machining metals and composites and the limitations of metal machining theories in this regard. Chapter 4 discusses the phenomena of tool wear and provides analysis of tool materials and tool wear mechanisms in machining FRP composites. Once again the differences in tooling requirements for composites and metals machining are considered. Chapters 5 and 6 discuss the machinability of FRP composites by traditional and

nontraditional methods, respectively. These include turning, milling, drilling, abrasive, abrasive waterjet, and laser machining. Recommended industrial practices and tips are highlighted whenever possible. Finally, Chap. 7 discusses the important issue of health and safety in machining FRP composites. This chapter familiarizes the readers with the health hazards involved in machining and some of the current standards set by appropriate authorities to deal with these hazards.

This book should serve as a valuable reference for those engaged in research and for manufacturing and design engineers who are engaged in process selection and design of cutting tools for machining FRP composites. It also serves as a complete and comprehensive textbook for one semester course on the subject at the graduate and upper undergraduate levels in manufacturing, mechanical, or materials engineering.

Its my pleasure to acknowledge many of my graduate students at Wichita State University who contributed directly or indirectly to this book. Many of the references I have used in preparing the Chaps. 3–6 were collected and reviewed by my students as a part of their research work or as a required assignment for the course on machining composites. Several students, whose names appear in the references lists, have provided necessary experimental results included in the book. My appreciation is also extended to several colleagues from academia and industry who reviewed parts of the manuscript and provided valuable feedback. Finally, a special note of thanks is due to my editors Steve Elliot and Angela DePina for their indispensable assistance in preparing the manuscript.

Abu Dhabi, UAE *Jamal Y. Sheikh-Ahmad*

Contents

Chapter 1
Introduction to Polymer Composites

Man has discovered long ago that clay bricks can be made stronger and more durable by reinforcing the clay with straw and sticks. There are also many naturally occurring composites, such as wood and bones. Wood consists of strong cellulose fibers held together by a lignin matrix. Bones consist of short and soft collagen fibers embedded in a mineral matrix. Both wood and bones demonstrate the outstanding adaptability and capabilities of composite materials in supporting loads under diverse conditions. Composite materials, thus far can be defined as materials consisting of two or more constituents (phases) that are combined at the macroscopic level and are not soluble in each other. Modern synthetic composites using reinforcement fibers (one phase) and matrices (another phase) of various types have been introduced as replacement materials to metals in civilian, military, and aerospace applications. The marking point in the composites revolution has been associated with the development of carbon and boron fibers in the 1960s [1]. These new fibers, which have higher stiffness than glass fibers, gave a significant increase in the stiffness of composites structures. The ability to tailor these materials to the specific needs and their superior properties are the driving force behind this increased utilization. The high strength, high stiffness-to-weight ratio of carbon-fiber-reinforced polymers made them more suitable for aerospace and high-performance sporting equipment. The superior resistance of glass fibers to environmental attack made glass-fiber-reinforced polymers more attractive for marine products and in the chemical and food industries.

While the advantages of composites over conventional materials are obvious, one must not overlook their limitations. Being relatively new materials, there is an apparent lack in knowledge and experience that limits their fast incorporation into existing and new designs. The high cost of materials and complexities in their manufacturing is perhaps the most serious problem that designers with composites have to deal with. Components fabricated from composite materials are endeavored to be made net shape. This in part is made possible because of the fact that many components are built layer by layer out of contoured two-dimensional plies that closely capture the final shape of the product.

J.Y. Sheikh-Ahmad, *Machining of Polymer Composites*.
DOI: 10.1007/978-0-387-68619-6,

Even though composite components are often made near-net shape, some machining is often unavoidable. In many cases, excess material is added to compensate for material conformity to complex mold shapes and for locating and fixturing purposes. Resin flashing may also result after molding and curing of fiber–resin preforms. This excess material has to be removed by machining. Machining is also an indispensable process for shaping parts from stock composite materials and for finishing tight-tolerance components. Some of the common machining processes used are edge trimming and routing, milling, drilling, countersinking, and grinding. In current aircraft manufacturing, milling and drilling are critical for finishing trimmed edges of panels, cutting windows or openings, or making accurate holes to rivet pieces together.

Machining composites is vastly different from machining metals, despite the fact that mostly metal machining tools and technology are used with composites. Unlike metals, composites are inhomogeneous and their interaction with the cutting tool during machining is a complex phenomenon that is not well understood. Machining may adversely affect the quality of the composite part because of the rise during machining to defects such as delamination, cracking, fiber pull-out, and burning. The abrasiveness of the reinforcement fibers and the need to shear them neatly put additional requirements and constraints on the selection of tool materials and geometry. Machining by-products such as dust and decomposition gaseous compounds is also a major concern for the health and safety of the worker. All of these complexities associated with machining composites require great attention from the scientific community and industry in order to establish sound knowledge of this important manufacturing process. The following chapters in this book are an attempt to provide a comprehensive coverage of the phenomenon of machining fiber-reinforced polymers (FRPs) including a review of the latest scientific research and technical development.

1.1 Definitions and Classification

Composite materials are composed of mixtures of two or more distinct constituents or phases separated by a distinct interface. For a material to be called a "composite material" within the context of the technical discussion in this book it must satisfy the following conditions or criteria [2, 3]:

1. It is manufactured (naturally occurring composites such as wood and bones are excluded).
2. It is composed of two or more physically and/or chemically distinct and suitably arranged constituents. This arrangement of constituents is imparted into the composite during early manufacturing stages. Metal alloys that produce second phase or intermetallic precipitates during solidification or during subsequent heat treatment are not considered as composites.
3. The constituents are present in reasonable proportions.
4. It has characteristics that are not depicted by any of the constituents alone.

Thus, a metal alloy that develops second phase particles subsequent to heat treatment (e.g., precipitation hardening) is not a composite. On the other hand, tungsten carbide powder that is mixed with a binder metal, compacted, and sintered forms a cemented carbide composite.

The constituent that is continuous and most of the time is present in the greater quantity is called the matrix. The normal view is that it is the matrix properties that are improved on incorporating another constituent to produce a composite. The main purpose of the matrix is to enclose and bind the reinforcement, thus effectively distributing applied load to it, and to protect it from outside and hostile environment. The majority of current applications of composites utilize polymeric matrices, but metal and ceramic matrices are also found in specific high-temperature, high-wear applications.

The second constituent in a composite is the reinforcement phase, which is in most cases made of a stronger and stiffer material than the matrix. The reinforcement is the primary load-bearing constituent in the composite and its shape, volume, and arrangement adversely affect the properties of the composite material. Reinforcements can be in the form of long fibers, short fibers, particles, or whiskers.

Composites are classified according to the type of matrix material into metal matrix, ceramic matrix, or polymer matrix composites. It is further classified according to the reinforcement form and arrangement into particulate reinforced (random, preferred orientation) and fiber reinforced (continuous, discontinuous, aligned, random) as illustrated in Fig. 1.1. Hybrid composites are multilayer composites with a mix of fibers in each (or some) of the layers. Advanced composites are those composite materials traditionally used in aerospace applications and are characterized by high specific stiffness and strength. Examples of these are given in Fig. 1.2. Commonly, composite materials show marked anisotropy (properties are dependent on direction) because of the distinctive properties of the constituents and the inhomogeneous or textured distribution of the reinforcement. The composite materials approach isotropic state as the reinforcement phase becomes smaller in size and randomly oriented, as illustrated in Fig. 1.1.

1.2 Advantages and Limitations

When comparing the properties of composites to monolithic materials, the stiffness or strength of a composite may not be greatly different, and perhaps lower, than that of metal. But when specific strength (strength-to-weight ratio) and specific stiffness (stiffness-to-weight ratio) are considered, composites generally outperform metals. This is illustrated in Fig. 1.2 for a number of polymeric matrix materials, metals, and unidirectional polymer composites. The tremendous improvement in strength and stiffness imparted to the matrix material by the reinforcement fibers, along their direction is apparent. Also apparent is the difference in mechanical properties along

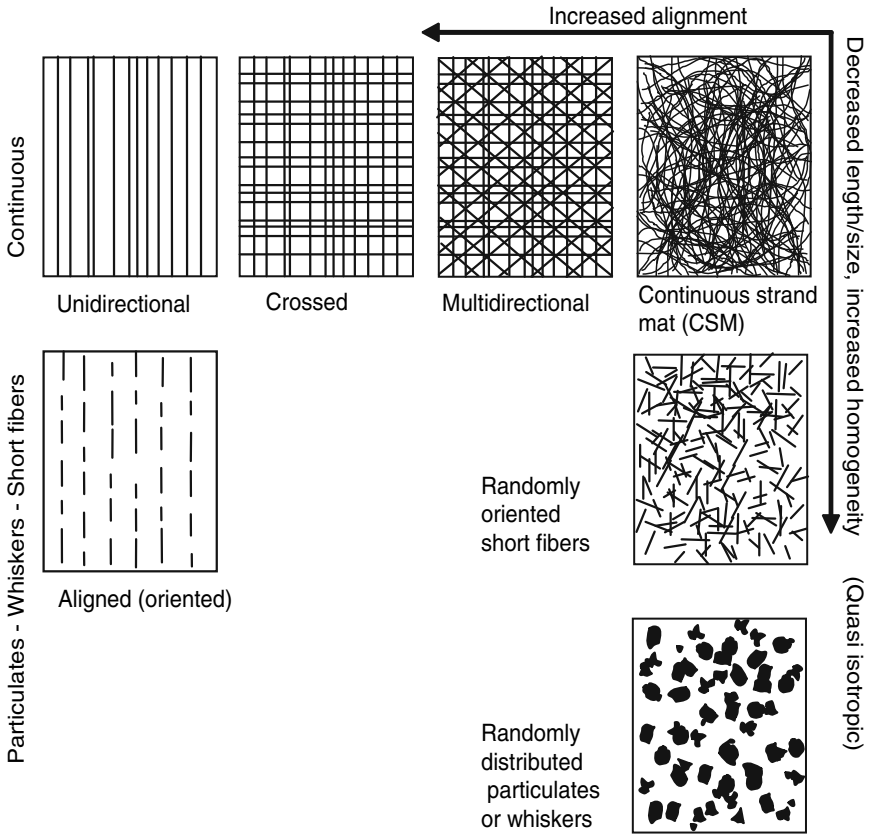

Fig. 1.1 Schematic of different reinforcement arrangements in composites

the fiber direction and transverse the fiber direction. In contrast to the strong directional property of unidirectional composites, one can note the slight improvement in matrix properties imparted by the randomly distributed short fibers in a sheet molding compound (SMC). In addition to improving structural properties, composites are in many cases better in corrosion resistance, fatigue resistance, thermal insulation, conductivity, and acoustic insulation than metals. From a manufacturing standpoint, designing with composites results in significant reduction in parts, tooling, and assembly. Complex sheet metal assemblies can in many cases be conveniently and effectively replaced by monolithic one-step manufacturing composite parts.

There are drawbacks to designing with composites as well. The cost of manufacturing is high as compared to that of metals, even though the tooling may be simple. This is attributed to the high cost of constituents, especially high-performing fibers, the dependence to a large degree on skilled labor, and a lack of high productivity manufacturing methods. Because composites are relatively new, there is also a lack of simple analysis tools, reliable material property data bases, and easy to implement

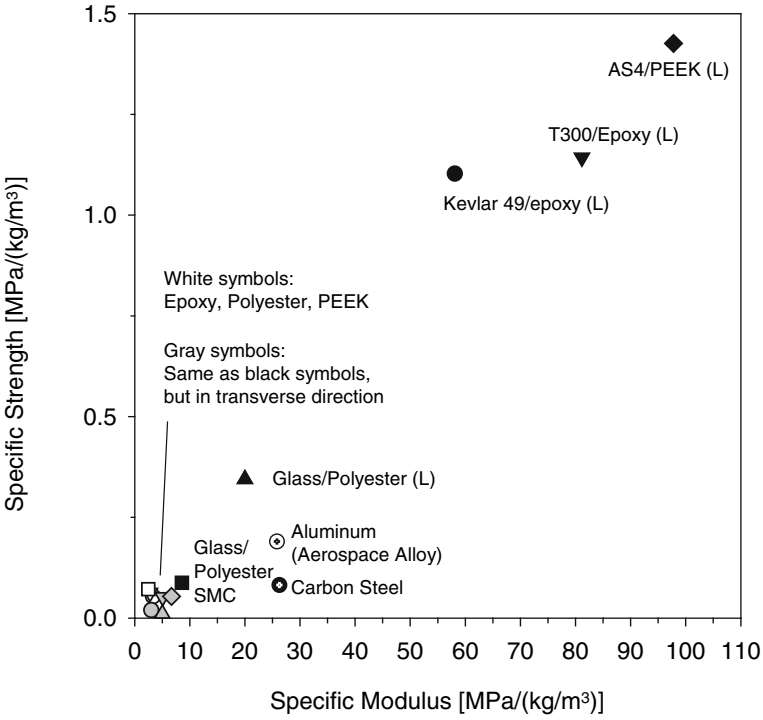

Fig. 1.2 Specific strength and modulus of some composites and monolithic materials. The volume fraction of reinforcement fibers is as follows: Epoxy and PEEK composites, 60%; polyester composite, 50%; SMC, 20%. *L* longitudinal; *T* transverse. Data from [3, 4]

design rules. Composites, such as thermoset polymer composites, suffer from sensitivity to hygrothermal environments. This requires that extra care is taken to protect the matrix material against the hostile environment.

1.3 Applications

Polymer-reinforced composites have proven to be flexible and adaptable engineering material for many applications, including aerospace, aircraft, automotive, construction, marine, commodity, and sports. A number of typical applications of composites are shown in Table 1.1. This table by no means represents inclusive list of all applications of polymer composites, but serves as a good indication of their importance in modern day society. Each industrial sector seeks desirable features that the composite material must satisfy. Aerospace structures for example require high specific stiffness and strength and a very high degree of dimensional stability under a wide range of temperatures that are encountered in space. Carbon- and

Table 1.1 Some applications of polymer matrix composites

Application area	Examples
Aerospace	Space structures, satellite antenna, rocket motor cases, high pressure fuel tanks, nose cones, launch tubes
Aircraft	Fairings, access doors, stiffeners, floor beams, entire wings, wing skins, wing spars, fuselage, radomes, vertical and horizontal stabilizers, helicopter blades, landing gear doors, seats, interior panels
Chemical	Pipes, tanks, pressure vessels, hoppers, valves, pumps, impellers
Construction	Bridges and walkways including decks, handrails, cables, frames, grating
Domestic	Interior and exterior panels, chairs, tables, baths, shower units, ladders
Electrical	Panels, housing, switchgear, insulators, connectors
Leisure	Tennis racquets, ski poles, skis, golf clubs, protective helmets, fishing rods, playground equipment, bicycle frames
Marine	Hulls, decks, masts, engine shrouds, interior panels
Medical	Prostheses, wheel chairs, orthofies, medical equipment
Transportation	Body panels, dashboards, frames, cabs, spoilers, front end, bumpers, leaf springs, drive shafts

graphite-reinforced polymers offer the high strength and stiffness required. Because of a negative coefficient of thermal expansion (CTE) of the carbon fibers along their axis, aerospace structures can be designed such that a zero-dimensional change is achieved over a wide range of temperatures.

The high specific strength and stiffness of composites make them also attractive for both military and civilian aircraft components. Military aircraft being more concerned with performance than cost has witnessed the most utilization of advanced composites. Polymer-fiber-reinforced composites are being used extensively in the primary structures as well as secondary structures and control surfaces of military aircraft. Reinforcement fibers are mostly carbon and graphite, but glass, aramid, and hybrids are also used. Common components include wing skins and substructures, rudders, flaps, rotors and blades, vertical and horizontal stabilizers, radome, and various access doors. The utilization of composites in the civilian aircraft manufacturing has been much slower, especially in the commercial aircraft sector. This is mainly due to high cost, difficulties in manufacturing, and lack of performance data required for certification. An exception to this trend was seen in the corporate aircraft sector, where aircrafts entirely made of composites were introduced. Examples of an almost all composites aircraft are the Beechcraft Starship (Fig. 1.3) first introduced in the late 1980s and Raytheon's Premier I business jet introduced about 10 years later. The utilization of composites in the civilian transport aircraft has increased slowly from less than 5% of total weight in the Boeing 757/767 (1980s) to almost 50% in the new Boeing 787 Dreamliner. The Airbus 380, the world largest aircraft is also utilizing about 25% of its total weight in composites. Common components made of composites include interior components (sidewall, ceiling and floor panels, storage and cargo bins), doors, radome, wing and tail leading edge components, wing skins, tail and elevator panels, fairings, and cowlings. In addition, entire

Fig. 1.3 The almost all-composite Beechcraft Starship (courtesy of Robert Scherer, http://www.bobscherer.com)

sections of the Boeing 787 fuselage are made of composites [5,6]. In the land transport industry, glass–polyester composites are used for body panels, frames, interior structural components, and bumpers. Carbon–polymer composites are used in leaf springs, drive shafts, and various chassis parts.

The leisure and sports industry is the largest beneficiary of polymer composites, after the aerospace and aircraft industries. Boat structures and hulls incorporate composites to a large extent. Glass–polyester composites dominate in pleasure boat building because of its lightweight and resistance to corrosion. Carbon–epoxy composites are also used in high-performance race boats and cars. Sports products include tennis rackets, bicycle frames, golf clubs, skis, and fishing poles. Carbon–polymer composites dominate in sports applications because of its extraordinary strength and stiffness.

1.4 Constituent Materials

It has been stated before that composites consist of two or more distinctly different materials. In most cases, the composite is made of matrix and reinforcement materials that are mixed in certain proportions. The matrix material may be made from metals, ceramics, or polymers. It may be pure, or mixed with other materials (additives) to enhance its properties. The reinforcement may also be treated to enhance bonding to the matrix. Examples of metal matrices are aluminum and

titanium alloys. Aluminum and its alloys have received by far the most attention. Metal matrices are reinforced with continuous fibers, particulates, and whiskers that are made from metals (stainless steel, boron, carbon) or ceramics (SiC, Al_2O_3). Aluminum metal matrix composites are used in a vast number of applications where strength and stiffness are required. This includes structural members in aerospace applications and automotive engine components. Ceramic matrix composites use ceramics for both the matrix and the reinforcement phases. Because of the high stiffness and excellent thermal stability of ceramics, their composites are attractive for applications where high strength and high stiffness are required at high temperatures. An example of ceramic matrix composites is SiC_w (whiskers)-Al_2O_3, which is used in making cutting tools, drawing dies, and other wear parts. Polymer matrices by far are most widely used in composites applications. The wide range of properties that result from their different molecular configurations, their low price and ease of processing make the perfect material for binding and enclosing reinforcement. Polymer matrices are normally reinforced with glass, carbon, and aramid fibers. Polymer matrix composites have found a wide range of applications in sports, domestic, transportation, and aerospace industries. The following sections provide an overview of the most common polymer matrices and reinforcement fibers.

1.4.1 Polymer Matrices

It has been stated earlier that the matrix material acts as a binder that holds together reinforcement fibers, transfers and distributes applied loads, and protects the fibers from hostile operating conditions. Polymer matrices exhibit inferior properties when compared to engineering metal alloys with regard to strength, stiffness, toughness, and elevated temperature properties. This is clearly shown in Fig. 1.2 for three commonly used polymeric matrices. Therefore, polymeric matrices are often considered the weak link in a composite material and their properties often dictate the operating temperatures of the composite parts. We will see later that polymer matrix thermal and mechanical properties have profound effects on the machining behavior of composites.

Polymers consist of long molecules (chains) of hydrogen and carbon atoms held together by primary or covalent bonds. Depending on the arrangement of hydrocarbon chains, different molecular configurations and hence different properties are obtained. There is a strong relationship between the configuration of a polymer and its macroscopic properties in the liquid and the solid states. These relationships are attributed to the ease or the difficulty of mobility of polymer molecules relative to each other under applied loading and temperature. Polymeric matrices are classified into two major categories: *thermoplastics* and *thermosets*, which differ in their respective intermolecular bonds and the resulting structures.

Thermoplastics consist of long hydrocarbon molecules that are held together by secondary (van der Walls) bonds and mechanical entanglements. The secondary

bonds are much weaker than the primary covalent bonds and hence a thermoplastic can be easily melted by increasing its temperature. Large temperature increases would also free the mechanical entanglement of the polymers, thus increasing its mobility. Thermoplastics can be formed repeatedly by heating to an elevated temperature at which softening occurs. If the arrangement of molecules is random in both the melted and solid states, the thermoplastic is called amorphous. As the polymer solidifies from the melt state, its molecules may arrange itself in a regular pattern. The resulting polymer is said to be semicrystalline. The degree of crystallinity of the polymer depends on the cooling rate, with the degree of crystallinity increasing with slower cooling rates. Amorphous thermoplastics are generally stiffer than semicrystalline ones.

Thermoset polymers also consist of long hydrocarbon molecules with primary bonds holding the atoms in the molecule together. However, the polymer molecules are also crosslinked together with covalent bonds as well, instead of the secondary bonds that exist in thermoplastics. This results in gigantic three-dimensional solid structures that are less mobile, stiffer, stronger, and less ductile than thermoplastics. The arrangement of thermoset molecules is random and they are amorphous both in the liquid and in the solid states. Since the intermolecular covalent bonds cannot be broken easily without breaking the intramolecular covalent bonds, thermosets cannot be melted by heating. Instead, when heated enough it starts disintegrating and may ignite.

All polymers undergo a notable reduction in stiffness when heated to a characteristic transition temperature known as the glass transition temperature, T_g. Upon heating, semicrystalline and amorphous polymers gradually transform from a rigid solid to a rubbery material at the glass transition temperature and then to liquid at the melting temperature, T_m. The reduction in stiffness is attributed to sudden gains in molecular mobility associated with the transition from solid to a rubbery material. Abrupt changes in heat capacity and CTE are also associated with this transition. Because of crosslinking, thermosets have higher glass transition temperatures than thermoplastics. In practice, the glass transition temperature defines the maximum temperature the polymer can withstand during service. The melting and glass transition temperatures also influence the fabrication and processing procedures for composites as discussed later. Tables 1.2 and 1.3 list representative mechanical and thermal properties for common polymeric matrices. Data is also included for metal and ceramic matrices for the sake of comparison. It is noted that polymer matrices are inferior in stiffness and strength to metals and ceramics. Their thermal conductivity is also several magnitudes less than that of metals, but their specific heat is approximately one magnitude higher. Thus their ability to retain heat during processing is higher than metals. The strain to failure (ductility) of thermoplastic polymers is much higher than that of metals and thermosets.

Various kinds of additives are used to modify polymers with regard to its mechanical and electrical properties, shrinkage characteristics, resistance to hostile environmental, fire tolerance, and color. Crosslinking agents are added to thermosets to transform them to the solid state. Plasticizers are added to thermoplastics to lower their melt viscosity. Inert fillers are added to improve stiffness, strength, impact

Table 1.2 Room temperature mechanical properties of matrix materials

	Density (mg/m^3)	Young's modulus (GPa)	Tensile strength (MPa)	Strain to failure (%)
Polymers – Thermosets				
Unsaturated polyester, UP	1.10–1.23	3.1–4.6	50–75	1.0–6.5
Epoxy, EP	1.10–1.20	2.6–3.8	60–85	1.5–8.0
Phenolics (Bakelite)	1.00–1.25	3.0–4.0	60–80	1.8
Bismaleimide, BMI	1.20–1.32	3.2–5.0	48–110	1.5–3.3
Vinylesters, VE	1.12–1.13	3.1–3.3	70–81	3.0–8.0
Polymers – Thermoplastics				
Polypropylene, PP	0.90	1.1–1.6	31–42	100–600
Polyamide (nylons), PA	1.10	2.0	70–84	150–300
Poly(phenylene sulfide), PPS	1.36	3.3	84	4.0
Poly(ether ether ketone), PEEK	1.26–1.32	3.2	93	50
Poly(ether sulfone), PES	1.37	3.2	84	40–80
Poly(ether imide), PEI	1.27	3.0	105	60
Poly(amide imide), PAI	1.40	3.7–4.8	93–147	12–17
Ceramics				
Alumina Al_2O_3 (99.9% pure)	3.98	380	282–551	–
Silicon nitride Si_3N_4 (sintered)	3.30	304	414–650	–
Silicon carbide SiC (sintered)	3.20	207–483	96–520	–
Metals				
Aluminum alloys (7075 T6)	2.80	71	572	11
Steel alloy (1020 Cold drawn)	7.85	207	420	15 (min)

resistance, and wear resistance of the matrix. Additives are also used to improve the matrix resistance to ultraviolet light. Pigments are added to color the matrix and eliminate the need for painting. It is important to note that while additives are beneficial from the point of improving desired properties of the matrix, they inadvertently result in diluting the bulk properties of the matrix.

The processing requirements for thermosets and thermoplastics are quite different because of the differences in their physical properties. The factors that are most important for processing polymers as a composite matrix are viscosity, temperature, cycle time, and work environment. Table 1.4 provides a qualitative comparison of the two groups of polymers from a processing standpoint. Viscosity of the liquid phase is important for completely wetting the fibers during impregnation. Not yet crossed thermosets have shear viscosities several magnitudes lower than melted thermoplastics, which mean it is much easier to complete impregnation of the reinforcements with thermosets than with thermoplastics. Most thermosets are delivered by suppliers in the liquid form. Crosslinking and solidification then takes place after the addition of crosslinking agents and may require 7 h to several days to complete. Epoxies may also be delivered partially crosslinked, and the crosslinking interrupted by storing the material at $-18\,^{\circ}C$ for a limited shelf life. The user would remelt the partly crosslinked polymers and complete crosslinking by subjecting it to a curing

Table 1.3 Room temperature thermal properties of matrix materials

	K (W/m°C)	C_p (kJ/kg°C)	α (10^{-6} °C)	T_g (°C)	T_m (°C)
Polymers – Thermosets					
Unsaturated polyester, UP	0.17–0.22	1.3–2.3	55–100	70–	–
Epoxy, EP	0.17–0.20	1.05	45–65	65–175	–
Phenolics	0.12–0.24	1.4–1.8	25–60	300	–
Bismaleimide, BMI				230–345	–
Vinylesters, VE				70–	–
Polymers – Thermoplastics					
Polypropylene, PP	0.11–0.17	1.8–2.4	80–100	−20 – 5	165–175
Polyamide, PA	0.24	1.67	80	55–80	265
Poly(phenylene sulfide), PPS	0.29	1.09	49	85	285
Poly(ether ether ketone), PEEK	0.25	1.34	40–47	145	345
Poly(ether sulfone), PES	0.26	1.0	55	225	–
Poly(ether imide), PEI	0.07	47–56		215	–
Poly(amide imide), PAI			245–275		–
Ceramics					
Alumina Al_2O_3 (99.9% pure)	39	0.775	7.4		
Silicon nitride Si_3N_4 (Sintered)	33	1.10	3.1		
Silicon carbide SiC (Sintered)	71	0.59	4.1		
Metals					
Aluminum alloys (7075 T6)	130	0.960	23.4		
Steel alloy (1020 Cold drawn)	51.9	0.486	11.7		

K Thermal conductivity, C_p Specific heat, α Coefficient of thermal expansion, T_g Glass transition temperature, T_m Melting temperature

cycle of heat and pressure. During the mixing of crosslinking agents and curing, thermosets may omit volatile gasses that are hazardous, thus creating an unhealthy work environment. Thermoplastics on the other hand are delivered in the solid state in the form of powder, pellets, or film. They have to be melted or dissolved for impregnation. While the curing cycle for thermosets may take several hours, the melting and solidification of thermoplastics takes place in few seconds. One significant advantage of thermosets is their low cost and long history of use. Thermosets, therefore, dominate applications in composites for both civil and aerospace sectors. However, there is an increased interest in thermoplastics because of their high temperature tolerance, toughness, short processing time, recyclability, and favorable work environment. As technological advances are made in the processing of thermoplastics, their use would exceed that of thermosets.

Table 1.4 Qualitative comparison of processing requirements for thermosets and thermoplastics

Processing requirement	Thermosets	Thermoplastics
Cost	Low	High
Damage tolerance	Average	Good
Environmental durability	Good	Exceptional
Fiber impregnation	Easy	Difficult
Prepreg drape	Good	Poor
Know-how and material data	Extensive	Limited
Prepreg shelf time	Short	Indefinite
Prepreg tack	Good	None
Processing cycle	Long	Short
Processing temperature	Low	High
Processing pressure	Low	High
Reformability	None	Good
Viscosity	Low	High

Table 1.5 Comparison of mechanical properties of materials in the fibrous (F) and monolithic (M) forms

	Carbon		Glass		Polyethylene	
	M	F(HM)	M	F(E)	M	F
Young's modulus (GPa)	10	400	76	80–81	0.4	172
Tensile strength (MPa)	–	2,500–4,500	–	3,100–3,800	–	2,964
Flexural strength (MPa)	20	–	100	–	26	–

HM High modulus, *E* E-glass

1.4.2 Reinforcement

Reinforcement materials are used in the form of continuous fibers, short fibers, particulates, and whiskers. Fibers are materials that have one very long axis compared to the others. The other axes are often circular or near circular. Fibers have significantly higher strength and stiffness in the length direction than in the other directions. This limits their use in a stand-alone form and underscores the need for a tough matrix in the composite structure. Thus fibers are most commonly used for the reinforcement of a softer matrix. Fibers are usually produced by drawing a liquid material from an orifice or by pulling a precursor, which results in aligning its crystals or molecules along the length of the fiber and thus imparting significantly higher strength and stiffness along their axis. Most materials are stronger and stiffer in the fibrous form than in any other form, as shown in Table 1.5. This is because fewer and smaller flaws would exist in a smaller volume of the material than in a larger volume. Material failure usually commences at the largest flow and fracture strength drastically decreases with an increase in flaw size.

Particles have no preferred orientation and their shape is less important than that of fibers. Their size varies from less than a micrometer to less than a millimeter. Whiskers are pure single crystals manufactured by chemical vapor deposition, thus

whiskers are anisotropic. Their length to diameter ratio is in the order of 10–1,000 and their diameter is in the order of 0.1–1 μm. Particles and whiskers are mainly used to improve the properties of isotropic materials, such as in the case of Al–SiC_p and Al–SiC_w metal matrix composites and Al_2O_3–SiC_w ceramic matrix composite. Because their distribution is largely random, the reinforced material can be assumed to remain isotropic in the macroscopic scale.

1.4.2.1 Glass Fibers

Glass is by far the most widely used fiber, because of the combination of low cost, corrosion resistance, and in many cases efficient manufacturing potential. It has relatively low stiffness, high elongation, and moderate strength and weight, and generally lower cost relative to other fibers. It has been used extensively where corrosion resistance is important, such as in piping for the chemical industry and in marine applications. Their use is limited in high-performance applications because of their relatively low stiffness, low fatigue endurance, and rapid degradation in properties with exposure to moisture. Glass fibers are produced by drawing a molten mixture of silica (SiO_2) and other oxides through small holes in a platinum-alloy bushing. The fibers emerging from the bushing are drawn to size at constant speed and then quenched by air or water spray. A protective coating, or size, is applied to the fibers to protect their surface and to enhance their bonding to the polymer matrix. Fiber diameters for composites applications are in the range from 10 to 20 μm. The fibers are gathered in a collimated assembly called a yarn or a tow, or a strand. A group of collimated yarns is called a roving. Glass is an amorphous material, and thus does not develop a preferred orientation in microstructure when drawn. It is therefore considered isotropic. Glass is also highly abrasive, which poses a major challenge when machining glass-fiber-reinforced composites. Glass fiber comes in several types, with E (electrical) and S (high strength) being the most common. E-glass offers excellent electrical properties and durability, is a cheaper general-purpose reinforcement. S-glass offers improved strength, stiffness, and high temperature tolerance. They are considerably more expensive than E-glass. Typical mechanical and physical properties of E- and S-glass fibers are found in Table 1.6.

1.4.2.2 Carbon Fibers

The high stiffness and strength combined with low density and intermediate cost have made carbon fiber second only to glass fiber in use. Carbon fibers are widely used for advanced composites in aerospace and some sporting goods applications, taking advantage of the relatively high stiffness-to-weight and high strength-to-weight ratios of these fibers. Carbon fibers vary in strength and stiffness with the processing variables, so that different grades are available such as high modulus (HM), intermediate modulus (IM), or high strength (HS), with the trade-off being between high modulus and high strength. The intermediate-modulus and

Table 1.6 Properties of reinforcement fibers

Characteristics	PAN-based carbon		Kevlar 49	E-glass	S-glass
	HM	HS			
Diameter (μm)	5–8	6–8	8–14	10–20	10–20
Density (kg/m^3)	1.81	1.78	1.44	2.62	2.46–2.49
Young's modulus (GPa)					
Parallel to fiber axis	400	230	131	80–81	88–91
Perpendicular to fiber axis	12	20	70	–	–
Tensile strength (GPa)	2.5–4.5	3.8–4.2	3.6–4.1	3.1–3.8	4.38–4.59
Strain to failure (%)	0.6	2.0	2.8	4.6	5.4–5.8
Coefficient of thermal expansion ($10^{-6}\,K^{-1}$)					
Parallel to fiber axis	−0.5	−0.6	−4.3	6.0	2.9
Perpendicular to fiber axis	7.0	10.0	41	–	–
Thermal conductivity (W/m K)	70	11	0.04–1.4	10–13	1.1–1.4
Specific heat (kJ/kg K)	0.7–0.9		0.769	0.45	0.41

high-strength grades are almost universally made from a PAN (polyacrylonitrile) precursor, which is then heated and stretched to align the structure and remove noncarbon material. Higher-modulus fibers with much lower strength can be made from a petroleum pitch precursor at lower cost. The pitch-based fibers have a higher modulus, but lower strength than the PAN. The starting point for PAN fibers is textile fibers, whereas pitch fibers are spun directly from the melted precursor. The fibers are first drawn and oxidized in air at temperatures below 400 °C to crosslink them, then they are carbonized in nitrogen atmosphere at temperatures above 800 °C in a process called pyrolysis. This ensures the removal of noncarbon atoms and creates fibers that consist of carbon only. Graphitization is further carried out at temperatures above 1,000 °C in order to improve purity and crystallinity of the fibers. After graphitization, surface treatment and size are applied. Even though carbon and graphite are used interchangeably when referring to carbon fibers, the two materials are not exactly the same. Graphite is processed at temperatures in the order of 1,900 °C and thus has higher carbon content (99%) and crystallinity than carbon fibers. Carbon fibers typically have a diameter in the order of 5–8 μm. Because of this small size, the fibers are grouped into tows or yarns consisting of from 2 to 12,000 (12k) individual fibers, with the new low-cost fibers having tow sizes up to 48k.

Carbon fibers are anisotropic (transversely isotropic) and their properties are mainly affected by the degree of orientation of the graphite layers with respect to the fiber axis. Graphite layers are based on hexagonal rings of carbon in which carbon atoms are held with a strong covalent bond. Secondary bonds hold the graphite layers together, which provides slip along the hexagonal planes. This explains why graphite fibers are much stronger in the longitudinal direction than in the transverse direction. A higher temperature of graphitization promotes orientation of the

graphite layers in the fiber direction, and thus resulting in higher tensile modulus. One peculiar property of carbon fibers is their electrical conductivity, which poses a serious problem in manufacturing and service environment. When abraded (during machining for example), the fibers' dust may penetrate machine tool controls and short circuit electrical equipment. The dust is also abrasive and may cause wear in machine guides and moving surfaces. Carbon reinforcement may also cause galvanic corrosion of metal inserts because of their electrical conductivity. Another characteristic property of carbon fibers is their negative CTE in the longitudinal direction. This property allows the design of structures with zero-dimensional variation over a wide range of temperatures.

1.4.2.3 Aramid Fibers

Aramid fibers (sold under the trade name Kevlar) are organic fibers manufactured from aromatic polyamides (Aramids) by solution spinning. Polymer solution in sulfuric acid is extruded by spinning through small holes into fibers in which the molecules are aligned with the direction of shear. Further alignment of the fibers may be achieved by heat treatment under tension. Aramid fibers offer higher strength and stiffness relative to glass coupled with lightweight, high tensile strength, but lower compressive strength. Aramid also exhibits an outstanding toughness and damage tolerance. It tends to respond under impact in a ductile manner, as opposed to carbon fiber, which tends to fail in a more brittle manner. The outstanding toughness of aramid fibers also creates a problem during machining. The fibers are very difficult to cut and special tooling and techniques are required. Aramid fiber is used as a higher-performance replacement for glass fiber in industrial applications and sporting goods, and in protective clothing.

1.4.2.4 Other Fibers

Oriented polyethylene, marketed under the trademark of Spectra fiber, is another fiber that is manufactured by spinning. It exhibits similar properties to aramid in terms of strength and stiffness. But because of their extremely lightweight (specific gravity of 0.97) its specific strength and modulus are higher and comparable to that of carbon fiber. It has a very low range of temperature usage, and the difficulty of obtaining adhesion to matrix materials has limited its application in structural composites. It is being used as a hybrid with carbon fiber in certain applications, in an attempt to combine the lightweight and toughness of the Spectra fiber with the stiffness of carbon fiber. It is also used in cordage and in protective clothing. A number of other fibers used for polymer reinforcement include boron and silicon carbide. These fibers may prove to be important in high-temperature applications. Their present use is a very small fraction of the use of glass, carbon, and aramid fibers, however.

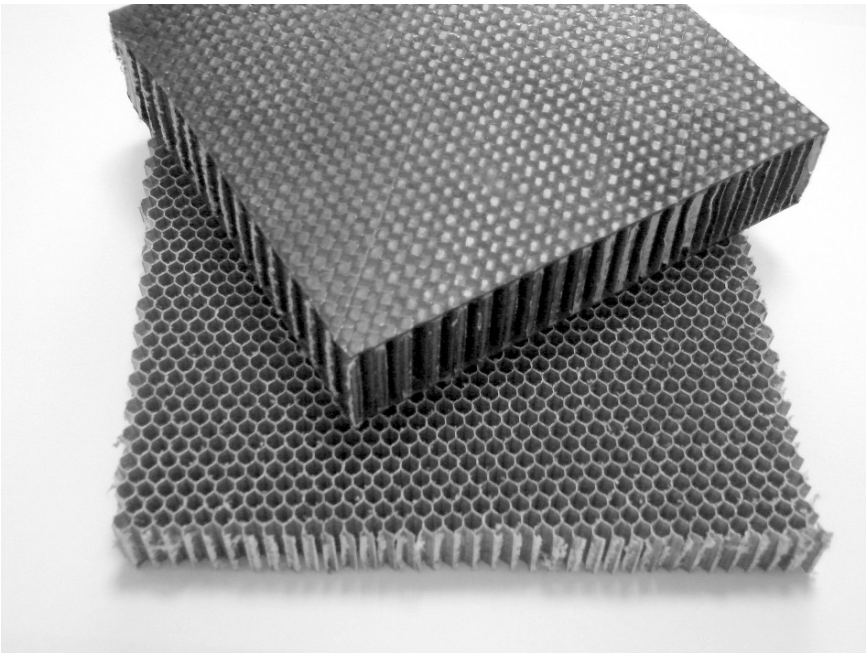

Fig. 1.4 Nomex honeycomb core (*bottom*) used in sandwich composites (*top*)

1.4.3 Core Material

Core material is used to support lateral loads on a composite sandwich structure. The most common core materials are wood, honeycomb, corrugated, and expanded polymer foams. Honeycomb core has a hexagonal cellular structure similar to the beeswax honeycomb (Fig. 1.4). Among the many materials used to manufacture honeycomb cores are unreinforced and fiber-reinforced polymers, metals, and paper. Aluminum and Nomex (the commercial name for aramid paper) honeycomb cores are the most common in aerospace applications. A strong core-face interface is important for the functioning of sandwich material in load bearing. This interface may be enhanced by the use of special adhesives.

1.5 Material Forms and Manufacturing

We have seen that the reinforcement material is fabricated in the basic forms of continuous fibers, particulates (powders), or whiskers. While the latter two are used in their basic form, fiber reinforcement is utilized in many different forms depending on the manufacturing process and the desired product's properties. The filament winding process, for example utilizes continuous fibers assembled in tows,

roving, or yarn. On the other hand, chopped fibers are more suitable for closed die compression molding and injection molding. Thus, it is useful to consider both the material forms and the manufacturing process at the same time. The discussion below provides an overview of the most relevant material forms and manufacturing processes utilized for fabricating advanced or high-performance composites. Processes more common in non-high-performance applications such as wet-layup and spray-up will not be discussed here. The reader is advised to consult references [4,7] for more detailed descriptions of polymer composites manufacturing processes and their process variables.

1.5.1 Continuous Reinforcement Forms

Fibrous reinforcement is typically produced in the continuous form. The fibers themselves are very small in diameter, in the range of 10–20 μm, which is much smaller than a typical human hair. A large number of fibers, typically in the thousands are gathered together in the manufacturing process to form a tow (also called a yarn or strand). A group of collimated yarns is called a roving. When glass fiber yarns and roving are formed, they may receive a twist in order to enhance yarn and roving integrity and handling. Carbon and aramid yarns receive little or no twist. The fiber yarn and roving are used as is in processes such as filament winding and pultrusion. The tows may be further processed by preimpregnation, which is the process of coating the individual fibers with the matrix material. This process is widely used with thermoset polymeric resins. The dry, spooled fiber is combined with the resin and results in the form of unidirectional prepreg tape, partially cured to a point that it can be handled and wound on spools with a removable paper backing. Prepreg tape with thermosetting polymer resin matrices must be stored under refrigeration to prevent further cure until final use. Prepreg has a limited shelf life in the freezer and a further limited "out time" during assembly of the final product. Both of these times are highly variable with the specific system. The unidirectional prepreg can then be cut and stacked to form the final product. Because the individual fibers are relatively straight, the use of a unidirectional prepreg provides a method, along with filament winding, of achieving finished products with excellent mechanical properties.

Continuous fibers are often used in the form of textile fabrics in a variety of shapes and configurations. Further, it is not uncommon that different fiber materials are mixed into hybrid fabrics. The fibrous yarn running in the longitudinal direction of the fabric is called the warp, and the one running in the transverse direction is called the weft or fill. Woven fabrics may be characterized in terms of the fabric crimp, which is a measure of the degree of bending the yarn receives as it crosses over perpendicular yarns in the fabric. A higher crimp is associated with stiffer fabrics and results in poor drapeability and reduced fiber load bearing capability. Drapeability is an important manufacturing characteristic of the reinforcement form because it describes the ability of the reinforcement to conform to the shape of a complex die. A low crimp means the yarn has little bending, which results into

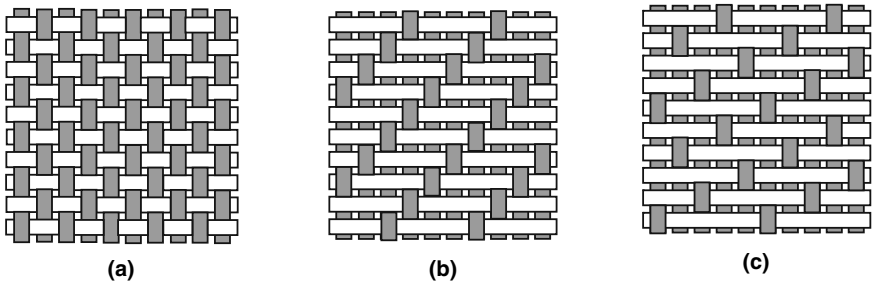

Fig. 1.5 Schematics of woven fabrics (**a**) plain weave; (**b**) three-harness satin weave (crowfoot); and (**c**) five-harness satin weave (long-shaft)

more flexible fabric, better drapeability, and better mechanical properties. Figure 1.5 shows a schematic of common textile forms used in composites. The most common weave is the plain weave, in which the weft alternatingly crosses over and under the warp. This creates the highest crimp with the tightest fabric and poorest drapeability. But plain weave fabrics are also the most resistant to in-plane shear movement. A basket weave is similar to a plain weave, except that two yarns are used for warp and two yarns are used for weft. Satin weaves are those in which the weft yarn crosses over or skips a number of warps before it crosses under a single warp again. This results in minimizing the crimp and increasing flexibility and drapeability of the fabric. This is one reason why satin weaves are preferred for many aerospace applications where complex shapes are common. Satin weaves are made in standard four-, five-, or eight-harness forms.

Fabric preforms are used both dry and preimpregnated, with fabric prepregs being the most widely used forms. The fabric preimpregnation takes place by passing the fabric directly into a resin-solvent bath. A solvent is used to lower the viscosity of the resin and ensure thorough wetting of the fibers. The resin is partially cured and the resulting preimpregnated ply is placed on a paper backing. The prepregged material is available in continuous tape rolls of widths from 75 to 1,000 mm. These rolls must be kept refrigerated until they are assembled and placed in the curing process. Note that the ply consists of a number of fibers through the thickness, and that these fibers are aligned and continuous. Typical volume fractions of fiber are on the order of 60%. These material forms are then used with a variety of specific manufacturing techniques. Thermoplastic prepreg on the other hand does not have to be stored under refrigeration. The layers tend to be stiff and are usually softened before assembly. The final manufacture could involve heating and forming in matched molds.

1.5.2 Molding Compounds

Molding compounds consist primarily of polymer resins, mostly thermosets, reinforced with randomly oriented short fibers or continuous fibers. The fiber content in

these compounds is typically between 20 and 30% by weight. Fillers are utilized to reduce the use of more expensive resins, and pigments may be added for coloring. Since the fiber content in molding compounds is much less than that in prepregged fabrics, its flow into complex shapes of closed dies is easier. Therefore, this material form is best suited for compression molding and injection molding of complex shapes. These compounds are also considerably cheaper than prepregged fabrics and tapes. The process lends itself to high rates of production, and has been commonly used in the automotive industry where it is utilized for manufacturing body panels and internal structural members.

SMC is the most widely utilized form of molding compounds. As illustrated in Fig. 1.6, the glass fiber is typically used in chopped-fiber form and added to a resin mixture, typically unsaturated polyester, that is carried on plastic carrier film. Fillers, catalysts, and other additives are introduced to the resin before its application to the carrier film. Compression rolls help mixing the formulated resin through the chopped fibers and attaining complete impregnation. After partial cure, the rolls are stored in sealed bags for later use. A typical glass fiber SMC contains 28% of its weight as fibers; 35% polyester resin; and the balance in filler, thickener, pigment, catalysts, and other additives. Fiber lengths may vary from 6 to 75 mm and fiber orientation is random in the plane [4]. At the time of use, SMC material is cut into lengths and placed into matched metal dies under heat and pressure. SMC is also manufactured with thermoplastic resin films or powders which are heated to melt impregnate the fibers. The thermoplastic version of SMC is called glass mat reinforced thermoplastic (GMT).

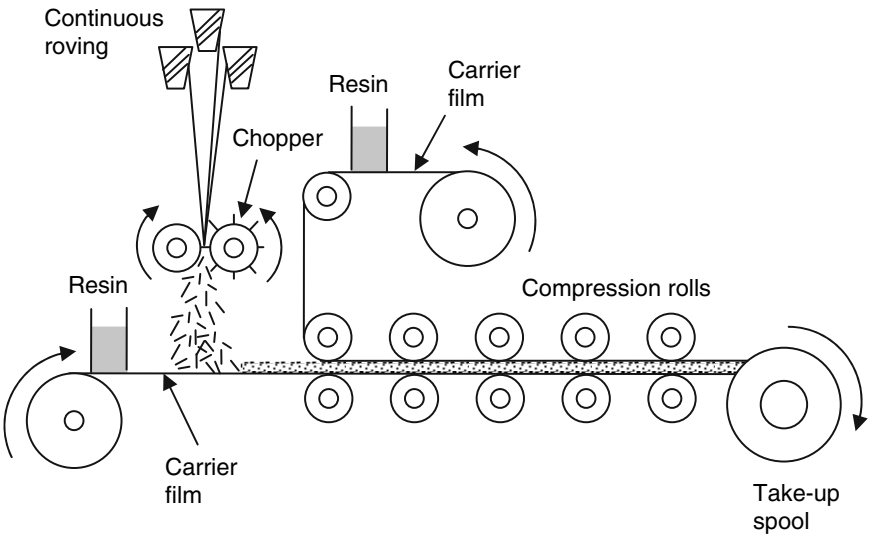

Fig. 1.6 Schematic of sheet molding compounding process

Another form of molding compounds is bulk molding compound (BMC), which has the same constituents as the SMC, but is manufactured by mixing the ingredients in bulk. The dough-like mixture is then shaped in the form a log or a rope. A typical glass fiber BMC contains 20% of its weight as fibers; 30% polyester resin; and the balance in filler, thickener, pigment, catalysts, and other additives. The fibers are generally shorter than in SMC and therefore the mixture have better flow properties. It is commonly used in injection molding processes.

1.5.3 Prepreg Layup and Autoclave Processing

Prepreg layup is the preferred manufacturing method for producing high-performance parts. It is done by hand or by automated tape placement machines. Figure 1.7 schematically shows prepreg layup of a composite part over a contoured tool surface. The manufacturing procedure involves removing the prepreg tape or roll from the freezer, allowing it to thaw while in the bag, cutting the prepreg to the final shape, removing the paper backing and assembling (stacking) the individual layers (plies) together in the desired orientations, placing the assemblage in tooling to control the final shape, and then covering with appropriate materials for the cure process. The individual prepreg plies can be cut easily with scissors or a razor, or with laser

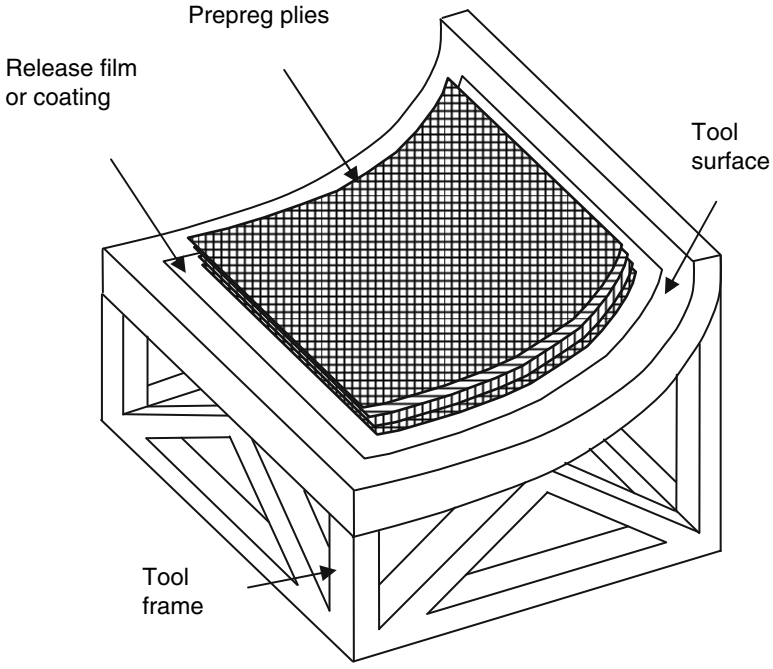

Fig. 1.7 Schematic of prepreg layup over a contoured mold

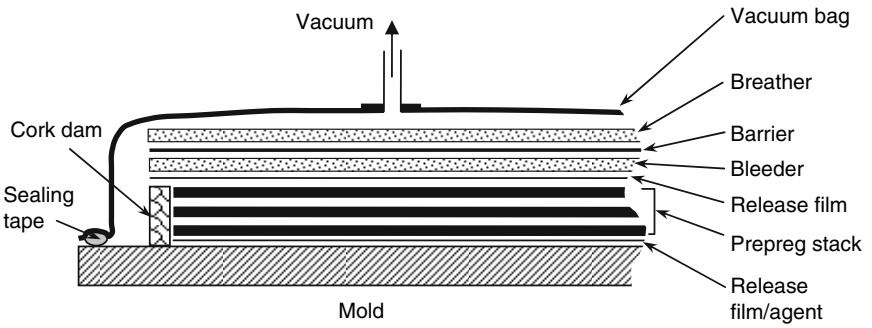

Fig. 1.8 Vacuum bagging

tools and automated machinery. Large-scale and highly automated equipment can be employed. Note that because the individual plies are relatively thin (on the order of 0.13 mm), a large number of plies will be required with thicker parts. A small increase of temperature of the prepreg is often employed to make the prepreg more pliable and increase tackiness during assembly. Appropriate tooling must be used to control the final part geometry. The tooling can be constructed of metal or a variety of other materials, including other composites, but must be capable of withstanding the temperatures used in the curing process. Extra care is taken in composite tooling design to account for differences in thermal expansion between the mold and workpiece. Separation of the part from the tooling requires release agents in either liquid or spray-on form, or a sheet of release film.

The prepreg material and often the tooling are then wrapped with several additional materials that are used in the curing process. A schematic of this is shown in Fig. 1.8. The objective of the cure process is to remove volatiles and excess air, to facilitate consolidation of the laminate, and to apply temperature and pressure to ensure good bonding during cure. To this end, the laminate is covered with a peel ply (for removal of the other curing materials), and a breather ply, which is often a flint or fiberglass mat. A bleeder, which might be of the same material as the breather, is used to absorb excess resin. Finally, the assemblage is covered with a vacuum bag and sealed at the edges, usually with an adhesive sealant tape. A vacuum is drawn, and after inspection, the heat-up process is started. If an autoclave is used, pressure on the order of 0.1–0.7 MPa is then applied to ensure the final consolidation. Autoclave processing ensures good lamination but requires a somewhat expensive piece of hardware. Removal of the cured part from the tooling may be easy in many cases, but if closed forms with internal mandrels are used, such as for tubular parts, it requires careful consideration.

1.5.4 Filament Winding

The filament winding process consists of winding continuous-fiber tow, yarn, or tape around a form or mandrel to form the structure. Typically, the mandrel itself

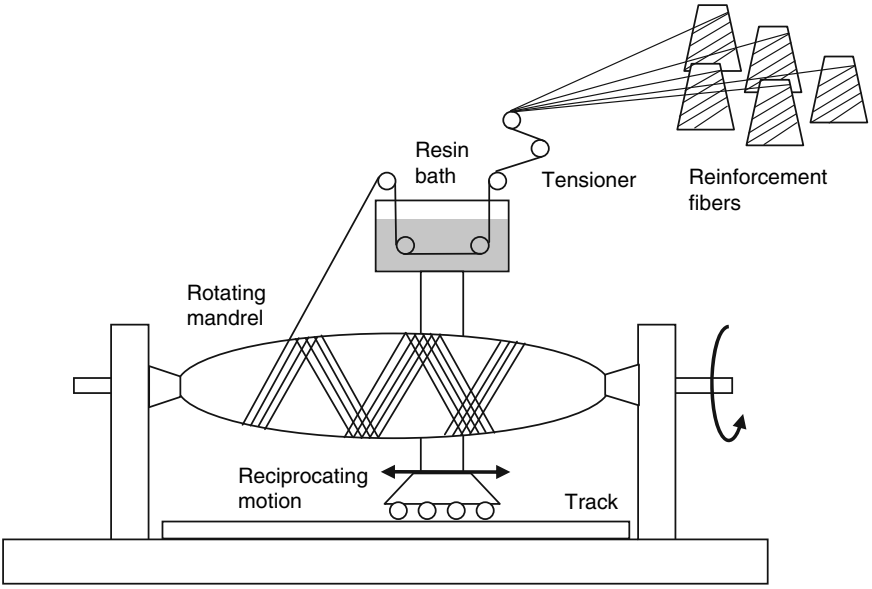

Fig. 1.9 Filament winding process

rotates while the fiber placement is controlled to move longitudinally in a prescribed way to generate the required fiber inclination angle with respect to the axis of rotation. The motion may be synchronized using CNC machines or by conventional machines similar to the lathe. The matrix, generally a thermoset, may be added to the fiber by running the fiber tow through a matrix bath at the time of placement, in a process called wet winding, or else the tows may be prepregged prior to winding. Usually the cure of the component is done at room temperature or by applying heat without vacuum bagging or autoclave consolidation. The mandrel is then removed and trimming and other finishing operations are conducted to complete the process. Figure 1.9 illustrates a common setup for a filament winding machine.

Filament winding has been widely used for making glass-fiber pipe, rocket motor cases, drive shafts, golf shafts, drilling risers, and other similar products. The advantages are that it is a highly automated process, with typically low manufacturing costs. Obviously, it lends itself most readily to convex axisymmetric articles, but a number of specialized techniques are being considered for more complicated shapes. Filament winding is typically a low-cost method because of the use of fibers and resins in their lowest-cost form, and because of the potential for high production rates. Mandrels must be constructed so that they can be removed from the finished article. Mandrels for nonuniform shapes are made from dissolvable materials or designed to remain as a liner of the structure, such as the case of fuel tanks and driveshafts. The winding tension is typically sufficient to consolidate the part, and shrink tape can be wrapped over the outside to give additional consolidation pressure during cure. Thus, additional pressure during cure is usually not used.

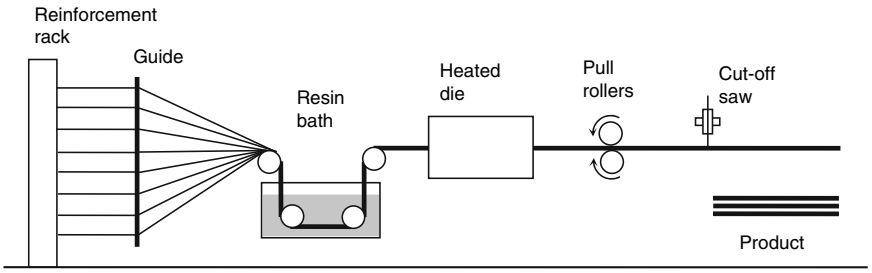

Fig. 1.10 Schematic of pultrusion process

1.5.5 Pultrusion

The pultrusion process is illustrated in Fig. 1.10. Pultrusion is a process in which a collection of reinforcement fibers saturated with the matrix are pulled through a heated die to gain its final shape. Pultrusion is similar in overall function to extrusion in metals and polymer materials, except that the fibers are pulled rather than pushed. The pultrusion apparatus provides the functions of assembling the fibers, impregnating the resin, shaping the product, and curing the resin. The die is heated and the heat that is transferred to the liquid matrix initiates crosslinking. Glass-fiber and unsaturated polyester or vinyl ester resin are widely used in the pultrusion process, as well as other material systems such as aramid or carbon fibers with epoxy resin. Surface mats are also introduced along with the fiber roving in order to produce a resin-rich smooth and environmentally resistant surface layer. Pultruded products are limited to components with constant cross section and include solid and hollow shapes in standard sizes, as well as custom shapes for a variety of specific applications. Common applications of these products include beams, gratings, walkways, ladders, equipment housing, fishing rods, and ski poles.

1.5.6 Compression Molding

Compression molding is similar in many ways to sheet metal forming that is widely used to manufacture automotive parts and other consumer products. It is considered the largest primary manufacturing process used for automotive composite applications today. Part of the reasons for this dominance is the familiarity with the process and its cost effectiveness for producing large volumes. The matrix material in these components is either thermoset or thermoplastic and the reinforcement is predominantly glass fibers. The three main groups of material forms used in compression molding are SMC and BMC thermosets and glass mat thermoplastics (GMT). Examples of compression-molded products include automotive body panels, spare wheel wells, bumper beams, under the hood structural parts, electrical components, and bathroom interiors.

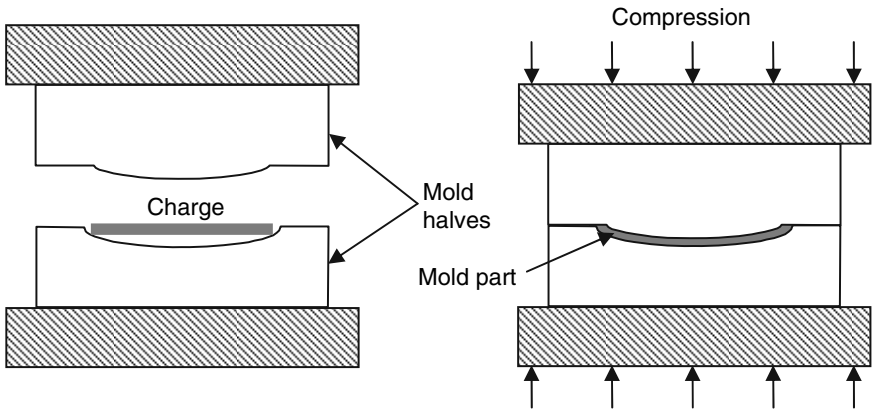

Fig. 1.11 Schematic of compression molding process

Compression molding is schematically shown in Fig. 1.11. In this process, a measured amount of the molding compound is placed in an open heated compression mold and formed into final shape forcing the material to flow under the pressure that is applied by closing the mold halves. In the case of SMC, the charge is cut to the required shape from a mat and placed in the mold. The mold is heated, to a temperature in the range 120–180 °C for polyester resins, to allow for crosslinking of thermoset resin. Once the part has cured the mold is opened and the part is removed. Mold coatings are sometimes used to improve the surface finish of the molded part. The cycle time for closing and opening the die depends on part size, thickness, shape, and resin type and may vary from 1 to 4 min [4].

Processing of GMT is different than SMC and BMC in that the charge is heated before it is placed in the mold. For large scale manufacturing, GMT blanks precut to shape from a GMT solid panel are delivered to the molder. Heating is typically done at stages in a long-wave infrared oven and the material is heated to a temperature approximately 40 °C above the melting point of the matrix. During heating and melting, the reinforcement material springs back to its original shape in a process called lofting and the GMT blank increases in thickness by a factor of two or three. The material is then rapidly transferred to the mold and formed under pressure. The material flows into the mold cavity and solidifies. Because of the apparent complexity of GMT forming, it is less popular than thermoset compression molding and is best suited for automated manufacturing of large volumes [8].

1.5.7 Liquid Molding

In liquid molding a dry-fiber preform, usually with the fibers in one or more textile forms, is assembled and placed in a mold and the mold is then closed. The resin is transferred into the closed mold to impregnate the fiber perform and cure, sometimes

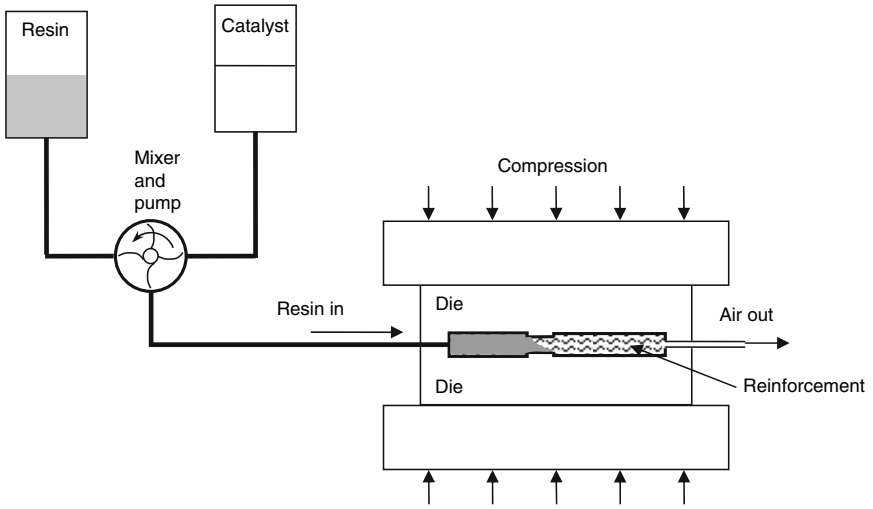

Fig. 1.12 Schematic of resin transfer molding (RTM)

with the aid of heat, before the mold is opened and the composite part is removed. Liquid molding processes include resin transfer molding (RTM), vacuum injection molding (VIM), also known as vacuum assisted resin transfer molding (VARTM), and structural reaction injection molding (SRIM). RTM is the most common liquid molding technique for manufacturing large and complex structural components with a quality surface finish. A schematic of RTM is shown in Fig. 1.12. Glass fibers and polyester resin dominate the application of RTM, although vinylesters and epoxies are also used in combination with high-performance reinforcement forms. The resin mixture is typically introduced under low pressure (up to 2.1 MPa) and air is displaced from the mold cavity and discharged from vent holes. Sometimes vacuum is used at the vent holes to aid drawing the resin through the mold cavity. Reinforcement impregnation occurs due to the low pressure and capillary effects. Multiple injection ports and vent holes may be used to distribute the resin and ensure access to all parts of reinforcement. Once the resin emerges from the vents, all access holes are closed and the resin is allowed to cure. Curing of unsaturated polyesters and vinylesters may take place at room temperature. Heat may also be introduced to accelerate crosslinking. In VARTM, vacuum drawn from vents in the mold is the driving force in transferring the resin to the reinforcement. This requires that a lower viscosity resin than that in RTM is used. The mold may be of the same closed type as the RTM mold, or it may have a lower solid part carrying the shape of the product and a vacuum bag for the upper part, similar to vacuum bagging of prepregs. SRIM is similar to RTM, except for a higher pressure used for injecting a metered charge of highly reactive matrix components. SRIM is most suitable for large volume production of complex parts. Applications of liquid molding include automobile parts (RTM, SRIM), boats, offshore structures, and automobile bodies (VARTM).

1.6 Properties of Composites

Properties of composites, particularly continuous-fiber reinforced, are different from those of metals in that they are highly directional. A material is called anisotropic when its properties at a point vary with direction. The orientation of the reinforcement within the matrix affects the state of isotropy of the material. When the reinforcement is in the form of equiaxed particles that are uniformly distributed, the composite behaves essentially as an isotropic material whose properties are independent of direction. When the dimensions of the reinforcement are unequal, the composite may behave as quasi-isotropic, provided the reinforcement is randomly oriented, as in a randomly oriented, short fiber-reinforced composite. In a composite with long fibers that are perfectly aligned, the composite is anisotropic. The relationship between the state of isotropy and the reinforcement shape and distribution in the matrix is qualitatively demonstrated in Fig. 1.1. In addition to directional variation of properties of composites high variability in the properties also arises from variations in the manufacturing process. Therefore it is extremely important that designers check predicted properties against experimentally determined values. Exhaustive tables of experimentally determined mechanical and thermal properties of typical composites may be found in [4, 9, 10].

Properties of composites are also described with respect to the scale at which the material is analyzed. Consider a composite lamina, which is the simplest possible form of a composite consisting of an assembly of anisotropic fibers in an isotropic matrix. At the microscopic scale, analysis is conducted at the fiber diameter level. This is called micromechanics analysis and it deals with relationships between stress and deformation in the fibers, matrix and fiber–matrix interface. Micromechanics analysis allows for the prediction of the average lamina properties as a function of the properties of the constituents and their relative amounts in the structure. At the macroscopic level, the lamina is treated as a whole and the material is considered as homogeneous and anisotropic. Lamina average properties are used to study the overall lamina behavior under applied loads. Macromechanics is also concerned with analysis of the behavior of laminates consisting of multiple laminas stacked in a certain sequence based on the average properties of the lamina. This section provides a brief description of micromechanics relationships for predicting composite lamina properties. For more comprehensive treatment of micro and macromechanics analysis of composites, the reader is advised to consult specialized texts such as [9, 10].

1.6.1 Density

Consider a composite consisting of matrix and reinforcement phases of known densities. The weight of the composite, w_c is given by the sum of the weights of its constituents, w_f and w_m

$$w_c = w_f + w_m, \tag{1.1}$$

where the subscripts f and m refer to the reinforcement and the matrix, respectively. Substituting for w by ρv, (1.1) can also be written as

$$\rho_c v_c = \rho_f v_f + \rho_m v_m, \tag{1.2}$$

where v_c, v_f, and v_m denote the volume of the composite, reinforcement, and matrix, respectively. Dividing (1.2) by v_c it becomes

$$\rho_c = \rho_f V_f + \rho_m V_m, \tag{1.3}$$

where V_f and V_m denote the volume fractions of the constituents, v_f/v_c and v_m/v_c, respectively. Equation (1.3) is known as the *law of mixtures* and it shows that the density of a composite is given by the volume fraction adjusted sum of the densities of the constituents. Also we can express the weight fraction of the reinforcement as

$$W_f = \frac{w_f}{w_c} = \frac{\rho_f v_f}{\rho_c v_c} = \frac{\rho_f}{\rho_c} V_f$$

and substituting for ρ_c from (1.3) gives

$$W_f = \frac{V_f \rho_f}{V_f \rho_f + V_m \rho_m}. \tag{1.4}$$

In a similar way, the volume fraction of the reinforcement may be expressed in terms of constituents' weight fractions as follows:

$$V_f = \frac{W_f \rho_m}{W_f \rho_m + W_m \rho_f}. \tag{1.5}$$

So, we can convert from weight fraction to volume fraction provided that densities are known. Note that in the absence of voids,

$$V_f + V_m = 1 \text{ and } W_f + W_m = 1. \tag{1.6}$$

Voids are introduced during the manufacture of composites due to air and volatiles entrapment and incomplete consolidation. The presence of voids has detrimental effects on its mechanical properties since they act at stress concentration and crack initiation sites. Acceptable amount of voids are typically in the range 1–5 vol%. Voids result in lowering the density of the composite materials and the difference between the measured density and predicted density is used to calculate the volume fraction of voids [9].

$$V_v = \frac{w_c}{\rho_{ce}} \left(\frac{\rho_c - \rho_{ce}}{\rho_c} \right), \tag{1.7}$$

where ρ_c is the predicted density (1.3) and ρ_{ce} is the measured density. Including the volume fraction of voids in (1.6) results in

$$V_f + V_m + V_v = 1. \tag{1.8}$$

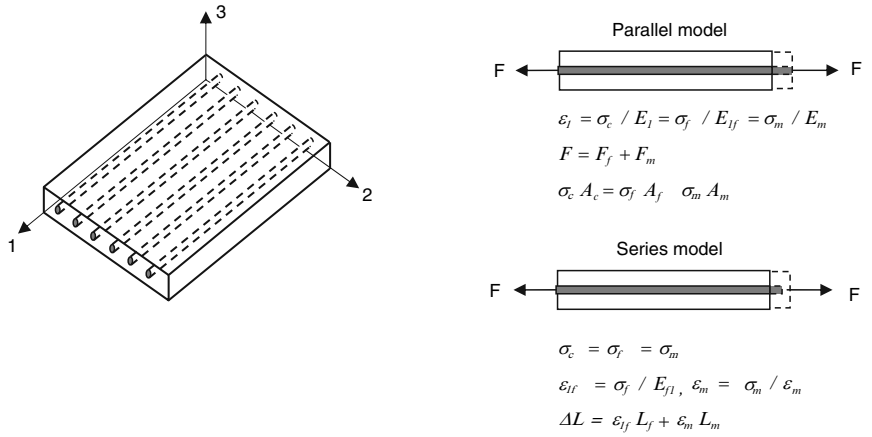

Fig. 1.13 Lamina elastic response in parallel and series models

1.6.2 Elastic Properties

The micromechanics analysis attempts to characterize the elastic behavior of a lamina based on the properties of the constituents. The composite lamina is assumed to be macroscopically homogeneous and linearly elastic. The matrix and the fibers are assumed to be linearly elastic and homogeneous, with the fibers being also anisotropic (transversely isotropic). The interface is completely bonded and both the fiber and matrix are free of voids. The response of the lamina under load can be analyzed using a parallel model or a series model as shown in Fig. 1.13. In the parallel model (also called Voigt model and equal strain model), it is assumed that the fiber and the matrix undergo equal and uniform strain. This leads to the following expression for stiffness in the longitudinal direction

$$E_1 = V_{\mathrm{f}} E_{1\mathrm{f}} + V_{\mathrm{m}} E_{\mathrm{m}}. \tag{1.9}$$

Here the subscripts 1f refer to the longitudinal direction of the fibers. Note that (1.7) is similar to (1.3) and it gives the elastic modulus as the weighted mean of the fibers and the matrix modulus. In a series model (also called Ruess model), it is assumed that the fibers and the matrix are under equal and uniform stress. This leads to the following expression for compliance along the longitudinal direction

$$C_1 = V_{\mathrm{f}} C_{1\mathrm{f}} + V_{\mathrm{m}} C_{\mathrm{m}}. \tag{1.10}$$

Knowing that $C = 1/E$, (1.10) is rewritten as

$$E_1 = \frac{E_{1\mathrm{f}} E_{\mathrm{m}}}{V_{\mathrm{f}} E_{\mathrm{m}} + V_{\mathrm{m}} E_{1\mathrm{f}}}. \tag{1.11}$$

In reality, the state of stress and strain in the lamina is not uniform and (1.9) and (1.11) represent the upper and lower bounds of the lamina longitudinal stiffness, respectively.

The transverse modulus is determined using the series model, but this time by loading the matrix in the transverse direction and using the fiber modulus $E_{2\mathrm{f}}$,

$$E_2 = \frac{E_{2\mathrm{f}} E_{\mathrm{m}}}{V_{\mathrm{f}} E_{\mathrm{m}} + V_{\mathrm{m}} E_{2\mathrm{f}}}. \tag{1.12}$$

In similar manners, the remaining equations for the major Poisson ratio and in plane shear modulus are determined using the equations

$$\nu_{12} = V_{\mathrm{f}} \nu_{12\mathrm{f}} + V_{\mathrm{m}} \nu_{\mathrm{m}}, \tag{1.13}$$

$$G_{12} = \frac{G_{12\mathrm{f}} G_{\mathrm{m}}}{V_{\mathrm{f}} G_{\mathrm{m}} + V_{\mathrm{m}} G_{12\mathrm{f}}}. \tag{1.14}$$

The law of mixture may also be extended to predict the properties of composites that are not unidirectional, such as fabric composites and SMCs. By introducing a reinforcement efficiency factor, β the law of mixtures may be expressed as

$$E_1 = \beta_{\mathrm{f}} V_{\mathrm{f}} E_{1\mathrm{f}} + V_{\mathrm{m}} E_{\mathrm{m}}. \tag{1.15}$$

The reinforcement efficiency factor takes into account the amount of fibers that are effective in the direction of interest. For example, $\beta = 1$ for unidirectional reinforcement, 0.5 for bidirectionally symmetric reinforcement and 0.375 for randomly in-plane arranged reinforcement [4].

1.6.3 Thermal Properties

Expressions for thermal properties of the laminate may also be obtained using micromechanics analysis [10, 11]:

$$\alpha_1 = \frac{\alpha_{1\mathrm{f}} E_{1\mathrm{f}} V_{\mathrm{f}} + \alpha_{\mathrm{m}} E_{\mathrm{m}} V_{\mathrm{m}}}{V_{\mathrm{f}} E_{1\mathrm{f}} + V_{\mathrm{m}} E_{\mathrm{m}}}, \tag{1.16}$$

$$\alpha_2 = \left(1 + \nu_{12\mathrm{f}} \frac{\alpha_{1\mathrm{f}}}{\alpha_{2\mathrm{f}}}\right) \alpha_{2\mathrm{f}} V_{\mathrm{f}} + (1 + \nu_{\mathrm{m}}) \alpha_{\mathrm{m}} V_{\mathrm{m}} - \alpha_{1\mathrm{f}} \nu_{12}, \tag{1.17}$$

$$k_1 = V_{\mathrm{f}} k_{1\mathrm{f}} + V_{\mathrm{m}} k_{\mathrm{m}}, \tag{1.18}$$

$$k_2 = \frac{k_{2\mathrm{f}} k_{\mathrm{m}}}{V_{\mathrm{f}} k_{\mathrm{m}} + V_{\mathrm{m}} k_{2\mathrm{f}}}, \tag{1.19}$$

$$C = \frac{C_{\mathrm{f}} \rho_{\mathrm{f}} V_{\mathrm{f}} + k_{\mathrm{m}} \rho_{\mathrm{m}} V_{\mathrm{m}}}{V_{\mathrm{f}} \rho_{\mathrm{f}} + V_{\mathrm{m}} \rho_{\mathrm{m}}}. \tag{1.20}$$

It is noted that all equations in this section have been derived based on a number of assumptions, some of which may not be representative of real situations. It is therefore safe to regard these as upper bound properties.

1.6.4 Multiply Laminates

Practical structures made out of composites have laminas or plies placed in more than one direction because laminas are weak in directions transverse to the fiber direction. The micromechanics relationships discussed above may be useful in predicting lamina properties with some degree of accuracy. They, however, do not apply for predicting the properties of multiply laminates. Analysis of multiply laminates is treated by macromechanics methods beyond the scope of this book. However, it will be useful to the reader to understand some terminology that is used to describe composite laminates. Laminate code is a shorthand code that is used to specify layup sequence of unidirectional plies or ply groups. The code contains specifications of angles and number of plies used in making the laminate. For example, $[0_2/90/90/0_2]$ is a laminate consisting of 2(0), 1(90), 1(90), 2(0) layup. The subscript in the notation refers to the number of adjacent plies of a given orientation. $[0/45/–45/90]_s$ is a symmetric laminate about the middle plane, the subscript "s" indicates symmetry with respect to the laminate midplane. A number subscript may also be used to indicate the number of repeats of the bracketed sequence. Thus, the layup sequence for the previous notation is 1(0), 1(45), 1(−45), 1(90), 1(90), 1(−45), 1(45), 1(0). An interesting category of laminates is achieved by having equal numbers of plies at 0, 45, −45, and 90°, or at 0, 60, and −60°. Both of these laminate families exhibit inplane elastic properties that are independent of direction (quasi-isotropic).

Example 1.1. Determine the elastic properties of a unidirectional carbon (T300)/epoxy composite with fiber volume fraction $V_f = 0.6$. Compare the results with the data in Table 1.6. The properties for carbon T300 are: $E_1 = 230\,\text{GPa}$, $E_{2f} = 15\,\text{GPa}$, $G_{12f} = 27\,\text{GPa}$, $\nu_{12f} = 0.20$. The properties of epoxy are listed in Table 1.2.

Density:

$$\rho_c = \rho_f V_f + \rho_m V_m = 1{,}760(0.6) + 1{,}150(1-0.6) = 1{,}516\,\text{kg/m}^3\ (1{,}540\,\text{kg/m}^3).$$

Longitudinal modulus:

$$E_1 = V_f E_{1f} + V_m E_m = 0.6\ (230) + (1-0.6)\ (3.2) = 139.3\ \text{GPa}\ (125\ \text{GPa}).$$

Transverse modulus:

$$E_2 = \frac{E_{2f} E_m}{V_f E_m + V_m E_{2f}} = \frac{15\ (3.2)}{0.6\ (3.2) + (1-0.6)\ (15)} = 6.1\ \text{GPa}\ (7.8\ \text{GPa}).$$

In-plane shear modulus:

$$G_{12} = \frac{G_{12f}G_m}{V_f G_m + V_m G_{12f}} = \frac{27\ (1..26)}{0.6\ (1..26) + (1-0.6)\ (27)} = 2.94\ \text{GPa}\ (4.4\ \text{GPa}).$$

Major Poisson ratio:

$$\nu_{12} = V_f \nu_{12f} + V_m \nu_m = 0.6\ (0.20) + (1-0.6)\ (0.35) = 0.26\ (0.34).$$

The experimental values for the elastic properties are given in parenthesis. Note that micromechanics equations work reasonably well for predicting density and longitudinal modulus, but perform poorly in predicting transverse modulus, in-plane shear modulus, and the major Poisson ratio. Semiempirical models have been proposed for better prediction of the lamina properties. Halphin and Tsai models are the most widely used. The reader is referred to [9] for a detailed description of these models.

1.7 Summary

Composite materials consist of a mixture of two or more distinct phases. Generally, the matrix and reinforcement are the two major constituents of a composite material, but other materials such as fillers and additives may also be included. The matrix is the bulk and continuous phase and it could be of metallic, ceramic, or polymeric material. The reinforcement phase is embedded in the matrix in order to enhance its properties by imparting strength and stiffness. The role of the matrix is to transfer external loads to the reinforcement, to support the reinforcement in compression loading, and to protect the reinforcement from adverse environmental conditions. The reinforcement form could be continuous fibers, short fibers, particulates, or whiskers. The reinforcement material could be metallic, ceramic, or organic. The resulting material will have properties that are different than the individual constituents. Depending on the form and volume fraction of the reinforcing phase, the composite material may have isotropic, quasi-isotropic, or anisotropic properties.

FRP composites are a class of composite materials that have polymeric matrix and carbon, glass or aramid fibers as the reinforcement. These materials are characterized by their high specific strength and high specific stiffness. They are also excellent corrosion resistance materials and provide better resistance to fatigue loading. This makes them suitable for various applications in the chemical, marine, transportation, and aerospace industries. In addition, they find wide applications in the sporting and leisure industries. From a manufacturing point of view, designing with composites results in significant reduction in the number of parts, tooling, and assembly. The main disadvantages of composites are low-temperature tolerance, higher cost of manufacturing, and the lack of know-how and material data bases, as compared to metals.

The polymeric matrix in FRPs is a high molecular-weight organic compound consisting primarily of carbon and hydrogen atoms held together by covalent bonds.

Depending on the length and arrangement of these molecular chains, different types and properties of polymers are obtained. There are two major types of polymers: thermoplastics or thermosets. Thermoplastics consist of long hydrocarbon molecules that are held together by secondary bonds and mechanical entanglements. Since these bonds are much weaker than covalent bonds, greater mobility of the molecular chains can be imparting by heating and the polymer can undergo a transition from solid to liquid state. Thermosets consist of hydrocarbon chains that are cross-linked with covalent bonds. Because covalent bonds cannot be broken by heating, thermosets cannot be melted. The molecular arrangement also affects mechanical properties of the polymers. The lack of mobility of thermoset molecules translates into higher strength and stiffness and lower strain to failure than thermoplastics. All polymers undergo a notable reduction in stiffness when heated to a specific temperature. This temperature is known as the glass transition temperature and it practically defines the maximum temperature the polymer can withstand.

The commonly used reinforcements in polymer composites are glass, carbon, or aramid fibers. Fibers are usually produced by drawing liquid material or by pulling a precursor from an orifice. This results in alignment of molecules along the fiber direction and hence imparting higher strength and stiffness along the fiber direction. This is especially the case for carbon and aramid fibers. Glass is an amorphous material and glass fibers are isotropic. Glass fibers are by far the most widely used reinforcement material because of their low cost and good mechanical and thermal properties. Carbon and aramid fibers offer much better mechanical properties at higher cost. Therefore, their use is mostly in advanced composites for the aircraft, aerospace, and defense industries. The most common fiber forms used in manufacturing composites are yarns, woven fabrics, knitted fabrics, braids, and random mats. These forms may be used in the dry form (as in filament winding and pultrusion) or they may be preimpregnated with matrix material and partially cured prior to processing. This is widely used with thermoset polymer resins and the resulting material is called prepreg. Prepregs are usually stored in a freezer and have a limited shelf life.

Manufacturing components with FRP composites involves mixing specific amounts of reinforcement and matrix, forming the compound in the desired shape, and then holding this shape while the matrix is solidified cured by crosslinking. This done under controlled temperature and pressure throughout the process in order to maintain the dimensional stability of the part. Thermoset resins dominate the manufacturing of composites because they offer lower viscosity (better fiber impregnation), lower temperature, and lower pressure processing requirement than thermoplastics. The actual sequence of wetting (mixing) and forming steps may vary from one process to another. The forming of the compound may take place inside a closed mold or over a contoured mold surface. In all cases, the mold surfaces give the part its final shape. There are several processes by which FRP composites are manufactured. These include filament winding, pultrusion, compression molding, liquid transfer molding, wet layup, and prepreg layup. The selection of any particular process depends on the size of component, reinforcement form, production rate, and dimensional accuracy. Filament winding is limited to manufacturing

rotationally symmetric components such as pipes, tanks, and pressure vessels. Pultrusion is limited to manufacturing components of constant cross section such as bars, beams, and channels. In both filament winding and pultrusion the reinforcement form is continuous yarn or roving which is impregnated with resin during the manufacturing process. Compression molding is suited for producing high volumes of parts using preimpregnated molding compounds such as SMC and BMC. Typical components produced include automotive body parts. In RTM techniques the liquid resin is transferred into the mold cavity which contains the reinforcement perform. The resin transfer is aided by gravity, vacuum, and/or pressure. Prepreg layup is the most widely used process in the aircraft industry. In this process the component is made by hand layup of prepreg layers of reinforcement cloth to the desired thickness and fiber orientation. The part is then sealed in a vacuum bag and the entire mold-part assembly is placed in an autoclave for consolidation. Because of the tight control of the layup sequence, temperature, and pressure, high-quality components are produced.

Review Questions and Problems

1. Identify a part that is made from composite materials. Examine the part and describe the following:

   (a) The part shape, appearance and function
   (b) Material(s) it is made from
   (c) Why is the part made from composites?
   (d) Possible manufacturing process(es) used in its manufacture
   (e) Any machining work done on it

2. Indicate the general purposes fulfilled by the matrix in a composite material.
3. Define the terms specific strength and specific modulus. Why are these terms important in discussing composites?
4. What are the major impediments to the widespread adoption of composites in the aircraft industry?
5. Describe the major differences between thermosets and thermoplastics, both in properties and processing methods.
6. Define T_g and discuss its importance in terms of the processing and service conditions of composites.
7. When would aramid fibers be used in preference to carbon fibers?
8. Describe the differences between thermosets and thermoplastics in both molecular structure and method of curing or processing.
9. Distinguish between a finely extruded rod and a fiber (both made form the same material) in both properties and the additional processing that is done to the fiber.
10. Indicate three differences or concerns in using traditional thermoplastics processing methods with composite materials.

11. Describe plain weaves and satin weaves and discuss their ability to conform to complex molds.
12. Discuss the terms isotropic and anisotropic as it applies to the matrix and fibers.
13. Discuss the differences between sheet molding compound and bulk molding compound in terms of manufacturing and molding.
14. Describe vacuum bagging and discuss the purpose of the materials used in making the vacuum bagging?
15. Determine the transverse modulus of a unidirectional carbon/epoxy composite with the properties $E_{2f} = 14.8\,\text{GPa}$, $E_m = 3.45\,\text{GPa}$, $\nu_m = 0.36$, $V_f = 0.65$.
16. The fiber and matrix properties and in-plane properties of AS4/3501-6 carbon/epoxy laminate (60 vol% carbon) are given in the table below. Use the law of mixture to calculate the in-plane laminate properties E_1, ν_{12}, G_{12}, α_1, and ρ. Compare and discuss results with those in table.

Matrix properties	E_m (GPa)	ν_m	$\alpha_m(^\circ C^{-1})$	ρ_m (g/cm^3)
Epoxy	4	0.39	60×10^{-6}	1.25

Fiber properties	E_{1f} (GPa)	E_{2f} (GPa)	ν_{12f}	ν_{23f}
AS4 Carbon fiber	228	14.2	0.2	0.25

Fiber properties	G_{12f} (GPa)	G_{23f} (GPa)	α_{1f} ($^\circ C^{-1}$)	α_{2f} ($^\circ C^{-1}$)	ρ_f (g/cm^3)
AS4 Carbon fiber	14.2	7.1	-0.99×10^{-6}	10.1×10^{-6}	1.88

Composite properties	E_{11} (GPa)	E_{22} (GPa)	ν_{21}	G_{12} (GPa)	α_1 ($^\circ C^{-1}$)	α_2 ($^\circ C^{-1}$)	ρ (g/cm^3)
AS4/3501-6	131.0	11.2	0.28	6.55	-6.3×10^{-8}	2.88×10^{-5}	1.55

17. Determine the inplane shear modulus of a glass epoxy composite with the properties $G_f = 28.3\,\text{GPa}$, $G_m = 1.27\,\text{GPa}$, and $V_f = 0.55$.
18. Determine the elastic properties of a glass/polyester sheet molding compound having a volume fraction of 0.20. Compare the results with Fig. 1.2.

References

1. M. F. Ashby, Technology of the 1990s: Advanced Materials and Predictive Design, Philosophical Transactions of The Royal Society of London A322, 393–407, 1987.
2. K. K. Chawla, Composite Materials: Science and Engineering, Springer, New York, NY, 1987.
3. F. L. Matthews and R. D. Rawlings, Composite Materials: Engineering and Science, Chapman & Hall, London, 1994.
4. B. T. Astrom, Manufacturing of Polymer Composites, Nelson Thornes, UK, 2002.

5. Aerospace Engineering Online: Top Fifteen Technologies, Page 8, CNC Fiber Placement Used to Create an All-Composite Fuselage, 10 April 2000, http://www.sae.org/aeromag/techinnovations/1298t08.htm, visited 13 March 2008.
6. R. B. Aronson, Cutting Composites, Manufacturing Engineering 136(3), 2006.
7. S. G. Advani and E. M. Sozer, Process Modeling in Composites Manufacturing, Marcel Dekker, New York, NY, 2003.
8. ASM. Handbook, vol. 21: Composites, ASM International, 2001
9. A. K. Kaw, Mechanics of Composite Materials, 2nd Edition, Taylor & Francis, Boca Raton, FL, 2006
10. I. M. Daniel and O. Ishai, Engineering Mechanics of Composite Materials, 2nd Edition, Oxford University Press, New York, NY, 2006.
11. C. C. Chamis, Simplified Composite Micromechanics Equations for Hygral Thermal and Mechanical Properties, SPI Composites Institute Annual Conference, 38, 21-C, 1983.

Chapter 2
Conventional Machining Operations

Despite the fact that fiber-reinforced polymer components (FRP) are mostly produced near net shape, machining is often required in order to bring the component into dimensional requirements and prepare it for assembly. Machining of FRPs may take place before and/or after layup and curing. The machining before curing involves cutting the reinforcement material to the proper size to fit the contour before it is laid in/onto a mold and cured. The reinforcement material is either dry or resin impregnated fibers, fiber weaves, and fabrics. The predominantly two-dimensional contouring is most appropriately carried out by cutting techniques common to the textiles industry. These include ultrasonic cutting, reciprocating knife, shearing, and punching. Waterjet cutting and laser beam are also widely used. Cutting of prepregs and dry reinforcement is beyond the scope of this book and will not be discussed here. Our discussion is focused on the more important processes of machining of cured composites.

Machining of cured FRPs is carried out by conventional or nonconventional material removal methods. The conventional methods most frequently used are edge trimming, milling, drilling, countersinking, turning, sawing, and grinding. Among the nonconventional machining processes are abrasive waterjet and laser beam cutting. Some of these processes were originally developed either for the woodworking or for the metal working industries. However, they were conveniently transferred to machining FRPs after proper adjustments to tool geometry, cutting speeds, and feed rates are made. Nevertheless, kinematics of the machining process remains the same and most of the kinematic relationships in metal machining still hold. This chapter provides a discussion of the most important kinematics relationships for conventional machining processes that are frequently used in machining cured FRPs. Detailed analysis of these and other machining processes can be found in [1–3].

J.Y. Sheikh-Ahmad, *Machining of Polymer Composites*.
DOI: 10.1007/978-0-387-68619-6,

2.1 Requirements for Machining FRPs

Machining FRPs is different in many aspects from machining metals. FRPs are inhomogeneous materials that consist of distinctly different phases. The reinforcement fibers are strong and brittle and may have poor thermal conductivity, as in the case of aramid and glass fibers. The polymer matrix, on the other hand, is weak and somewhat ductile. Its thermal properties are poor and its tolerance for high temperatures is a limiting factor in postcure processing. The machining of most homogeneous and ductile metals is characterized by shearing and plastic deformation and the shearing action forms a continuous chip that flows on the tool face. Eventually, under fixed cutting conditions the cutting process reaches a steady state for which the cutting forces, cutting temperatures, and surface conditions could be predicted to an acceptable accuracy. The machining of FRPs, on the other hand, is characterized by uncontrolled intermittent fracture. Oscillating cutting forces are typical because of the intermittent fracture of the fibers. The machinability of FRPs is primarily determined by the physical and mechanical properties of the fiber and matrix, fiber content, and fiber orientation. While glass and carbon fibers break in a brittle manner ahead of the cutting edge, the tougher aramid fibers evade shearing and tend to bend ahead of the advancing cutting edge. Thus the surface quality of the machined edge is greatly affected by the type of fiber reinforcement and its orientation. The cutting forces are also dependent on the fibers as the matrix strength is typically inferior to that of the fibers.

The cutting temperatures are also affected by the thermal properties and orientation of the fibers. Carbon fibers are more capable of conducting heat along their direction than glass or aramid fibers and thus are responsible for dissipating heat away from the cutting zone. The polymeric matrix is not capable of withstanding high temperatures common in machining metals and precautions should be made not to expose the matrix to excessive heat for a prolonged time. During the application of coolant, moisture absorption by the matrix or fibers may jeopardize form, dimensional accuracy, and mechanical properties of the machined part. Different thermal expansion coefficients of matrix and fibers lead to thermal stresses which may result in deformation and part damage.

Machined edge quality is the deciding factor when evaluating the machinability of FRPs. The term “quality” refers to both geometric features and the extent of material damage caused by the machining process. The measurement of both of these criteria is much more difficult for FRPs than for metals because of the inhomogeneous structure of the former. At present, commonly accepted standards of measurement techniques and characteristic indices do not exist. The aviation industry, which is becoming a substantial beneficiary of composites technology, has the most stringent requirements on machining quality. Delamination is not tolerated on components that are classified as primary structural components while some repairable delamination may be tolerated on secondary components. Delamination is caused by the low interlaminate strength of the composite structure and high transverse forces resulting from cutting. High cutting forces, in turn result from the use of improper speeds and feeds, improper tool geometry and tool wear.

Tool materials in machining composites should be capable of withstanding the abrasiveness of fibers and debris resulting from machining. The tool geometry should provide a keen edge capable of neatly shearing the fibers. These two requirements are distinctively different from those expected of a cutting tool in metal machining.

2.2 Turning

Turning utilizes a single cutting tool to create a surface of revolution. The cylindrical workpiece is rotated around its axis while a cutting tool is fed parallel to the axis of rotation. As the cutting tool is engaged into the workpiece, a new surface of revolution is generated by removing a layer of material whose thickness is equal to the depth of the tool engagement. A typical machine tool that generates the necessary motions for carrying out this operation is an engine lathe. A typical engine lathe is shown in Fig. 2.1. CNC lathe operates on similar kinematics principles.

The machine tool provides a primary motion to the workpiece in revolutions per minute and a secondary motion to the cutting tool in millimeters per revolution. The combined motion that generates the surface is the vector addition of these two motions. For most practical applications, the feed motion is much smaller than the primary motion and the cutting speed is determined by the primary motion alone.

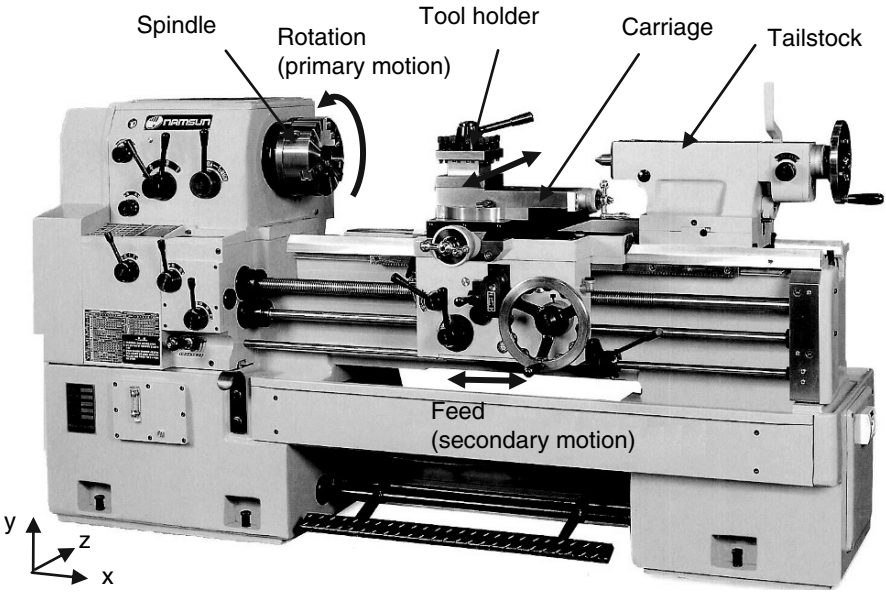

Fig. 2.1 Principal components and movements of a typical lathe

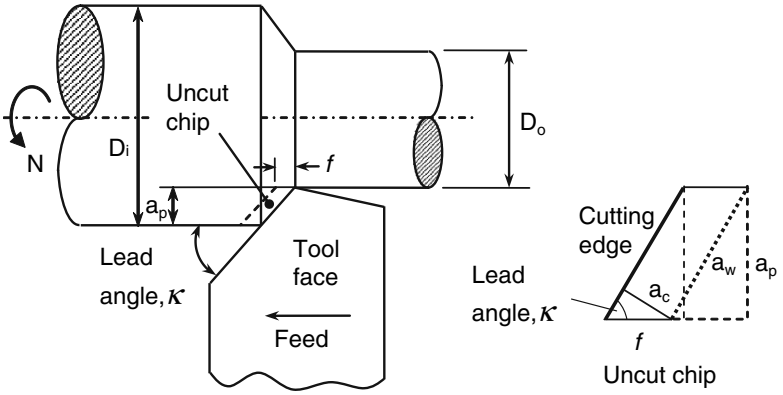

Fig. 2.2 Cutting geometry in turning

The following relationships apply to single point tools with small corner radius or when the depth of cut is very large as compared to the corner radius Fig. 2.2 shows the cutting geometry with a single point cutting tool.

The cutting speed is determined by the rotational speed of the spindle, N, given in rev/min, and the workpiece initial and final diameters, D_i and D_o, respectively

$$v = \pi N \frac{D_\mathrm{i} + D_\mathrm{o}}{2} \cong \pi N D_\mathrm{i}. \tag{2.1}$$

The average feed motion advances the tool per revolution along a specified direction. The feed, f, is given in mm/rev and the feed speed, v_f, is related to the feed by

$$v_\mathrm{f} = fN \tag{2.2}$$

The radial depth of cut describes the thickness of material removed from the workpiece and is given by

$$a_\mathrm{p} = \frac{D_\mathrm{i} - D_\mathrm{o}}{2}. \tag{2.3}$$

This material is removed in the form of a chip (swarf) which flows upward on the tool rake face. The uncut chip thickness is measured normal to the cutting edge and is given by:

$$a_\mathrm{c} = f \sin\kappa, \tag{2.4}$$

where κ is the cutting edge lead angle. The width of the uncut chip is given by

$$a_\mathrm{w} = a_\mathrm{p} / \sin\kappa. \tag{2.5}$$

Therefore, the uncut chip cross-sectional area is given by

$$A_\mathrm{c} = a_\mathrm{c} a_\mathrm{w} = f a_\mathrm{p}. \tag{2.6}$$

The material removal rate, Z_w, is given as the product of cutting speed and uncut chip area

$$Z_\mathrm{w} \approx A_\mathrm{c} v = f a_\mathrm{p} v = \pi f a_\mathrm{p} N D_\mathrm{i}. \tag{2.7}$$

The time required for turning a length, l_w, in the feed direction is given by

$$t_m = \frac{l_w}{v_f} = \frac{l_w}{fN}. \tag{2.8}$$

The specific cutting power, also referred to as specific cutting pressure, is the net power required to remove a unit volume of the material in a unit time. It is related to the cutting force in the direction of cutting speed, F_c, and to the material removal rate by

$$u_s = \frac{F_c v}{Z_w} = \frac{F_c}{A_c}. \tag{2.9}$$

Then the power required to remove material is given by the product of material removal rate and specific cutting power for the workpiece material, u_s

$$P_m = u_s \cdot Z_w. \tag{2.10}$$

The spindle motor power can be estimated as:

$$P_e = \frac{P_m}{\eta} + P_i, \tag{2.11}$$

where P_i is the idling power and η is the drive system efficiency.

2.3 Single Point Cutting Tools

Single point cutting tools are the primary cutting tools used in turning. These tools have a single cutting surface and a single cutting edge that is responsible for material removal. The active cutting element is shaped by three oblique surfaces that meet at the tool corner or nose. The geometry of a standard single point cutting tool is shown in Fig. 2.3. The three surfaces making the cutting element are the rake face, flank face, and heel. The inclination of these surfaces with respect to the shank defines a set of angles that are used along with the corner radius as the tool identification, or signature. During cutting the chip flows on the rake face and its flow direction is affected by the rake angles. The forces generated are also affected by the rake angles and the lead angle. The purpose of the side and end relief angles is to provide clearance between the cutting element and the workpiece surface. The side relief angle profoundly influences flank tool wear. Traditionally, single point cutting tools were ground from high-speed steel blanks. The toughness of high-speed steel allows it to be ground to a keen cutting edge, which is highly desirable when machining FRPs. A sharp cutting edge in combination with a positive rake angle allows the fibers to be neatly sheared and thus provides a good surface roughness. However, high-speed steel tools wear quite rapidly when machining FRPs because of the high abrasiveness of the fibers, and their use generally becomes impractical. Steel shanks holders tipped with brazed or indexable carbide inserts (Fig. 2.4) are more commonly used.

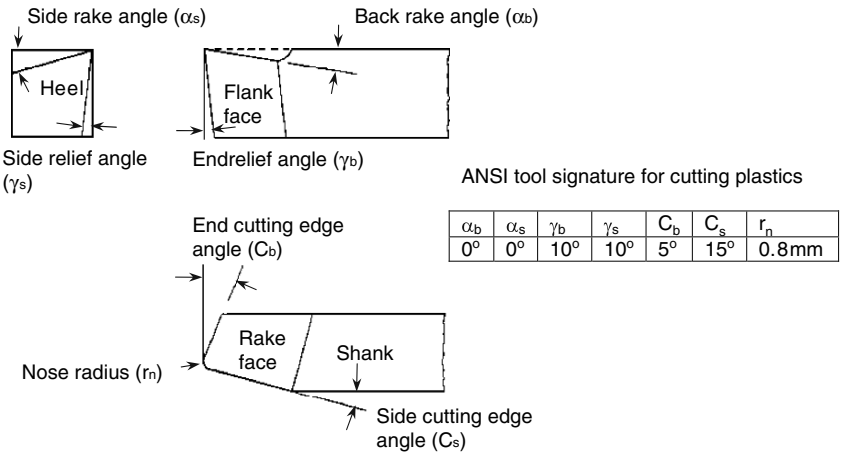

α_b	α_s	γ_b	γ_s	C_b	C_s	r_n
0°	0°	10°	10°	5°	15°	0.8mm

Fig. 2.3 Standard ANSI terminology describing a single point cutting tool

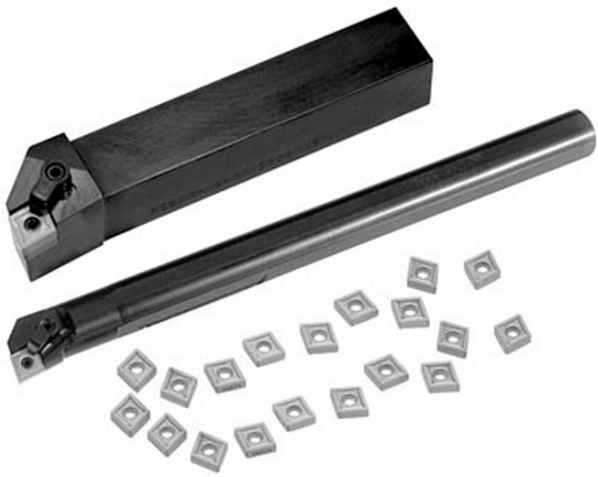

Fig. 2.4 Typical insert tipped single point turning and boring tools

2.4 Milling and Trimming

In milling, material is removed from the workpiece by a rotating cutterhead that may have more that one active cutting edge. The types of milling operations that are most common in machining FRPs are peripheral milling or profiling and end milling. Figure 2.5 illustrates these milling operations. Peripheral milling uses the cutting edges on the periphery of the tool. The machined surface is parallel to the

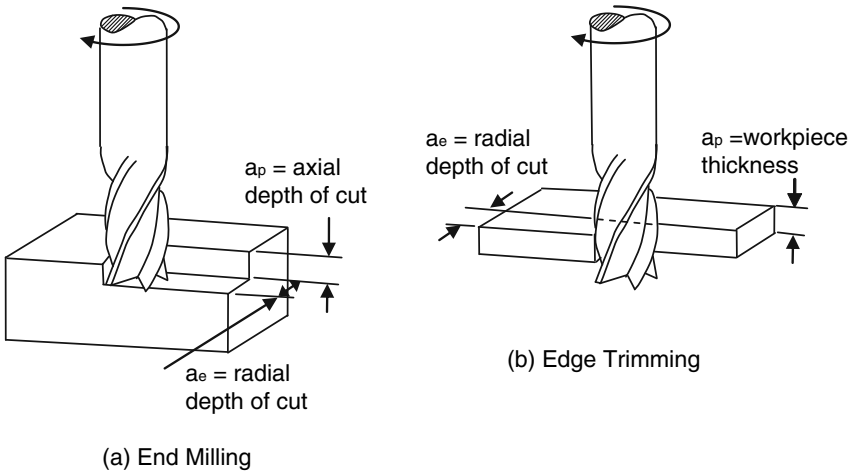

Fig. 2.5 Types of milling operations

axis of rotation of the cutter and the engagement into the workpiece is in the radial direction of the cutter (Fig. 2.5b). Peripheral milling is more appropriately called edge trimming because the tool diameter is usually small and the axial engagement encompasses the entire thickness of the workpiece. End milling is similar to peripheral milling, except that the axial engagement may be less than the thickness of the part and a slot is obtained (Fig. 2.5a). The machine tool most commonly used is a vertical milling machine. The machine tool provides the primary motion to the spindle (to which the cutter is held) and feed motions to the machine table (to which the workpiece is held). CNC routers capable of providing higher spindle speeds and feed rates, more flexibility, and larger workspace than a typical milling machine are commonly used in high production facilities. Figure 2.6 shows the principal components and movements of typical industrial three-axis CNC router. Hand-held routers are commonly used for edge trimming of thin workpiece. The router provides the primary rotational motion to the cutter while the operator feeds the tool into the workpiece manually.

End milling and trimming operations are further classified into up (or conventional) milling and down (or climb) milling, depending on how the cutting edge approaches the workpiece. These operations are illustrated in Fig. 2.7. In up milling, the direction of cutting speed of the edge in contact with the workpiece is opposite to the direction of feed. In down milling, the direction of the cutting speed is the same as that of the feed. The resulting chip area in both cases has a "comma" shape and the length of the chip is described by a torchoid that results from the superposition of peripheral motion and feed motion. In up milling the cutting edge begins engaging the chip at the thin section of the comma shape. This results in low engagement forces and in lifting up of the workpiece. In down milling, the cutting edge engages the chip at the thick section of the comma shape. The engagement forces are high

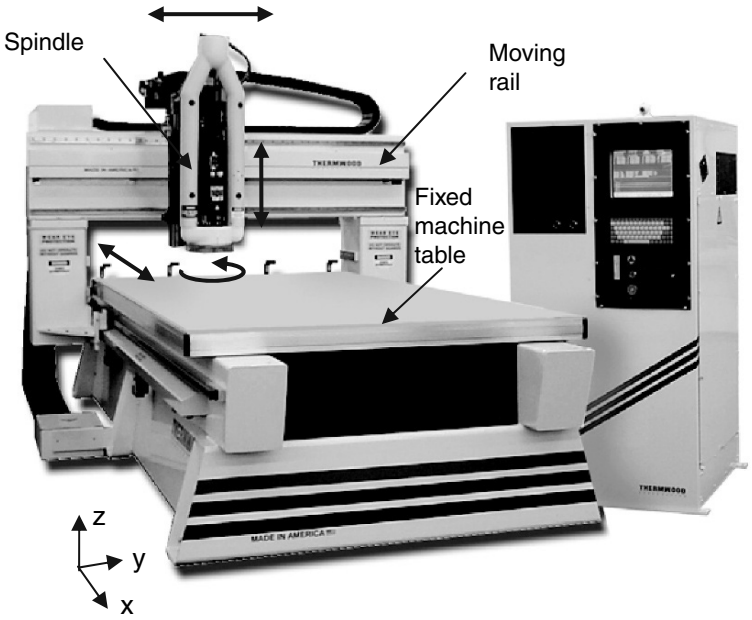

Fig. 2.6 Principal components and movements of a three-axis gantry bridge router (courtesy of Thermwood Corporation)

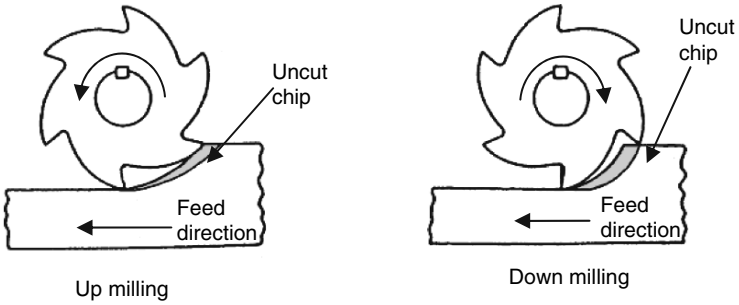

Fig. 2.7 Illustration of up and down milling operations

and result in pushing the workpiece against the workholding surface. Cutting forces in milling are also not continuous. In up milling, the forces gradually increase from zero at beginning of tool engagement to a maximum when the cutting edge is about to leave the workpiece. Forces drop to zero again when the cutting edge leaves the workpiece.

Figure 2.8 shows a schematic of the cutting geometry for one cutting edge in up milling. The tool path is torchoidal and is generated from the combination of rotational (spindle) and translational (feed) motions. The exact geometry and kinematics of up and down milling have been thoroughly investigated by Martellotti [4, 5] and

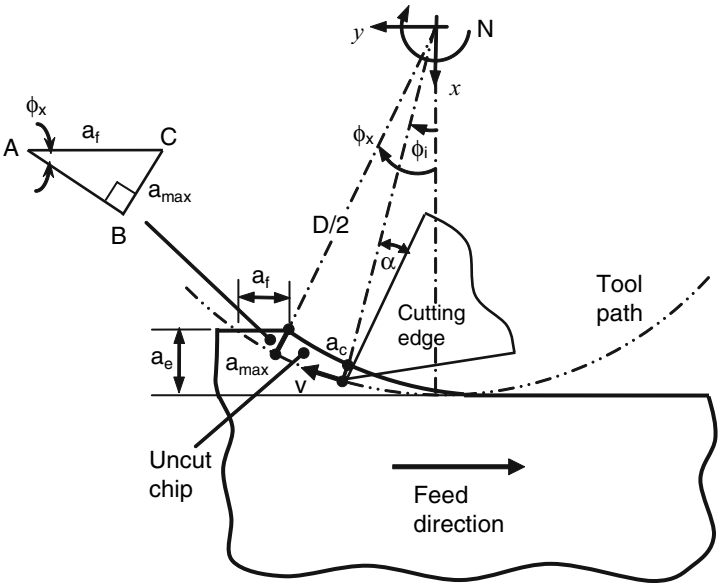

Fig. 2.8 Cutting geometry in end milling, peripheral milling and edge trimming

Foenigsberger and Sabberwal [6] among others. The basic expressions describing this motion are given here. The cutting speed is given as a function of the spindle speed, N, and tool diameter, D, by the relationship

$$v = \pi DN. \tag{2.12}$$

The feed speed, v_f, and the feed per revolution, f, are related by

$$f = \frac{v_\mathrm{f}}{N}. \tag{2.13}$$

The feed per tooth, a_f, which defines the translation of the workpiece between the engagement of successive cutting edges, is expressed as a function of the feed speed, v_f, the spindle speed, N, and the number of cutting edges on the cutterhead, T

$$a_\mathrm{f} = \frac{v_\mathrm{f}}{TN}. \tag{2.14}$$

The length of the cutting edge engagement in the workpiece is given by the expression:

$$L_\mathrm{c} = \frac{D}{2}\cos^{-1}\left(1 - \frac{2a_\mathrm{e}}{D}\right) \pm \frac{a_\mathrm{f}T}{\pi D}\left(Da_\mathrm{e} - a_\mathrm{e}^2\right)^{1/2}, \tag{2.15}$$

where the plus sign is used for up milling and the negative sign is used for down milling. The average thickness of the undeformed chip is given by

$$a_\mathrm{avg} = \frac{a_\mathrm{f}a_\mathrm{e}}{L_\mathrm{c}}. \tag{2.16}$$

From these equations it is observed that the tool path is longer in up milling than in down milling. The uncut chip areas are the same for up milling and down milling, but the average chip thickness in down milling is greater. For a given depth of cut, a_e, the maximum uncut chip thickness for up milling is smaller than that for down milling. This explains the higher requirement of cutting power and the higher cutting forces associated with down milling.

For small feed speeds as compared to the spindle speed, the torchoidal path can be approximated by a circular arc and the uncut chip geometry for up and down milling becomes approximately the same. This happens to be the case for most machining applications of FRPs. The total engagement angle, ϕ_x, is given as a function of the tool diameter and the radial depth of cut, a_e

$$\cos\phi_x = 1 - \frac{2a_e}{D}. \tag{2.17}$$

The instantaneous uncut chip thickness, a_c, measured normal to the cutting path varies continuously with engagement angle, ϕ_i, and is maximum at the exit angle ϕ_x. A lead angle may be given to the cutting edge, similar to what is shown in Fig. 2.2, and results in thinning the uncut chip. The lead angle is 90° for peripheral and end milling. The maximum uncut chip thickness, a_{max}, is calculated from the triangle ABC as

$$a_{max} = a_f \sin\kappa \sin\phi_x. \tag{2.18}$$

For small depths of cut as compared to tool diameter, the maximum chip thickness can also approximated by

$$a_{max} = 2a_f\sqrt{\frac{a_e}{D}}. \tag{2.19}$$

The instantaneous uncut chip thickness, a_c, at engagement angle ϕ_i, and the average chip thickness, a_{avg}, are given by:

$$a_c = a_f \sin\kappa \sin\phi_i \tag{2.20}$$

and

$$a_{avg} = a_f\sqrt{\frac{a_e}{D}}, \tag{2.21}$$

respectively. The length of chip being cut is approximated by

$$L_c = 0.5D\cos^{-1}\left(1 - \frac{2a_e}{D}\right) \approx \sqrt{a_e D}. \tag{2.22}$$

The material removal rate, Z_w, in end milling is given by the products of the radial depth of cut, a_e axial depth of cut, a_p, and feed speed. In edge trimming and profiling, a_p represents the thickness of the workpiece

$$Z_w = a_e a_p v_f. \tag{2.23}$$

The time required for milling a length, L_w, is the time taken by the tool to traverse the length of the workpiece and any additional distance required to completely clear the tool off the workpiece. The machining time is given by:

$$t_m = \frac{L_w + L_e}{v_f}, \tag{2.24}$$

where L_e is the distance required to clear the workpiece by the tool and is given by

$$L_e = \sqrt{a_e(D - a_e)}. \tag{2.25}$$

Example 2.1. An edge trimming operation of particleboard uses a 19.0 mm cutterhead with one major cutting edge in a down-milling configuration. The spindle speed is 5,000 rpm and the feed rate is 1.27 m/min. The radial depth of cut is 1 mm, the length of workpiece is 500 mm and its thickness is 19 mm. The specific cutting power for particleboard is $65\,\mathrm{N/mm^2}$. Determine:

(a) Total engagement angle
(b) Maximum chip thickness
(c) Material removal rate
(d) Time to finish one edge
(e) Power required for machining

Solution

The figure below shows the cutting geometry.

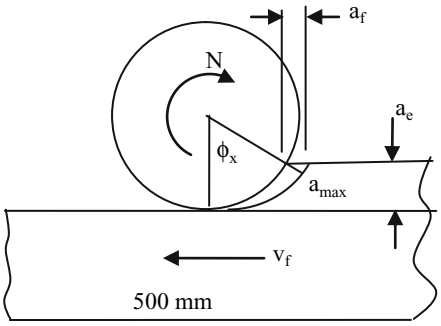

(a) Total engagement angle is given by

$$\phi_x = \cos^{-1}\left(1 - \frac{2a_e}{D}\right) = \cos^{-1}\left(1 - \frac{2(1)}{19}\right) = \cos^{-1}0.895, \quad \phi_x = 26.5^\circ.$$

(b) Maximum chip thickness is given by

$$a_{max} = \frac{v_f \sin\phi_x}{NT} = \frac{1.27\sin 26.5}{1(5{,}000)} = 1.134 \times 10^{-4}\,\mathrm{m} = 0.113\,\mathrm{mm},$$

where $T = 1$ is the number of cutting edges on the cutterhead.

(c) Material removal rate is given by

$$Z_w = a_e a_p v_f = (1)(19)(1.27 \times 10^3) = 24,130\,\text{mm}^3/\text{min} = 402.2\,\text{mm}^3/\text{s}$$

(d) Time to trim one edge $t_m = (L_w + L_e)/v_f$, where $L_e = \sqrt{a_e\,(D - a_e)}$

$$L_e = \sqrt{1(19-1)} = 4.24\,\text{mm},$$
$$t_m = (500 + 4.24)/1.27 \times 10^3 = 0.397\,\text{min} = 23.8\,\text{s}.$$

(e) Power required for machining

$$P_m = u_s Z_w = 65(402.2) = 26,141\,\text{N mm/s} = 26.14\,\text{W}.$$

This is an average power that does not reflect the actual variation in chip thickness and hence, the instantaneous power consumption. The chip thickness varies with ϕ_i according to the relationship

$$a_c = \frac{v_f \sin\phi_i}{NT} = \frac{1,270\sin\phi_i}{1(5,000)} = 0.254\sin\phi_i\,(\text{mm}).$$

The instantaneous chip area is

$$A_c = a_c a_p = 19(0.254\sin\phi_i) = 4.826\sin\phi_i\,(\text{mm}^2).$$

The instantaneous tangential cutting force is

$$F_{ti} = u_s A_{ci} = 65(4.826\sin\phi_i) = 313.69\sin\phi_i\,(\text{N}).$$

The instantaneous machining power is $P_{mi} = F_{ti} v$, where

$v = \pi DN = (3.14)(19)(5,000) = 298,451.3\,\text{mm/min} = 4,974.2\,\text{mm/s}.$
Then $P_{mi} = 313.69\sin\phi_i(4,974.2) = 1,560,356\sin\phi_i(\text{N mm/s}) = 1,560\sin\phi_i(\text{W}).$

The variation of power with ϕ_i is given as:

$\phi_i = 26.5^\circ$, $P_{mi} = 696\,\text{W}$ (at entry)
$\phi_i = 13^\circ$, $P_{mi} = 351\,\text{W}$ (halfway in the cut)
$\phi_i = 0$, $P_{mi} = 0$ (at exit)

2.5 Drilling

Drilling is the most common material removal operation in metals and composites machining. It is used for making holes required for assembly. Drilling is done on conventional upright drilling machines, milling machines, and various specialized machines. In drilling on a vertical drill press, the spindle provides the primary rotational motion to the drill bit and the feed into the workpiece is provided through the

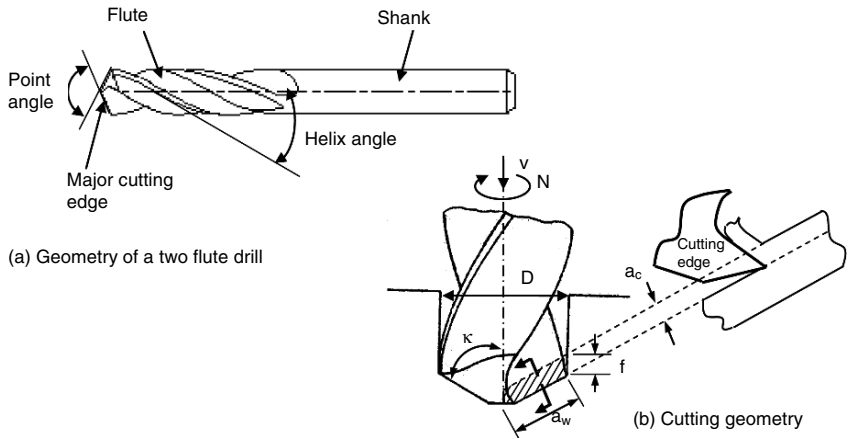

Fig. 2.9 Cutting geometry in drilling

spindle axis. The most common drill bit is a two flute twist drill depicted in Fig. 2.9. A two flute twist drill has two major cutting edges forming the drill point angle. Each one of the major cutting edge acts like a single point cutting tool as shown in Fig. 2.9b. The lead angle for the cutting edge is half of the drill point angle. The flute provides a way for the chip to clear the cutting zone and for coolant to be supplied to the cutting tip.

For a drill of diameter D, which is being rotated by N revolutions per minute, the cutting speed is given by (2.12). The drill bit is feed into the workpiece with a feed per revolution, f. The feed speed, v_f, is related to the feed per revolution by

$$v_f = fN. \tag{2.26}$$

The feed per tooth is related to the feed per revolution and the number of flutes, T, by

$$a_f = \frac{f}{T}. \tag{2.27}$$

The width of the chip is related to the tool diameter and half the drill point angle, κ (also known as the lead angle) by

$$a_w = \frac{D}{2\sin\kappa}. \tag{2.28}$$

The uncut chip thickness is given by

$$a_c = a_f \sin\kappa = \frac{f}{T}\sin\kappa. \tag{2.29}$$

The material removal rate, Z_w, is given by

$$Z_w = v_f\left(\frac{\pi D^2}{4}\right) = \frac{\pi f D^2 N}{4}. \tag{2.30}$$

The time required to drill a through hole in a workpiece of thickness, L_h, is calculated as the time required for the drill point to traverse the thickness and clear the drill cone. An additional distance, L_e, is required to clear the drill cone, which is given by

$$L_e = \frac{D}{2\tan\kappa}. \tag{2.31}$$

The time to drill through the workpiece is given by

$$t_m = \frac{L_h + L_e}{v_f}. \tag{2.32}$$

Example 2.2. A two-flute twist drill is used to drill a hole in a particleboard that is 19 mm thick. The drill diameter is 5 mm, the drill point angle is 90°, and the spindle speed is 500 rpm and the feed rate is 0.5 mm/s. The specific cutting energy for particleboard is $65\,\mathrm{N/mm^2}$. Determine:

(a) The cutting speed
(b) Maximum chip thickness
(c) Material removal rate
(d) The time required for drilling one hole
(e) The power required for drilling

Solution

(a) $v = \pi DN = (3.14)(5/1{,}000)(500) = 7.85\,\mathrm{m/min}$.
(b) $f = \frac{v_f}{N} = \frac{0.5}{(500/60)} = 0.06\,\mathrm{mm/rev}$,

$$a_c = a_f \sin\kappa = \frac{f}{T}\sin\kappa = (0.06/2)\sin 45^\circ = 0.0212\,\mathrm{mm}.$$

(c) $Z_w = v_f\left(\frac{\pi D^2}{4}\right) = \frac{\pi f D^2 N}{4} = \frac{(0.5)(3.14)(5^2)}{4} = 9.82\,\mathrm{mm^3/s}$.
(d) $L_e = \frac{D}{2\tan\kappa} = \frac{5}{2\tan 45} = 2.5\,\mathrm{mm}$,

$$t_m = \frac{19 + 2.5}{0.5} = 43\,\mathrm{s}.$$

(e) $P_m = u_s Z_w = 65(9.82) = 638.6\,\mathrm{N\ mm/s} = 0.6386\,\mathrm{W}$.

Again, it is noted here that this power is not indicative of the cutting power, but rather the feed power. To determine the cutting power, follow the steps used in the milling example. Determine uncut chip thickness, estimate cutting forces, and determine torque and power from cutting forces

$$A_c = a_c a_w = \frac{f}{T}\sin\kappa\frac{D}{2\sin\kappa} = \frac{fD}{2T} = \frac{(0.06)(5)}{2(2)} = 0.075\,\mathrm{mm^2}.$$

The tangential cutting force is estimated as

$$F_t = A_c u_s = 65(0.075) = 4.875\,\mathrm{N}.$$

The torque required to overcome this force is calculated as

$$M = F_t D/2 = 4.875(0.0025) = 0.0122\,\text{N m}.$$

Finally, the machining power is calculated as

$$P_m = M(2\pi N/60) = 0.0122(2)(3.14)(500)/2 = 19.154\,\text{W}.$$

2.6 Abrasive Cutting

Abrasive wheels are commonly used in finishing operations of metals and ceramics where the resulting surface finish is the criterion. Abrasive wheels and cutters are also used in machining FRPs because they provide less mechanical damage and better surface finish than traditional cutting tool geometries. Examples of diamond abrasive cutting tools are shown in Fig. 2.10. In these tools, many diamond particles are brazed or bonded to the tool shank or body and act as multiple cutting points. Abrasive cutters are mainly classified by the abrasive particle size and the method by which the particles are bonded to the tool body. The size of abrasive particles is identified by a grit number, which is a function of sieve size. The smaller the sieve size, the larger the grit number.

Abrasive cutting is characterized mainly by negative rake angles, by small depths of cut, by wide edge angles, and by a limited grain protrusion as shown in Fig. 2.11. Each one of these diamond particles acts as a single point cutting tool and is responsible for removing a tiny chip (2–50 μm) as illustrated in this figure. Because each abrasive particle only removes a tiny chip at a time, many abrasive particles are needed to produce significant material removal rates. In addition, the power required for grinding is far higher than that for other machining operations because the specific cutting energy increases rapidly with a decrease in chip size.

Fig. 2.10 Diamond abrasive cutting wheels (*left*) and routers (*right*). Courtesy of Abrasive Technology, USA

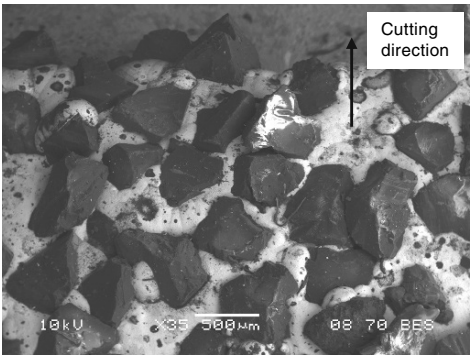

Cutting edge of a diamond abrasive cutter. The diamond particles were mounted by electroplating on a steel shank.

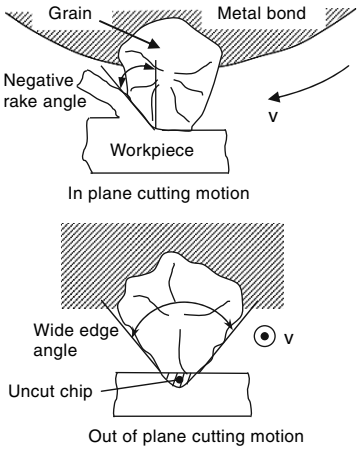

Fig. 2.11 Multiple point cutting with negative rake in an abrasive cutter

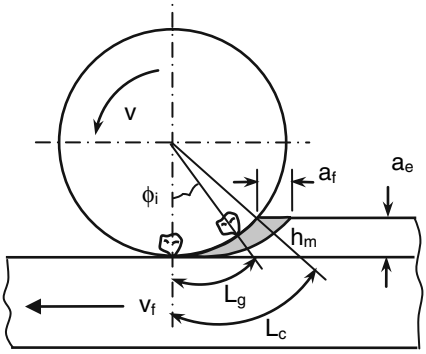

Fig. 2.12 Material removal with abrasive cutter

Trimming with abrasive cutters is similar to trimming with an end mill and kinematic analysis of the tool path is similar. Detailed analysis of grinding and abrasive cutting is given in [3]. The cutter removes material in the form of a "comma"-shaped chip. In a real situation, this chip consists of many tiny "comma"-shaped chips, each of which is removed by an abrasive particle. For simplicity, an idealized distribution of the particles around the cutter periphery may be assumed where the particles are equally spaced by a distance L_g as shown in Fig. 2.12. The angular position, ϕ_i, of grain G_i may be determined by (2.17). The cutting velocity of a cutting point is determined by (2.12). The feed per cutting point is equal to the product of the feed speed v_f and the time elapsed between successive cutting points, L_g/v

$$a_f = \frac{L_g v_f}{v}. \tag{2.33}$$

The maximum uncut chip thickness taken by a cutting point is indicated by h_m and is determined from the expression:

$$h_m = 2a_f \left(\frac{a_e}{D}\right)^{1/2} \left(1 - \frac{a_e}{D}\right)^{1/2} - \frac{a_f^2}{D} \tag{2.34}$$

and for small depths of cut as compared to tool diameter ($a_e \ll D$),

$$h_m = 2a_f \left(\frac{a_e}{D}\right)^{1/2} - \frac{a_f^2}{D}. \tag{2.35}$$

Or substituting a_f from (2.33),

$$h_m = 2L_g \left(\frac{v_f}{v}\right) \left(\frac{a_e}{D}\right)^{1/2} - \frac{L_g^2}{D} \left(\frac{v_f}{v}\right)^2. \tag{2.35a}$$

The magnitude of h_m is typically an order of magnitude smaller than the depth of cut a_e and is much less than L_c. In this case the shape of the undeformed chip is nearly triangular. In order to calculate the undeformed chip thickness an estimate of the grain spacing, L_g is needed. A number of methods have been devised to measure wheel topography and obtain information on grain density C. The grain spacing is related the grain density and maximum chip thickness by

$$L_g = \frac{2}{Crh_m}, \tag{2.35b}$$

where r is the ratio of effective undeformed chip width to the average chip thickness, h_a. For $h_m \ll L_c$ the average chip thickness is approximately half of the maximum chip thickness, $h_a \cong 0.5h_m$.

The contact length between the wheel and the workpiece, L_c can be determined using (2.15) or (2.22) by assuming the contact length to be a circular arc. This relationship can be adjusted to account for the feed motion, resulting into what is known as the kinematic contact length, L_k,

$$L_k = L_c \left(1 \pm \frac{1}{q}\right) + \frac{a_f}{2}, \tag{2.36}$$

where $q = v/v_f$ and positive is used for up grinding and negative is used for down grinding. For most grinding applications $v \gg v_f$ and the contribution of a_f is very small, in which case

$$L_k \approx L_c = \sqrt{a_e D}. \tag{2.37}$$

The material removal rate in abrasive cutting may be determined from the product of feed speed and the cross section of the chip normal to the feed speed,

$$Z_w = a_e \cdot a_p \cdot v_f. \tag{2.38}$$

Here, a_p denotes the width of the workpiece in edge trimming and the width of the cutter in peripheral grinding. The material removal rate can also be represented by a band of material of a uniform thickness h_q and width a_p that is being removed at the cutting speed v,

$$Z_w = h_q \cdot a_p \cdot v. \tag{2.39}$$

The uniform thickness h_q is referred to as the equivalent chip thickness and is given by

$$h_q = a_e \frac{v_f}{v}. \tag{2.40}$$

The cutting time relationship for grinding is similar to that given for peripheral milling (2.24),

$$t_m = \frac{l_w + l_e}{v_f}. \tag{2.24}$$

In slot cutting with an abrasive wheel, the wheel makes a through-thickness slot in the workpiece which is fed relative to the wheel with a feed speed v_f as shown in Fig. 2.13. Many abrasive particles are engaged in the cut at one specific time, and the number of these particles or their distribution in the cutting region is difficult to determine. Therefore, it is not easy to determine the size of the chip removed by each abrasive particle. Instead, bulk quantities are determined. The material removal rate is determined by (2.38) where a_e is the workpiece thickness and a_p is the width of cut, which in this case is the width of the cutting wheel. The machining time is determined by (2.24) where $l_e = 2\sqrt{a_e(D - a_e)}$ for $z > 0$. Because the wheel fully penetrates the workpiece, there are two engagement angles involved, one at entry and one at exit. At entry the engagement angle is determined by

$$\cos\phi_e = \frac{2z}{D}. \tag{2.41}$$

And at exit it is determined by:

$$\cos\phi_x = \frac{2(z + a_e)}{D}, \tag{2.42}$$

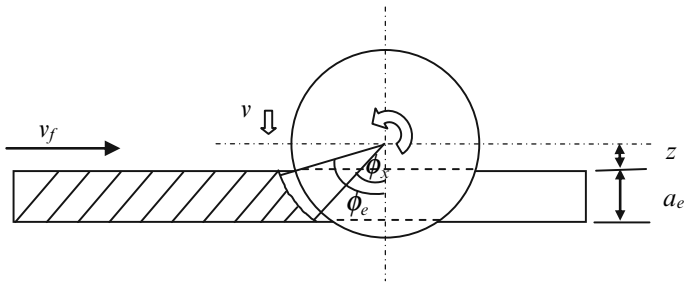

Fig. 2.13 Cutting geometry for abrasive wheel slot cutting

where z is the distance between the wheel center and the top surface of the workpiece.

2.7 Surface Finish

In a machining process, a specific surface geometry is produced as a result of the prescribed machine tool kinematics. This surface geometry is called an ideal or theoretical surface geometry, which follows a repeated pattern. In real life, however, the actual machined surface deviates from the ideal surface because of the occurrence of tool wear, machine vibrations, material inhomogeneity, and other factors not related to machine tool kinematics. The actual machined surface may not have a regular geometry. These effects result in what is called natural surface finish. Figure 2.14 shows the different definitions used to describe machined surface geometric characteristics. The surface profile is typically described by its lay, waviness, and roughness.

Lay is the macroscopic contour of the surface and describes the direction of the predominant surface pattern. The term lay is mostly used to describe flat surfaces and shape is used for contoured surfaces. Errors in lay and shape result from misalignment of machine components and from distortions resulting from clamping forces. Waviness is the recurrent deviations from an ideal surface that are relatively of large magnitude ($>0.1\,\text{mm}$). These deviations result from deflections in the machine tool and cutting tool, from errors in the tool geometry and from machine vibrations. Roughness is the finely spaced irregularities or irregular deviations characterized by short wavelength as shown in Fig. 2.14. Roughness is affected by tool shape and feed (ideal surface finish) as well as by machining conditions (natural surface finish).

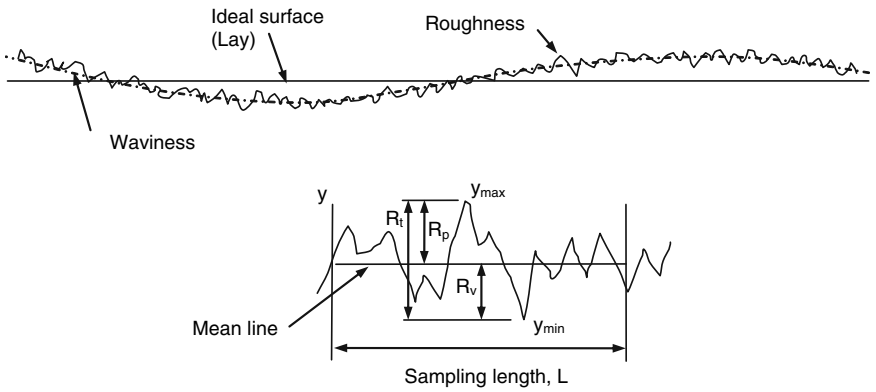

Fig. 2.14 Schematic representation of a machined surface

Surface roughness is most often used to characterize machined surfaces. It is commonly quantified by statistical parameters such as the arithmetic mean value R_a, maximum peak to valley height R_t, maximum peak to mean height R_p, mean to valley height R_v, and ten point average height R_z. Machined surface profile is most commonly measured by a stylus surface profilometer. Modern profilometers trace the machined surface over a prescribed sampling distance and compute the statistical parameters for the user. A representative surface profile is shown in Fig. 2.14 for the purpose of illustrating the statistical parameters. For a sampling length, L, the surface variations are described as a function of distance x, $y = f(x)$. The mean line of the profile for this segment is determined as

$$\bar{y} = \frac{1}{L}\int_0^L y\,\mathrm{d}x \tag{2.43}$$

The maximum peak-to-valley height within the sampling length is determined by

$$R_t = y_{max} - y_{min}. \tag{2.44}$$

The maximum peak-to-mean height and valley-to-mean height are determined, respectively, by

$$R_p = y_{max} - \bar{y} \tag{2.45}$$

and

$$R_v = \bar{y} - y_{min}. \tag{2.46}$$

The average of the numerical deviations from the mean line of the surface within the sample length, R_a is determined by

$$R_a = \frac{1}{L}\int_0^L |y - \bar{y}|\mathrm{d}x. \tag{2.47}$$

Finally, the ten-point average, R_z is determined as the difference between the five greatest peaks and the five lowest valleys within the sampling length

$$R_z = \frac{1}{5}\left(\sum_1^5 y_i^p - \sum_1^5 y_i^v\right). \tag{2.48}$$

The ideal roughness of machined surfaces depends primarily on cutting edge geometry and feed rate. Figure 2.15 shows the ideal surfaces generated when turning with a sharp tool and a round cornered tool. For a sharp cornered tool, the surface roughness can be determined geometrically as a function of the feed rate, f, and the major and minor cutting edge angles, κ and κ', respectively [1]:

$$R_t = \frac{f}{\cot\kappa + \cot\kappa'}, \tag{2.49}$$

$$R_a = \frac{f}{4\left(\cot\kappa + \cot\kappa'\right)}. \tag{2.50}$$

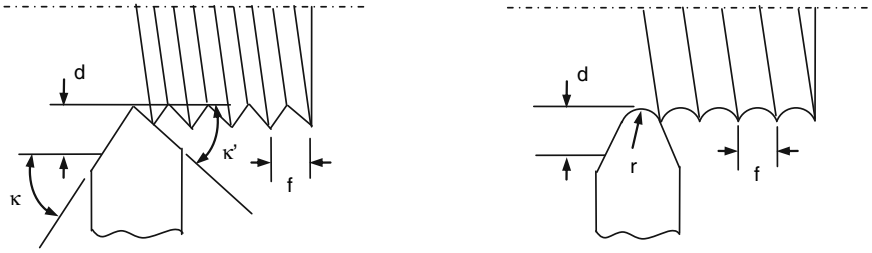

Fig. 2.15 Ideal surface roughness obtained in turning with a sharp tool and rounded tool

Table 2.1 Ranges of ideal surface roughness for selected material removal operations

Process	Roughness R_a (μm)
Turning	3–12
Planning	3–12
Drilling	3–25
Milling	1–10
Grinding	0.25–3

For a round cornered tool, it can be shown that [1]:

$$R_t \cong \frac{f^2}{8r}, \tag{2.51}$$

$$R_a \cong \frac{f^2}{32r}, \tag{2.52}$$

where r is the tool corner radius.

Equation (2.51) can also be used to approximate the surface roughness for end milling (trimming). In this case, f becomes equal to a_f and r becomes the cutter radius, $D/2$. For abrasive cutting $a_f = v_f L_g / v$, where L_g is the spacing around the periphery between successive cutting points. Equations (2.51) and (2.52) become [3]:

$$R_t \cong \frac{1}{4}\left(\frac{v_f L_g}{v D^{1/2}}\right)^2, \tag{2.53}$$

$$R_a \cong \frac{1}{9\sqrt{3}}\left(\frac{v_f L_g}{v D^{1/2}}\right)^2. \tag{2.54}$$

As illustrative information, Table 2.1 gives typical roughness values for different processes corresponding to normal workshop practice.

Example 2.3. An edge trimming operation of particleboard uses a 19.0 mm cutter with one cutting edge in a down-milling configuration. The spindle speed is 5,000 rpm and the feed rate is 1.27 m/min. Determine the effect of the following on surface roughness R_t and R_a:

(a) Doubling the number of teeth
(b) Doubling feed rate

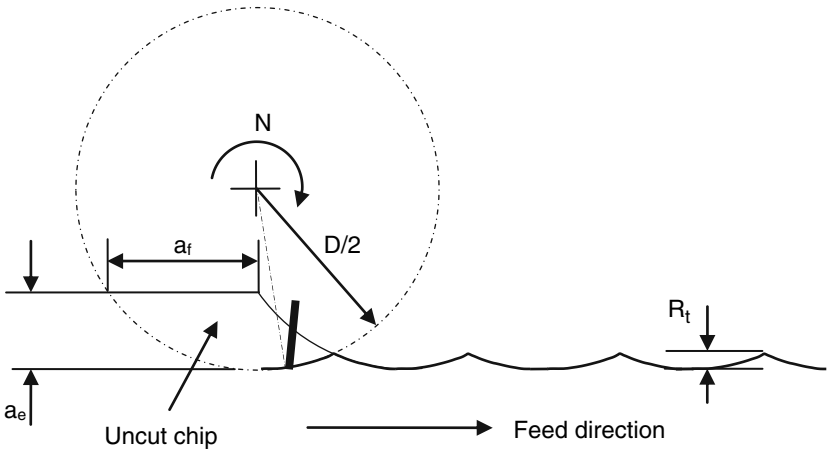

Fig. 2.16 Cutting geometry for Example 2.3

Table 2.2 Effect of cutting parameters on ideal surface roughness in edge trimming

Parameter	$a_f = \frac{v_f}{NT}$	R_t	R_a
$r = 9.5\,\text{mm}$ $v_f = 1.27\,\text{m/min}$ $N = 5,000\,\text{rpm}$ $T = 1$	0.254 mm	0.85 µm	0.21 µm
(a) $T = 2$ All other parameters remain unchanged	0.127 mm	0.21 µm (75% decrease)	0.05 µm (76% decrease)
(b) $v_f = 2.54\,\text{m/min}$ All other parameters remain unchanged	0.508 mm	3.40 µm (300% increase)	0.85 µm (300% increase)
(c) $r = 19.0\,\text{mm}$ All other parameters remain unchanged	0.254 mm	0.42 µm (50% decrease)	0.11 µm (50% decrease)
(d) $N = 10,000\,\text{rpm}$ All other parameters remain unchanged	0.127 mm	0.21 µm (75% decrease)	0.05 µm (75% decrease)

(c) Doubling cutter diameter.
(d) Doubling spindle speed

Geometry of the trimmed surface is shown in Fig. 2.16. The size of chip per tooth and the resulted uncut chip are exaggerated for clarity. As a first approximation it is assumed that the cutter completes one turn then intermittently advances a distance a_f, as opposed to a continuous path prescribed by a torchoid. This allows the surface profile to be approximated by (2.50) and (2.51) after replacing f with a_f and r with $D/2$

$$R_t = \frac{a_f^2}{8(D/2)} \text{ and } R_a = \frac{a_f^2}{32(D/2)}. \tag{2.55}$$

The effect of (a), (b), (c), and (d) on surface roughness is shown in Table 2.2. It is apparent that significant reduction in R_a and R_t can be obtained by doubling number of teeth, doubling spindle speed or reducing feed rate in half.

2.8 Summary

Machining of composites is necessary for finishing parts to the required tolerances and for preparing components for subsequent assembly. Conventional machining processes such as turning, milling, drilling, abrasive cutting, and grinding are used to generate complex features by removing material in the form of tiny chips. The machining process takes place as a result of engaging a rigid cutting tool into the workpiece and prescribing the necessary relative motions between the tool–work pair that will result in material removal and generating new surfaces. The size and shape of the chip removed, material removal rate and resulting ideal surface finish are closely related to the kinematic relationships between the cutting tool and the workpiece.

Turning utilizes a single point cutting tool that is steadily feed against a rotating workpiece in order to generate cylindrical surfaces. The key process parameters that affect the turning process outcome are tool geometry, feed rate, depth of cut, and rotational speed. The cross-sectional area of the chip removed is proportional to the product of feed rate and depth of cut, while material removal rate is a function of the speed by which this cross section is swept. The ideal roughness of the machined surface is proportional to the square of feed rate and is inversely proportional to the cutting edge nose radius. Drilling is another process that produces circular surfaces (holes). The difference between drilling and turning, however, is that in drilling the cutting edge is rotated and advanced along its axis of rotation, as opposed to a nonrotating cutting edge in turning. Nevertheless, most of the kinematic relations in drilling are similar to those in turning.

In a milling process, the cutting tool which often has multiple cutting edges rotates around its axis while a translation motion (feed motion) is introduced relative to the workpiece. Milling is capable of producing complex contoured surfaces. Depending on the relationship between the feed motion and the rotational motion, either up milling or down milling is produced. Up (conventional) milling is produced when the rotational speed and feed speed are in opposite directions whereas down (climb) milling is produced when the two motions are in the same direction. In both cases, the thickness of chip removed is not constant and continuously changes from cutting edge entry to exit. The chip thickness is a function of the cutting edge position along the cutting circle and the feed speed. The material removal rate in milling is proportional to the width of cut, depth of cut, and feed speed. Similar to turning, the ideal surface roughness is proportional to the feed speed and is inversely proportional to the tool radius. Abrasive machining is similar to milling in a way that material removal is caused by the engagement of tiny cutting edges of the abrasive

grit. However, the material removal rate is much smaller and surface roughness is much better than those in milling.

Even though most of the conventional machining practices are well established and have substantial supportive data bases for metal machining, their application to machining FRPs is relatively new and the necessary expertise is lacking. It is imperative that one recognizes the differences in machining FRPs as compared to metals. Unlike metals, FRPs are inhomogeneous materials that generally fail by brittle fracture. Thus the concept of continuous chip formation that is characteristic of metal machining does not exist in machining FRPs. The machining characteristics such as surface finish and cutting forces are strongly influenced by the reinforcement volume fraction, form, and orientation. The requirements of machining FRPs include a sharp cutting edge in order to shear effectively the fibers, low material removal rates, and lower temperatures than those encountered in metal machining.

Review Questions and Problems

1. Define cutting speed, feed, chip thickness, chip width, uncut chip area, and material removal rate for turning, drilling, and milling.
2. What is the significance of material removal rate and specific cutting pressure in machining process selection and design?
3. Identify the tool signature: major (side) cutting edge, minor (end) cutting edge, cutting-edge inclination, corner (nose) radius, tool face, and major and minor flanks for the cutting tools shown below. Refer to Fig. 2.3 for terminology.

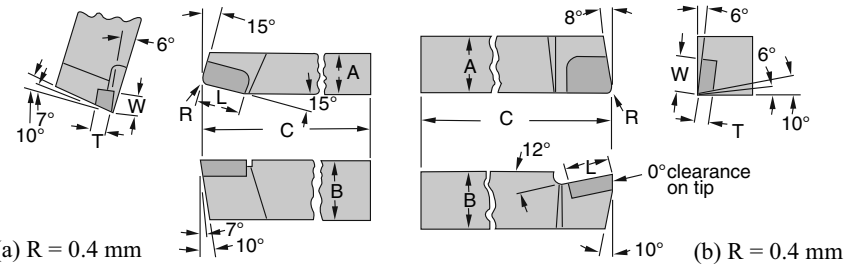

4. The rpm for a 1.00-in. diameter piece of stock that is being turned at a cutting speed of 400 sfpm is (show calculations):
   (a) 450 (b) 1,528 (c) 764 (d) 532
5. The feed speed for a two (2) toothed milling cutter that is being rotated at 500 rpm while cutting 0.002 in. per tooth is (show calculations):
   (a) 4.0 ipm (b) 2.0 ipm (c) 8.0 ipm (d) 0.02 ipm
6. It is required to turn down a 10.0-in. long rod from a 3.0-in. diameter to a 2.5-in. diameter using a depth of cut of 0.1-in., a feed speed of 0.05 ipr and a spindle speed of 900 rpm. The total cutting time required is (show calculations):
   (a) 13.30 s (b) 0.67 s (c) 40 s (d) 13.30 min

7. It is required to finish-turn the diameter of a glass-fiber-reinforced axle from 77.0 to 75.0 mm at a length of 50.0 mm on each end of the axle. The axle is 1,000.0 mm long. The axle is turned at 800 rpm, the feed is 0.1 mm/rev and the depth of cut is 1.0 mm. Determine the material removal rate, cutting power, and the cutting time required for finish-turning one axle. Use a specific cutting energy for glass FRPs of approximately $500\,\mathrm{N/m^2}$.

8. In a drilling operation using a twist drill, the rotational frequency of a drill is $5\,\mathrm{s^{-1}}$, the feed 0.25 mm, the major cutting-edge angle 60°, and the drill diameter 12 mm. Assuming that the specific cutting energy of the work material is $0.75\,\mathrm{GJ/m^3}$, calculate:

   (a) The maximum material removal rate
   (b) The undeformed chip thickness
   (c) The drill torque, in Newton-meter

9. In a turning application of a glass/epoxy composite, an unsatisfactory surface roughness was produced. Which one of the following actions would you recommend in order to improve surface roughness? Justify your answer by reference to pertinent material in class notes.

   (a) Increase cutting speed
   (b) Increase feed speed
   (c) Increase both cutting speed and feed speed
   (d) Decrease cutting speed
   (e) Decrease feed speed
   (f) Decrease both cutting speed and feed speed
   (g) Other action – explain

10. In a down end-milling operation, the thickness of the workpiece is 11 mm, its length is 200 mm, and the radial depth of cut is 1 mm. The cutter has four straight flutes and a diameter of 10 mm. The spindle speed is 2,000 rpm and the feed speed is 1,270 mm/min. Determine the following:

    (a) The maximum undeformed chip thickness
    (b) The feed per tooth
    (c) The entry angle, exit angle, and total angle of engagement of the cutter
    (d) The maximum material removal rate

11. Consider a milling operation of unidirectional CFRP with a cutter diameter of 20 mm, and one cutting edge on the cutter. The cutter speed is 1,000 rpm, the feed speed is 100 mm/rev, and the depth of cut is 2 mm. The thickness of the workpiece is 4.0 mm. A schematic of the cutting configuration is shown below.

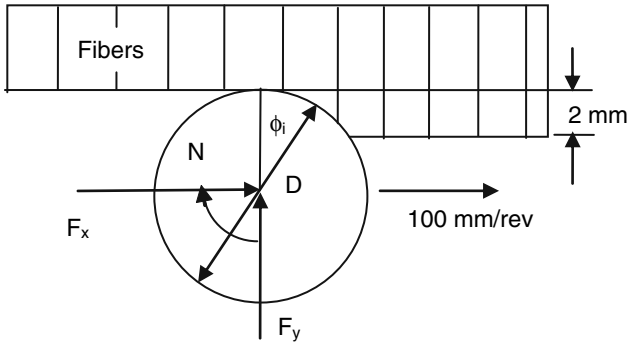

(a) Determine the total engagement angle ϕ_x.
(b) Determine the instantaneous fiber orientation angle θ_i, which is the angle between the fibers and the cutting velocity vector, as a function of the instantaneous engagement angle ϕ_i. Evaluate the fiber orientation angle for an instant that is halfway between entry and exit of the cutting edge.

References

1. Boothroyd, G., Knight, W., Fundamentals of Machining and Machine Tools, 2nd Edition, Marcel Dekker, New York, NY, 1989.
2. Stephenson, D., Agapiou, J., Dekker, M., Metal Cutting Theory and Practice, Marcel Dekker, New York, NY, 1997.
3. Stephen, M., Grinding Technology, Society of Manufacturing Engineers, Industrial Press, New York, NY, 1989.
4. Martellotti, M. E., An analysis of the milling process. Transactions of ASME 63, 677–700, 1941.
5. Martellotti, M. E., An analysis of the milling process, part-ii down milling. Transactions of ASME 67, 233–251, 1945.
6. Koenigsberger, F., Sabberwal, A.J.P., Chip section and cutting force during the milling operation. CIRP Annals 10, 197–203, 1961.

Chapter 3
Mechanics of Chip Formation

The study of chip formation under controlled laboratory conditions gives an insight of how the work material is deformed and then removed ahead of a moving wedge-shaped tool. The simplified conditions of orthogonal machining used in studying chip formation makes it possible to gather information about chip shape and size, shear stress and strain in the chip, friction conditions, cutting forces, and cutting temperatures. Much work has been conducted over the past century to study the mechanics of chip formation in metal machining. As a result, metal machining is a well-established science and we generally have a very good idea how metal chips are formed and removed. Furthermore, the wealth of information and expertise in this field has allowed the advancement of metal machining theory to the level of astounding predictive capabilities. Naturally, similar techniques to those used in studying metal machining have been transferred to the study of composites machining but only limited success have been reported. Composite materials are not homogeneous and the chip formation process in machining fiber-reinforced polymers (FRPs) is significantly different from that in machining of metals. However, as will be explained later in this chapter, there are some common aspects in which the behavior in machining of the two materials is to some extent similar. Therefore, metal cutting theories can sometimes be applied to explain the cutting action in FRPs, but with some caution.

In this chapter, we will first consider the mechanics of orthogonal machining of metals, as this is the basis for most of the work done in machining metals and composites. Understanding of orthogonal machining is certainly necessary for explaining the machining phenomenon of FRPs. This will be followed by discussion of orthogonal machining of pure polymers, unidirectional and multidirectional composites. Differences in the machining behavior of metals and composites and the effect of process parameters on machining outcomes are also discussed. The fundamental influence of fiber orientation on machining behavior of FRPs is explained in detail. Because prediction is an important end-result of any machining theory, the predictive capabilities and limitations of orthogonal machining models of FRPs are also discussed.

J.Y. Sheikh-Ahmad, *Machining of Polymer Composites*.
DOI: 10.1007/978-0-387-68619-6,

3.1 Fundamental Considerations

In conventional machining processes, material is removed in the form of a chip by the action of a wedge-shaped tool that is in relative motion with respect to the workpiece. Chip formation takes place at the microstructure level. For ductile materials such as most metals, the material is pushed ahead of the cutting edge until the compression stress is high enough to cause plastic deformation by slip between atomic planes. No breakage of atomic bonds occurs during the machining of ductile materials. Figure 3.1a shows the different deformation zones involved in the chip formation process of ductile metals. Since the main deformation mechanism in these zones is plastic shear, these zones are commonly called shear zones. The primary shear zone (1) whose size is exaggerated in the figure is a few atomic planes thick. As the material approaches the primary shear zone, it does not deform until this zone is reached. It then undergoes a substantial amount of plastic shear as it crosses this thin shear zone. This event is the primary event responsible for generating the chip. The chip then flows upward on the face of the tool and receives further shearing in the secondary shear zone (2). This deformation is typically ignored in a first treatment of the mechanics of machining and the movement of the chip along the face of the tool is considered to be a friction slider [1]. The third shear zone (3) originates from the material rubbing against the clearance face of the tool. The size of this zone depends on the tool nose radius, the amount of flank wear, and the elastic rebound of the material under the tool.

Different types of chips are formed in metal cutting operations. Figure 3.1 shows two significant types of chips, but other chip types are also described in the metal machining literature [1, 2]. The first type, Fig. 3.1a, is the continuous type chip that is generated by the steady-state machining of ductile metals such as mild steel, aluminum, and copper. For brittle materials, Fig. 3.1b, chips are formed by brittle fracture due to initiation and propagation of cracks in the primary shear zone after the chip is partly formed. The segments are fully separated from each other by

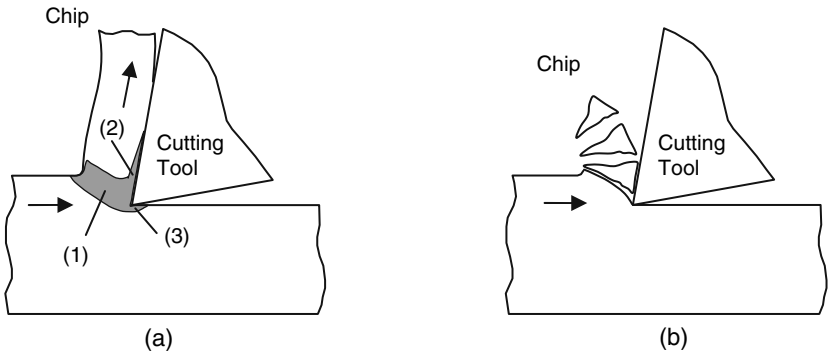

Fig. 3.1 Chip formation in (**a**) ductile and (**b**) brittle materials. *Arrows* indicate the relative motion between workpiece and cutting tool

brittle fracture of the material in or in front of the primary shear zone. This type of chip occurs when machining brittle materials such as cast iron, ceramics, thermosetting plastics, and most fiber-reinforced composites. Better surface quality is generally produced when continuous (ductile) chips are formed. When brittle materials like ceramics are cut, a crack is produced in front of the tool, which causes fractured surfaces and poor surface finish. Other types of chips that are discussed in the literature include wavy chip, continuous chip with build-up edge, and segmented chip [1, 2].

Some of the differences and similarities in machining metals and composites are explained here. The chip formation analysis in metal cutting is primarily based on the concept that a shear plane extends from the tip of the cutting edge and runs upward to the free surface of the workpiece (Fig. 3.1a). The chip is formed by plastic deformation of the material as it passes the shear zone. This is not at all the case when machining FRPs, and is true to some extent when machining thermoplastic polymers under certain conditions. FRPs on the other hand exhibit very little plastic deformation, if any at all, and their chip formation is predominantly controlled by fracture. Thermosetting plastics exhibit some plastic deformation before fracture, but not to the extent required for producing a continuous chip, and their behavior is thus classified as brittle. Thermoplastics, however, exhibit significant elastic and plastic deformation before fracture, which ultimately influences the machining behavior of their composites in proportion to their volume fraction in the composite. When cutting polymers and their composites, elastic deformation plays a significant role in determining the cutting forces, especially in the tertiary deformation zone (Fig. 3.1a). Because of elastic recovery, rubbing in this zone can be substantial and the resulting temperature rise may heat the polymer matrix above the glass transition temperature, causing significant plastic flow in this region. Nevertheless, the concept of shear plane was applied with some success in the analysis of machining FRPs in a narrow range of fiber orientations.

3.1.1 Orthogonal Machining

To simplify the analysis of chip formation, it is advantageous to start with a two-dimensional or orthogonal cutting process. In orthogonal cutting, the tool edge is perpendicular to the direction of the cutting speed vector, v. Orthogonal cutting represents a two-dimensional problem, and hence, it lends itself well to research work. A schematic representation of orthogonal cutting is shown in Fig. 3.2. A shear plane of area A_s is formed in the material from the point of the cutting edge and upward to the root of the chip. An uncut material of thickness a_c passes through the shear zone and is subjected to shear deformation. This forms a chip of thickness a_o, which is typically greater than the uncut chip thickness. The chip is held in equilibrium by the resultant force R acting on the chip by the shear plane and R' acting on the rake face of cutting tool. In orthogonal cutting, all forces, motions, and deformations are

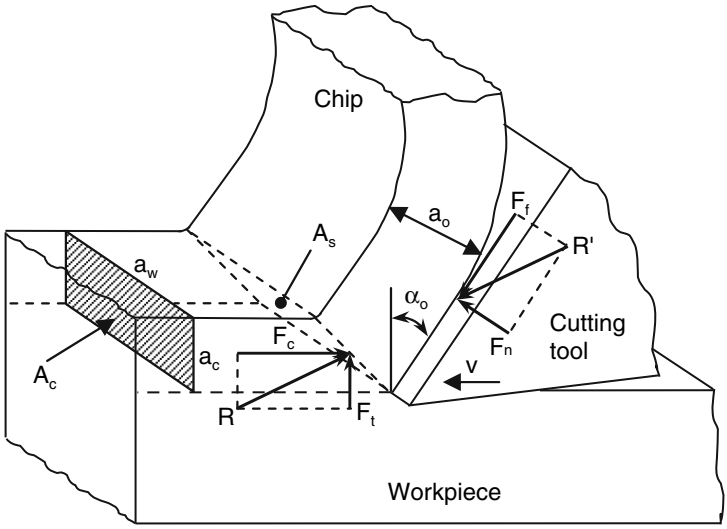

Fig. 3.2 Schematic diagram illustrating orthogonal cutting showing cutting forces acting on the chip. $R = R' =$ resultant force, F_c is cutting force acting along direction of cutting speed (also called the principal force), F_t is thrust force acting normal to direction of speed, F_f is frictional force on the rake face, and F_n is normal to the rake face

in the plane formed by the cutting velocity vector and the direction normal to it. The following assumptions are made to further simplify the analysis:

1. The tool cutting edge is perfectly sharp and straight, cuts perpendicular to the direction of motion, and has a width greater than that of the workpiece.
2. The cutting edge generates a plane surface, at constant depth of cut as the work moves past it with a uniform velocity.
3. The chip does not flow to either side, since it has the same width as the workpiece.
4. A continuous chip is produced without a built-up edge.
5. The shear surface is a plane extending upward from the cutting edge.
6. There is no contact between the workpiece and the clearance surface of the tool.

As it will be shown later, these assumptions were originally associated with metal machining and some of them would not hold true when machining FRPs. The following calculations can be made directly from the cutting geometry and using simple trigonometric relationships.

3.1.1.1 Shear Plane Angle

Figure 3.3 is a two-dimensional representation of orthogonal machining. All forces, motions, and deformations are assumed to be confined to the plane of the figure. It is common in this analysis to assume that the material is moving against a fixed cutting tool as shown in the figure. The material of thickness a_c is being removed by

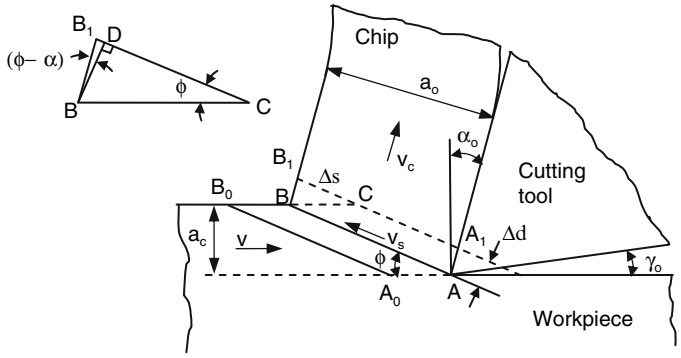

Fig. 3.3 Two-dimensional representation of orthogonal cutting. *AB* is the shear plane, ϕ is shear plane angle, α_o is rake angle, γ_o is clearance angle, a_c is uncut chip thickness, and a_o is deformed chip thickness

the cutting edge. A shear plane *AB* is formed and the material is sheared as at passes across the shear plane and forms a chip of thickness a_o.

The shear plane angle can be obtained by measuring the chip thickness after machining, a_o and comparing it with the depth of cut, a_c, which is also known as the uncut chip thickness. The cutting ratio r is defined by as a_c/a_o. The relationship between r and ϕ can be obtained from Fig. 3.3 as follows:

$$\sin\phi = \frac{a_c}{AB}, \tag{3.1}$$

$$\cos(\phi - \alpha_o) = \frac{a_o}{AB}, \tag{3.2}$$

$$r = \frac{a_c}{a_o} = \frac{AB\sin\phi}{AB\cos(\phi - \alpha_o)} = \frac{\sin\phi}{\cos(\phi - \alpha_o)}. \tag{3.3}$$

Solving for ϕ one can obtain:

$$\tan\phi = \frac{r\cos\alpha_o}{1 - r\sin\alpha_o}. \tag{3.4}$$

3.1.1.2 Shear Strain

As illustrated in Fig. 3.3, a material volume A_oABB_o passes through the shear plane and gets deformed by shear into the shape AA_1B_1B. The shear strain is defined as the ratio of deformation, Δs and the distance between the undeformed and deformed planes, Δd:

$$\gamma = \frac{\Delta s}{\Delta d} = \frac{B_1C}{BD} = \frac{DC}{BD} + \frac{B_1D}{BD} = \cot\phi + \tan(\phi - \alpha_o), \tag{3.5}$$

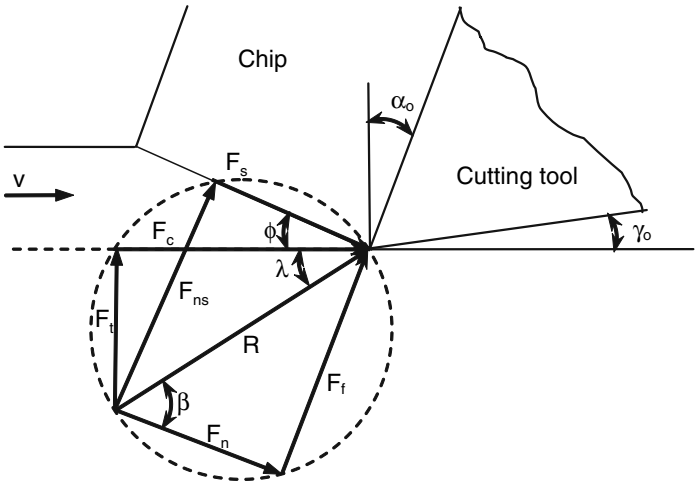

Fig. 3.4 Schematic diagram of orthogonal machining showing force equilibrium on the shear plane. R is the resultant force, $\lambda = (\beta - \alpha_o)$ the resultant force orientation, F_c the cutting force, F_t the thrust force, F_s the shear force parallel to shear plane, F_{ns} the normal force to the shear plane, F_f the frictional force on the rake face, F_n the normal force on the rake face, and β is the friction angle

which can be rearranged as

$$\gamma = \frac{\cos\alpha_o}{\sin\phi\cos(\phi - \alpha_o)}. \tag{3.6}$$

Substituting in (3.5) for the shearing speed as $v_s = \Delta s/\Delta t$ and the cutting speed as $v = \Delta d \sin\phi/\Delta t$, it can also be shown that the shear stress is related to these speeds by

$$\gamma = \frac{v_s}{v \sin\phi}. \tag{3.7}$$

3.1.1.3 Normal and Shear Stresses on the Shear Plane

The resultant force R is resolved into components in different ways as illustrated in Fig. 3.4. The two components along the cutting direction and normal to it are the cutting or principal force, F_c, and thrust force, F_t, respectively. The resultant force is also resolved into a component along the shear plane, F_s and a component normal to the shear plane, F_{ns}. The relationships between these components are determined from Fig. 3.4 as

$$F_s = F_c\cos\phi - F_t\sin\phi, \tag{3.8}$$

$$F_{ns} = F_c\sin\phi + F_t\cos\phi = F_s\tan(\phi + \beta - \alpha_o). \tag{3.9}$$

The apparent shear strength of the material in the shear plane is determined by dividing the shear force by the area of the shear plane, A_s:

$$\tau_s = \frac{F_s}{A_s} = \frac{(F_c \cos\phi - F_t \sin\phi)\sin\phi}{A_c}, \tag{3.10}$$

where $A_s = A_c / \sin\phi$.

Similarly, the normal stress on the shear plane is given by

$$\sigma_s = \frac{F_{ns}}{A_s} = \frac{(F_c \sin\phi + F_t \cos\phi)\sin\phi}{A_c}. \tag{3.11}$$

3.1.1.4 Mean Coefficient of Friction

The force F_f represents the frictional resistance met by the chip as it slides over the rake face of the tool, F_n is known as the normal force (see Fig. 3.4). The ratio of F_f to F_n is the mean coefficient of friction, μ. Forces on the rake face are

$$F_f = F_c \sin\alpha_o + F_t \cos\alpha_o = R\cos(90 - \beta), \tag{3.12}$$

$$F_n = F_c \cos\alpha_o - F_t \sin\alpha_o = R\sin(90 - \beta). \tag{3.13}$$

The mean coefficient of friction is determined as

$$\mu = \tan\beta = \frac{F_f}{F_n} = \frac{F_c \sin\alpha_o + F_t \cos\alpha_o}{F_c \cos\alpha_o - F_t \sin\alpha_o}. \tag{3.14}$$

Angle β is known as the friction angle.

3.1.1.5 Energy Considerations

The cutting force, F_c, in the direction of the relative motion between the tool and workpiece determines the amount of work required to remove material. The thrust force, F_t, is normal to the relative motion between the tool and workpiece and does no work. Thus, the machining power is defined as

$$P_m = F_c v. \tag{3.15}$$

The specific cutting energy (also called the specific cutting pressure) is the machining power per unit volume removed per unit time:

$$p_s = \frac{F_c v}{v A_c} = \frac{F_c}{A_c}, \tag{3.16}$$

which is independent of cutting speed and varies with chip geometry, feed rate, and hardness of workpiece material.

The shear energy per unit volume may be obtained from

$$u_s = \frac{F_s v_s}{v A_c} = \frac{F_s v_s}{v A_s \sin\phi} = \tau_s \cdot \gamma. \tag{3.17}$$

The friction energy per unit volume may be obtained from

$$u_f = \frac{F_f v_c}{v A_c} = \frac{F_f r}{A_c}. \tag{3.18}$$

In metal machining, the bulk of the total cutting energy is used to overcome shearing along the shear plane and friction along the tool rake face and essentially all of it ends up as thermal energy. Hence

$$p_s \approx u_s + u_f. \tag{3.19}$$

This equation may not hold when machining composites as very little shear and more fracture takes place in forming the chips. A more reasonable expression would be:

$$p_s \approx [(1 - V_f)u_m + V_f u_{fiber}] + u_d + u_f, \tag{3.20}$$

where u_m is the specific cutting energy for the matrix, u_{fiber} is the specific cutting energy for cutting the fibers, and u_d is the specific energy associated with debonding fiber and matrix.

Example 3.1. The cutting forces obtained from orthogonal cutting Polyamide nylon 6 [3] are $F_c = 104\,\text{N}$ and $F_t = 11.8\,\text{N}$. The cutting conditions are $v = 10\,\text{m/min}$, $a_w = 5.0\,\text{mm}$, $a_c = 0.2\,\text{mm}$, $\alpha_o = 10^\circ$. The chip thickness, a_o, was measured to be 0.225 mm. Determine the shear plane angle, the theoretical shear strain and theoretical shear in the shear plane, the coefficient of friction, specific cutting energy, specific shear energy, and specific frictional energy.

1. Cutting ratio $= a_c/a_o = 0.2/0.225 = 0.889$.
2. Shear plane angle $= \tan^{-1}\frac{r\cos\alpha_o}{1 - r\sin\alpha_o} = \tan^{-1}[(0.889\cos(10))/(1 - 0.889\sin(10))]$ $= \tan^{-1} 1.035 = 46^\circ$.
3. Shear strain: $\gamma = \frac{\cos\alpha_o}{\sin\phi\,\cos(\phi - \alpha_o)} = \cos(10)/[(\sin(46)\cos(46 - 10)] = 1.69$.
4. Shear stress on the shear plane: $\tau_s = \frac{F_s}{A_s} = \frac{(F_c\cos\phi - F_t\sin\phi)\sin\phi}{A_c} = (104\cos(46) - 11.8\sin(46))\sin(46)/(0.2 \times 5) = 45.9\,\text{N/mm}^2$.
5. Specific cutting energy: $p_s = \frac{F_c v}{v A_c} = \frac{P_m}{Z_w} = \frac{F_c}{A_c} = 104/(0.2 \times 5) = 104\,\text{N/mm}^2$.
6. Specific shear energy: $u_s = \tau_s \cdot \gamma = 45.9 \times 1.69 = 77.6\,\text{N/mm}^2$.
   Percent of cutting energy spent in shearing the material $= 100(77.6/104) = 74.6\%$.
7. Specific frictional energy:

$$F_f = F_c \sin\alpha_o + F_t \cos\alpha_o = 104\sin(10) + 11.8\cos(10) = 29.7\,\text{N},$$

$$u_f = \frac{F_f v_c}{v A_c} = \frac{F_f r}{A_c} = 29.7(0.889)/(0.2 \times 5) = 26.4\,\text{N/mm}^2.$$

Percent of cutting energy spend in overcoming friction $= 100(26.4/104) = 25.4\%$.

8. Check: $u_s + u_f = 77.6 + 26.4 = 104\,\mathrm{N/mm^2}$, which is equal to p_s.

3.2 Machining of Polymers

The machining of polymers has been extensively studied by Kobayashi and the results of his studies are documented in a classical monograph on the subject [3]. However, more recent studies can also be found in the literature [4–7]. Recent interest in machining polymers is spurred by their increased utilization in the optical, electronics, and consumer products. Even though the polymer matrix in a fiber-reinforced composite offers the least resistance to cutting due to their inferior strength and stiffness as compared to the reinforcement fibers, they have significant influence on the chip formation mode and the type of chip that results from machining. In addition, because of their peculiar thermal properties, especially their thermal conductivity, the polymer matrix plays an important role in determining the temperature at the cutting zone.

The behavior of polymers in machining is affected by process parameters such as tool material, rake angle, cutting-edge radius, depth of cut, and cutting speed. In addition, the effect of the rheological and the thermal properties of the polymers on chip formation is very profound. The mechanical response of thermosets and thermoplastics to applied load is drastically different. Thermosets exhibit brittle behavior with very little strain to fracture, while thermoplastics are generally ductile, with strain to fracture reaching several hundred percents. Due to its viscous behavior, the ultimate strength and elongation to fracture of polymers is also dependent on the rate of application of the load. The strength of the material increases and the ultimate elongation to fracture decreases as the rate of deformation increases. In other words, the material exhibits a transition from ductile to brittle behavior with an increase in deformation rate. Because of these differences, the type of chips formed and the quality of the machined surface of the different types of polymers will vary widely with cutting process parameters [3]. Increasing the rake angle and decreasing the depth of cut results in the reduction in the amount of deformation the material undergoes to form a chip. The increase in cutting speed affects the cutting process in two opposing ways. On the one hand, the material will experience a high strain rate, and as a result, will fail at a lower strain or in a brittle manner. On the other hand, the heat generated will raise the temperature in the cutting zone, increase the long-range mobility of the material's molecular chains, and thus increase its ductility. The molecular weight of the polymer and its glass transition temperature would be the determining factor as to which of these effects becomes dominant [6, 7].

The specific heat of polymers is usually greater than that of metals and its thermal conductivity is significantly lower (see Table 3.3). Therefore, the temperature rise in the polymer will be larger when a given quantity of heat is applied to equal volumes of a polymer and a metal. During the process of machining, heat is generated by

the shear in the primary deformation zone, and by friction between the chip and the tool face and between the workpiece and the tool clearance side. In the machining of metals, most of this heat (up to 70% at high cutting speeds) is removed from the cutting area by the chip [1]. In the machining of plastics, because of their low thermal conductivity, the heat generated in the primary shear zone does not quickly conduct to the tool and only the heat at a thin interfacial layer could play an important role in heat removal by conduction. It was shown in [7] that the amount of heat carried away from the primary shear zone by the chip is as high as 90% for higher cutting speeds. Also because of low thermal conductivity, localized heating because of rubbing at the machined surface may cause excessive heating, leading to burning in the machined surface of thermosetting polymers or gumming of thermoplastic polymers.

Several types of chips can be formed when machining polymers, depending on polymer type, tool geometry, and cutting conditions [3]. For materials that exhibit high capacity for elastic deformation a continuous elastic chip is produced at low cutting speeds and large positive rake angle. This type of chip is almost entirely formed by elastic deformation (there has to be separation of the polymer chains in order to form a chip, which is not elastic) and the chip thickness is equal to the depth of cut ($r = 1.0$). This type of chip is not produced in metal cutting. Another type of continuous chip, the shear-flow type chip is obtained when cutting thermoplastics and is caused by plastic deformation of the material as it passes through a shear plane. The inclination of the shear plane is determined by the condition of minimum machining power. This type of chip is similar to the chip produced when machining ductile metals. The chip thickness is typically greater than the depth of cut ($r < 1.0$). Figure 3.5a shows a shear-flow type chip obtained when machining polycarbonate, a thermoplastic used in making spectacle lenses [7]. Due to the ductile chip formation process, a better surface roughness can be achieved as shown in the figure. Discontinuous type chip is obtained when machining brittle materials, such as thermosets and some thermoplastics, with a large rake angle tool and large depth of cut. A crack

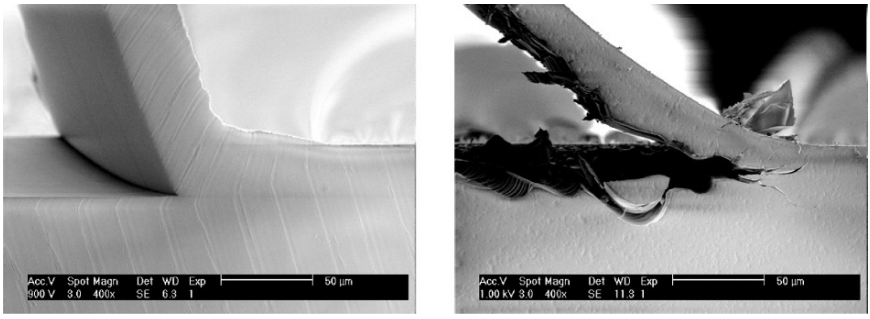

(a) (b)

Fig. 3.5 (**a**) Continuous chip formation in machining thermoplastic polycarbonate, (**b**) discontinuous chip formation in machining thermosetting allyl diglycol carbonate at cutting speed of 2.5 mm/s. Courtesy of Dr. Guido Gubbels [7]

occurs ahead of the cutting edge at an oblique downward angle, and the chip is produced by the bending moment, which acts on the chip after the crack grows to some length. This results in a poor surface quality after machining. Figure 3.5b shows this type of chip obtained when machining allyl diglycol carbonate, a thermoset used in making spectacle lenses [7].

3.3 Machining of Unidirectional FRPS

Multidirectional composites are of more practical interest than unidirectional composites. However, unidirectional composites lend themselves nicely to investigative research, as it is easier to relate their mechanical properties and machining characteristics to fiber orientation. Therefore, most of the work on the mechanics of chip formation was performed on unidirectional composites. In this section, we will review some of the experimental and analytical work in machining unidirectional FRPs.

An important factor in determining the mode of chip formation in unidirectional FRPs is the fiber orientation with respect to the cutting direction. Figure 3.6 shows the convention used for designating fiber orientation in machining studies. Fiber orientation angle is measured clockwise with reference to the cutting direction. Unidirectional fiber orientations greater than 90° are typically regarded as negative orientations by convention. Other factors that affect the mode of chip formation include cutting tool rake angle (which is second to fiber orientation in terms of influence), fiber material, and matrix martial.

3.3.1 Chip Formation Modes

The process of chip formation in orthogonal machining of unidirectional fiber-reinforced composites was studied by several researchers. Koplev et al. [8] were among the first to study this phenomena using the quick stop device and macrochip methods. The quick stop device is widely used in the study of metal machining,

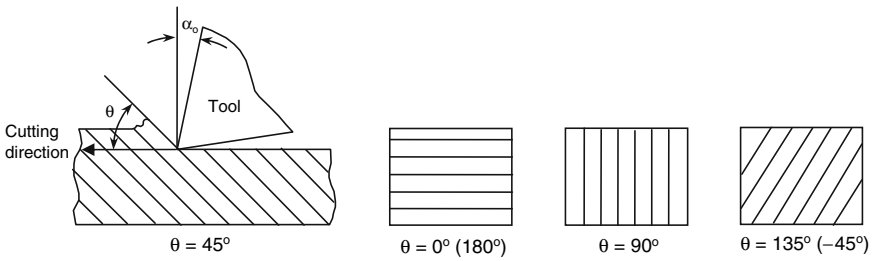

Fig. 3.6 Fiber angle convention with respect to cutting direction

and is well documented in the metal cutting literature [2] and thus will not be discussed here. In the macrochip method, the top surface of the workpiece parallel to the cutting plane is covered with a thin layer of rubber-based glue and is allowed to dry. When machining takes place the glued surface becomes the free surface of the chip and the chip segments remain stuck to the glue in a ribbon-like chip, which can be measured and examined under microscope. Despite the fact that the free surface of the chip is not truly "free" because its deformation is constrained by the rubbery glue, this method has proved useful in studies of the chip formation process and identification of chip types [8–10]. In situ observation of the chip formation during machining FRPs was also conducted [9–11]. Kaneeda and Masayuki [11] observed the chip formation of carbon-fiber-reinforced polymers (CFRP) inside a scanning electron microscope, while Arola et al. [9] and Nayak et al. [10] used CCD camera to observe the cutting of CFRP and glass-fiber-reinforced polymers (GFRP), respectively. These studies have concluded that the chip formation process in machining FRPs is critically controlled by the fiber orientation and the cutting edge rake angle. Material removal in machining FRPs was found to be governed by a series of uncontrolled fractures and the fractured chips exhibited very little plastic deformation, which is unlike what is normally observed in metal chips.

The chip formation process in machining unidirectional FRPs is categorized by into five different types, depending on fiber orientation and cutting edge rake angle. Figure 3.7 schematically shows the different modes of chip formation when machining FRPs with a sharp cutting edge (nose radius in the order of a few micrometers) and the resulting chip types. Delamination type chip formation (Type I) occurs for the 0° fiber orientation and positive rake angles (Fig. 3.7a). Mode I fracture and loading occur as the tool advances into the work material. A crack initiates at the tool point and propagates along the fiber–matrix interface. As the tool advances into the workpiece, the peeled layer slides up the rake face, causing it to bend like a cantilever beam. Bending-induced fracture occurs ahead of the cutting edge and perpendicular to the fiber direction. A small distinct chip segment is thus formed and the process repeats itself again. The fractured chip flattens out upon separation and returns to its original shape because of the absence of plastic deformation. The cutting forces widely fluctuate with the repeated cycles of delamination, bending, and fracture. The machined surface microstructure reveals fibers partly impeded in the epoxy resin matrix because of elastic recovery and the fracture patterns of the matrix suggest that it was stretched in Mode I loading before fracture. Fibers on the machined surface are fractured perpendicular to their direction as a result of microbuckling and compression of the cutting edge against the surface. Figure 3.8a shows an example of the machined surface for delamination type chip formation [14].

Fiber buckling type of chip (Type II) occurs when machining 0° fiber orientation with 0° or negative rake angles (Fig. 3.7b). In this case, the fibers are subjected to compressive loading along their direction, which causes them to buckle. Continuous advancement of the cutting tool causes Mode II loading (sliding) or in-plane shearing and fracture at the fiber–matrix interface. Successive buckling finally causes the fibers to fracture in a direction perpendicular to their length. This fracture occurs in

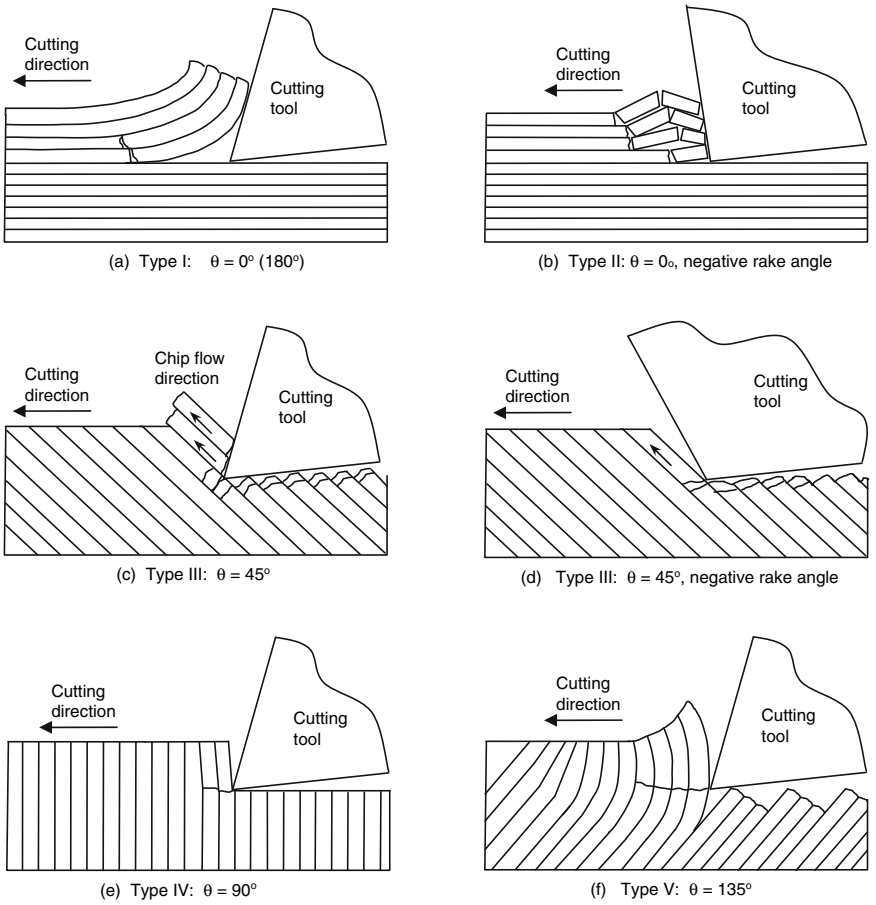

Fig. 3.7 Cutting mechanisms in the orthogonal machining of CFRP with a sharp edge [12, 13]

the immediate vicinity of the cutting edge and results in small discontinuous chips. The cutting forces fluctuation in this case is smaller than that for the delamination type (Type I) chip formation process. The machined surface for the buckling type chip is also similar to that of the delamination type chip machined surface.

Fiber cutting type chip formation occurs when machining fiber orientations greater than 0° and less than 90°, and for all rake angles (Fig. 3.7c–e). The chip formation mechanism consists of fracture from compression-induced shear across the fiber axes followed by interlaminar shear fracture along the fiber–matrix interface during the cutting tool advancement. During the compression stage of the chip formation process, cracks are generated in the fibers above and below the cutting plane. The cracks below the cutting plane remain in the machined surface and are visible when examined under microscope. Chip flow in machining all positive fiber angles up to 90° thus occurs on a plane parallel to fiber orientation. This makes

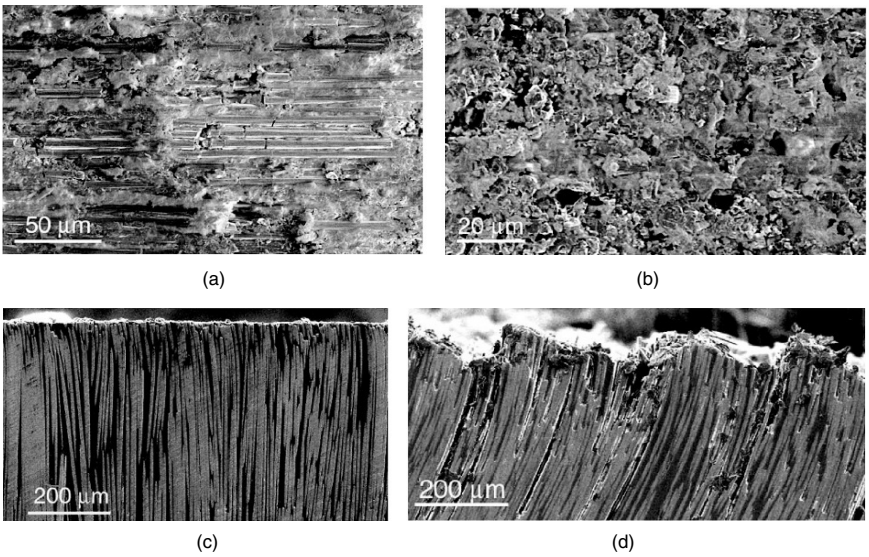

Fig. 3.8 Microstructure of machined CFRP specimens $\alpha_o = 20^\circ$, $a_c = 0.1\,\text{mm}$, (**a**) $\theta = 0^\circ$, (**b**) $\theta = 90^\circ$, (**c**) $\theta = 90^\circ$, and (**d**) $\theta = 120^\circ$ [14]

this particular type of chip formation similar in appearance to the chip formation in metal cutting where material is deformed by plastic shear as it passes across a shear plane. An important distinction, however, is the absence of plastic deformation in the case of machining FRPs. Material removal in these cases appears to be governed by the in-plane shear properties of the unidirectional composite material. The fiber cutting type of chip may be continuous (Type III) or discontinuous (Type IV). Depending on the amount of interlaminar shear that takes place as the chip segment slides up the tool rake face, the removed material may be loosely held together in a ribbon with some curl. The size of this distinct continuous chip decreases as the fiber orientation increases. As the fiber orientation increases toward 90° the interlaminar shear increases, leading to fracture of the chip segments along the fiber–matrix interface. The appearance of the machined surface in fiber cutting type chip formation is distinctively different than the machined surface of the delamination and buckling types. The surface is irregular and the fiber ends stick out of the surface with varying lengths. This is due to the fact that fiber cutting by fracture occurs at different points along their length. Transverse cracks in the fibers are often visible in the vicinity of the fiber ends.

Edge trimming of large fiber orientation angles (105–150°) is dominated by macrofracture. The advancing tool causes severe deformation of the fibers leading to delamination, intralaminar shear along fiber–matrix interface, and severe out-of-plane displacement. Extensive elastic bending is caused by the cutting edge compression against the fibers. The compressive stress ahead of the tool point causes the fibers and matrix to crack and a long but discontinuous chip is formed (Type V) (Fig. 3.7f). The chip thickness is often observed to be greater than the depth of cut

because fracture may occur below the cutting plane. Once the fibers are cut elastic recovery takes place and the cut fibers in the machined surface brush against the tool clearance face during their recovery. Figure 3.8b–d shows microstructures of machined surfaces demonstrating this type of chip formation mode.

3.3.1.1 Effect of Tool Geometry

As shown in Sect. 3.3.1, the chip formation mode in machining FRPs is critically dependent on fiber orientation, and to a much lesser extent on rake angle. Figure 3.9 shows a summary of the combined effects of fiber orientation and rake angle on chip type and chip formation mode. Cutting parallel to the fibers with a high positive rake angle produces chips by delamination and brittle fracture (peel fracture), while cutting with zero and negative rake tools produces chips by buckling of fibers perpendicular to fiber orientation by compression. The rake angle does not have a distinct effect on chip formation mode for positive fiber orientations $0^\circ < \theta \leq 75^\circ$, where fiber cutting is the dominant mode in this regime. The role of the rake angle is, however, in deciding whether a continuous or a discontinuous chip is formed. A continuous chip is formed for large positive rake angles and the transition to smaller positive rake angles favors the formation of discontinuous chips. Cutting perpendicular to the fibers with positive rake tools forms chips by fiber cutting, while cutting with a zero or negative rake tool forms chips by macrofracture.

Even though the effect of rake angle on chip formation mode is minor, its effect on surface topography and machining quality in general is clear. Matrix smearing over the machined surface decreased with an increase in rake angle. An increase in rake angle also served to increase the overall quality of the machined edge [9, 12].

The clearance angle does not seem to have any significant effect on the chip formation mode or machined surface topography, except for a slight enhancement in edge quality when a large clearance angle is used [9]. Clearance angle affects the tool forces because it controls the bouncing of fibers on the clearance face. Shallow clearance angles allow grater brushing of the fibers on the clearance face and thus higher normal (thrust) forces.

Rake angle, α_o (deg)											
30	I	III	III	III	III	III	IV			
20	I	III	III	III	III	III	IV			V
10	I	III	III	III	III	IV	IV	V	V	V
0	II	III	III	III	IV	IV	V	V	V	V
–10	II	IV	III	IV	IV	IV				
–20				IV			V			V
	0	15	30	45	60	75	90	105	120	135

Fiber orientation, θ (deg)

Fig. 3.9 Classification of chip formation types in machining FRP. I, Delamination type; II, fiber buckling type; III, fiber cutting type, continuous chip; IV, fiber cutting type, discontinuous chip; and V, macrofracture type, discontinuous chip

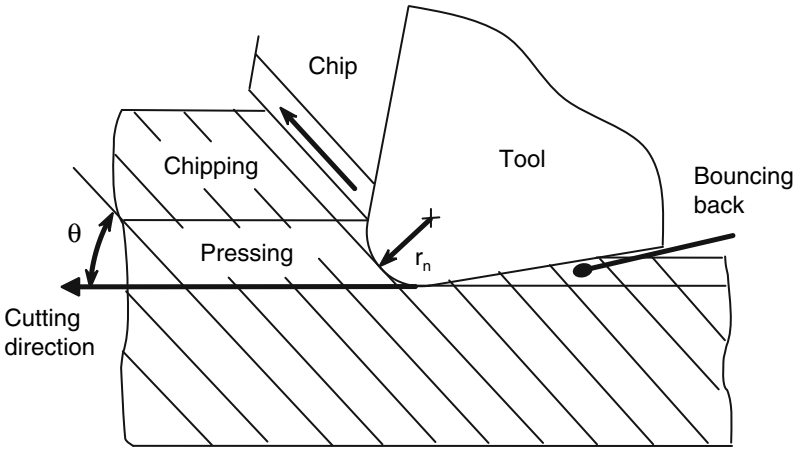

Fig. 3.10 Schematic showing processes involved in chip formation when cutting with a nose radiused cutting tool

3.3.1.2 Effect of Nose Radius

Section 3.3.1 has presented the chip formation modes when cutting with a relatively sharp cutting edge, and the prevailing mode for chip formation for positive fiber orientations ($0^\circ < \theta < 90^\circ$) has been identified as fiber cutting (both Types III and IV). When cutting with a large nose radiused tool or when the depth of cut is very small as compared to the nose radius, these chip formation modes no longer hold and other mechanisms become prevalent as illustrated in Fig. 3.10 [14]. The material in the path of the tool is divided into two regions, pressing and chipping, respectively. The material in the pressing region is pushed under the tool and then springs back because of elastic recovery after the tool passes over. The material in the chipping region forms the cut chip, which flows over the rake face by means of interlaminar shear in a plane parallel to the fibers. This action is similar to the fiber cutting chip formation mode (Type III) exhibited when cutting with a sharp cutting edge. Depending on the magnitude of depth of cut relative to the nose radius, the size of the pressing and bouncing back regions is equal to or slightly greater than the nose radius for positive fiber orientations ($0^\circ < \theta < 90^\circ$). For fiber orientations greater than 90° the size of the bouncing back region can be up to more than twice the nose radius. Figure 3.11 shows the variation of magnitude of bouncing back with depth for cut when cutting fiber orientation $\theta = 30^\circ$ with 50 μm nose radiused tool. It is shown that no cutting actually takes place for nominal depths of cut less that 100 μm, but mostly pressing of the material under the tool and bouncing back. The magnitude of bouncing back steadily increase as the nominal depth of cut increases up to 100 μm, and then only slightly increases with further increase in nominal depth of cut. The actual depth of cut, which is responsible for producing a chip, abruptly increases as the nominal depth of cut increases beyond 100 μm. This peculiar behavior of the material is also reflected in the magnitude of the thrust force, which is partly generated by the bounced back material pressing on the clearance face of the cutting tool [14].

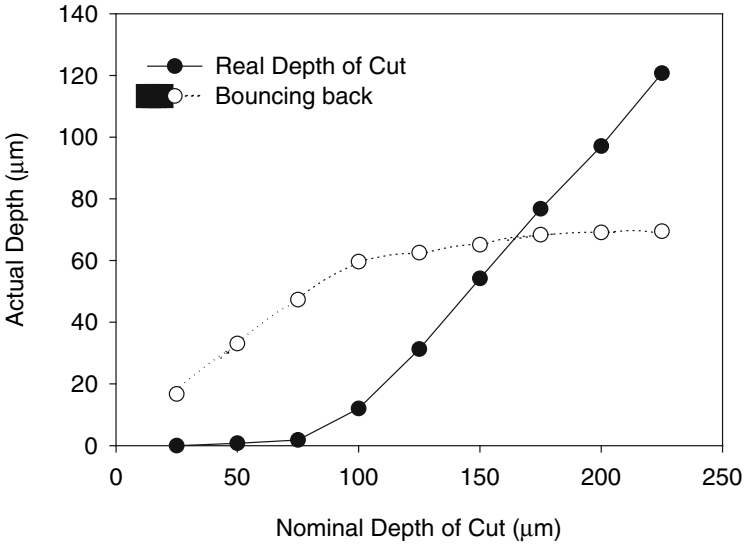

Fig. 3.11 Relationship between nominal depth of cut, actual depth of cut and bouncing back in machining CFRP with a nose radiused cutting tool. Cutting speed = 1 m/min, fiber orientation $\theta = 30°$, nose radius = 50 μm [14]

3.3.1.3 Effect of Matrix Material

The deformation behavior of the matrix material influences the chip formation process. Thermoset and thermoplastic matrix materials result in two different types of chips due to differences in their physical and mechanical properties. Sample chips from carbon–epoxy and carbon–PEEK composites are shown in Fig. 3.12. Epoxy thermoset, which are stronger and more brittle than thermoplastics produce fragmented and powdery chips by brittle fracture of the matrix as well as the fibers. Cracking of the matrix material near the tool tip is also evident. On the other hand, the ductile PEEK thermoplastic produces continuous and curling chips by plastic deformation. This phenomenon is attributed to the large elongation property under load and to slipping between the hydrocarbon chains in the polymer due to the increase in temperature during cutting. The chip morphology is also affected by the cutting conditions. For high cutting speeds and low feed rates the epoxy matrix fractures early because of high strain rates, resulting in smaller chip segments. The thermoplastic material exhibits considerable deformation due to the elevated temperatures generated by machining. This results in long ribbon-like chips to be produced. Low cutting speeds and high feed rates results in bulkier chips for both thermoset and thermoplastic materials.

3.3.1.4 Effect of Fibers

Fiber materials differing in their mechanical and physical properties exhibit different failure modes and machined surface morphology in composites machining.

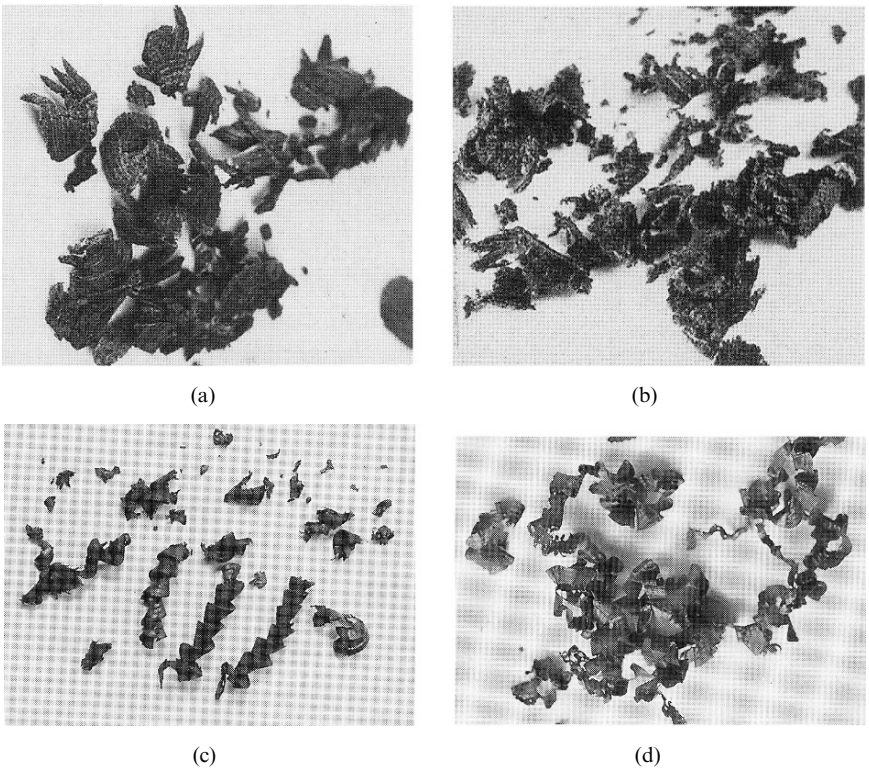

Fig. 3.12 Chip characteristics of Carbon–Epoxy composite (**a, b**) and Carbon–PEEK composite (**c, d**), (**a**) $V = 8\,\mathrm{m/min},\ f = 0.6\,\mathrm{mm/rev}$, (**b**) $V = 63\,\mathrm{m/min},\ f = 0.075\,\mathrm{mm/rev}$, (**c**) $V = 2\,\mathrm{m/min},\ f = 0.4\,\mathrm{mm/rev}$, (**d**) $V = 47\,\mathrm{m/min},\ f = 0.067\,\mathrm{mm/rev}$ [15]

SEM photographs of typical FRP chips are shown in Fig. 3.13. The chip morphology reveals the brittle fracture mode of inorganic fibers such as carbon and glass in contrast to the ductile failure mode of aramid fibers. Glass fibers produce chips with partial bending and cracking and result in pullout of both matrix material and fiber. Because glass is an amorphous material, the fracture surface of glass fibers is somewhat smooth as compared to the other fibers. Carbon fibers on the other hand produce chips by sharp fracture with very little deformation. Serrated fracture surfaces with individual facets inclined to the fiber axis can be seen. The self-lubricating effect of carbon and graphite fibers helps in easy gliding over the matrix, making CFRP more prone to debonding during machining. Aramid fibers possess greater toughness than glass and carbon fibers. This allows them to bend to a great extent in front of the advancing cutting edge. Thus, AFRP are very difficult to cut and produce a fussy lump of twisted fiber materials [16].

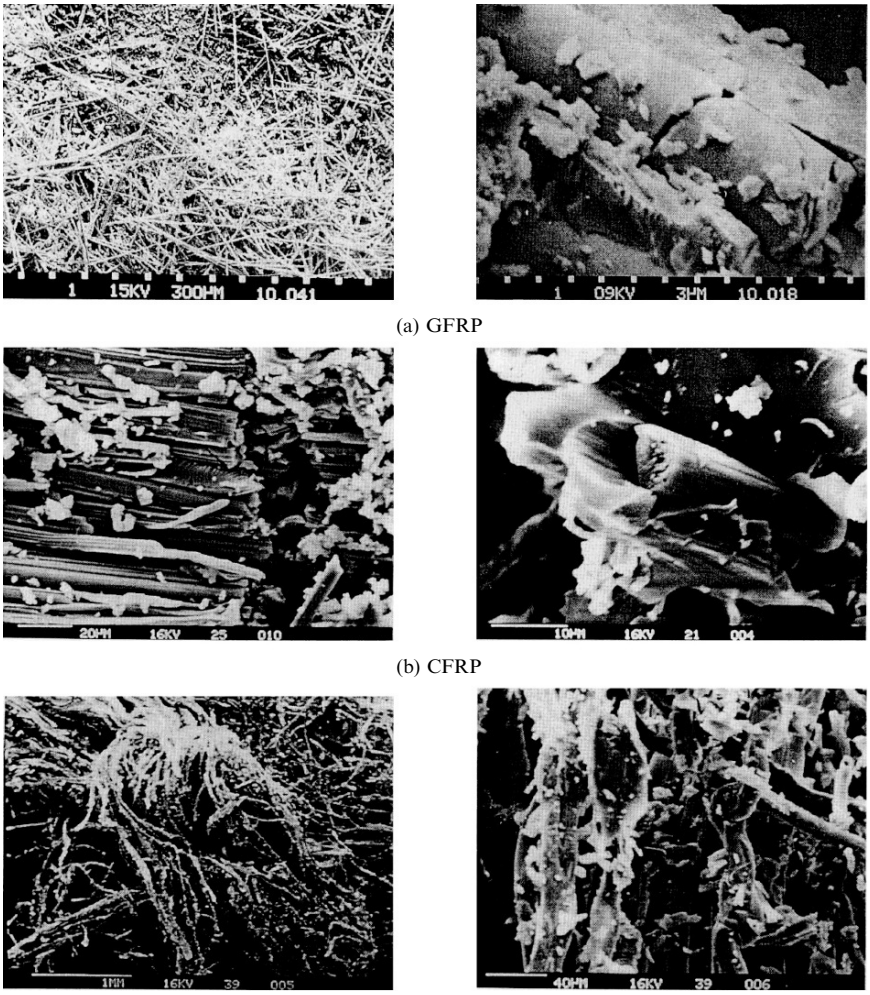

(a) GFRP

(b) CFRP

(c) AFRP

Fig. 3.13 SEM micrographs of chips from machining (**a**) glass, (**b**) carbon, and (**c**) aramid FRPs [16]

3.3.2 Cutting Forces

A high degree of fluctuation in the cutting forces is exhibited when machining FRPs as demonstrated in Fig. 3.14. The fluctuations in the principal or cutting force are observed to be higher than those in the thrust force. The degree of fluctuation depends primarily on fiber orientation and it correlates to a large extent with the mode of chip formation prevalent in cutting the particular fiber orientation as explained in Fig. 3.7. For cutting parallel to the fibers with positive rake angle, the force fluctuations are indicative of the peeling and bending/fracture action of the

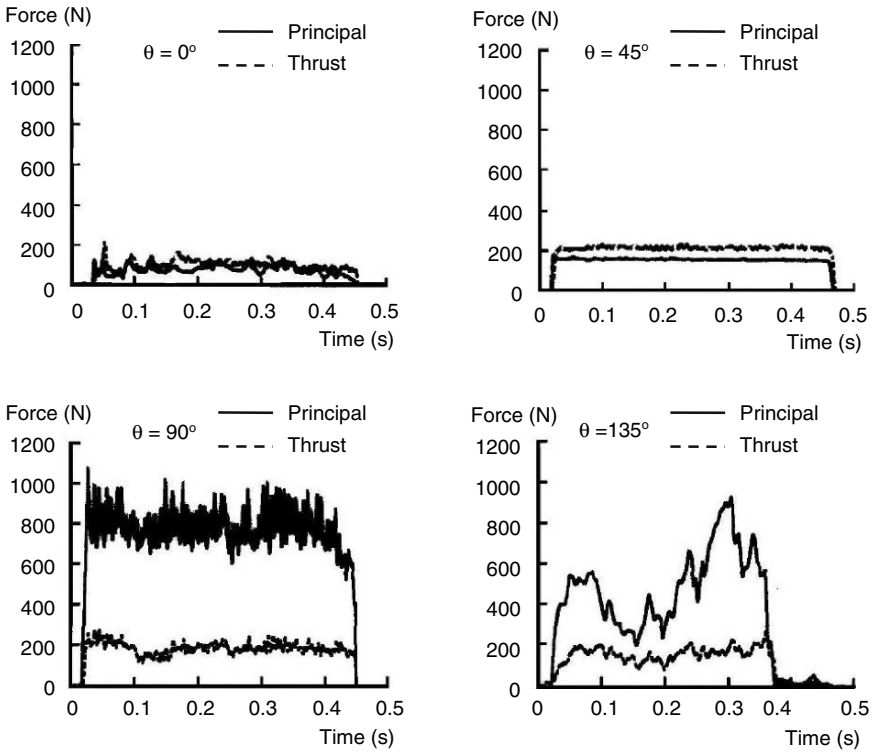

Fig. 3.14 Typical cutting (principal) and thrust force profiles in machining graphite/epoxy composite. Cutting conditions: $V = 4\,\mathrm{m/min}$, $a_c = 0.25\,\mathrm{mm}$, $a_w = 4.0\,\mathrm{mm}$, $\alpha_o = 10^\circ$ and $\gamma_o = 17^\circ$ [13]

fibers occurring on the rake face. For cutting positive fiber orientations, the principal force reflects changes in the process of shearing and fracture of the fiber and matrix materials with changes in fiber orientation. The thrust force reflects the interaction between the machined surface and the clearance face of the tool. The degree of force fluctuation decreased with an increase in fiber orientation and then increased when cutting fiber orientations of 90° and greater. It is noted that the nature of force fluctuations for trimming high fiber angles (above 90°) is distinctively different from that for trimming low-positive fiber orientations (0–75°) as it is evident from the mode of chip formation explained in Fig. 3.7. For cutting large positive fiber orientations, greater fluctuations are associated with pressing and then shearing the fibers and cracking the matrix.

3.3.2.1 Effect of Fiber Orientation

Cutting and thrust forces are found to be primarily dependent on fiber orientation, and operating conditions and tool geometry have far less influence on cutting

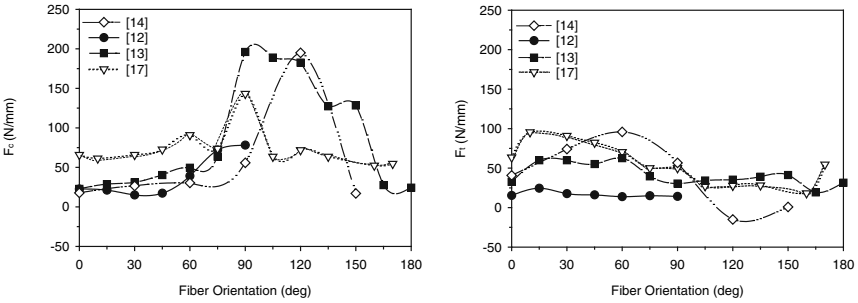

(a) CFRP and GrFRP

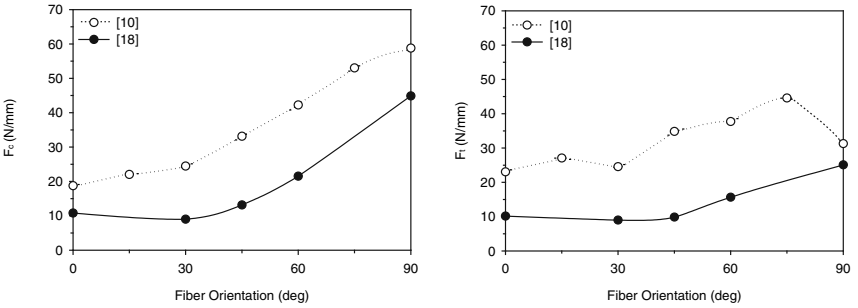

(b) GFRP

Fig. 3.15 Variation of cutting and thrust force per unit width with fiber orientation for different FRP composites

Table 3.1 Cutting conditions for data in Figs. 3.15 and 3.16

Source	V (m/min)	a_c (mm)	a_w (mm)	Cutting tool	α_o (deg)	γ_o (deg)	r_n (μm)
14	1.00	0.05	4.00	–	20	7	50
12	0.02	0.10	2.28	K10	10	10	2
13	4.00	0.25	4.00	PCD	10	17	–
17	1.18	0.25	2.20	K20	12	–	–
10	0.50	0.10	4.00	K10	10	6	20
18	100	0.10	5.00	–	5	–	–

forces. Average cutting (principal) and thrust forces measured during trimming of different FRP materials are shown in Fig. 3.15. The tool geometry and cutting conditions for this data is shown in Table 3.1. The properties of the workpiece material and its constituents are shown in Table 3.2. The cutting (principal) force generally increases gradually with fiber orientation up to approximately 60°, then exhibits a large increase when edge trimming 90° fiber orientation. The principal force then decreases with further increase in fiber orientation, with significant decreases occurring between 100° and 165° orientations. An apparent shift in the maximum principal force is exhibited by the data from [14]. A possible cause for this shift is the small depth of cut and the large positive rake angle used in this

Table 3.2 Mechanical properties of unidirectional composites used in Figs. 3.15 and 3.16

Fiber	ρ (kg/m^3)	d (μm)	E_1 (GPa)	E_2 (GPa)	G_{12} (GPa)	X_t (GPa)
Carbon (Torayca T300) [12]	1,760	8	230			3.53
Carbon T-300 [17]	1,760		230	40	24	
E-Glass/epoxy [18]	2,540	13	72.5			1.47

Composite	V_f	E_1 (GPa)	E_2 (GPa)	G_{12} (GPa)	ν_{12}	X_t (GPa)	Y_t (GPa)	X_c (GPa)	S (GPa)
Carbon/epoxy [12]	0.60	130	10	0.10		1.95	0.05		
Carbon (T300)/ epoxy [17]		96.3	7.9	2.8	0.31	1.037	0.0495		0.0885
Graphite (IM-6)/ epoxy [13]		117–138	9.0–11.0			1.378	0.041	1.309	
Carbon (F593)/ epoxy [14]		120				1.331		1.655	
Glass/epoxy [18]	0.597	44	15		0.3–0.6	1.2	0.059		0.25
Glass/epoxy [10]		48.0	12.0	6.0	0.19	0.55	0.03	0.40	0.0125

X_t Tensile strength in longitudinal direction, Y_t Tensile strength in transverse direction, X_c Compressive strength in longitudinal direction, Y_c Compressive strength in transverse direction, S In-plane shear strength

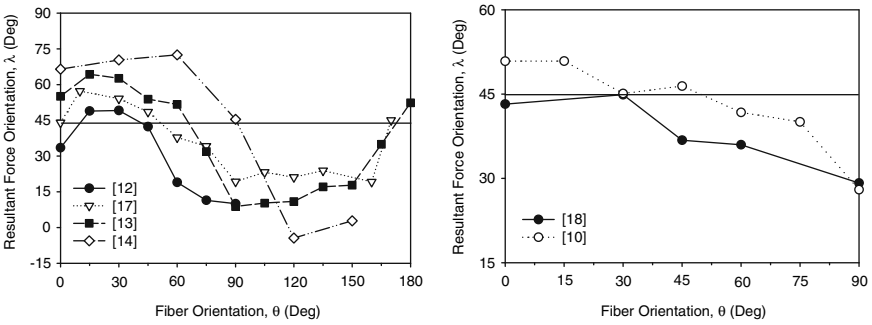

(a) CFPR and GrFRP (b) GFRP

Fig. 3.16 Direction of resultant force in orthogonal machining of different FRP composites

experiment. Significant bouncing back is associated with the small depth of cut used as explained in Sect 3.1.1. The drastic increase/decrease in the principal forces is probably associated with the change in mode of chip formation.

Figure 3.16 shows the orientation of the resultant force with respect to the cutting direction, which is defined by

$$\lambda = \tan^{-1}\left(\frac{F_t}{F_c}\right). \tag{3.21}$$

The resultant orientation signifies the magnitudes of F_c and F_t relative to each others. The thrust force is greater than the principal (cutting force) for resultant orientations greater than 45°. Contrary to the cutting force behavior in metal cutting, the thrust

force is found to be greater than the corresponding principal force for fiber orientations $0^\circ < \theta \leq 75^\circ$, except for the data from [12] and [18]. In general, the thrust force exhibited more complex behavior than the principal force. An increase in the thrust force is exhibited when cutting small positive fiber orientations, then the thrust force decreases with further increase in fiber orientation. High thrust forces are likely to be attributed to the elastic recovery of the fibers, which underwent deformation within the contact zone prior to fracture. The elastic energy of the fibers would be released after the fibers are severed, imparting a thrust force on the tool flank and providing a potent source for tool wear.

3.3.2.2 Relationship to Chip Formation Modes

The chip formation mode in cutting positive fiber orientations $(0^\circ < \theta < 90^\circ)$ has been described previously as fiber cutting mode which consists of fiber cutting by compression shear followed by chip flow upward on the rake face by interlaminar shear along the fiber–matrix interface. It has been noted that this type of chip formation is similar (if only in appearance because of the absence of plastic deformation) to the chip formation by shear in metal cutting. In theses cases, the principal (cutting) force F_c and the thrust force F_t can be resolved into a shear force, F_s, acting along the shear plane and a normal force, F_n, to the shear plane as shown in Fig. 3.17 and using (3.22), respectively. It is noted here that the shear plane in cutting FRPs is generally found to coincide with the plane of the fibers for fiber orientations $0^\circ < \theta < 90^\circ$.

$$\begin{aligned} F_s &= F_c \cos\theta - F_t \sin\theta \\ F_n &= F_c \sin\theta + F_t \cos\theta. \end{aligned} \tag{3.22}$$

It is also shown in Fig. 3.17 that that the resultant force, R, makes an angle λ_e to the fiber orientation. The behavior of angle λ_e and normal force F_n with fiber orientation may be linked to the chip formation mode as shown in Figs. 3.18 and 3.19. The

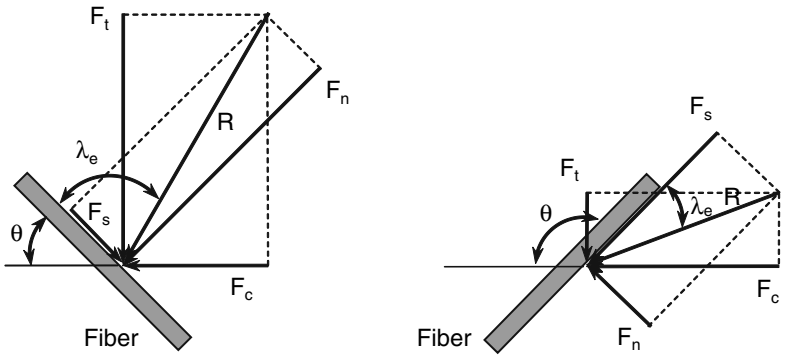

Fig. 3.17 Cutting force components along and perpendicular to the plane of the fibers

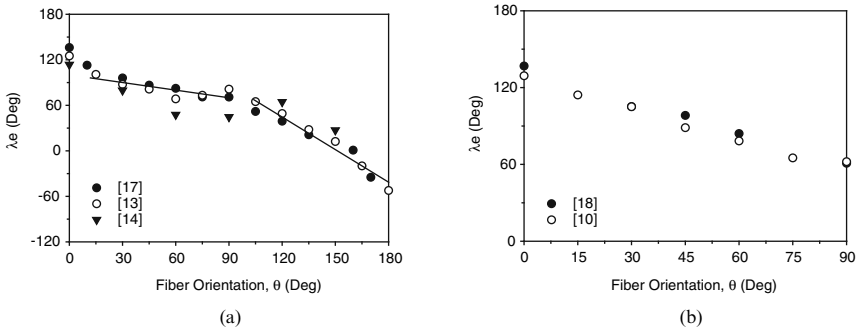

Fig. 3.18 Angle between resultant force and fibers for machining (**a**) CFRP and (**b**) GFRP

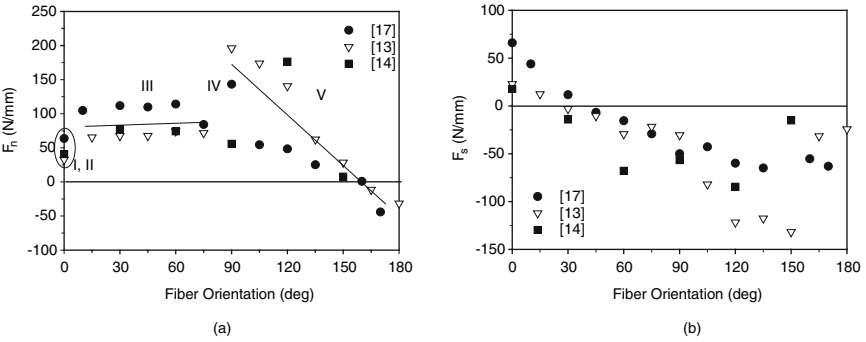

Fig. 3.19 Normal force, F_n, in the fiber direction and shear force, F_s in the transverse direction in orthogonal machining of CFRP. Cutting conditions are in Table 3.1

orientation of the resultant force with respect to the fibers (Fig. 3.18a) decreases abruptly from fiber orientation 0° to 15°, then continues to decrease slowly with further increase in fiber orientation up to $\theta = 90°$, then decreases more rabidly thereafter. The normal force on the shear plane (Fig. 3.19a) behaves in a similar manner. It increases with fiber orientation from 0 to 15° and then remains nearly constant to 75°. A large increase in normal force occurs in trimming the 90° orientation and then the normal force continues to decrease with increasing fiber orientation thereafter. The shear force changes from positive to negative with fiber orientation (Fig. 3.19b) and continues to increase in magnitude with fiber orientation up to 150°. The interruption in the shear force at 90° is negligible, but an abrupt decrease in the magnitude of the shear force is evident at fiber orientation of 150°. The behavior of the resultant orientation angle and normal force appears to be consistent with the chip formation modes discussed earlier and is consistent with the visual changes in chip formation according to fiber angle [13]. The different types of chip produced in machining unidirectional FRPs as discussed in Sect. 3.1 are labeled in Fig. 3.19a. The first interruption in the normal force from fiber orientation 0 to 15° is associated with the transition from Types I and II chips to Type III chip. The second interruption at 90° is associated with the transition from Type IV to Type V chip. This

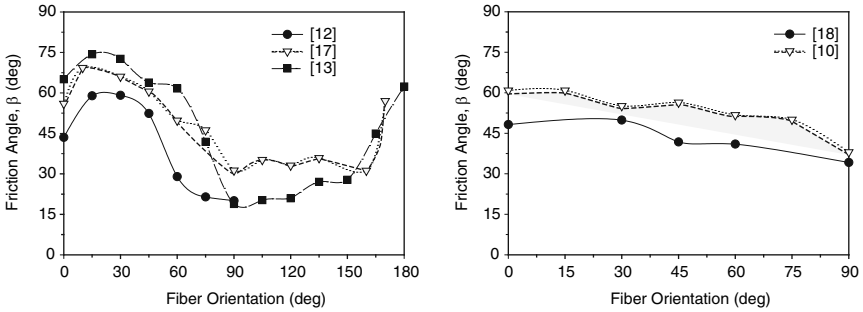

Fig. 3.20 Variation of friction angle with fiber orientation in machining (**a**) CFRP and (**b**) GFRP

transition is also associated with an interruption in the slope of the fiber orientation angle in Fig. 3.18a.

3.3.2.3 Friction Angle

Friction on the tool faces interacts strongly with the shearing process and influences the shear stress and shear strain in the shear plane and the resulting chip type. The friction coefficient on the tool face, μ, and friction angle, β, are determined from cutting forces using (3.14). The friction angle in machining FRPs as calculated from (3.14) is shown in Fig. 3.20. The friction angle in machining CFRP appears to be critically dependent of fiber orientation and assumes almost a sinusoidal shape. The agreement in friction angle behavior among the experimental results from different sources is striking and appears to be closely related to the chip formation process. An initial rise in friction angle from fiber orientations 0–15° is associated with the transition from Types I and II chips to Type III chip. A significant decrease in the angle of friction occurs in the fiber orientation range $15^\circ \leq \theta < 90^\circ$ and appears to be correlating with the Type III chip formation mode. Contrary to the behavior of CFRP, the friction angle in machining GFRP appears to vary only slightly with fiber orientation.

3.3.2.4 Effect of Tool Geometry

The effect of rake angle on tool forces when cutting unidirectional CFRP is shown in Fig. 3.21. There is generally a decrease in the cutting force and thrust force with an increase in rake angle. This can be explained by the fact that chips slide of and slide away a little easier as the rake angle increases. This trend has been confirmed by several studies in machining both CFRP and GFRP [10, 12, 14, 18], with the exception of [13] which showed an increase in the thrust force with an increase in rake angle. The rate of decrease in the cutting force depends also on fiber orientation. A greater decrease in the cutting force is exhibited for fiber orientations above 60°,

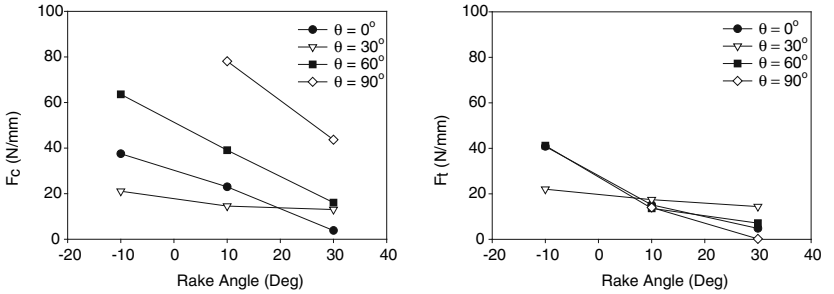

Fig. 3.21 (**a**) Cutting force vs. rake angle and (**b**) vertical force vs. rake angle when cutting CFRP. $v = 0.02\,\mathrm{m/min}$, $a_c = 0.1\,\mathrm{mm}$, and $a_w = 2.28\,\mathrm{mm}$ [12]

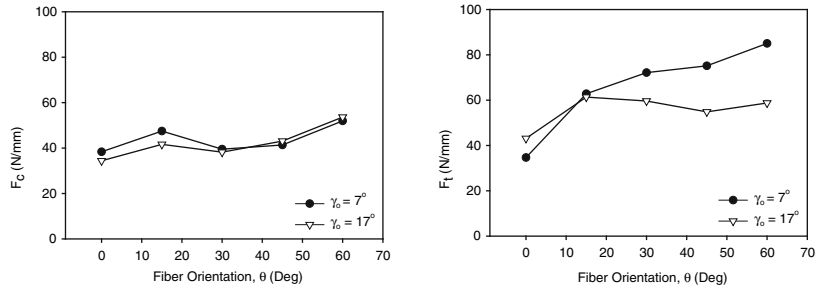

Fig. 3.22 (**a**) Cutting force vs. clearance angle and (**b**) vertical force vs. clearance angle when cutting GrFRP. Cutting conditions are shown in Table 3.1 [13]

while the decrease in the thrust force seemed to be independent of fiber orientation. It has been noted in [10] that increasing the rake angle beyond 30° results in an increase in the cutting force when machining unidirectional GFRP. It was suggested based on this observation that $\alpha_o = 30°$ is an optimum rake angle for machining GFRP. There is only a limited number of studies on effect of clearance angle on tool forces [8, 13]. This work generally indicates that an increase in the clearance angle leads to slight decrease in the principal (cutting) force, but to a drastic drop in the thrust (vertical) force as shown in Fig. 3.22. This can be explained by the size of the contact area between the tool and the workpiece. This area is a function of the relief angle in a way that a decreasing angle results in a larger area, and thus in an increasing thrust force.

The effect of nose radius on tool forces is discussed in association with depth of cut, because the relative magnitude of the latter decides how much cutting actually takes place. It has been pointed out earlier that for a small depth of cut as compared to the nose radius much of the material in the cutting edge path is pressed under the clearance face and then bounces back once the tool has passed [14]. The influence of this on the cutting forces is apparent from the data in Fig. 3.23 [10, 14]. For cutting CFRP with a nose radiused tool, the thrust force dramatically increases with an increase in depth of cut up to a depth of cut of 100 µm, then increases slowly

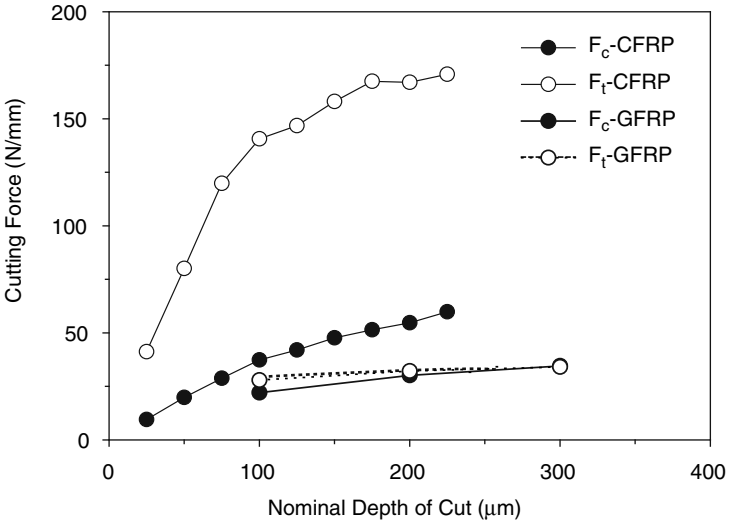

Fig. 3.23 Relationship between nominal depth of cut and cutting forces in machining CFRP [14] and GFRP [10] with a nose radiused cutting tool. Fiber orientation $\theta = 30°$, nose radius $= 50\,\mu m$

thereafter. The increase in the cutting force with depth of cut is smaller and is proportionate to the depth of cut. It is believed that the peculiar behavior in the thrust force is a result of the pressing of material under the clearance face. As the depth of cut increases beyond the critical value of 100 μm, the effect of fiber cutting denominates over the pressing action. Contrary to this behavior in cutting CFRP, it was shown in [10] that depth of cut has only marginal effect on the cutting and the thrust forces when machining GFRP.

3.4 Machining of Multidirectional Laminates

Studies of machining unidirectional laminates provided fundamental understanding of the relationships between fiber orientation, process parameters, and the mode of chip formation. Multidirectional laminates are of more practical interest than unidirectional laminates since most practical structures are made by laying unidirectional tapes in some desired arrangements. The cutting mechanisms of multidirectional laminates was studied experimentally by [12, 19] and results of their studies are presented below. In [19], edge trimming experiments were conducted on Graphite/Epoxy multidirectional laminate of layup sequence $[45°/-45°/(0°/90°/45°/-45°)_2]_s$. The panels were composed of 3501-6 resin and IM-6 fibers, 0.68 volume fraction, and 0.2-mm ply thickness. Rake angle, clearance angle, depth of cut, and cutting speed were varied according to a factorial design. The study in [12] consisted of cutting of cross-ply laminates of CFRP with lay up sequence

$[\theta_i/\theta_{i+90}]_s$ where $i = 0, 15, 30, 45, 60, 75, 90$. Eleven plies were included in each cross-ply laminate and volume fraction of the fiber was 0.52. The rake angle was varied from -10 to 30° and the clearance angle was held at 10°.

3.4.1 Chip Formation

Chip formation in trimming of the multidirectional laminate is very similar to that of unidirectional material despite the presence of multidirectional plies. Each ply in the composite laminate behaved independent of the surrounding plies and exhibited a similar chip formation mode to that of a unidirectional laminate. Discontinuous chips were noted as the chips progressed along the rake face. The length of chips was in general longer than that in unidirectional trimming. With the exception of 135° plies, the chip release fracture plane extended along the fiber–matrix interface for each particular ply. Bundles of 0° fibers were detached from the composite ply due to buckling or delamination followed by bending (Type I and II). Compression-induced fiber cutting was evident for the 45 and 90° plies (Type III) and very tiny chips were produced for the ply with chip release along the fiber direction. However, contrary to cutting unidirectional plies, cutting of the 90 and 135° plies took place without any indication of out-of-plane displacement. Support provided by the adjacent plies allowed machining of these fiber orientations with relatively small degree of structural damage. Damage to the 135° plies was more evident through shear failure along the fiber–matrix interface and fracture perpendicular to the fiber direction beneath the trimming plane. The machined surface clearly reflected the difference in fiber orientation of each ply in the multidirectional laminate. A smooth surface was produced for the 0 and 45° plies and matrix smearing on the surface was evident. The machined surface for the 135° ply exhibited irregularities like a saw-tooth profile. The fiber ends could be easily observed and it resided in a position lower than the machined surface. The best surface roughness was obtained for a cross ply $[0^\circ/90^\circ]_s$ and rake angle of 20° [12].

3.4.2 Cutting Forces

Fluctuations of the cutting forces in multidirectional laminates were nearly identical to those recorded in edge trimming of 90° unidirectional material. Contrary to the force behavior in cutting unidirectional laminates, the principal cutting force was always greater than the thrust force for all cutting conditions and tool geometries. Tool geometry has significant influence on cutting forces. The resultant force decreased with increasing rake angle from 0 to 5°, but then increased with a further rake angle increase to 10°. Minimum resultant force was obtained when cutting with 5° rake and 17° clearance angles. An empirical model in (3.23) was developed for the cutting and thrust forces in trimming of multidirectional laminate GrFRP using

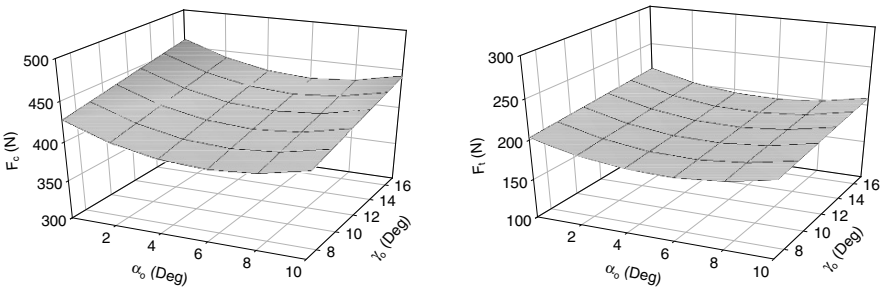

Fig. 3.24 Effect of tool geometry on the cutting forces in machining multidirectional graphite/epoxy. Cutting conditions: $v = 4\,\mathrm{m/min}$, $a_c = 0.254\,\mathrm{mm}$ [19]

analysis of variance, ANOVA [19]. It was found that rake angle, α_o, and depth of cut, a_c, have major effects on the cutting force and that clearance angle, γ_o, and depth of cut have major effects on the thrust force (Fig. 3.24). Depth of cut has the greatest influence and cutting speed has negligible influence on the cutting forces. Optimal rake angle, α_o, in terms of minimizing the principal cutting force was determined to be approximately 7°. The optimal tool geometry for minimizing the resultant force consists of 6–7° rake angle and 17° clearance angle.

$$\begin{aligned} F_c &= 10.68 - 11.67\alpha_o + 1{,}584.53a_c + 0.99\alpha_o^2 - 7.10Va_c + 12.74\gamma_o a_c \\ F_t &= 147.27 - 4.92\gamma_o + 188.55a_c + 0.77\alpha_o^2 - 32.54\alpha_o a_c + 24.19\gamma_o a_c. \end{aligned} \tag{3.23}$$

The resultant cutting force obtained in trimming multidirectional laminates is nearly equivalent to a summation of forces from independent unidirectional plies, based on a rule of mixture approach [19]. Thus, the multidirectional laminate behaves like an assemblage of unidirectional plies and its behavior will be governed by the ply with the most rigid structural characteristics. The cutting forces of cross-ply laminates were critically dependent on cross-ply orientation, decreasing with cross-ply orientation $[0°/90°]_s$ to $[30°/120°]_s$ and then increasing thereafter. The minimum cutting forces were obtained for $[30°/120°]_s$ or $[45°/135°]_s$ even though these orientations did not offer the best surface roughness. Increasing the rake angle also resulted in decreasing the cutting forces [12].

3.5 Modeling of the Chip Formation Process

3.5.1 Shear Plane Models

Only a few researchers have attempted to analyze the mechanics of chip formation process in orthogonal machining of unidirectional FRPs [17,18,20]. The works of [17,18] have attempted to employ the well-known Merchant's shear plane theory (minimum energy principle) from metal cutting to the problem of machining FRPs.

The work of [20] dealt with machining with a large nose radiused tool and considered the action of chip formation to be composed of shearing as well as indentation (pressing) with the rounded tool nose. The basis for all of these works is repeated observations of the chip formation process, which concluded that a close behavior to that of machining of ductile metals is exhibited over a wide range of fiber orientations $(15^\circ \leq \theta \leq 75^\circ)$.

It is generally assumed that the chip is formed by shear along a shear plane that emanates at the tip of the cutting edge and continues upward to a point where the chip free surface meets the workpiece free surface. According to the minimum energy principle, the shear plane angle assumes a value that makes the energy consumed in cutting to be a minimum. Material removal appeared to be governed by the in-plane shear properties of the unidirectional material which is considered to be a function of fire orientation and is determined by experiment.

3.5.1.1 Model of Takeyama and Iijima [18]

Takeyama and Iijima [18] proposed that chip formation in machining GFRP takes place by shearing the material along a shear plane that makes an angle ϕ with the cutting plane, as shown in Fig. 3.25. This proposal was made based on observations of the orthogonal cutting of GFRP, which concluded that it exhibits a close behavior to that of metal cutting over a wide range of fiber orientations. The proposed methodology uses Merchant's theory of minimum cutting energy to determine the shear plane angle and then calculate the cutting forces from force equilibrium and known shear stress in the shear plane.

For the purpose of estimating the cutting forces some assumptions were made as follows:

(1) Chip formation is performed by quasicontinuous shear.
(2) The shearing stress in the shear plane is independent of the normal stress in the shear plane and is only a function of fiber angle.

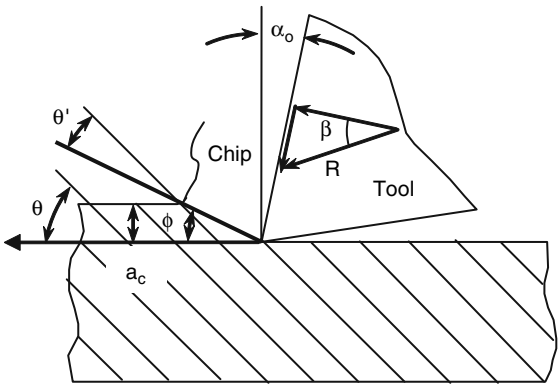

Fig. 3.25 Orthogonal cutting model of Takiyama and Iijima [18]

(3) The shearing strength, which can be obtained by simple shear test, is substituted for the yield stress.
(4) The type of cut is two-dimensional.
(5) The fiber angle θ is limited as $\theta^\circ \leq 90^\circ$.
(6) The effect of temperature is ignored.
(7) Shearing in chip formation takes place in a direction so as to minimize the cutting energy.

In this model, θ' is the shear fiber angle, the angle between shear plane and fiber direction and $\tau(\theta')$ is the in-plane shear strength of GFRP which is obtained experimentally. From the cutting force circle diagram in Fig. 3.4, it can be shown that

$$\begin{aligned} F_c &= R\cos\lambda = R\cos(\beta - \alpha_o) \\ F_t &= R\sin\lambda = R\sin(\beta - \alpha_o). \end{aligned} \tag{3.24}$$

Also, the shear force on the shear plane is given by

$$F_s = R\cos(\phi + \beta - \alpha_o). \tag{3.25}$$

The shear force can also be calculated from the in-plane shear strength of the material, which is assumed to be a function of the fiber orientation, $\tau(\theta')$:

$$F_s = \tau(\theta')A_s = \frac{\tau(\theta')A_c}{\sin\phi}, \tag{3.26}$$

where A_s is the shear plane area and A_c is the cross section of undeformed chip. Substituting (3.26) in (3.25) and for $A_c = a_c \cdot a_w$, then solving for the resultant force, R, the cutting force F_c and the thrust force F_t leads to:

$$R = \frac{\tau(\theta')a_c a_w}{\sin\phi}\frac{1}{\cos(\phi + \beta - \alpha_o)}, \tag{3.27}$$

$$F_c = \frac{\tau(\theta')a_c a_w}{\sin\phi}\frac{\cos(\beta - \alpha_o)}{\cos(\phi + \beta - \alpha_o)}, \tag{3.28}$$

$$F_t = \frac{\tau(\theta')a_c a_w}{\sin\phi}\frac{\sin(\beta - \alpha_o)}{\cos(\phi + \beta - \alpha_o)}. \tag{3.29}$$

The power consumed in machining, P_m, is then calculated as:

$$P_m = F_c v = \frac{v\tau(\theta')a_c a_w}{\sin\phi}\frac{\cos(\beta - \alpha_o)}{\cos(\phi + \beta - \alpha_o)}, \tag{3.30}$$

where v is the cutting speed. Referring to the assumption (7), for a minimum energy condition the derivative of P_m with regard to ϕ is made equal to zero as follows:

$$\frac{\partial\tau(\theta')}{\partial\phi}\sin\phi\cos(\phi + \beta - \alpha_o) - \tau(\theta')\cos(2\phi + \beta - \alpha_o) = 0. \tag{3.31}$$

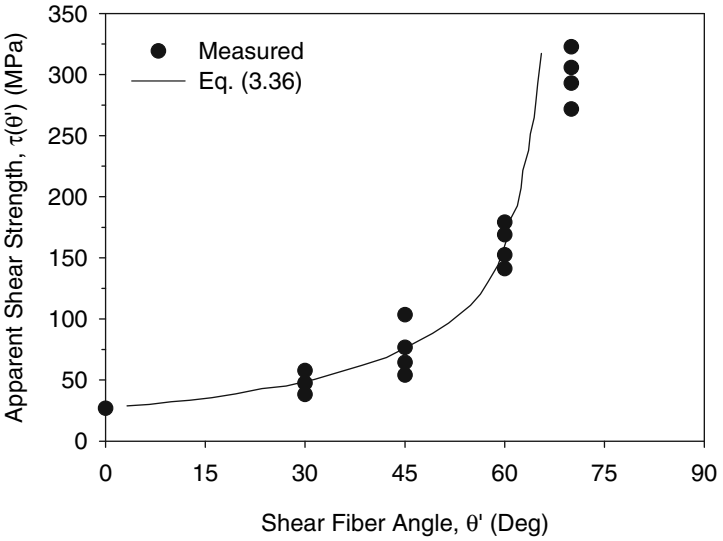

Fig. 3.26 Experimental relationship between apparent shear strength and fiber orientation [18]

Table 3.3 Solution of (3.33) for $\alpha_o = 5^\circ,\ \beta = 40^\circ$ and different fiber orientations

Fiber angle, θ	0	15	30	45	60	90
Shear plane angle, ϕ	30.4	28.9	27.9	29.0	30.3	43.2

In order to solve (3.31) for the shear plane angle ϕ, $\tau(\theta')$ should be obtained experimentally and its derivative with respect to ϕ evaluated. Figure 3.26 shows the relationship between the in-plane shear strength $\tau(\theta')$ and the shear fiber angle θ', for GFRP which has been obtained by simple shear test with varied shear fiber angle θ'. Since θ' cannot be larger than 60° in actual machining, fitting a curve for the observed points within the range $0^\circ \leq \theta' \leq 60^\circ$ gives the following (3.32). The equation is shown as solid line in Fig. 3.26 and shows reasonable fit of the experimental data in the range of fiber orientations considered.

$$\tau(\theta') = 23.03 + 0.10(\theta')^{1.63} + 0.26(\cos\theta')^{-7.71}, \tag{3.32}$$

where $\theta' = |\theta - \phi|$.

From (3.31) and (3.32), one can obtain the following relationship, which allows determining the shear plane angle ϕ as a function of fiber orientation:

$$\begin{aligned}&[0.163|\theta-\phi|^{0.63} + 2.005(\cos|\theta-\phi|)^{-8.71}\sin|\theta-\phi|]\sin\phi\,\cos(\phi+\beta-\alpha_o)\\&+[23.03 + 0.10|\phi-\theta|^{1.63} + 0.26(\cos|\phi-\theta|)^{-7.71}]\cos(2\phi+\beta-\alpha_o) = 0.\end{aligned} \tag{3.33}$$

Values of the shear plane angle obtained from (3.33) are shown in the Table 3.3 for a constant friction angle of $\beta = 40^\circ$. Note that the shear plane angle is almost independent of fiber orientation for fiber orientations less than 90°. Once the shear

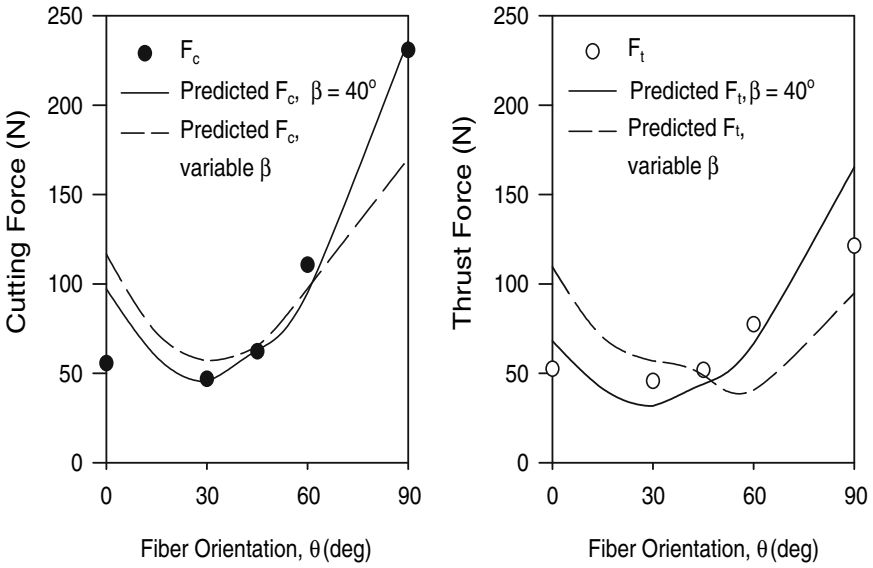

Fig. 3.27 Comparison of experimental and calculated cutting and thrust forces [18]. Cutting conditions are shown in Table 3.1

plane angle is obtained, the principal and the thrust forces can be calculated from (3.28) and (3.29) for a definite fiber angle θ. A comparison between the calculated cutting forces and measured ones is illustrated in Fig. 3.27, in which the rake angle is 5°. A fairly well coincidence between computed and experimental curves seems to indicate that the model is effective to estimate the cutting forces for fiber orientations $15° \leq \theta \leq 60°$. Bearing in mind that the friction angle varies with fiber orientation as shown in Fig. 3.20, the shear plane angle and resulting cutting forces are now evaluated for the actual values of angle β and the results are also shown in Fig. 3.27. Surprisingly, incorporating the actual values of the friction angle in the prediction model only deteriorates the model performance.

3.5.1.2 Model of Bhatnagar et al. [17]

It was argued in [17] that the chip flow in machining unidirectional FRPs almost always coincides with the plane of the fibers. Therefore, a solution was proposed in which the shear plane angle ϕ is made equal to the fiber orientation angle θ. It was assumed that this proposition is only reasonable for positive fiber orientations between 15 and 75°. The Iosipescu shear test was used to determine the in-plane shear strength for CFRP and the results of this test are shown in Fig. 3.28. A polynomial in (3.34) was obtained by fitting of the data

$$\tau(\theta) = 85.4285 - 2.2280 \cdot \theta + 0.0300 \cdot \theta^2 - 0.0001 \cdot \theta^3 \text{ MPa}. \tag{3.34}$$

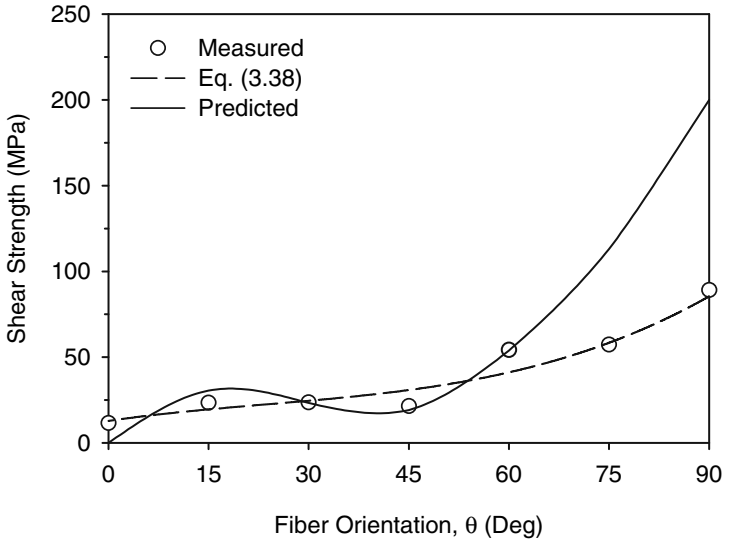

Fig. 3.28 Comparison of experimentally determined in-plane shear strength and predicted shear strength during machining CFRP [17]. Cutting conditions are shown in Table 3.1

An indirect method was used for validating the shear plane model. The apparent shear strength of the material being sheared along the fiber orientation plane is determined from (3.10) by setting the shear plane angle to be equal to the fiber orientation angle (3.35) and using the cutting forces from orthogonal cutting experiment. It was necessary to use the absolute value of the shear strength calculated from shear plane model because most values came out as negative. The results are compared with the Iosipescu shear test results as shown in Fig. 3.28. Reasonable agreement between the calculated and measured shear strength is evident for fiber orientations $15^\circ \leq \theta \leq 60^\circ$. The model predictions are too far off for fiber orientations in which departure from flow type chip is evident.

$$\tau_s(\theta) = \frac{(F_c \cos\theta - F_t \sin\theta)\sin\theta}{a_c a_w}. \tag{3.35}$$

Apparently, there are two obvious limitations to the shear plane models when applied to machining unidirectional composites. First, any resemblance to shearing in the sense of a homogeneous material behavior occurs only for a limited range of fiber orientations between 10 and 75°, and thus this approach would not apply to all possible fiber orientations in a composite structure ($0^\circ \leq \theta \leq 180^\circ$). Second, interfacial shearing mostly occurs along the fiber–matrix interface causing the chip to slide up the rake face. This, in a way, forces the shear plane angle to assume a value equal to the fiber orientation angle, regardless of the minimum energy principle. Therefore, results from this approach have shown reasonable agreement with experimental findings only in the range of fiber orientation from 10 to 60°.

3.5.2 Mechanics Model of Zhang et al. [20]

The mechanics model described here is based on observations of the orthogonal cutting process of FRPs with a nose radiused cutting tool. A description of this chip formation process was given in Sect. 3.1.1 and illustrated in Fig. 3.10. It is noted here that this model applies only to fiber orientations $0^\circ < \theta < 90^\circ$. According to this model, the cutting zone is divided into three distinct regions as shown in Fig. 3.29. The chipping region consists of the material that is subjected to shearing along the shear plane AB of inclination ϕ and forms the chip, in a similar manner to chip formation when cutting with a sharp tool. The depth of this region is the actual depth of cut, $\hat{a}_c$, which is less than the nominal depth of cut a_c (Fig. 3.11). The pressing region contains material that escapes cutting and undergoes elastic deformation as it is pushed under the tool nose. The thickness of this material is equal to the nose radius, r_n. As shown in Fig. 3.29, the nominal depth of cut equals to the sum of the thickness of the chipping region and the pressing region. The bouncing region represents the material bouncing back by elastic recovery as it passes point D on the clearance face. The thickness of this region is also assumed to be equal to the nose radius. Each of these regions generates force components in the principal directions, and assuming that the principle of superposition holds, the total cutting forces are the sum of the individual force contribution from each region.

The shear plane AB in that bounds the chipping region is formed by many microcracks of the fibers, normal to their direction, and fiber–matrix debonding, along the plane of the fibers. Therefore, the shear plane edge follows a jagged line from A to B with steps normal to and parallel to the fiber orientation. The general inclination of the shear plane, ϕ is not necessarily equal to the fiber orientation and has to

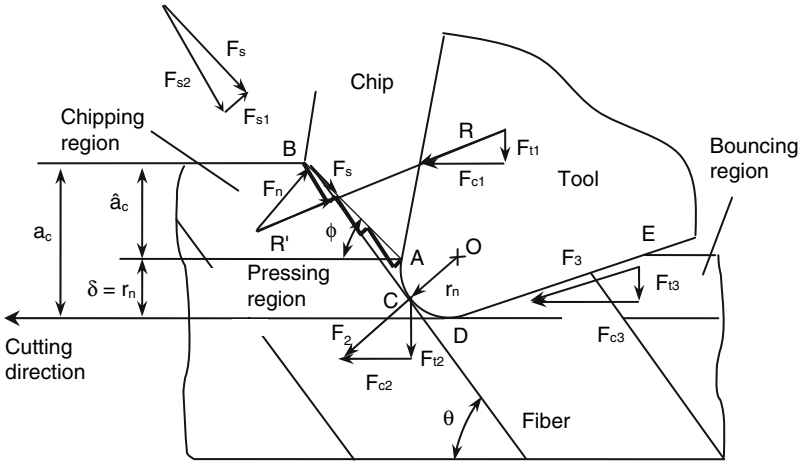

Fig. 3.29 Mechanics model of cutting with a nose radiused tool showing three regions of deformation, namely, chipping, pressing, and bouncing regions, and the force components in each region

be determined by the experiment. Because FRPs machine in a brittle manner with no significant plastic deformation, it is safe to assume that the final chip thickness equals the undeformed chip thickness, making the cutting ratio $r = 1$. Thus, the shear plane angle can be determined from (3.4) as

$$\phi = \tan^{-1}\left(\frac{\cos\alpha_o}{1-\sin\alpha_o}\right). \tag{3.36}$$

The removed chip is held in equilibrium by the resultant forces resultant forces R and R', which are further resolved into components F_s and F_n on the shear plane, and F_{c1} and F_{t1} in the principal directions, respectively, as shown in Fig. 3.29. The shear force, F_s on the shear plane is further composed of two components, F_{s1} and F_{s2}, which are responsible for shearing the fibers and for matrix–fiber delamination, respectively. These force components are functions of the work material shear strength normal to the fiber direction, τ_1, and in the fiber direction, τ_2, respectively. It can be shown from force equilibrium of the chip under the resultant force components that the cutting forces in the chipping zone are given by [20]

$$\begin{aligned} F_{c1} &= \tau_1 a_w \hat{a}_c \frac{\sin\phi\cdot\tan(\phi+\beta-\alpha_o)+\cos\phi}{\frac{\tau_1}{\tau_2}\cdot\cos(\theta-\phi)\cdot\sin\theta-\sin(\theta-\phi)\cdot\cos\theta}, \\ F_{t1} &= \tau_1 a_w \hat{a}_c \frac{\cos\phi\cdot\tan(\phi+\beta-\alpha_o)-\sin\phi}{\frac{\tau_1}{\tau_2}\cdot\cos(\theta-\phi)\cdot\sin\theta-\sin(\theta-\phi)\cdot\cos\theta}. \end{aligned} \tag{3.37}$$

In these equations, $\hat{a}_c$ is the actual depth of cut, and angles α_o, β, ϕ, and θ have their usual meaning.

The forces in the pressing region are caused by indentation of the work material with the tool nose of radius r_n. By using indentation mechanics of a circular cylinder in contact with a half-space, the tool forces in pressing region can be approximated as:

$$\begin{aligned} F_{c2} &= P_{real}(\sin\theta+\mu\cos\theta), \\ F_{t2} &= P_{real}(\cos\theta-\mu\sin\theta), \end{aligned} \tag{3.38}$$

where μ is the friction coefficient between the tool and the workpiece and P_{real} is the elastic indentation force scaled down by factor K to account for microcraking and delamination

$$P_{real} = \frac{K\pi E^* a_w r_n}{8}. \tag{3.39}$$

The scaling factor K is determined by experiment and E^* is the effective elastic modulus of the work material, which is given by:

$$E^* = \frac{E_2}{1-\nu}, \tag{3.40}$$

where E_2 is the elastic modulus of the work material in the direction of OC and ν is the minor Poisson's ratio.

The cutting forces in the bouncing region are caused by the contact between the workpiece and the clearance face of the tool along the contact surface DE. Using the contact mechanics between a wedge and a half-space, the cutting forces in the bouncing region can be calculated by:

$$\begin{aligned} F_{c3} &= \tfrac{1}{2} r_n E_3 a_w \cos^2\gamma_o, \\ F_{t3} &= \tfrac{1}{2} r_n E_3 a_w (1 - \mu \cos\gamma_o \cdot \sin\gamma_o), \end{aligned} \tag{3.41}$$

where E_3 is the effective elastic modulus of the material in the bouncing region and γ_o is the clearance angle of the tool. It is noted that E_3 is less than the elastic modulus of the original material because the material in the bouncing region has been damaged by fracture and delamination.

Finally, the total cutting forces, F_c and F_t are the sum of the individual cutting forces from all three regions:

$$\begin{aligned} F_c &= F_{c1} + F_{c2} + F_{c3}, \\ F_t &= F_{t1} + F_{t2} + F_{t3}. \end{aligned} \tag{3.42}$$

In this mechanics model, the parameters to be determined by experiment for a given workpiece material are τ_1, τ_2, β, ν, μ, E_2, E^*, and K. Figure 3.30 shows a comparison between the model predictions and experimental results. It can be seen that the model is able to capture the general trend of the data with reasonable accuracy in a limited fiber orientation $0^\circ \le \theta < 60^\circ$. The accuracy of model predictions also appears to be better for the cutting force than for the thrust force. The maximum error in predicting the thrust force is 37% and that in predicting the cutting force

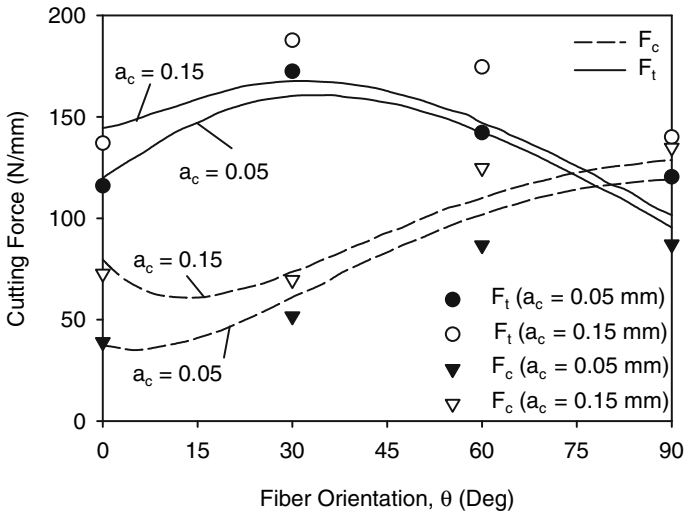

Fig. 3.30 Comparison between model predictions and experimental measurements when machining CFRP. Material parameters used are $\tau_1 = 90\,\text{MPa}$, $\tau_2 = 20\,\text{MPa}$, $\beta = 30^\circ$, $\nu_{23} = 0.026$, $\mu = 0.15$, $E_2 = 10\,\text{GPa}$, $E^* = 5.5\,\text{GPa}$, and $K = 0.5\,\tan^{-1}(30/\theta)$ [20]

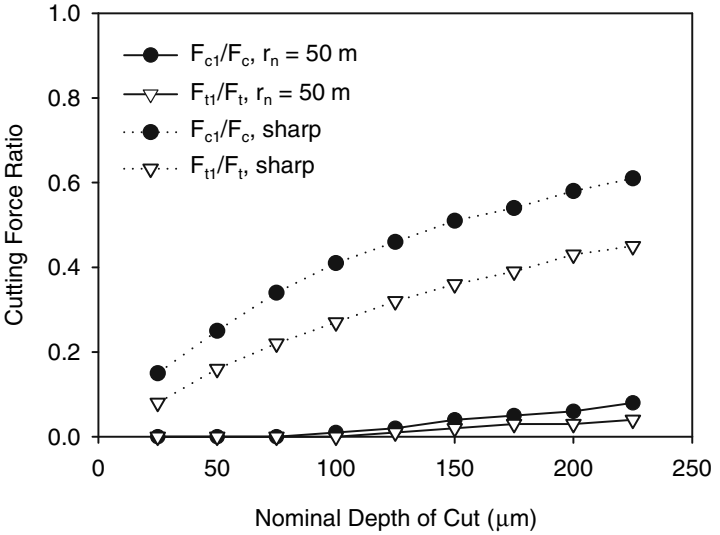

Fig. 3.31 Contribution of the chipping region to the overall cutting forces when machining with sharp ($r_n = 5\,\mu m$) and dull ($r_n = 50\,\mu m$) tools for various nominal depths of cut. Material parameters are the same as in Fig. 3.30. Fiber orientation = 30°

is 27%. The major contribution of this model, however, is the insight it provides on the influence of tool geometry including rake angle, clearance angle, and nose radius on the cutting process. Figure 3.31 shows comparisons of the cutting forces when cutting with a sharp tool, $r_n = 5.0\,\mu m$, and a nose radiused tool, $r_n = 50.0\,\mu m$, while holding all other parameters constant. It can be seen that the contribution of the chipping process to the overall cutting forces when cutting with a nose radiused tool is insignificant when compared to the contribution of the pressing and bouncing processes combined. The maximum contribution to the cutting force by the chipping action is 8%, while its contribution to the thrust force is 4%. When cutting with a sharp tool these percentages increase to 60% and 45%, respectively.

3.5.3 Mechanistic Modeling

Because of the obvious limitations of the shear plane theory approach and the wide range of possible mechanisms by which the chip formation may take place in machining FRPs, a mechanics approach to the problem of chip formation over the entire range of fiber orientations may not be possible. A simpler approach to treat this problem is by force prediction using the specific cutting energy, or mechanistic modeling. Mechanistic models attempt to predict the cutting forces directly from specific cutting energy functions and chip geometry. Specific cutting energy (also known as specific cutting pressure) is a material property that describes the amount of energy consumed in removing a unit volume of the workpiece material in the process of machining. Specific cutting energy for metals depends on the chip

thickness, the cutting speed, and the state of tool wear. Specific cutting energy for FRPs is also critically dependent fiber orientation. The cutting forces are determined as the product of the uncut chip area and the specific cutting energy. Various mechanistic models have been developed for predicting cutting forces in a number of metal machining processes and the success of these models has been documented in the literature. There is, however, very limited work on mechanistic modeling in machining FRPs [21, 22].

It has been previously shown in Sect. 1.1.6 that the specific cutting energy for a given tool–workpiece pair is defined as the machining power per unit volume per unit time and is determined experimentally from the cutting force and material removal rate. In a turning operation, for example, the specific cutting energy for a given pair of tool–workpiece is given by:

$$K_c = p_s = \frac{P_m}{Z_w} = \frac{F_c \cdot V}{f \cdot a_p \cdot V} = \frac{F_c}{f \cdot a_p}, \tag{3.43}$$

where f is the feed rate and a_p is the depth of cut. The product $f \cdot a_p$ defines the undeformed chip cross-sectional area, A_c. Therefore, the specific cutting energy depends on the strength of workpiece material, which influences the cutting forces, the chip geometry, and the tool geometry. Because the units of specific cutting energy are those of pressure, this quantity is also called specific cutting pressure. It is also customary in the machining literature to define specific cutting energy coefficients in the two principal directions, K_c and K_t, and to include edge coefficients, K_{ce} and K_{te} to account for the cutting forces that do not contribute to the shearing action. These extra edge coefficients change as the cutting tool wears or experiences chipping. The specific cutting energy coefficients are directly calibrated from machining experiments for a tool–workpiece pair. Conversely, if the specific cutting energy coefficients are known, the cutting force and thrust force for a given cutting geometry can be calculated [23].

$$\begin{aligned} F_c &= K_c(a_c, \theta) a_c a_w + K_{ce} a_w, \\ F_t &= K_t(a_c, \theta) a_c a_w + K_{te} a_w. \end{aligned} \tag{3.44}$$

3.5.3.1 Specific Cutting Energy of FRPs

The specific cutting energy coefficients for CFRP and GFRP were calculated from the cutting data in Fig. 3.15 using (3.45) and the results are shown in Fig. 3.32. It is noted that the specific cutting energy for FRPs is much lower than that for metals ($1{,}000\,\mathrm{N/mm^2}$ for low carbon steel). The specific cutting energy coefficient in the cutting direction is critically dependent on fiber orientation. It increases gradually with an increase in fiber orientation from 0 to 75° then a significant rise occurs at 90°. The specific cutting energy decreases sharply thereafter and continues to decrease with an increase in fiber orientation. The behavior of the specific cutting energy in the normal direction shows less dependence on fiber orientation than the one in the cutting direction.

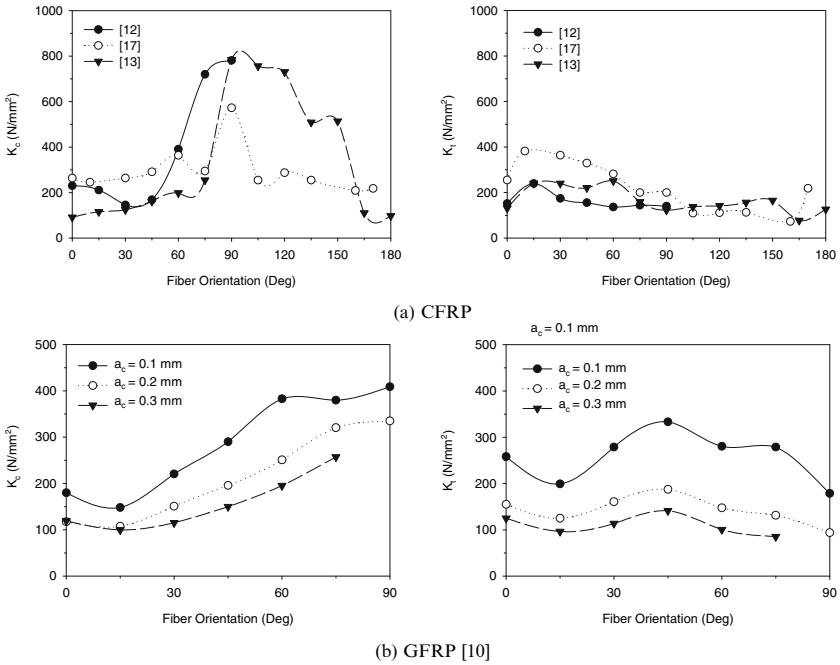

Fig. 3.32 Specific cutting energy when cutting (**a**) GrFRP and CFRP, (**b**) GFRP. Cutting data is shown in Table 3.1

$$K_c(a_c,\theta) = \frac{F_c}{a_c a_w},$$
$$K_t(a_t,\theta) = \frac{F_t}{a_c a_w}. \tag{3.45}$$

Figure 3.32b demonstrates similar behavior of the specific cutting energies for GFRP. The figure also exhibits the strong influence of depth of cut on the specific cutting energy. Similar to the behavior of homogeneous metals, the specific cutting energy increases exponentially with a decrease in the depth of cut. Equation (3.46) was found to provide a good fit for the data in Fig. 3.32b. Two distinct and decoupled terms are used in this equation to describe the behavior of the specific cutting energy. The first term is an exponential term that accounts for the dependence of specific cutting energy on depth of cut. The second term, a polynomial, captures the influence of fiber orientation. This equation and the data given in Fig. 3.32a can be a useful guide, in practice, to the cutting forces required to machine FRPs.

$$K_c = a_c^{-0.4533}(61.3011 - 1.1926\cdot\theta + 0.0646\cdot\theta^2 - 0.0005\cdot\theta^3),$$
$$K_t = a_c^{-0.8375}(35.0636 + 0.095\cdot\theta^2 - 0.0001\cdot\theta^3). \tag{3.46}$$

Example 3.2. Consider the graphite/epoxy laminate with layup $[45°/-45°/(0°/90°/45°/-45°)_2]_s$ that was used in [13]. This laminate has $4(0°)$, $6(45°)$, $4(90°)$, and $6(-45°)$ plies. It was noted in [19, 22] that the resultant cutting force obtained in

trimming multidirectional laminates is nearly equivalent to the summation of the forces from independent unidirectional plies, based on a rule of mixture approach. So, in principle, we can utilize force data from unidirectional machining to predict cutting forces in trimming multidirectional laminates. The total cutting forces according to an appropriate law of mixtures can be calculated using the expressions:

$$\begin{aligned} F_{\mathrm{c}} &= n_{\theta_1} F_{\mathrm{c},\theta_1} + n_{\theta_2} F_{\mathrm{c},\theta_2} + \cdots + n_{\theta_n} F_{\mathrm{c},\theta_n}, \\ F_{\mathrm{t}} &= n_{\theta_1} F_{\mathrm{t},\theta_1} + n_{\theta_2} F_{\mathrm{t},\theta_2} + \cdots + n_{\theta_n} F_{\mathrm{t},\theta_n}, \end{aligned} \tag{3.47}$$

where n_{θ_n} is the number of plies with orientation θ_n and F_{c,θ_n} and F_{t,θ_n} are the cutting and thrust forces from edge trimming a ply with fiber orientation θ_n. Substituting (3.44) into (3.47) and assuming a sharp cutting edge ($K_{\mathrm{ce}} = K_{\mathrm{te}} = 0$) we obtain:

$$\begin{aligned} F_{\mathrm{c}} &= n_{\theta_1} K_{\mathrm{c},\theta_1} A_{\mathrm{c},\theta_1} + n_{\theta_2} K_{\mathrm{c},\theta_2} A_{\mathrm{c},\theta_2} + \cdots + n_{\theta_n} K_{\mathrm{c},\theta_n} A_{\mathrm{c},\theta_n}, \\ F_{\mathrm{t}} &= n_{\theta_1} K_{\mathrm{t},\theta_1} A_{\mathrm{c},\theta_1} + n_{\theta_2} K_{\mathrm{t},\theta_2} A_{\mathrm{c},\theta_2} + \cdots + n_{\theta_n} K_{\mathrm{t},\theta_n} A_{\mathrm{c},\theta_n}, \end{aligned} \tag{3.48}$$

where K_{c,θ_n} is the cutting pressure for fiber orientation θ_n and A_{c,θ_n} is the undeformed chip area for the ply with fiber orientation θ_n, which is given as:

$$A_{\mathrm{c},\theta_n} = d_{\theta_n} a_{\mathrm{c}}, \tag{3.49}$$

where d_{θ_n} is the ply thickness and a_{c} is depth of cut. Applying (3.48) and (3.49) to the multidirectional laminate $[45^\circ/-45^\circ/(0^\circ/90^\circ/45^\circ/-45^\circ)_2]_{\mathrm{s}}$, we obtain:

$$\begin{aligned} F_{\mathrm{c}} &= 4K_{\mathrm{c},0}A_{\mathrm{c},0} + 6K_{\mathrm{c},45}A_{\mathrm{c},45} + 4K_{\mathrm{c},90}A_{\mathrm{c},90} + 6K_{\mathrm{c},135}A_{\mathrm{c},135}, \\ F_{\mathrm{t}} &= 4K_{\mathrm{t},0}A_{\mathrm{c},0} + 6K_{\mathrm{t},45}A_{\mathrm{c},45} + 4K_{\mathrm{t},90}A_{\mathrm{c},90} + 6K_{\mathrm{t},135}A_{\mathrm{c},135}. \end{aligned} \tag{3.50}$$

Note that the (-45°) ply was replaced by (135°) according to the convention used for fiber orientation in this book. Now the data from Fig. 3.32a is used to evaluate the cutting forces given by (3.50). Here, the ply thickness $d = 0.2$ mm and depth of cut $a_{\mathrm{c}} = 0.25$ mm. The resulting data is shown in Table 3.4, and the predicted results appear to be reasonably accurate.

Table 3.4 Ply force contribution and total cutting and thrust forces in machining multidirectional laminate

n_θ	θ	d	K_{c}	K_{t}	F_{c} (N)	F_{t} (N)
4	0	0.80	93.16	1.47	18.6	27.3
6	45	1.20	161.48	1.35	48.4	65.2
4	90	0.80	776.44	0.16	155.3	24.8
6	135	1.20	509.28	0.32	152.8	48.5
	Totals	4.00			375.1	165.9
				Calculated	$R = 410.2$	$\lambda = 23.9$
				Experiment	$R = 490$	$\lambda = 25$
				Error (%)	16.3	4.4

R Resultant force, λ Resultant force orientation

3.6 Summary

This chapter outlines the basic principles and analysis of orthogonal machining and discusses its application to the machining pure and FRPs. The relationship between material structure and properties, process parameters, and the mechanisms of chip formation are delineated. Results of some attempts to model the chip formation process are discussed and a predictive model for cutting forces is explained. The main marked concept in the treatments in this chapter is the fundamental influence of fiber orientation on the chip formation phenomena.

The machining of polymers and quasi-isotropic polymer composites (such as paper-filled, short-fiber-filled, and particulate-filled thermoplastics) is to a great extent similar to the machining of homogeneous metals. For ductile thermoplastics, a continuous shear-type chip is largely formed by plastic deformation in a well-defined shear plane. An exception to this is the formation of continuous elastic-type chip that occurs when machining polymers that show high rubber-like elasticity (such as polyethylene) at low cutting speeds. The chip in this case is formed entirely by large elastic deformation and no evidence of shearing is visible. For the continuous shear-type chip formation, the mechanics of orthogonal machining is applicable for determining shear strain, shear stresses, friction conditions, and cutting forces. On the other hand, machining of the stiffer and stronger thermosets is marked by fracture and discontinuous chip formation. The resulting surface quality is much better when machining takes place with a continuous chip. In general, the machining behavior of thermoplastics is dependent on cutting speed and rake angle. A transition from ductile to brittle behavior takes place as the cutting speed is increased. This is attributed to the rate sensitivity of the polymers. Due to the viscous behavior of the material, the ultimate strength of the material increases and elongation to fracture decreases as the rate of load application is increased. In addition, increasing the rake angle and decreasing the depth of cut results in reducing plastic deformation and promotes continuous shear-type chip formation. Because of the low thermal conductivity and high heat capacitance of polymers, they are more capable of retaining the heat from machining than metals. This in turn results in increasing the material temperature and ductility.

The machining of unidirectional FRPs is critically controlled by the fiber orientation, and to a lesser extent by the rake angle. The chip formation mode for a particular fiber orientation determines the resulting surface quality and dynamic characteristic of the cutting forces. The formation of continuous chip is generally not common in machining unidirectional FRPs. Depending on tool geometry and fiber orientation, one of the following chip types is formed.

(a) Delamination Type I chip is produced when machining 0° laminates with positive rake angle tool. In this case, a layer of the composite is peeled of due to Mode I loading and the peeled layer slides up the rake face. This caused the peeled layer to act as a cantilever beam in bending and the chip eventually breaks off when the bending stress exceeds the bending strength of the fibers. The cutting force oscillation in this regime is indicative of the cycles of

peeling and bending and they generally tend to be low. The surface is smooth and characterized by broken fibers laying in the cutting direction and considerable smearing of the matrix material.

(b) Type II buckling chip type is produced when machining 0° laminates with zero or negative rake angle tool. In this case, the material is pushed ahead of the rake face in Mode II loading. This causes the fibers to buckle and eventually fail due to bending stress. The cutting forces and machined surface characteristics are similar to those associated with Type I.

(c) Type III cutting chip is produced when machining positive fiber orientation laminates in the range $15^\circ < \theta < 75^\circ$ with positive rake angle tool. In this type of chip formation mode, the fibers fail normal to their axes by compression shear ahead of the cutting point. This is followed by interlaminar shear, which causes the chip to flow up the rake face. A continuous chip may actually be produced under these conditions. This behavior of material flow is somewhat similar to shear-type chip formation in metal cutting. In a way the interlaminar shear takes place along the fiber–matrix interface in what resembles shearing along a shear plane in metal cutting (with a drastic difference in the magnitude of plastic deformation involved). The cutting forces are characterized by the lowest fluctuations and the surface roughness is composed of fibers sticking out of the surface, fiber pullout, and cracking in the fibers below the surface.

(d) As the fiber orientation is increased above 75° the chip transitions to discontinuous type (Type IV) due to the severity of interlaminar shear. For fiber orientations larger than 90° and for negative rake angles the chip is formed by gross fracture in the fibers and matrix and bulky discontinuous chips are formed (Type V). The chip flow under these conditions may not be restricted to the two dimensions. For these two types of chip, the cutting forces fluctuation and magnitude are the highest and the surface roughness is the poorest.

The cutting of multidirectional composites is similar to that of cutting unidirectional composites. Each ply in the multidirectional structure behaves independent of the surrounding plies under the conditions of orthogonal cutting. The cutting forces in machining multidirectional composites may be obtained by adding the cutting forces corresponding to each unidirectional ply in the structure. Furthermore, the machined surface characteristics of the individual plies in the multidirectional structure resembles to a great extent those obtained from unidirectional machining of the individual plies. The surrounding plies, however, do provide constraining effect against the out of plane deformation that is common in machining large orientation angles.

Mechanics modeling of the chip formation process largely followed the theories previously developed for metal machining. It was found that the shear plane theory is capable of predicting the cutting forces and shear stresses only in a limited range of fiber orientations ($15^\circ < \theta < 75^\circ$), which is the range in which the cutting Type III chip is produced. The reason for this is that the chip formation in this range is somewhat similar to that in metal machining. The shearing of the material is governed by its in-plane shear strength and the chip is formed by shearing along the fiber orientation. For fiber orientations outside this range, it is found that mechanistic modeling is more capable of predicting the cutting forces than mechanic approach.

Review Questions and Problems

1. Discuss the geometry of orthogonal machining.
2. Why is orthogonal machining important for fundamental studies of chip formation?
3. Which of these two tools would provide orthogonal machining conditions when fixed on a lathe with shank perpendicular to axis of rotation and when cutting with major cutting edge?

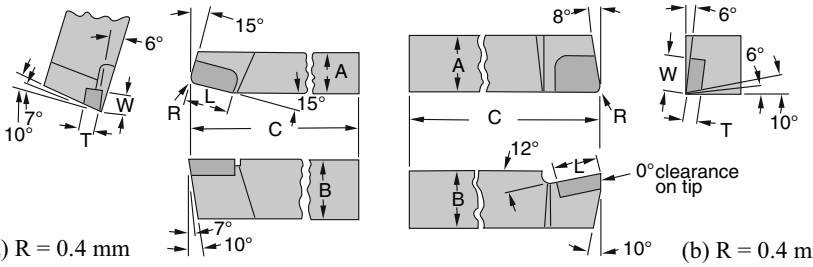

(a) R = 0.4 mm (b) R = 0.4 mm

4. Discuss the major differences in chip formation mechanisms when metals, polymers, and FRPs are machined.
5. Discuss the assumptions made in the shear plane theory for analysis orthogonal machining. How realistic are these assumptions when applied to machining polymers, FRPs?
6. What is the significance of the shear angle in the shear plane theory of orthogonal machining?
7. Discuss three modes of chip formation when machining unidirectional FRPs. Discuss the influence of fiber orientation and rake angle on each mode.
8. Describe the machined surface characteristics resulting from Type I and Type III chip formation modes and highlight the differences.
9. Discuss the influence of fiber orientation and rake angle on the cutting forces when machining FRPs.
10. Discuss the influence of rake angle and clearance angle on the machined surface characteristics in machining FRPs.
11. What are the significant differences between cutting forces when machining metals and FRPs?
12. You have seen that in machining multidirectional composites we could use the law of mixtures to determine the cutting forces using data obtained from machining unidirectional composites. What is the justification for this approach?
13. Suppose that in a machining operation of unidirectional FRPs you are getting high principal (cutting) forces. Which action would you take to reduce the principal forces?
    (a) Reduce cutting speed
    (b) Increase rake angle
    (c) Reduce depth of cut
    (d) Increase clearance angle
    (e) All of the above

14. Suppose that in a machining operation of unidirectional FRPs you are getting high normal (thrust) forces. Which action would you take to reduce the thrust forces?

    (a) Reduce cutting speed
    (b) Increase rake angle
    (c) Reduce depth of cut
    (d) Increase clearance angle
    (e) All of the above

15. Suppose that in a machining operation of multidirectional FRPs you are getting high principal (cutting) forces. Which action would you take to reduce the principal forces?

    (a) Reduce cutting speed
    (b) Increase rake angle
    (c) Reduce depth of cut
    (d) Increase clearance angle
    (e) All of the above

16. Suppose that in a machining operation of multidirectional FRPs you are getting high normal (thrust) forces. Which action would you take to reduce the thrust forces?

    (a) Reduce cutting speed
    (b) Increase rake angle
    (c) Reduce depth of cut
    (d) Increase clearance angle
    (e) All of the above

17. The following data was obtained from orthogonal turning of PEEK and short-fiber-reinforced PEEK (C/PEEK, $V_f = 0.3$) [24]. Refer to Fig. 2.2 for definition of cutting variables. The cutting conditions are $v = 100\,\text{m/min}$, depth of cut $a_p = 2.0\,\text{mm}$, $\kappa = 90^\circ$, $\alpha_o = 0^\circ$, $\gamma_o = 7^\circ$.

f (mm/rev)	PEEK			C/PEEK		
	a_o/a_c	F_c (N)	F_t (N)	a_o/a_c	F_c (N)	F_t (N)
0.05	1.43	39.29	18.14	1.38	41.76	33.52
0.10	1.35	66.14	21.42	1.32	68.06	40.10
0.15	1.33	92.51	24.88	1.31	90.69	44.41
0.20	1.30	118.82	28.41	1.17	111.68	47.93

Calculate the following for each cutting condition, for both PEEK and C/PEEK:

(a) Shear plane angle, ϕ
(b) Theoretical shear strain in the chip
(c) Theoretical shear stress and normal stress in the shear plane
(d) Friction angle

(e) Specific cutting energy, p_s, specific shear energy, u_s, specific frictional energy, u_f, and the difference $[p_s - (u_s + u_f)]$. Discuss the results.
(f) Plot shear plane angle vs. $(\beta - \alpha_o)$ for both materials
(g) Plot shear stress and normal stress in the shear plane vs. feed rate for both materials
(h) Plot shear strain vs. feed rate for both materials
(i) Using the results from (f), (h), and (i), discuss the applicability of the shear plane theory to the machining of PEEK and C-PEEK, highlighting the differences, if any, between the two materials.

18. The following data was obtained in orthogonal cutting of phenolic paper-base laminate (this consists of a phenolic resin and paper reinforcement) at the following conditions [3]: $v = 400\,\text{m/min}$, $a_w = 6.2\,\text{mm}$, $a_c = 0.011\,\text{mm}$, $\alpha_o = 10^\circ$. $F_c = 39.24\,\text{N}$, $F_t = 12.75\,\text{N}$, and $r = 0.982$. Determine the following:

(j) Chip thickness, a_o
(k) Shear plane angle, ϕ
(l) Theoretical shear strain, γ
(m) Theoretical shear stress in the chip, τ_s
(n) Coefficient of friction, μ
(o) Specific cutting energy, p_s
(p) Specific shear energy, u_s
(q) Specific frictional energy, u_f

19. Takeyama and Iijima [18], Bhatnagar et al. [17], and Wang et al. [13] have postulated that shear plane theory of orthogonal machining in metals could be applied in the analysis of chip formation of unidirectional composites in a specific range of fiber orientations. Study the approaches used by these investigators and answer the following questions:

(a) In which range of fiber orientations was their hypothesis verified?
(b) Why was this hypothesis verified in this specific range?
(c) What are the difference in the hypotheses of Takeyama and Iijima and that of Bhatanagar et al. and Wang et al.?
(d) Where these hypotheses supported by experimental evidence? How good was the correlation between experiment and theory?
(e) Which hypothesis do you think is more realistic? Why?

20. Given below are the results from orthogonal cutting of graphite/epoxy unidirectional laminate [25]. The cutting speed = 4.0 m/min, the depth of cut = 0.381 mm and the width of cut = 3 mm.

θ (Deg)	$\alpha_o = 0^\circ$, $\gamma_o = 7$		$\alpha_o = 5^\circ$, $\gamma_o = 7$		$\alpha_o = 10^\circ$, $\gamma_o = 7$	
	F_c (N)	F_t (N)	F_c (N)	F_t (N)	F_c (N)	F_t (N)
15	169.02	316.70	194.16	267.88	213.37	242.69
30	206.72	387.91	186.49	331.82	172.74	272.95
45	207.59	338.28	189.89	301.04	169.70	278.07
60	265.59	412.31	248.22	335.00	217.01	321.32

(a) Plot this data in an appropriate way and discuss the influence of fiber orientation and rake angle on cutting and thrust forces.
(b) Calculate the friction angle for each cutting condition. Plot the friction angle vs. fiber orientation for the different rake angle and discuss the influence of fiber orientation and rake angle on the friction angle.
(c) Assuming that the chip thickness is equal to the depth of cut $(r = 1)$, calculate the shear plane angle for each cutting condition. Plot the shear plane angle vs. $(\beta - \alpha_o)$ for the different fiber orientations and discuss the results.
(d) Calculate the normal stress and shear stress on the shear plane. Plot the results against fiber orientation and discuss.
(e) From the results in (a), (b), and (c), discuss the applicability of the shear plane theory to the machining of this material.

21. Calculate the cutting and thrust force in the orthogonal machining of unidirectional 45° CFRP laminate that has the following properties: $\tau_1 = 90\,\text{MPa}$, $\tau_2 = 20\,\text{MPa}$, $\beta = 30°$, $\nu_{23} = 0.026$, $\mu = 0.15$, $E_2 = 10\,\text{GPa}$, $E^* = 5.5\,\text{GPa}$ and $K = 0.5\ \tan^{-1}(30/\theta)$. The cutting tool has the geometry: $\alpha_o = 5°$, $\gamma_o = 10°$, $r_n = 100\,\mu\text{m}$. Assume that the bouncing region thickness is equal to the nose radius and the chip thickness is equal to the depth of cut, which is 0.2 mm.
22. Use mechanistic modeling to predict the cutting forces for one complete revolution in edge trimming of unidirectional GFRP 90° laminate 5 mm thick with the following cutting conditions (refer to Fig. 2.8 for explanation of the milling terminology): Cutter diameter: 4.0 mm with one major cutting edge; Milling configuration: down milling; Spindle speed: 5,000 rpm; Feed rate: 1.27 m/min; Radial depth of cut: 1 mm. Note that in milling operation the fiber orientation relative to the cutting velocity is dependent on cutting edge position. Therefore, this problem is better treated using spreadsheet calculations of the appropriate equations while incrementing the cutting edge engagement angle from entry to exit. Assume that the specific cutting energies given by (3.46) apply to this material.

References

1. Shaw, M.C., Metal Cutting Principles, 2nd Edition, Oxford University Press, New York, NY, 2005.
2. Boothroyd, G., Knight, W., Fundamentals of Machining and Machine Tools, 2nd Edition, Marcel Dekker, New York, NY, 1989.
3. Kobayashi, A., Machining of Plastics, Robert E. Kreiger, Malabar, FL, 1981.
4. Carr, J.W., Feger, C., Ultraprecision machining of polymers. Precision Engineering 15, 221–237, 1993.
5. Alauddin, M., Choudhury, I.A., El Baradie, M.A., Hashmi, M.S.J., Plastics and their machining: A review. Journal of Materials Processing Technology 44, 40–47, 1995.
6. Xiao, K.Q., Zhang, L.C., The role of viscous deformation in the machining of polymers. International Journal of Mechancial Sciences 44, 2317–2336, 2002.
7. Gubbels, G.P.H., Diamond Turning of Glassy Polymers, PhD Thesis, Technische Universiteit Eindhoven, Eindhoven, 2006.

8. Koplev, A., Lystrup, A., Vrom, T., The cutting process, chips, and cutting forces in machining CFRP. Composites 14, 371–376, 1983.
9. Arola, D., Ramulu, M., Wang, D.H., Chip formation in orthogonal trimming of graphite/epoxy composite. Composites: Part A 27A, 121–133, 1996.
10. Nayak, D., Bhatnagar, N., Mahajan, P., Machining studies of uni-directional glass fiber reinforced plastic (UD-GFRP) composites part 1: Effect of geometrical and process parameters. Machining Science and Technology 9, 481–501, 2005.
11. Kaneeda, T., Masayuki, T., CFRP cutting mechanism (1st report): Surface generation mechanism at very low speeds. Journal of the Japan Society of Precision Engineering 55, 1456–1461, 1989.
12. Kaneeda, T., CFRP cutting mechanism. Transaction of North American Manufacturing Research Institute of SME 19, 216–221, 1991.
13. Wang, D.H., Ramulu, M., Arola, D., Orthogonal cutting mechanisms of graphite/epoxy composite. Part I: Unidirectional laminate. International Journal of Machine Tools and Manufacture 35, 1623–1638, 1995.
14. Wang, X.M., Zhang, L.C., An experimental investigation into the orthogonal cutting of unidirectional fiber reinforced plastics. International Journal of Machine Tools and Manufacture 43, 1015–1022, 2003.
15. Hocheng, H., Puw, H.Y., Yao, K.C., Experimental aspects of drilling of some fiber-reinforced plastics. Proceedings of the Machining of Composites Materials Symposium, ASM Materials Week, Chicago, Illinois, 1–5 November, 1992, 127–138.
16. Krishnamurthy, R., Santhanakrishnan, G., Malhotra, S.K., Machining of polymeric composites. Proceedings of the Machining of Composites Materials Symposium, ASM Materials Week, Chicago, Illinois, 1–5 November, 1992, 139–148.
17. Bhatnagar, N., Ramakrishnan, N., Naik, N.K., Komanduri, R., On the machining of fiber reinforced plastic (FRP) composite laminates. International Journal of Machine Tools and Manufacture 35, 701–716, 1995.
18. Takeyama, H., Iijima, N., Machinability of glass-fiber reinforced plastics and application of ultrasonic machining. Annals of CIRP 37, 93–96, 1988.
19. Wang, D.H., Ramulu, M., Arola, D., Orthogonal cutting mechanisms of graphite/epoxy composite. Part II: Multi-directional laminate. International Journal of Machine Tools and Manufacture 35, 1639–1648, 1995.
20. Zhang, L.C., Zhang, H.J., Wang, X.M., A force prediction model for cutting unidirectional fiber-reinforced plastics. Machining Science and Technology 5, 293–305, 2001.
21. Puw, H.Y., Hocheng, H., Milling force prediction for fiber reinforced thermoplastics. Machining of Advanced Composites. Proceedings of the 1993 ASME Winter Annual Meeting, American Society of Mechanical Engineers, Materials Division (Publication) MD, vol. 45, 1993, 73–88.
22. Sheikh-Ahmad, J., Yadav, R., Force prediction in milling of carbon fiber reinforced polymers. Proceedings of IMECE2005, Oralndo, FL, Paper No. IMECE2005-81909.
23. Altintas, Y., Manufacturing Automation: Metal Cutting Mechanics, Machine Tool Vibration, and CNC Design. Cambridge University Press, New York, NY, 2000.
24. Davim, J.P., Mata, F., Physical cutting model of Polyetheretherketone composites. Materials and Design 27, 847–852, 2006.
25. Wang, D.H., Machining Characteristics of Graphite/Epoxy Composite, PhD Thesis, University of Washington, Seattle, WA, 1993.

Chapter 4
Tool Materials and Tool Wear

Machining of fiber-reinforced polymers (FRPs) is a challenging process from the point of cutting tool requirements. Unlike metal cutting where plastic deformation is the predominant cause of chip formation, the cutting of FRPs takes place by compression shearing and fracture of the fiber reinforcement and matrix. This puts stringent requirements on the cutting edge geometry and material. A sharp cutting edge and large positive rake angle are often required to facilitate clean shaving of the fibers, and a tool material with high hardness and toughness is required to resist the abrasiveness of the fibers and the intermittent loads generated by their fracture. Only a limited choice of tool materials that can meet these demands is available. This chapter is an overview of cutting tool materials and their wear characteristics in machining FRPs. The types of tool wear, tool wear measurement, and the controlling wear mechanisms are discussed. Recommendations for good practices in selecting tool materials for specific applications are also made.

4.1 Tool Materials for Machining FRPs

A wide range of cutting tool materials is available for machining applications. These materials are generally classified into three main groups according to their hardness, strength, and toughness, as shown in Fig. 4.1, which also demonstrates the opposing relationship between hardness and toughness. The three groups are high-speed steels (HSS), cemented carbides, and ceramics/superhard materials. Each group has its own characteristic mechanical and thermal properties, which makes its application more suitable for certain machining operations. Hardness describes the material's ability to resist abrasive wear and toughness describes its ability to resist fracture under heavy and/or intermittent loads. Unfortunately, materials that are very hard tend to have very poor toughness and vice versa. The trade-off involved in trying to have both toughness and wear resistance is obvious in Fig. 4.1. An ideal tool material, which is yet to be discovered, would have both high hardness and high toughness.

J.Y. Sheikh-Ahmad, *Machining of Polymer Composites*.
DOI: 10.1007/978-0-387-68619-6,

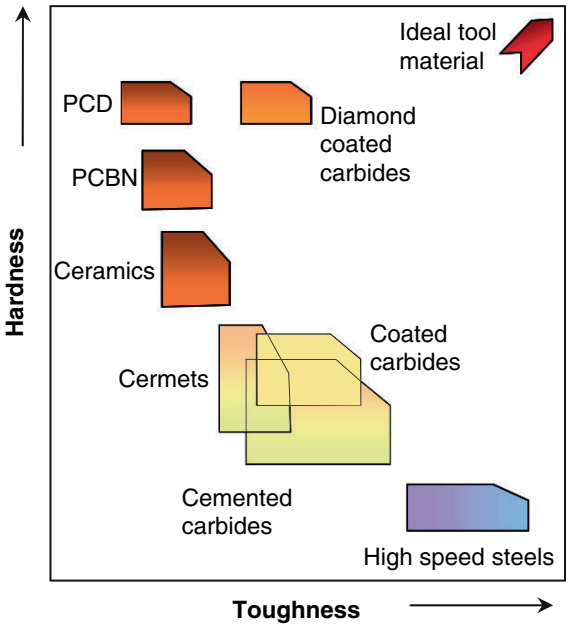

Fig. 4.1 Interrelations between toughness and hardness for the three main groups of cutting tool materials

Tool steels are the oldest tool materials of the three groups and include HSS as well as other high alloy steels. This group possesses the highest toughness, moderate strength, and low to moderate hardness (up to 68 HRC), which is imparted by heat treatment. Because of these features, tools from this group can be easily ground into complex shapes and to very sharp edges, such as in the case of helical end mills of various sizes and shapes. HSS tools can also be reground, heat treated, and reused after being worn out. The metallurgy and processing of these materials has been around for many years and thus their cost is low compared to the other tool materials. However, their biggest disadvantage is its inability to retain hardness at high temperatures (austenitic transformation temperatures), and thus they are not suitable for high-speed machining. Also, because of its low hardness and moderate strength, they cannot be practically used to machine abrasive materials such as FRPs and particulate-reinforced polymers, aluminum–silicon alloys and cast iron, or for roughing cuts.

The cemented carbide group of tool materials is mostly based on tungsten carbides (WC) as the hard phase, but also include other carbides such as TiC and TaC. The tool blanks are produced near net shape by cold pressing of a suitable mixture of powders of carbides and a binder metal, such as cobalt. The tool blanks are then sintered at temperatures in the range from about 1,350 to $1,650\,^{\circ}\mathrm{C}$, to melt the binder and create bonding between the binder metal and the carbide grains. The hardness of cemented carbides is imparted by the hard carbide phase, while the binder metal

provides the necessary toughness. For decades cemented carbides have been the work hoarse for the machining industry. Their processing technique allows them to be produced in different shapes and sizes. They can also be relatively easily ground using diamond or CBN wheels. They also provide high hardness and high strength, and retain their properties at relatively high temperatures. Their hardness and thermal stability can be further improved by applying thin film coatings of hard ceramics on the cutting surfaces. The technology of cemented carbides is well developed, which allows their production in mass and at low cost. All of this makes cemented carbides suitable for general purpose cutting tools that fit many applications. The wide range of available carbide types, grain sizes, and binder content make it easy to tailor specific carbide grades for specific applications. The shortcomings of cemented carbides, however, are their inadequate hardness for machining advanced and highly abrasive engineering materials, and their susceptibility to chemical wear at conditions of high cutting temperatures.

Superhard tool materials were developed mainly for applications where the demands on long tool life and high productivity are of main concern. Except of single crystal diamond, these tool materials are also made by sintering of the hard phase, provided in the form micrograin particles, with or without a binder phase. The binder phase, which could be ceramic or metallic, improves the toughness and manufacturability of the cutting tools. Sintering is performed at extremely high temperatures and high pressures to help consolidating and bonding the tool material. This makes their production cost very high.

Table 4.1 lists key properties for materials mainly from the second and the third group. The wide contrast in mechanical and thermal properties among the different materials within the same group and from one group to another is quiet obvious. Noted are the high toughness of tungsten carbide, the high hardness, high strength and excellent thermal conductivity of diamond, and the poor thermal conductivity

Table 4.1 Representative properties of some cutting tool materials

Material	TRS (MPa)	S_c (MPa)	K_{IC} (MPa $m^{-1/2}$)	Hardness		α ($\times 10^{-6}/°C$)	K (W/m°C)
				HV30	Knoop (MPa)		
Al_2O_3	550	3000	4.0	1600	16	8.2	10.5
Al_2O_3–TiC	800	4500	4.5	2200	17	8.0	16.7
Al_2O_3–ZrO_2	700	–	5.5	2230	–	8.5	10.5
SiAlON	800	3500	6.5	1870	17	3.2	20–25
WC-Co (6% Co)	1900	5380	12	1600	14	4.3–5.6	80
PCBN	700–1200	3500	4.5	–	27–31	3.2–4.2	110–200
PCD	860–1950	7700	3.0–9.0	–	39–54	1.5–3.8	543
CVD diamond film	1300	9000	5.5–8.5	–	85–100	3.84	500–2200
Single crystal diamond	1350	6900	3.4	–	59–88	0.8–4.8	600–2100

TRS Transverse rupture strength, S_c Compressive strength, K_{IC}, Fracture toughness, α Coefficient of thermal expansion, *K* Thermal conductivity

of ceramics. All of these properties have tremendous influence on the wear behavior of the cutting tool during machining. The following sections explain the differences between the different groups of tool materials, their suitability for machining fiber-reinforced composites, and the processes by which it wears when machining.

4.1.1 Cemented Tungsten Carbides

Cemented tungsten carbides are a range of composite materials that consist of hard carbide particles (mainly WC) bonded together by a metallic binder (mainly Co) as shown in Fig. 4.2a. The proportion of the binder phase ranges from 70 to 97 wt%. The carbide grain size ranges from 0.4 to 10 µm. This wide range of microstructure combinations provides different carbide grades with different properties for a wide range of applications as shown in Fig. 4.2b. Examples of chemical composition and properties of tungsten carbides are listed in Table 4.2. These grades are basically composed of WC-Co, with variations in grain size and binder content. Generally, the hardness increases and the transverse rupture strength (TRS) decreases with an increase in grain size. An apparent exception to this general rule occurs in the micrograin (0.5–1 µm) and ultra-fine grain size carbides (below 0.5 µm) where for the same hardness the submicron grades show a higher TRS than the conventional grades (see for example grades 5 and 7). This combination of high hardness and toughness makes submicron carbides most suitable for machining composites.

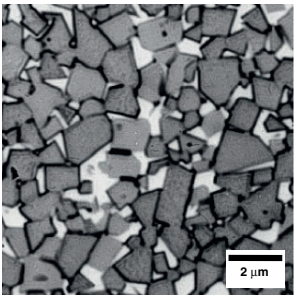

(a)

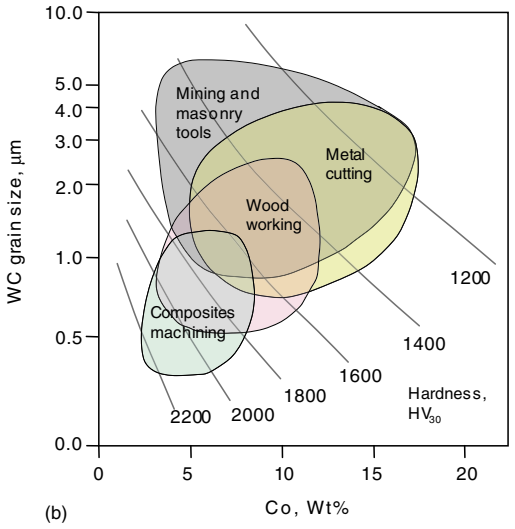

(b)

Fig. 4.2 (**a**) Typical microstructure of WC-Co material, WC grains are shown appear as the *dark phase* and the cobalt binder is shown with a *lighter color*. (**b**) Effect of WC grain size and Co content on hardness and use of cemented carbide cutting tools

Table 4.2 Properties of some cemented carbide grades

Carbide grade	ISO class	USA class	Composition (wt%)		WC grain size (μm)	HRA	TRS (MPa)	S_c (MPa)	K_{IC} (MPa $m^{-1/2}$)
			WC	Co					
1	K30	C1	90.5	9.5	1.7	90.4	2,600	5,200	14
2	K20	C2	94.0	6.0	1.7	92.1	2,200	6,200	12
3	K10	C3	96.0	4.0	1.3	92.9	2,300	–	–
4	K10	C3/C4	96.5	3.5	1.2	93.0	1,900	6,900	9
5	–	–	97.0	3.0[a]	1.2	94.0	2,100	–	–
6	–	–	97.0	3.0	0.7	93.9	3,300	7,800	7
7	–	–	95.0	5.0[a]	0.8	94.0	2,300	–	–
8	–	–	97.0	3.0	0.8	94.1	2,000	8,500	5.4
9	–	–	97.5	2.5	0.4	95.4	1,800	12,500	4.5

[a]Binder phase consists of Co–Ni alloy

The ISO classification of tungsten carbides puts them in three groups, P, M, and K, according to their machining use. Each group is further divided into subgroups such as K01, K10, K20, etc. The C-classification is used primarily in the United States and puts carbides into groups from C1 to C8. Group P (C5–C8) is for cutting materials with long chips, such as carbon steels and ferritic stainless steels. The cutting forces are generally high and crater wear is the dominant form of wear. Group M (C5–C8) is generally for cutting materials with long to medium chips such as ductile cast iron and austenitic stainless steels. The cutting forces are large to medium and chipping of the cutting edge is likely to occur. Group K (C1–C4) is for cutting nonferrous metals and nonmetallic materials such as polymers and their composites. Generally the cutting forces are low and abrasion is the most common form of wear. Because of the inhomogeneous nature of composite materials, the cutting forces show a great deal of fluctuation, which causes the cutting tool to fail by chipping. Furthermore, the cutting tool must have a sharp edge to produce good surface finish. In light of these requirements, submicron-cemented carbides are most suitable as shown in Fig. 4.2b.

4.1.2 Coated Carbides

Hard ceramic coatings of several micrometers thick are deposited on cemented carbides in order to improve their wear resistance, particularly thermally driven wear such as crater formation on the rake face. The coatings are formed at high temperatures (900–1,050 °C) by chemical vapor deposition (CVD). Single layer and multilayer coatings of TiC, TiN, TiCN, and Al_2O_3 are implemented. Physical vapor deposition (PVD) was later developed to take advantage of low temperature vapor deposition (400–450 °C), which includes finer microstructures, higher toughness, and less deterioration to the carbide substrate at high temperatures. In addition, the residual stresses in CVD coatings are tensile and in PVD coatings are compressive.

Table 4.3 Properties of some coating materials

Material	Density (g/cm^3)	Melting point (°C)	Hardness (HV)	Friction coefficient	Coefficient of thermal expansion	Thermal conductivity ($W/m°K$)
TiC	4.94	3,150	3,000	0.4	7.7	29
TiN	5.44	2,950	2,100	0.2	9.4	19
Al_2O_3	3.98	2,300	2,300	0.3	8.0	30
Cemented carbides	11–15	1,298	1,300–1,800	0.3–0.4	5–6	30–80

Hence, PVD coatings have higher TRS and higher chipping resistance than CVD coatings. However, the adhesion strength and wear resistance are superior in CVD coatings. Because of these contrasting properties, CVD coatings are used in general turning and milling, while PVD coatings are applied where cutting forces are high and chipping resistance is required. PVD coatings are also more suitable for coating sharp cutting tools, such as solid carbide end mills and drills for machining composites.

Properties of some coating materials are listed in Table 4.3. The properties of cemented carbides are also listed for reference. The ceramic coatings possess higher high temperature hardness and are more thermally stable than the tungsten carbide. Therefore, it acts as a thermal barrier in machining at high cutting speeds and high chip loads. Because the cutting temperatures in machining composites are relatively low, and because the cutting edges are sharper than those for metal cutting, coated carbides have not been able to deliver the same benefits seen in metal machining. Only marginal improvements in wear resistance and tool life have been realized when machining composites with coated carbides. Edge chipping and coating delamination are the most common forms of wear under these circumstances [1].

4.1.3 Ceramics

Ceramic tools are generally based on sintered alumina (Al_2O_3) at high temperatures and pressures. Table 4.1 lists mechanical and thermal properties of some alumina-based ceramics. Figure 4.3a shows a typical microstructure of Al_2O_3–TiC ceramics (alumina is the dark phase). Ceramics have the highest thermal stability among the tool materials and exhibits excellent performance in high-speed machining where the cutting temperatures are extremely high. On the other hand, their toughness is poor and they suffer from failure by chipping when used in heavy cuts or under interrupted loads. Ceramic tools are usually ground into negative rake angles (with cutting edge angle greater than 90°) in order to enhance its mechanical strength. Ceramics are also notorious of poor resistance to thermal shock because of their low thermal conductivity, another reason for their poor performance in interrupted cutting. It is noted that significant improvements in TRS and compressive strength are achieved by introducing other ceramics such as TiC and ZrO_2 to the alumina

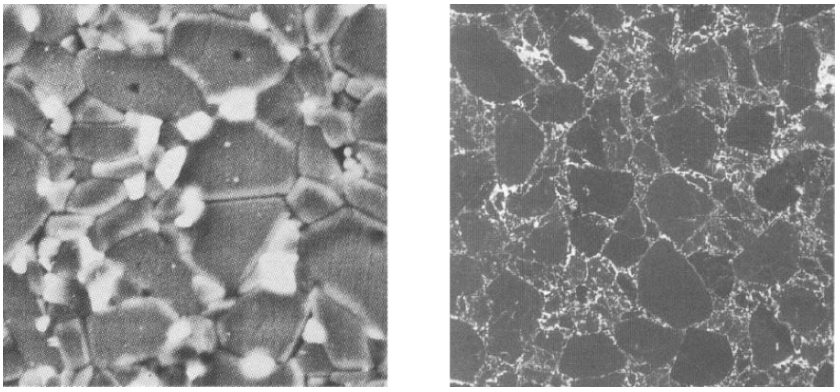

(a) (b)

Fig. 4.3 Typical microstructure of (**a**) Al_2O_3-TiC ceramic, with alumina appearing as the *dark phase* and (**b**) sintered CBN

base. This results in less chipping wear and better tool life. However, similar to coated carbides, the advantages of ceramic tooling in machining fiber-reinforced composites could not be realized because of their tendency to fail by chipping and the inability to produce them in sharp edges.

4.1.4 Polycrystalline Diamond

Diamond is the hardest material known to man, and single crystal diamond has been used as cutting tools for a long time. Diamond also provides good thermal conductivity, low coefficient of friction, and nonadherence to most materials. All these qualities are highly desirable for a cutting tool material. However, the applications of single crystal diamond are limited because of limitations on cutting tool size, susceptibility to fracture and its high cost. Therefore, single crystal diamond cutting tools have been limited to ultra precision machining such as in the case of machining optical surfaces.

Polycrystalline diamond (PCD) is made by compacting PCDs and small amounts of metallic binder, such as cobalt, under high temperatures and pressures. The sintered PCD blanks are later cut using laser or electrical discharge machining (EDM) to the required shape and then brazed to a tungsten carbide substrate. The thickness of the PCD wafer forming the cutting edge is less than 1 mm. The advantages of PCD over single crystal diamonds are its uniform mechanical properties because of the random orientation of the diamond crystals, higher shock resistance, and larger tool size. The biggest disadvantage of sintered PCD tools is their cost. PCD tools typically cost ten times or more than conventional carbides and ceramics tools. The technology for high temperature, high pressure sintering is expensive and cutting

and grinding the cutting edge is very difficult. Therefore, production cost is the main factor affecting PCD tools cost. However, when used under proper cutting conditions, PCD tools are economically viable because they provide superior tool life and higher productivity. Another disadvantage of diamond cutting tools is their propensity to react with ferrous metals at high temperatures.

The performance of PCD tools depends on the size of diamond crystals. These tools are produced with different size of diamond grit, ranging from 2 to 30 μm. The fracture toughness and hardness increases with an increase in grain size. Fine grades (2–5 μm) provide good abrasion resistance, excellent surface finish, very good polish, and edge sharpness. They are used for moderately abrasive materials, wood composites, aluminum, and plastics. Medium grade (10 μm) is considered the best "general purpose" grade, because it provides excellent abrasion resistance, while maintaining a moderate surface finish. It is used for very abrasive materials, hardwood, laminates, ceramics, medium-silicon aluminum, fiberglass, rubber, copper, and carbon. Coarse grades (25–30 μm) provide high impact strength and tool loads, low surface finish, and long tool life. Applications include extremely abrasive materials, interrupted cuts, and rough machining.

4.1.5 Polycrystalline Cubic Boron Nitride

Polycrystalline cubic boron nitride (PCBN) tools are sintered from a mixture of CBN crystals and metallic or ceramic binder like TiC and TiN using similar technology to that of diamond tools. Figure 4.3b shows a typical microstructure of PCBN. CBN does not occur in nature and it is produced by high temperature–high pressure synthesis in a process similar to that used to produce synthetic diamond. Its hardness is next only to diamond and it is more stable against ferrous metals than diamond. As a result, it is used in cutting super alloys, hardened steels, and hard cast iron. Because of their poor toughness, PCBN tools are formed into cutting edges with negative rake angle. The predominant form of wear is microchipping. Therefore, these tools are not suitable for cutting inhomogeneous materials or in interrupted cutting.

4.1.6 Diamond Coated Carbides

Low-pressure diamond synthesis by CVD permits processing of diamond as a tool coating. Diamond crystals similar to the ones shown in Fig. 4.4 are grown from a carbon rich gas, mostly CH_4, over a heated carbide substrate into a film that is several μm thick. The film is composed of pure PCD and thus in principle, would provide better hardness and toughness characteristics than sintered diamond. The advantages of diamond coatings over PCD are large scale production, lower production cost, and complex shaped tools such as drills and end mills. The biggest

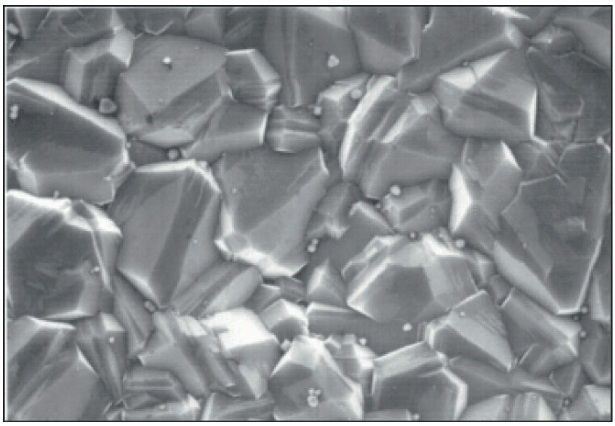

Fig. 4.4 Microstructure of CVD diamond film deposited on WC-Co substrate

obstacle in the widespread implementation of diamond coatings in machining is the poor adhesion of the diamond film to the substrate. In the case of FRP composites cutting tools, this problem is further aggravated by the requirement of a sharp edge and a small cutting edge-included angle. The presence of a sharp edge during diamond film synthesis at high temperatures reduces edge toughness and increases compressive residual stresses in the diamond film because of differences in thermal expansion coefficients of the film and the substrate. A number of improvements have been effected particularly in surface pretreatment technologies of the substrate. Some of these treatments include mechanical roughening of the surface, chemical etching of the cobalt binder to enhance diamond nucleation, etching of the tungsten carbide in order to increase surface roughness and mechanical interlocking, and the deposition of intermediate layers of hard coatings to act as chemical barriers. Some improvements have been reported and considerable tool life improvements have been realized in machining highly abrasive materials such as graphite, wood-based composites, and FRPs [2–4]. The failure mode of diamond-coated carbides is by uniform wear of the diamond film and by film delamination.

4.1.7 Future Outlook

In the previous sections, the most relevant cutting tool materials were surveyed and their suitability for machining FRPs has been discussed. Figure 4.5 shows the relative amount of wear these materials underwent when turning carbon-fiber-reinforced polymers [5]. It can be seen that, in the absence of chipping or catastrophic failure, sintered diamond provides by far the lowest amount of tool wear. At distant second are the sintered CBN and alumina–ZrO_2 ceramic. The coated and uncoated carbides show very inferior performance when compared to the sintered diamond and CBN

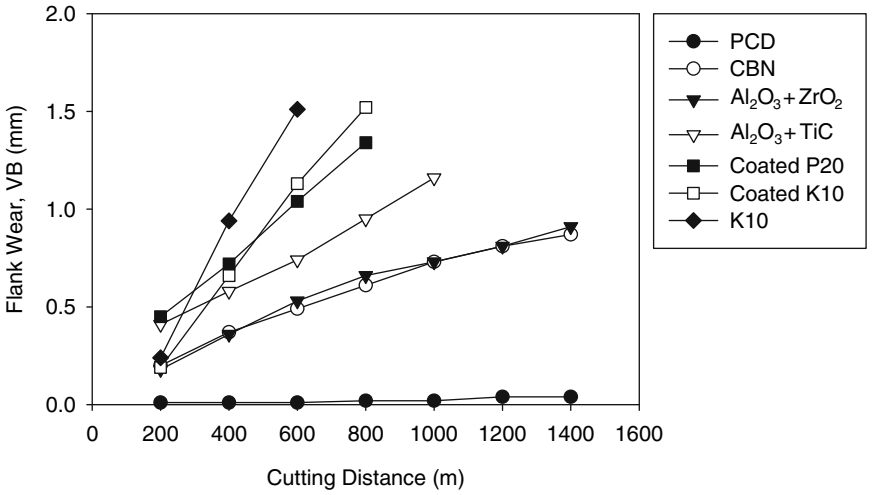

Fig. 4.5 Wear of different cutting tool materials in turning CFRP [5]

tools. It has been pointed out, and will also be explained in greater depth in the next sections, that the dominant wear mechanisms in machining FRPs are abrasion and microchipping. The former arises from the abrasive nature of the fibers and its debris in the cutting region, and the later is caused by the material inhomogeniety which causes fluctuating forces at the cutting edge. Thus, the demand on tool materials and cutting technology is to minimize the wear effects of these two mechanisms.

Combating abrasion is done by utilizing the hardest tool material available. In this case, sintered diamond and diamond-coated carbides are the two logical candidates. Developments in diamond coating technology, particularly in substrate surface engineering and treatment in order to increase adhesion and reduce thermal stresses, is an active area of research and progress is being made on this front. There are opportunities in development of graded carbide substrate that would help reduce the mismatch in thermal expansion coefficient between diamond and the carbides, which is considered the major cause of thermal stresses in the diamond-coated tool. Furthermore, significant improvements in coating characteristics can be imparted by depositing nanocoatings, both in nanomicrostructure and nanomultilayers. Nanocoatings are expected to be harder, tougher, and chemically more stable than several micrometer coatings.

Fiber-reinforced composites are produced near net shape, and the need for roughing operations and heavy cuts is not great. This allows lighter cutting forces to be applied to the tool and helps reduce chipping. The emphasis therefore turns to the machine tool and its structure. The demand for higher productivity requires the use of high spindle speeds and high feed rates, much higher than those utilized in metal cutting. Improvements in machine tool stiffness and spindle technology would help prevent chipping and allow the full utilization of the harder, but less tough tool materials such as ceramics, sintered CBN, and coated diamond tools.

Much greater emphasis will also be placed on consistency of performance of the cutting tools, particularly in unmanned machining situations. Because these tools are produced in mass, variations in their properties are quite common but are not desirable. New developments in coating technology would provide uniformity in properties of coated film in the same batch of cutting tools.

4.2 Tool Wear

Tool wear is defined as the unwanted removal of tool material from the cutting edge or the permanent deformation of the cutting edge leading to undesirable changes in the cutting edge geometry. Once the initial cutting geometry is altered, the cutting tool becomes less effective in performing its principal functions, which are material removal and generating good quality machined surface. Tool wear leads to undesirable consequences such as reduction in cutting edge strength, increased tool forces and power consumption, increased cutting temperatures, degradation in surface finish, loss of part dimensional accuracy, and eventually loss of productivity. Therefore, it is extremely desirable that tool wear is considerably minimized and controlled. Attempts are continuing to achieve this objective through the development of better wear resistant materials, better workpiece machining characteristics, and proper choices of machining conditions that promote long tool life.

Tool wear is a complex phenomena and it occurs by several mechanisms or processes, which include abrasive wear, diffusion wear, erosive wear, corrosive wear, and fracture [6]. Abrasive wear is associated with the presence of hard particles in the workpiece, which under high cutting pressure between the tool face and the workpiece would indent into the tool and microcut tiny groves in the tool surface. Diffusion wear is associated with the migration of atoms from the tool to the workpiece and vice versa, under conditions of high temperatures and high pressures. Erosive wear is similar to abrasive wear in regard to the gouging or cutting action of loose abrasive particles carried in a fluid medium. Corrosive wear occurs by chemical attack of the tool surface and is mainly driven by oxidation under sufficiently high cutting temperatures. Fracture wear (chipping) and delamination wear occur in brittle materials by the initiation, propagation, and coalescence of microcracks transverse and parallel to the tool surface, leading to removal of particles or flakes from the tool surface. The above-mentioned wear mechanisms do not behave in a similar manner under a given set of cutting conditions, and interactions between them may occur. The relative effects of these wear mechanisms are functions of cutting temperatures, cutting forces, and workpiece machining properties.

Under proper cutting conditions, the cumulative effect of the various wear mechanisms causes gradual degradation of the cutting edge with cutting time as shown in Fig. 4.6. The wear of the cutting edge starts at a high rate (regime I) which is caused by the initial breakdown of the sharp corners and weak spots in the cutting edge.

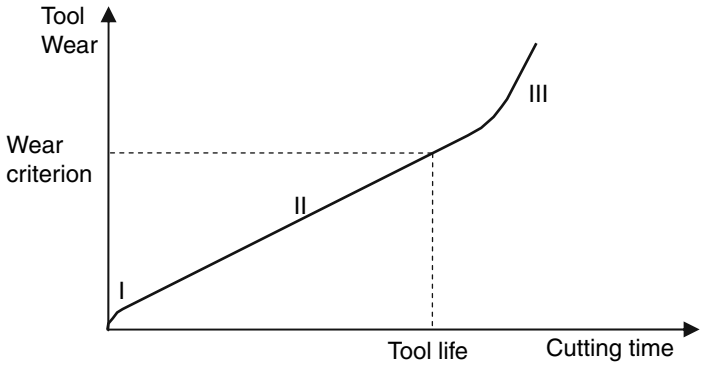

Fig. 4.6 Stages of tool wear. I, initial break-in; II, progressive uniform wear; III, accelerated or catastrophic wear

The cutting edge is then stabilized and the wear proceeds by gradual removal of the tool material (regime II) up to a point when the cutting edge geometry becomes dysfunctional and rapid or catastrophic wear sits in (regime III). Regime II which corresponds to wear at a uniform rate represents the useful life of the cutting edge. Wear in this regime is predictable and has been modeled mathematically. This has allowed successful prediction of tool life and scheduling of tool replacement.

4.2.1 Types of Tool Wear

Wear of the cutting tool is exhibited in various forms or types as shown in Fig. 4.7. When machining FRPs under stable conditions the most common type of wear is edge rounding which is caused by the gradual abrasion of the control surfaces forming the cutting edge. Figure 4.7b shows a cross section of a replica of a worn cutting edge in which edge rounding is clearly visible. It is seen that most of the wear takes place on the clearance face, creating a slightly curved wear land known as flank wear. The rounding of on the rake face is more severe and creates a much narrower curved wear land. The wear land on the clearance face is almost parallel to the cutting direction. Flank wear may not be uniform along the cutting edge and its width closely reflects the variations in workpiece properties along the contact length. For multiply FRP laminates for example, visible waviness in flank wear would reflect the differences in wear characteristics of the fiber and the polymer phases in the different plies. In applications where both primary and secondary cutting edges are engaged in the cut, maximum flank wear would occur at the tool corner. Another type of wear that is exhibited in machining FRPs is edge chipping. This type of wear is more common when the cutting tool does not have sufficient toughness to withstand the highly fluctuating cutting forces, when the depth of cut is too large and under interrupted cutting conditions.

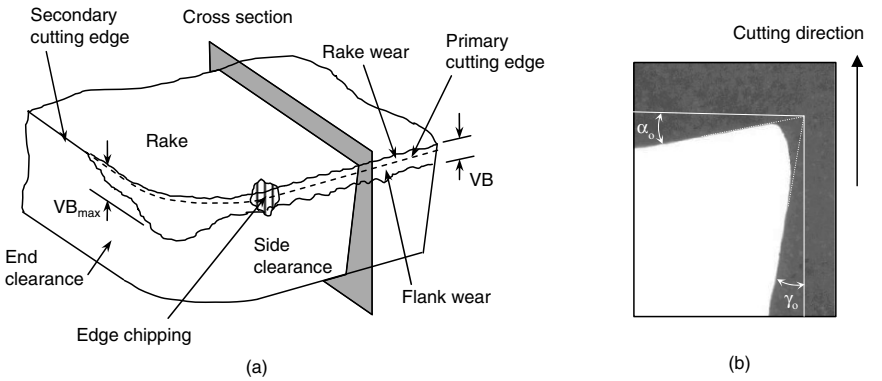

Fig. 4.7 Types of tool wear in machining FRPs (**a**), and cross section of a replica of the cutting edge (**b**)

4.2.2 Measurement of Wear

Quantifying wear is important for setting up tool life criterion and for process control. Wear is measured directly on the cutting tool or its replica, or indirectly by measuring some of the cutting process responses to wear, such as cutting forces and cutting power, and relating them back to actual tool wear. Flank wear, shown as the width of wear land, VB, in Fig. 4.7, has been widely used as a measure of tool wear in metal cutting. This is in part because in metal cutting the wear land on the clearance face tends to be relatively flat and parallel to the cutting direction and hence its measurement under an optical microscope is straight forward. It has been noted, however, that the wear of the cutting edge in machining FRPs is demonstrated by severe rounding of the cutting edge. Both wear lands on the clearance and rake faces are curved and their measurement under an optical microscope might be somehow problematic because of the limited depth of field of optical microscopy.

Figure 4.8 depicts the profile of a cutting edge that has been severely rounded by abrasion during machining wood-based polymer composites. A significant portion of the work on tool wear in machining FRPs indicates that the profile of the worn edge assumes a characteristic shape similar to the one shown in the figure. Furthermore, cutting process responses such as the surface quality and the normal force component are particularly sensitive to changes in this wear profile. Various geometrical features of this profile have been considered for quantifying wear. These include rake recession, RR, which describes the retraction of the most forward point on the profile in a direction parallel to the rake face, clearance recession, CR, which describes retraction of the cutting edge parallel to the clearance face, rake wear land, LR, clearance wear land, VB, and the nose radius, r_n [7].

Practical measurement of the different wear parameters described in Fig. 4.8 using an optical microscope is subject to several limitations and usually involves a great deal of difficulty. Because of the extreme curvature of the wear land, measurements of flank wear and rake wear should be conducted with great care. Most

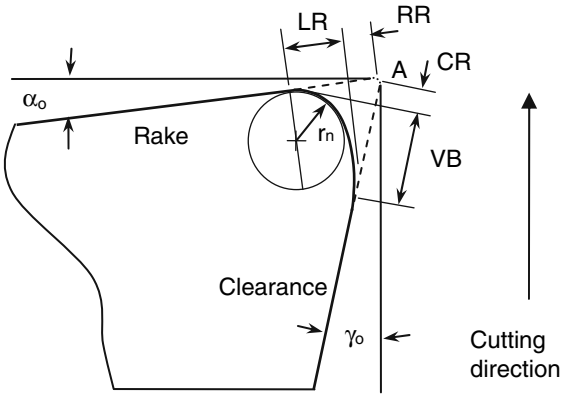

Fig. 4.8 Schematic of the profile of a worn cutting edge and the various measurements that can be performed. A, initial position of an ideally sharp cutting edge; LR, width of wear land on rake face; RR, edge recession parallel to the rake face; VB: flank wear; CR: edge recession parallel to the clearance face, r_n, nose radius

of the time only one parameter, namely VB, is measured and used to describe the state of bluntness of the cutting edge. However, one parameter alone does not provide information about the characteristic profile of the worn edge. The radius of the extreme edge of the worn tool, r_n, was considered for some time to be a good criterion for bluntness. It was however found that this radius tends to stabilize at a particular value and does not increase with further increases in cutting distance. The measurement of RR and CR are usually made in reference to either the unworn edge or a distinguishing mark on the tool surface. For applications where a portion of the cutting edge is not used (e.g., in peripheral milling), the measurement of RR can be easily made by viewing the rake face in a perpendicular direction [7].

Measurement of tool wear is also problematic in cases of complex tool geometries, such as abrasive cutters and burr tools. In these cutting tools, multiple faces and cutting edges are engaged in the cut and wear is often not uniform [8]. It is found to be more reasonable in such cases that tool wear is measured indirectly, and online by monitoring the cutting forces, cutting power, acoustic emission, as well as many other cutting process responses.

4.2.3 Tool Wear Mechanisms

During the cutting of fiber-reinforced composites several wear mechanisms may contribute to the overall wear of the cutting tool. Among these wear mechanisms are gross fracture or chipping, abrasion, erosion, microfracture or microchipping, chemical and electrochemical corrosion, and oxidation. While gross fracture results in the sudden or catastrophic failure of the cutting edge usually in the early stages of cutting, the other wear mechanisms result in gradual or progressive wear. Abrasion,

erosion, and microfracture involve the mechanical removal of microscopic wear particles. Corrosion and oxidation involve the chemical transformation of the tool material into softer or more brittle compounds which can be easily removed from the cutting edge by abrasion. Depending on the cutting conditions (e.g., cutting speed, feed speed, chip thickness, etc.) and workpiece conditions (e.g., fibers type and content, layup, etc.) some of these mechanisms may play a dominant role and become rate controlling. However, it has been pointed out in several works that the cutting temperatures in machining FRPs are very low in comparison to those found in metal machining. For example, a temperature of 260 °C was measured when machining carbon-fiber-reinforced polymers at a cutting speed of 200 m/min [9]. Similar temperatures were measured in the cutting of particleboard [10], but higher temperatures between 260 and 400 °C were measured when machining glass-fiber-reinforced polymers at the same cutting speed, apparently due to the poor thermal conductivity of GFRP [11]. These relatively low cutting temperatures would rule out the dominance of chemical wear, and the wear rate in machining FRPs is most likely dominated by mechanical processes.

4.2.3.1 Wear of WC-Co Tools

Tungsten carbide tools suffer from severe rounding of the cutting edge and flank wear when machining FRPs as illustrated in Fig. 4.7. Figure 4.9 shows a scanning electron microscope micrograph of a tungsten carbide tool after machining medium density fiberboard, a wood-based composite. It is apparent from this figure that most of the wear occurs on the clearance face of the tool because of the rubbing action between the clearance face and the workpiece surface. This rubbing is facilitated by the elastic spring back of the reinforcement fibers and matrix after cutting. Less wear is caused by flow of the chip dust and particles over the rake face. This is shown by the extent of removal of the original grinding marks from the rake face and the degree of roundness of the cutting edge. Flank wear may not be uniform and

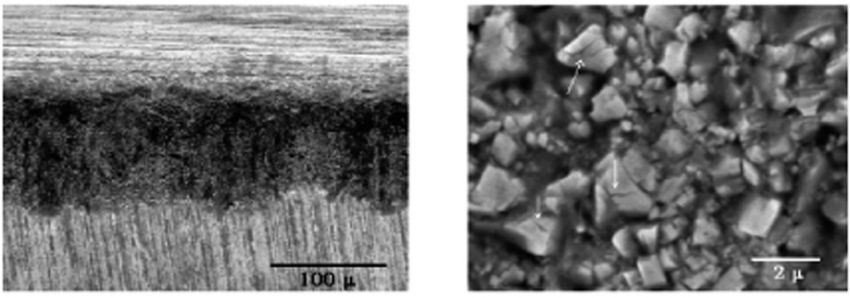

Fig. 4.9 SEM pictures showing wear land on WC-6%Co tool. (**a**) Low magnification of wear surface, with clearance face on bottom. (**b**) High magnification of wear microstructure showing voids where carbide grains once resided and visible cracks on carbide grains as indicated by *arrows*

it may reflect the density variations across the thickness of the workpiece. Shallow grooves in the direction of cutting are also visible. Voids may also be seen on the tool nose, indicating material that was broken off the tool edge by microfracture. These voids are later smoothed out by wear. A high magnification micrograph of the worn surface shows tungsten carbide grains standing in relief on the wear surface as well as cavities once occupied by carbide grains, which have been removed as shown in Fig. 4.9b. Similar microstructure was also observed when machining CFRP [9]. The micrograph clearly shows that the cobalt binder was removed from between the carbide grains and that individual grains are standing in relief. Arrows on the photomicrographs indicate the presence of transgranular cracks in the WC grains. The presence of smaller than nominal grain size fragments of WC on the wear surface indicates that large grains have been fractured into smaller fragments. There is no evidence of wear (oxidation/corrosion pits, rounding) on the tungsten carbide grains themselves and they appear to have retained their original angular sharp appearances.

The characteristic microstructure of the wear surface in Fig. 4.9 indicates that wear of tungsten carbide cutting edge in machining FRPs occurs by preferential removal of the cobalt binder followed by the fragmentation or fracture and uprooting of the WC grains [9, 12]. The binder phase is first partly removed from between the tungsten carbide grains by a combination of plastic deformation (extrusion) and microabrasion. The second stage of wear occurs when sufficient binder has been removed and it involves removal of the carbide grains from the surface by fracture and uprooting. FRPs are inhomogeneous materials consisting of soft and hard phases. Moreover, loose microfragments of the hard and abrasive reinforcement phase at the interface between the tool and the workpiece are able to penetrate, under cutting pressure, between the carbide grains and preferentially erode the cobalt binder by microabrasion. High fluctuating forces that are generated by material inhomegeneity would then cause the tungsten carbide grains to rock slightly in their position in the WC-binder composite. This, in turn, would result in the partial extrusion of the binder to the surface of the cutting tool where it is later removed by the workpiece. In addition, the relative motion of the brittle carbide grains would result in developing cracks across the grains, which is followed by fracture and removal of parts of or the whole grain from the binder matrix leaving large voids as shown in Fig. 4.9b. The wear mechanism described above has been previously called “soft abrasion” and is found to be the controlling wear mechanism in applications where cemented tungsten carbides are used against softer abrasives such as sandstone and zirconia [13, 14].

The extent of edge wear of WC-Co tools is found to depend on the bulk hardness of the carbide grade as shown in Fig. 4.10 [12]. It can be seen from this figure that tool wear generally decreases with an increase in hardness according to a linear relationship. Either increasing the binder content or increasing the WC grain size decreases the bulk hardness of the WC-based composite as shown in Fig. 4.2, and hence decreases the wear resistance. Moreover, for wear to take place by cobalt extrusion and microabrasion, the wear rate would depend on binder content and WC grain size (or more precisely the mean free path in the binder phase) and the

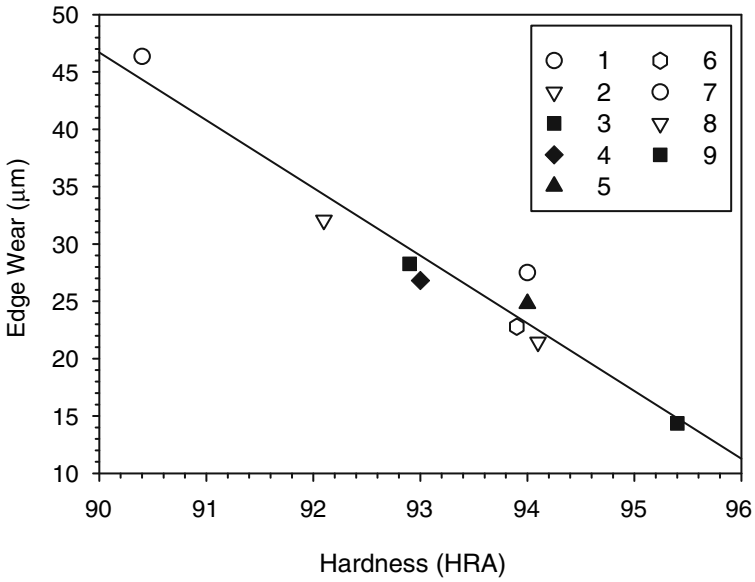

Fig. 4.10 Relationship between bulk hardness of WC-Co tools and edge wear when machining particleboard [12]. Properties of the carbide grades are shown in Table 4.2

frictional load which is responsible for the relative movement of the WC grains. The mean free path in the binder phase is a measure of the thickness of the binder layers between the WC grains and it describes the distance which dislocations can move in order for plastic deformation to occur (provided that the binder phase is free of precipitates). Therefore, the mechanical properties of the binder and the WC-Co will be strongly dependent on the mean free path [15]. The mean free path, h_b, is a function of both the binder phase content, f_b, and the carbide grain size, d_{WC}, and can be determined from the expression

$$h_b = \alpha_{WC} \cdot d_{WC} \cdot f_b/(1 - f_b), \tag{4.1}$$

where α_{WC} is a factor which depends on the shape and contiguity of the carbide grains. Figure 4.11 shows the relationship between the ratio h_b/α_{WC} and the amount of wear for the nine carbide grades shown in Table 4.2. It can be seen from this figure that a good correlation exists between the amount of wear and the ratio h_b/α_{WC}. An increase in both the binder content and the carbide grain size leads to an increase in the ratio h_b/α_{WC}, which, in turn, leads to an increase in the amount of wear. It can be seen that, for compositions with fine and medium grain size, the effect of increasing the binder content on wear is greater than the effect of increasing the carbide grain size. This confirms the importance of binder removal by extrusion and microabrasion as a controlling wear mechanism. In addition, the increase in the amount of wear with the increase in the ratio h_b/α_{WC} occurs more rapidly for ratios of 0.06 and lower. Beyond this value, the curve approaches a straight

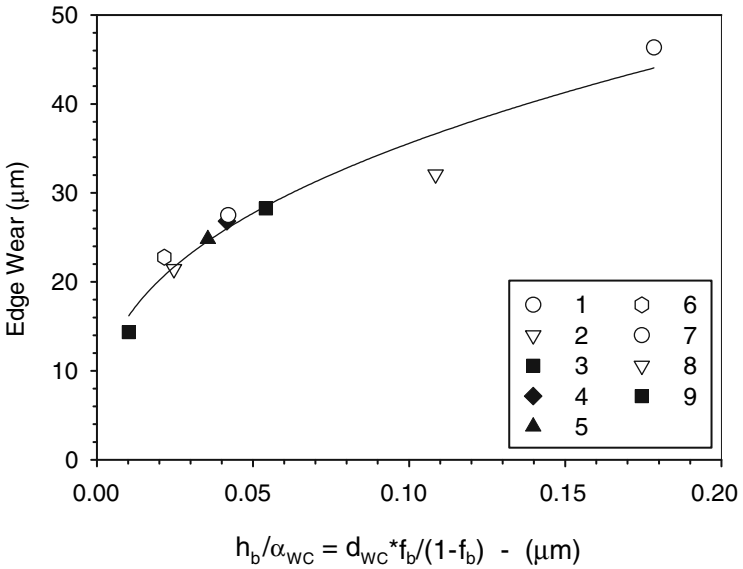

Fig. 4.11 Dependence of edge wear on binder mean free path [12]. Properties of the carbide grades are shown in Table 4.2

line and the wear becomes proportional to h_b/α_{WC}. This means that significant enhancements in wear resistance can be achieved by developing ultrafine and nanostructured cemented carbides with grain size of less than 0.5 µm (h_b/α_{WC} less than 0.015). There is also a good correlation between the compressive strength of the carbide grade and the amount of wear as shown in Fig. 4.12. Compressive strength is strongly dependent on the weight fraction and the hardness of the binder phase and a correlation between wear and compressive strength further supports the concept of binder removal by extrusion and microabrasion.

4.2.3.2 Wear of Diamond-Coated Carbides

CVD diamond coatings on tungsten carbide substrate are notorious for having problems in adhering to the substrate under practical cutting conditions. This in part is caused by large residual stresses in the film and the substrate, which are generated by the CVD process. Because of mismatches in thermal expansion coefficients of the diamond film and the substrate ($\alpha_D = 2.85 \times 10^{-6}\,°C^{-1}$ for the diamond coating and $\alpha_s = 5.0 \times 10^{-6}\,°C^{-1}$ for the substrate), and the high temperatures required for the CVD process (600–1,000 °C), high thermal residual stresses are formed in the coating and substrate on cooling. These stresses affect the behavior of the coated tool in machining. Furthermore, additional stresses are introduced to the cutting edge by the external loads from machining and the peculiar shape of the cutting edge. A specific requirement for machining fiber-reinforced composites is the

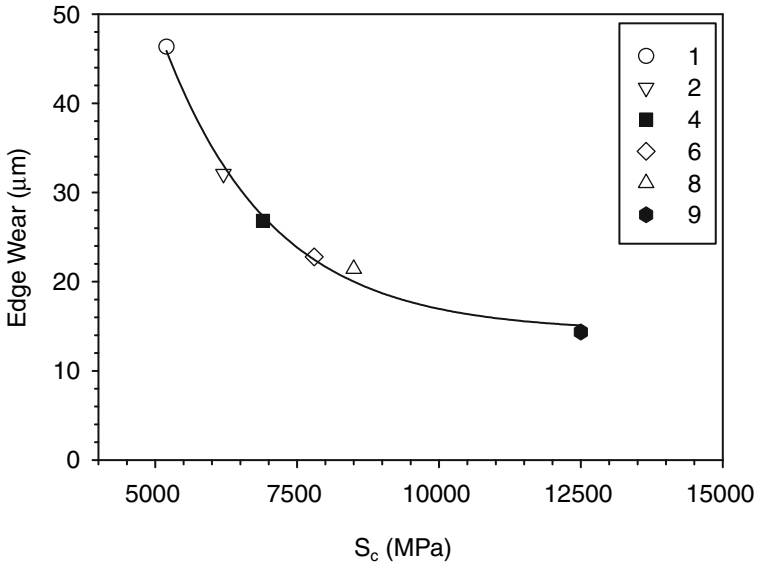

Fig. 4.12 Dependence of edge wear on carbide compressive strength [12]. Properties of the carbide grades are shown in Table 4.2

availability of a sharp cutting edge with a small included angle in order to cleanly sever the fibers and produce good surface quality. This, however, makes the edge mechanically weak, creates complex residual stresses, and only accelerates edge wear. Therefore, performance of diamond coated tools is critically dependent on the feed rate, workpiece material, cutting edge geometry, substrate type and preparation, and coating thickness [4].

In the absence of premature failure and crumbling of the cutting edge because of lack of mechanical strength, two wear mechanisms determine the wear characteristics of diamond-coated tools in machining FRPs. These are uniform abrasion and fracture-controlled delamination of the diamond film. When the film adhesion is sufficient, the diamond-coated tools wear by uniform abrasion of the diamond film, as shown in Fig. 4.13, and generally exhibit very long tool life in comparison to uncoated tools. This is attributed to the extreme hardness of the diamond film, its low coefficient of friction, and its high thermal conductivity. The wear by abrasion proceeds by gradual smoothing and shedding of the diamond grains, leading to thinning of the diamond film. This in turn leads to fracture and localized removal of the film from the substrate. Accelerated wear by abrasion of both substrate and diamond film follows. When the film adhesion is not sufficient or when conditions of residual stresses in the film are not favorable, localized fracture initiates at the nose of the cutting edge in the form of a radial crack as shown in Fig. 4.14a. Under conditions of large compressive stresses in the film the crack penetrates the coating and bends in the direction of the substrate as it reaches the coating–substrate interface. This crack causes large scale delamination of the diamond film as shown in Fig. 4.14b, c.

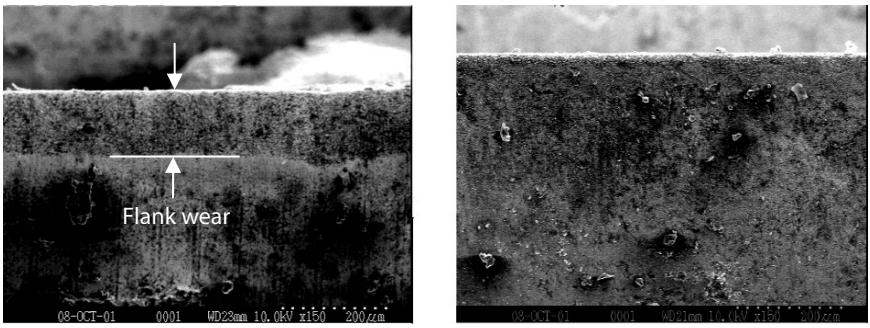

Fig. 4.13 SEM pictures showing flank wear on uncoated cemented carbide tool (*left*) and diamond coated tool (*right*) after cutting the same distance of medium density fiberboard

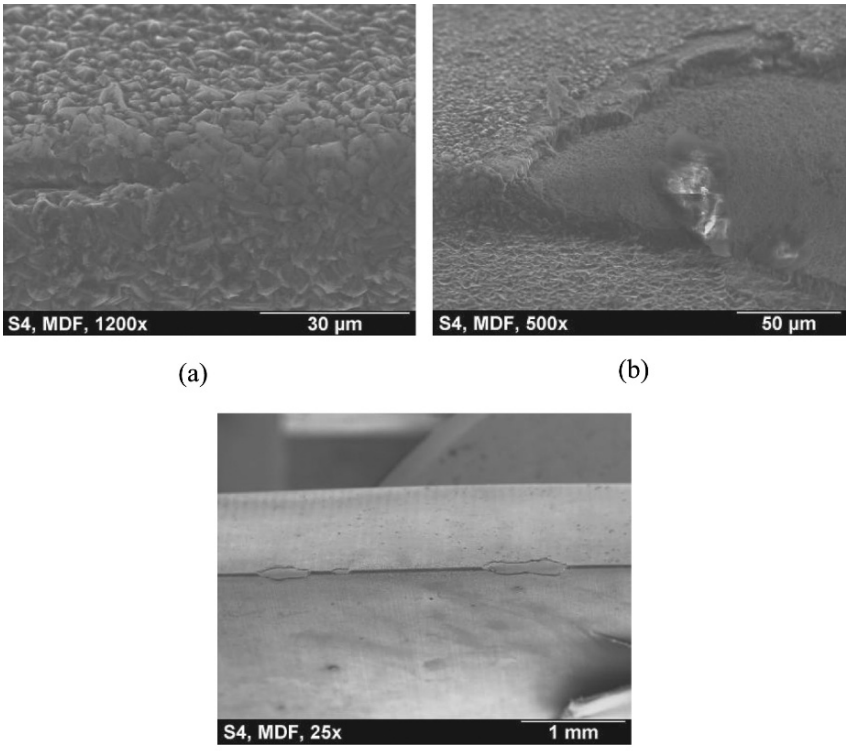

Fig. 4.14 SEM micrographs showing the evolution of fracture and delamination of diamond film. (**a**) Radial crack initiation and growth at the tool nose, (**b**) crack growth toward the substrate and propagating along the substrate resulting in delamination of diamond film, and (**c**) large scale delamination

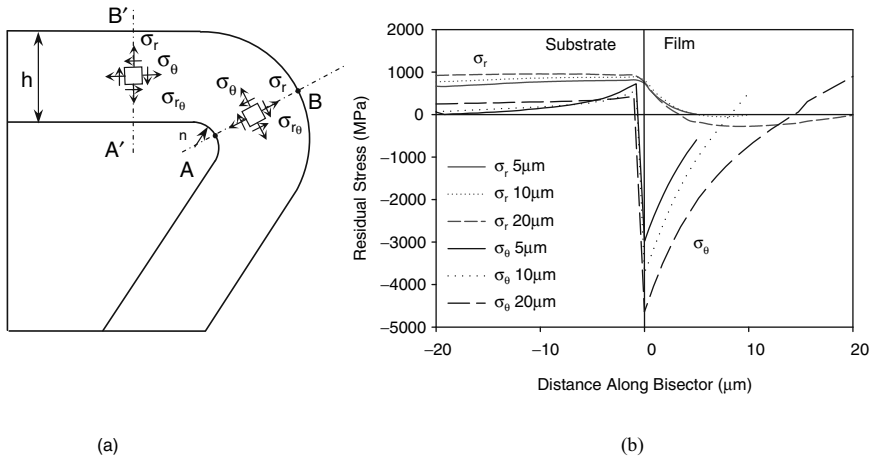

Fig. 4.15 (**a**) State of stress in the diamond film. (**b**) Variation of radial and tangential stress in the thickness of the film along line AB. Cutting edge angle = 55°, nose radius = 5 μm [17]

The substrate is then severely exposed, and accelerated wear by abrasion of the substrate and diamond film follows. High feed rates and small film thickness are found to promote wear by fracture and delamination of the diamond film [3, 4].

The state of stress in the diamond film plays an important role in facilitating or prohibiting crack growth. Finite element analysis of thermal stresses in diamond-coated carbides revealed that gigantic stresses are developed in the diamond film upon cooling [15, 16]. Figure 4.15a shows a schematic of a cross section of thin film coated cutting edge. The nose radius of the cutting edge is r_n and the thickness of the diamond film is h. At locations far enough from the curvature of the cutting edge (line A′B′) the residual stresses in the direction of the film, σ_θ, tend to be large and compressive. Stresses normal to the direction of the film, σ_r, are tensile and much smaller in magnitude than σ_θ. The shear stresses are of negligible level and the directions along the film and normal to the film are practically the directions of principal stresses. Approaching the curvature of the cutting edge, a transition from compressive to tensile and an increase in stress magnitude occurs in σ_θ. Figure 4.15b shows variation of the radial and the tangential stresses in the film and the substrate along line AB, which bisects the cutting edge angle, for different film thicknesses and a nose radius of 10 μm. It can be seen that the residual stresses in substrate are tensile and of relatively small magnitude. At the film–substrate interface, the normal stresses in the film are tensile while the tangential stresses are compressive and considerably larger than the normal stresses. Traversing toward the free surface of the film a transition in direction occurs for both stresses. The radial became small and compressive while the tangential stresses become tensile. Knowing that cracks propagate in tensile stress fields, it becomes apparent that the transition in the tangential stress is favorable for crack propagation from the surface and toward the substrate, as shown in Fig. 4.14a. As the crack propagates toward the

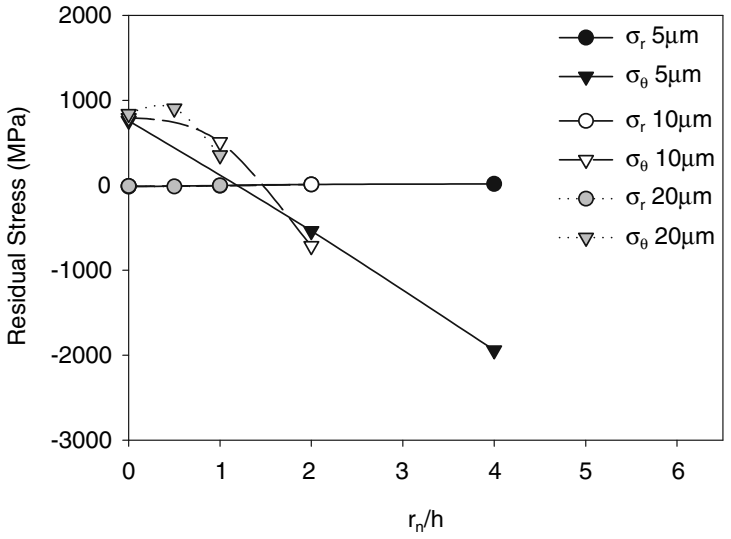

Fig. 4.16 Variation of residual stresses in the diamond film with r_n/h ratio. Cutting edge angle = 55° and nose radius = 5 μm [17]

interface, it is faced by increasing compressive stresses. This will result in deflecting the crack path to be parallel to the interface as it propagates deeper into the film thickness [16]. The large compressive stresses would eventually lead to film delamination by crack propagation along the interface as shown in Fig. 4.14b, c.

As seen in Fig. 4.15, the edge geometry, in particular the ratio of film thickness to nose radius (r_n/h) determines if and where a transition from compressive to tensile stresses occurs. Figure 4.16 shows the state of stress at the free surface of the film (point B in Fig. 4.15a) for different values of r_n/h. It can be seen that the transition from tensile to compressive in the tangential stress component occurs in the range 1.25–1.5. Larger values of r_n/h (thinner diamond films) promote extremely high compressive stresses, which lead to delamination. On the other hand, smaller values of r_n/h (thicker films) cause tensile stresses in the outer surface of the film, which is favorable for crack initiation at the surface. Once a surface crack is formed, it will be driven into the film following the path of maximum shear stress and it may lead to chipping a large segment of the film. Evidence from cutting experiments with diamond-coated tools with honed nose has shown considerable improvement in wear resistance over sharp-coated tools [3]. Another factor that affects the response of the diamond film is the external forces applied to the film by the cutting process. It has been shown that high feed rates, resulting in larger cutting forces, cause accelerated chipping and delamination of the diamond film [18].

4.2.3.3 Wear of PCD Tools

The wear of PCD tools is characterized by uniform flank wear by abrasion, after an initial shedding of weakly held particles from the cutting edge by microchipping [18]. Rounding is also noticed on the rake face, but the wear land on the rake face is much narrower than that on the clearance face. Shallow abrasive grooves formed on the flank face and ran in the direction of cutting. Coarse PCD grades were found to perform better than the fine ones in the long run, as it provided smaller flank wear rate. On the other hand, fine grain PCD is less susceptible to microchipping of the cutting edge than coarse grain PCD [19, 20]. Uniform abrasion wear is the dominant wear mechanism when machining homogenous composites with low feed rates. The wear mechanism appears to be similar to that present when machining with tungsten carbides. Voids on the wear surface indicate locations where diamond grains were dislodged. The cobalt binder is first removed from between the diamond grains, which facilitates its dislodgment from the cutting edge. As the work material becomes less homogeneous or when using high feed rates, especially in interrupted cutting, the oscillating forces on the cutting edge give rise to microchipping and fracture as the dominant wear mechanism. Chipping could occur at a scale much larger than the diamond grain size, causing severe damage to the cutting edge.

4.2.4 Tool Life

Tool life is defined as the cutting time required for reaching an amount of wear as specified by a tool-life criterion. A tool-life criterion is defined by a machining objective such as predetermined acceptable levels of cutting forces, surface quality, dimensional stability, or production rate. These machining objectives are considered separately or in combination and are associated with a certain level of tool wear. Under proper cutting conditions, tool life is reached gradually because of progressive wear as shown in Fig. 4.6. But the tool life could also end prematurely because of excessive chipping or breakage of the cutting edge. This scenario is avoided in all practical machining applications. In metal cutting a threshold value of $\mathrm{VB} = 0.3\,\mathrm{mm}$ for uniform wear or $\mathrm{VB}_{\max} = 0.6\,\mathrm{mm}$ for irregular flank wear is used as a tool-life criterion. There is no agreement yet on similar criteria for machining FRPs, but a value of $\mathrm{VB} = 0.2\,\mathrm{mm}$ has been frequently used.

4.2.4.1 Tool-Life Equation

Early work in metal machining by Taylor [21] has shown that tool life is strongly dependent on cutting speed. An empirical relationship was produced to relate tool life to cutting speed:

$$vT^n = C, \tag{4.2}$$

Table 4.4 Taylor's tool life equation coefficients for several tool-workpiece combinations. T in minutes, feed = 0.1 mm/rev, $VB = 0.2$ mm [22]

Workpiece	Tool	d (mm)	n	C	Cutting speed (m/min)
UD-GFRP ($V_f = 0.7$)	K10	2.0	0.2334	90	30–50
UD-GFRP ($V_f = 0.7$)	PCD	2.0	0.1684	398	200–250
CFRP filament wound	K10	2.0	0.7813	1,640	80–300
CFRP filament wound	PCD[a]	2.0	0.4237	2,900	500–1500
GFRP ($V_f = 0.5$)	K10[b]	1.0	0.4069	565.6	100–300
GFRP ($V_f = 0.5$)	K10	1.0	0.2710	152.66	100–300

[a]VB = 0.1 mm
[b]Diamond-coated K10

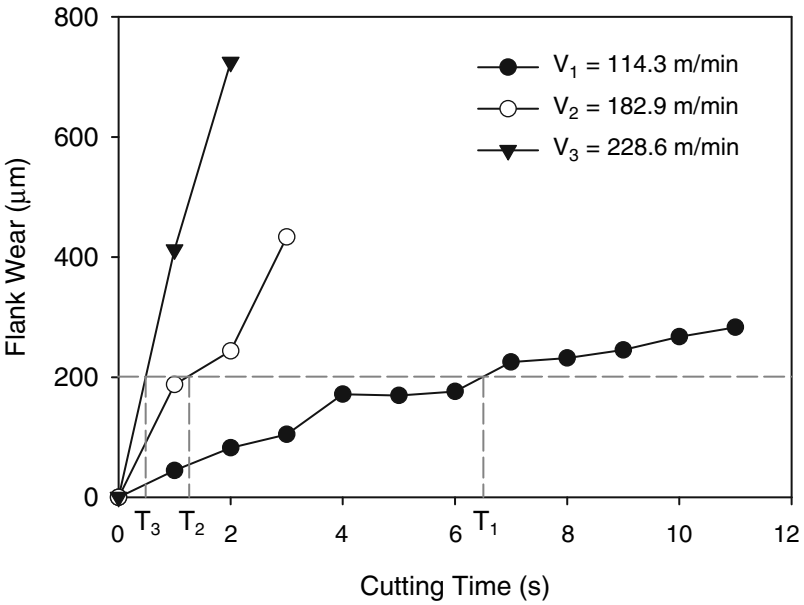

Fig. 4.17 Progressive wear of C5 carbide tool in turning of graphite/epoxy [23]

where v is the cutting speed, T is tool life, and n and C are empirical constants. In the SI system of units, v is measured in m/min, T in minutes, and C becomes the cutting speed for a tool life of 1 min. Values for the emprical constants C and n for different tool–workpiece pairs in turning are shown in Table 4.4 [22].

Example 4.1. Tool wear data for machining a disk made of graphite/epoxy tape with a C6 carbide insert is shown in Fig. 4.17 [23]. Use this data to determine Taylor's tool-life equation constants n and C. Use a tool-life criterion of VB = 0.2 mm.

A horizontal line is drawn at flank wear of VB = 200 µm and the corresponding cutting times are obtained and recorded in the table below.

V_1	114.3 m/min	1.905 m/s	T_1	5.7 s
V_2	182.9 m/min	3.048 m/s	T_2	1.2 s
V_3	228.6 m/min	3.810 m/s	T_3	0.5 s

To determine the values of C and n, select two of the three points, substitute in (4.2) and solve two simultaneous equations. Choosing the two extreme points ($V_1 = 1.905,\ T_1 = 5.7$) and ($V_2 = 3.81,\ T_1 = 0.5$), we have

$$1.905(5.7)^n = C \text{ and } 3.81(0.5)^n = C.$$

Setting the left sides equal gives,

$$1.905(5.7)^n = 3.81(0.5)^n.$$

Taking the natural logarithm of each term,

$$\begin{aligned}
&\ln(1.905) + n \times \ln(5.7) = \ln(3.81) + n \times \ln(0.5)\\
&0.64448 + 1.740n = 1.33763 - 0.693\ln\\
&0.6931 = 2.4336n
\end{aligned}$$

then, $n = 0.2848$ and $C = 1.905(5.7)^{0.2848} = 3.1274\,\text{m/s}$.
Taylor's tool-life equation for this tool–workpiece combination is finally given as:

$$vT^{0.2848} = 3.1274,$$

where v is in m/s and T is in seconds. Figure 4.18 shows a log–log plot of the data showing a linear relationship between log v and log T. The slope of the straight line is $-1/n$.

Note: if the data points do not give a good fit of a straight line then the procedure above is not accurate. Instead, standard curve fitting techniques are used to determine the slope and y-intercept of the best fitting line.

4.2.4.2 Factors Affecting Tool Life

Tool life is affected mainly by cutting speed, because cutting speed is the major factor influencing cutting temperatures. Tool life is also affected by feed speed, depth of cut, and cutting tool geometry. Only very little work in the literature points to the effect of cutting tool geometry on tool wear in machining FRPs. But the substantial data from metal cutting indicate that flank wear increases with a decrease in clearance angle. The cutting forces were found to decrease with an increase in rake angle, which causes an increase in tool life. However, one cannot increase the rake angle without the risk of weakening the cutting edge and making it more fragile. Thus an optimum rake angle exists for a given tool–workpeice material pair. Based on cutting forces alone, an optimum tool geometry for cutting multidirectional graphite/epoxy with sintered diamond was determined as $\alpha_o = 6°$–$7°$ and $\gamma_o = 17°$ [24].

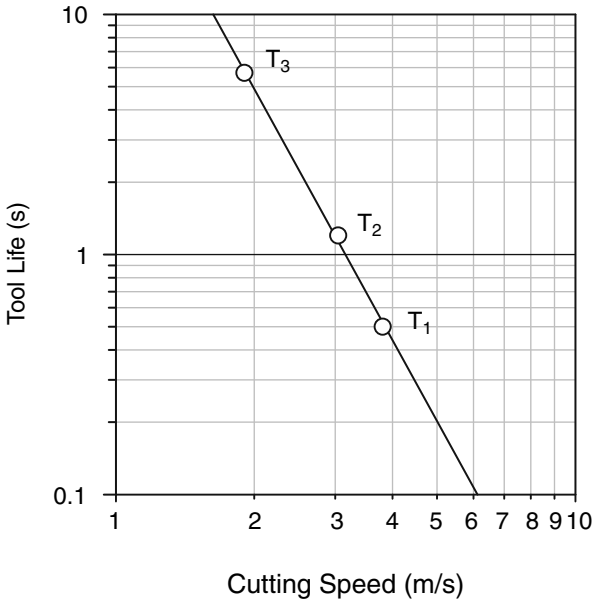

Fig. 4.18 Tool life of C6 carbide tool in turning tape graphite/epoxy composite, obtained from Fig. 4.17

A generalized tool-life equation that accounts for the effects of speed, feed rate, and depth of cut on tool life has the form:

$$K = vT^n f^m d^q, \tag{4.3}$$

where f is feed rate; d is depth of cut; and K, n, m, and q are empirical constants. Typical values for C6 carbide insert in cutting graphite/epoxy composite are $n = 0.2765$, $m = 0.1476$, and $C = 2.3227$. Figure 4.19 shows a plot of (4.3) for this tool material. It can be seen that cutting speed has the major influence on tool life and that the role of feed rate is secondary. The interaction between the effects of speed and feed on tool life is also obvious at high cutting speeds.

Example 4.2. The tool-life equation for C6 carbide when machining graphite/epoxy composite is given by

$$2.3227 = VT^{0.2765} f^{0.1476}.$$

At cutting speed of 2.5 m/s and feed rate of 0.14 mm/rev, the tool life is predicted to be 2.19 s. Determine the effects on tool life of (a) 20% increase in speed, (b) 20% increase in feed rate, and (c) 20% increase in both cutting speed and feed rate.
Tool life is determined from the equation

$$T^{0.2765} = \frac{2.3227}{Vf^{0.1476}} \text{ or } T = \left(\frac{2.3227}{Vf^{0.1476}}\right)^{\frac{1}{0.2765}}.$$

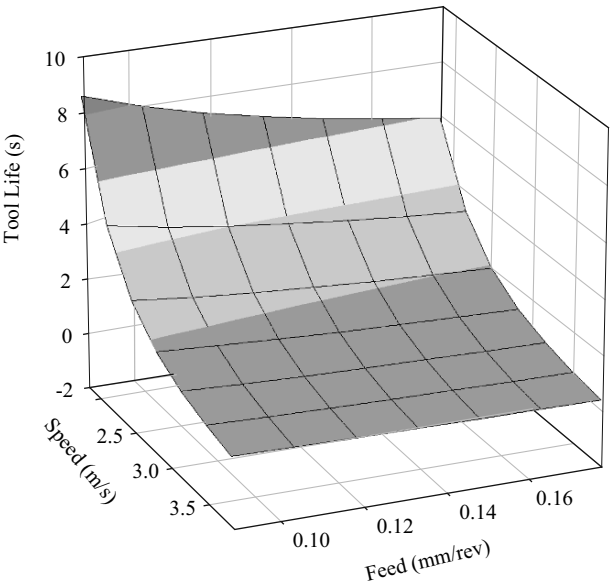

Fig. 4.19 Effect of cutting speed and feed rate on tool life. Coefficients of (4.3), $n = 0.2765$, $m = 0.1476$, and $C = 2.3227$

The following table summarizes the results obtained by using the equation above:

Condition	Speed (m/s)	Feed (mm/rev)	Tool life (s)	Percent change in tool life
Reference	2.5	0.14	2.19	0
(a)	3.0	0.14	1.13	−48.3
(b)	2.5	0.168	1.99	−9.3
(c)	3.0	0.168	1.03	−53.1

4.3 Summary

Tool wear in machining FRPs occurs primarily by abrasion and microchipping. Abrasive wear is caused by sliding of the tool surfaces under pressure against the abrasive fiber material embedded in the polymer matrix and by three-body abrasion caused by the debris of fibers and matrix. Abrasive wear is manifested by clear rounding of the cutting edge and in the form of wear lands on the rake and the clearance surfaces of the cutting tool. These wear lands are often marked by shallow grooves running in the cutting direction, which are indicative of the microstructure variation of the workpiece across its thickness. Microchipping is caused by the oscillating cutting forces that result from repeated fracture of the fiber reinforcement. This type of wear is characterized by small and large voids on the cutting

edge which are caused by pieces of the tool material being dislodged from the cutting edge. At the microstructural level, the wear surface of cutting tool materials made from sintered hard particles (such as cemented carbides and PCD) is characterized by hard particles standing in relief and by cracked and broken hard particles. This is caused by removing the binder phases from between the hard particles by extrusion and erosion. This causes the hard phase particles to break and fall off the tool surface.

In general, the cutting tool material requirements to resist these types of wear are high hardness and high toughness. Unfortunately, cutting tool materials that have high hardness generally suffer from low toughness. An example of this is the family of sintered PCD tools commonly used in machining FRPs. These tools commonly fail by chipping due to the lack of toughness. This problem is often avoided by designing the cutting edge with a large included angle, small rake, and a chamfer. Cemented carbides on the other hand offer higher toughness but lower hardness than PCDs. Nevertheless, they remain the most versatile and economically feasible choice of cutting tool material. The ability to hot press these tools from powders of the constituent materials (tungsten carbide phase and metallic binder phase) allows them to be produced in different shapes and properties to suit a particular machining application. The wear of cemented carbides occurs mostly by abrasion, and therefore, grades with higher hardness are better performers in machining FRPs. Significant improvement in the wear resistance is achieved by selecting smaller grain size and lower binder content grades. This is due to reduction in the binder mean-free path and less susceptibility of these grades to wear by binder erosion. Moreover, the emerging technique of diamond coating of carbides adds the high hardness required for machining FRPs.

Tool wear is typically measured by the width of flank wear land and a common criterion for tool life is wear land width of 0.2 mm, even though lower values have been used. Tool life is influenced by cutting tool parameters (such as rake angle, clearance angle) and by process parameters (such as cutting speed, feed speed, and depth of cut). The effect of tool geometry on tool wear stems from its effect on cutting forces and cutting edge strength. In general, the larger the rake and clearance angles, the lower the cutting forces, and hence the lower tool wear. But these conditions also make the cutting edge weaker and hence accelerate tool wear. Therefore, optimum cutting tool geometry may be sought by experimental and analytical techniques. Tool life also decreases with an increase in cutting speed, an increase in feed rate, and an increase in depth of cut. The effect of cutting speed on tool life is the most significant. This is perhaps due to the direct relationship between cutting speed and cutting temperatures.

Review Questions and Problems

1. Describe the key properties of tool materials important for machining FRPs and discuss their influence on the performance of cutting tools in machining.

2. What are the advantages of micrograin carbides compared to conventional alloys. Make specific reference to machining of composites.
3. Describe the wear mechanism of cemented carbides in machining FRPs.
4. Describe the wear mechanism of PCD tools in machining FRPs.
5. In a machining application with cemented carbide tools you notice that tool wear occurs predominantly by microchipping. Which action would you take to reduce tool wear?
6. In a machining application with diamond-coated carbide you notice that tool wear occurs predominantly by delamination of the diamond film. Which action would you take to reduce tool wear?
7. What are the advantages and limitations of coated carbides over uncoated ones. Make specific reference to machining of composites.
8. This problem is aimed at comparing the effects of possibly changing one of the cutting conditions, namely cutting speed and the cutting tool material. Throughout, assume that except for cutting speed, all other cutting conditions are kept constant and that the machining time is inversely proportional to the cutting speed as described by Taylor's tool life equation. Coefficients of tool life equations for this problem are given in Table 4.4.

   (a) Assume that the current cutting edge material is K10 carbide and the workpiece material is GFRP. Furthermore, assume that the current speed is 20 m/min. Estimate the tool life T for this tool material at this cutting speed.
   (b) As a change in operating strategy, cutting speed will be selected to give a tool life of 3.5 h, so that cutting edges are changed about twice per shift. Find the cutting speed that will give this tool life for K10 carbide, and compute the *ratio* of this new machining time to the machining time in part (a).
   (c) Retain the operating strategy from part (b), i.e., the cutting speed is selected so that the tool life is 3.5 h. This time, PCD tool will be used as a tool material. With this new tool material, for $T = 3.5$ h, compute the cutting speed and the *ratio* of this new machining time to the machining time in part (a).

9. It is required to finish-turn the diameter of a glass-fiber-reinforced axle from 77.0 to 75.0 mm at a length of 50.0-mm on each end of the axle. The axle is 1,000.0 mm long. The axle is turned at 800 rpm, the feed is 0.1 m/rev and the depth of cut is 1.0 mm. You have an option of using three tool materials for this turning job. The tool materials are a K10 carbide, a diamond-coated K10 carbide and a PCD tool. The tool life curves for the three different tools are given in Table 4.4. Determine the following:

   (a) The cutting time required for finish-turning one axle.
   (b) The number of axles that can be finish-turned by each cutting edge before the tool reaches the end of its usable life.
   (c) Knowing that the cost of a K10 carbide insert is $5.0 (one insert has two edges), the coast of a diamond coated carbide insert is $25 per insert (one

insert has two edges), the cost of a PCD insert is $80 (one edge per insert), machine and operator cost is $40/h, loading and unloading time for each axle is 5 min, setup time per edge is 5 min, which of the three tool materials would be most economical? Assume that 500 axles need to be finish-turned.

10. In Table 4.4, the tool-life constants of a PCD tool when cutting GFRP and CFRP are given. The value of n for machining CFRP is almost twice as that for machining GFRP. This means that tool life of PCD is less dependent on cutting speed when machining CFRP. Explain why.
11. Determine, by analysis, the cutting speed at which the PCD and diamond coated carbide will have the same tool life.

References

1. Sheikh-Ahmad, J., Morita, T., Tool coatings for wood machining: Problems and prospects. Forest Products Journal 52, 43–51, 2002.
2. Usuki, H., Narutaki, N., Yamane, Y., A study of cutting performance of diamond coated tools. International Journal of the Japan Society of Precision Engineering 25, 35–36, 1991.
3. Sheikh-Ahmad, J., Stewart, J.S., Feld, H., Failure characteristics of diamond-coated carbides in machining wood-based products. Wear 255, 1433–1437, 2003.
4. Köpf, A., Feistritzer, S., Udier, K., Diamond coated cutting tools for machining of non-ferrous metals and fibre reinforced polymers. International Journal of Refractory Metals and Hard Materials 24, 354–359, 2006.
5. Ferriera, J.R., Coppini, N.L., Miranda, G.W.A., Machining optimization in carbon fibre reinforced composites materials. Journal of Materials Processing Technology 92–92, 135–140, 1999.
6. Shaw, M.C., Metal Cutting Principles, 2nd Edition, Oxford University Press, New York, NY, 2005.
7. Sheikh-Ahmad, J.Y., McKenzie, W.M., Measurement of tool wear and dulling in the machining of particleboard. Proceedings of the 13th International Machining Seminar, Vancouver, BC, Vol. 2, 1997, 659–670.
8. Janardhan, P., Sheikh-ahmad, J., Cheraghi, H., Edge trimming of CFRP with diamond interlocking tools. SAE Technical Paper 2006–01–3173.
9. Masuda, M., Kuroshima, Y., Chujo, Y., Failure of tungsten carbide-cobalt alloy tools in machining of carbon materials. Wear 169, 135–140, 1993.
10. Sheikh-Ahmad, J.Y., Lewandowski, C.M., Bailey, J.A., Stewart, J.S., Experimental and numerical method for determining temperature distribution in a wood cutting tool. Experimental Heat Transfer 16, 255–271, 2003.
11. Spur, G., Wunsch, U.E., Turning of fiber-reinforced plastics. Manufacturing Review 1, 124–129, 1988.
12. Sheikh-Ahmad, J., Bailey, J.A., The wear characteristics of some cemented tungsten carbides in machining particleboard. Wear 225–229, 256–266, 1999.
13. Larsen-Basse, J., Devani, N., Almond, E., Brooks, C., and Warren, R. (Eds.), Science of Hard Metals, Adam Higler, Bristol, 1986, pp. 883–895.
14. Jia, K., Fischer, T.E., Abrasion resistance of nanostructured and conventional cemented carbides. Wear 200, 206–214, 1996.
15. Exner, H.E., Gurland, J., Review of parameters influencing some mechanical properties of tungsten carbide cobalt alloys. Powder Metallurgy 13, 13–31, 1970.
16. Gunnars, J., Alahelisten, A., Thermal stresses in diamond coatings and their influence on coating wear and failure. Surface and Coating Technology 80, 303–312, 1996.

17. Parakshit, C., Finite Element Analysis of Diamond Coated Tools. Masters Thesis, Wichita State University, Wichita, KS, 2003.
18. Sheikh-Ahmad, J., Sirdhar, G., Edge trimming of CFRP composites with diamond coated tools: edge wear and surface characteristics. SAE Technical Paper 2002–01–1526.
19. Ramulu, M., Faridnia, M., Garbini, J.L., Jorgensen, J.E., Machining of graphite/epoxy materials with polycrystalline diamond (PCD) tools, in Ramulu, M., Hashish, M. (eds), Machining Characteristics of Advanced Materials. ASME Publication, New York, NY, vol. 16, 1989, pp. 33–40.
20. Philbin, P., Gordon, S., Characteristics of the wear behavior of polycrystalline diamond (PCD) tools when machining wood-based composites. Journal of Materials Processing Technology 162–163 (2005) 665–672.
21. Taylor, F. W., On the Art of Cutting Metals, ASME Trans., 28, 31–350, 1907.
22. Spur, G., Lachmund, U., in Jahanmir, S., Ramulu, M., Koshy, P. (eds.), Machining of Ceramics and Composites, Marcel Dekker, New York, 1999, pp. 209–248.
23. Wang, D.H., Wern, C.W., Ramulu, M., Rogers, E., Cutting edge wear of tungsten carbide tool in continuous and interrupted cutting of polymer composites. Materials and Manufacturing Processes 10, 493–508, 1995.
24. Wang, D.H., Ramulu, M., Arola, D., Orthogonal cutting mechanisms of graphite/epoxy composite. Part II: multi-directional laminate. International Journal of Machine Tools and Manufacture 35, 1639–1648, 1995.

Chapter 5
Conventional Machining of FRPs

This chapter provides a detailed survey of the machining characteristics of fiber-reinforced materials undergoing material removal by conventional or traditional processes. Because machinability is dependent on the type of machining process used, the chapter will review the machining characteristics of fiber-reinforced polymers (FRPs) separately for each one of the major conventional machining processes. These include turning, milling and routing, drilling, abrasive machining, and grinding. Tool wear, cutting forces, cutting temperatures, surface quality, and chip formation are all used to assess the machinability of FRPs and thus will be discussed here for each machining process whenever data is available. The effect of materials, composition, and architecture on machinability will also be delineated. Because of the critical influence of fiber orientation on the machining characteristics, a separate section is dedicated to define the convention for fiber orientation in each machining process. It is worthwhile reminding the reader about the context of machining in relation to FRPs. It has been noted earlier that machining FRPs tends to be generally a finishing process with light depths of cuts or material removal rates. This is because the parts are typically produced near net shape and any subsequent machining work required to the part is secondary. This does not of course preclude emerging applications of bulk machining of FRP components by milling or abrasive machining of cured close forms of the part.

5.1 Machinability of FRPs

The machinability of materials refers to the ease or difficulty with which these materials can be machined [1–3]. Machinability is not a material property like hardness, tensile strength, or ductility. It is rather an assessment of the material's response to a system of machining, which includes, in addition to the work material itself, the cutting tool, machine tool, machining operation, and cutting conditions. It is therefore not easy to obtain quantitative and consistent measures of machinability under the wide range of combinations and conditions available. But quantitative rankings

J.Y. Sheikh-Ahmad, *Machining of Polymer Composites*.
DOI: 10.1007/978-0-387-68619-6,

of different materials under standardized tests may be possible. Machinability has been mainly assessed by three parameters or criteria including tool wear or tool life, cutting forces or power consumption, and surface finish. Thus, good machinability means small amounts of tool wear, low cutting forces, and good surface finish. Machinability may also be assessed by the type of chips produced and the cutting temperatures. There is often a correlation between the type of chip produced and surface finish. The generation of a ribbon-like continuous chip is associated with steady-state cutting conditions and good surface finish, while discontinuous chips are often associated with brittle fracture and poor surface finish. The type of chip is also considered from the point of chip disposal and the effects on machine tool health. Powder-like chips are more difficult to collect and dispose of and pose a major risk to the operator, machine tool components, and controls. Some machining criteria are also related. The cutting temperatures influence tool wear and machined surface conditions. The cutting forces and power consumption influence cutting temperatures because most of the power spent in machining is converted to heat. On the other hand, cutting temperatures, cutting forces, and surface finish are directly or indirectly related to tool wear. Therefore, tool life tests are most commonly used to assess machinability.

FRPs have their unique characteristics that affect their machinability in different ways than metals. The properties of FRP materials are primarily determined by the physical properties of the fiber and the matrix, fiber volume fraction, and fiber orientation or architecture. Tool wear is greatly influenced by the type and volume fraction of the fibers. Glass and carbon fibers break in a brittle manner under critical bending stresses and produce abrasive debris that could be smaller in size than the fiber diameter. This debris cause accelerated wear by abrasion of the cutting edge. The strength of the fibers is also high, and depending on fiber orientation, the cutting forces produced by machining can be instantaneously high. The fiber orientation and type of fibers also control the chip formation mechanism and thus the appearance of the machined surface as previously discussed in Chap. 3. Aramid fibers evade shearing fracture under high deformation bending loads and tear under tensile loading. The binder matrix on the other hand is much weaker than the fibers and its contribution to the cutting forces is insignificant. Low interlaminate strength permits damage during machining, i.e., delamination and chip-off of boundary layers. The matrix does, however, affect the type of chip produced. Thermosetting matrix is brittle and machines by fracture, while thermoplastic materials have the capability to withstand large elastic and plastic strains. The chip produced in case of machining fiber-reinforced thermoplastics tends to be continuous. Different thermal properties of the fibers and matrix also affect machinability. The high thermal conductivity of carbon and graphite fibers assists in conducting the heat generated away from the cutting zone into the workpiece. This may help reducing tool wear, but is also responsible for enlarging the heat affected zone. On the other hand, the low thermal conductivity of glass and aramid fibers result in the cutting tool conducting most of the heat away from the cutting zone. This results in higher cutting tool temperatures and higher wear rates. Different thermal expansion coefficients of matrix and fibers lead to residual stresses after curing, which may be released during machining resulting in deformation and part damage.

5.2 Turning of FRPs

A number of axisymmetric FRP composite parts are finish machined by turning. These include axles, columns, bearings, rolls, drag links, and steering columns. Advances in the filament winding technology have facilitated the increased use of these parts in construction, industrial and transportation applications. In addition, axisymmetric parts are also turned from prismatic bars made by tape or ply layup. Consequently, turning has become an important process for finish machining of high accuracy parts and highly precise joint areas. Therefore, proper understanding of the behavior of composite components in turning is necessary for its successful implementation. The machinability of composites in turning is studied in terms of tool wear, cutting forces, cutting temperatures, and surface quality. Fiber type, orientation, and volume fraction are the most significant material properties that influence machinability.

5.2.1 Fiber Orientation in Turning

It has been shown earlier (Sect. 3.3.1) that the relative angle between the fiber direction and the cutting speed vector, defined as the fiber orientation angle, has a major influence on the chip formation mode, the cutting forces, and the resulting surface quality. In the turning process, the cutting speed vector of the cutting edge relative to the workpiece is always tangent to the cutting circle in a plane perpendicular to the axis of rotation as shown in Fig. 5.1. Thus, the fiber orientation angle in turning depends on the fiber placement method used for producing the composite cylindrical part. For parts produced by ply or tape layup (Fig. 5.1a) the fibers are laid in parallel planes that are also parallel to the axis of rotation. The end of each ply forms a chord whose length depends on the distance of the ply plane from the axis of rotation. For

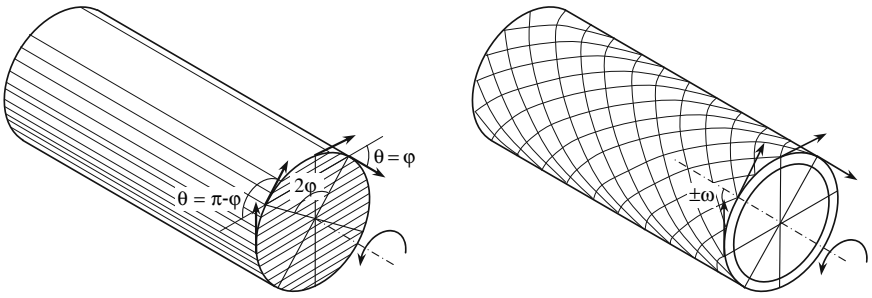

Fig. 5.1 Fiber orientation angle in turning (**a**) part made by layup of unidirectional or bidirectional laminates and (**b**) filament wound pipe

fibers in this plane that run in the transverse direction, the fiber orientation is equal to half of the chord angle (or its supplementary, depending on which end of the chord is considered),

$$\theta = \begin{cases} \varphi & \text{Left end of chord} \\ \pi - \varphi & \text{Right end of chord} \end{cases}, \tag{5.1}$$

where φ is half of the chord angle. For fibers running in the longitudinal direction, the fiber orientation angle is always 90° regardless of circumferential position. In a helically filament wound tube, as shown schematically in Fig. 5.1b, the fibers are laid along a geodesic path that makes an angle ω with the axial direction. For a cylindrical tube, the winding angle is the same at any point along the helical geodesic path. Therefore, regardless of circumferential position along the cutting circle, the fiber orientation angle for a helically wound cylindrical tube is equal to the complementary to the winding angle,

$$\theta = 90^\circ - \omega. \tag{5.2}$$

Other, but less common layup patterns are also used in filament winding. These include polar winding and hoop winding. Polar winding places the fibers in a direction almost parallel to the axis of rotation. In a way the wound part will be similar to that in Fig. 5.1a, except for the cylinder ends, which most likely are dome shaped and the fibers are laid on it in a diagonal direction. In hoop, or circumferential winding, the helix angle is almost 90°. Axially symmetric FRP tubes are also fabricated by wrapping a fabric weave around a mandrel. In this case, the resulting part topography will be similar to that of a filament wound tube.

5.2.2 Tool Wear in Turning of FRPs

Tool materials and the tool wear phenomena have been presented in great detail in Chap. 4. Therefore, the reader is advised to review that chapter before reading this section. The discussion that follows is mainly concerned with the wear behavior and tool life of different tool materials in turning of glass- and carbon-fiber-reinforced polymers.

The tool materials suitable for turning FRP's are those which possess high hardness and good thermal conductivity. Hardness is required for resisting abrasion, and thermal conductivity is required for dissipating heat – which is particularly important when machining low thermal conductivity FRPs such as aramid and glass FRPs. The most common tool materials used are cemented carbides, cubic boron nitride (CBN), and polycrystalline diamond (PCD). Diamond-coated carbides are promising class of materials with many desirable properties. As the diamond-coating technology advances, and the problems with film adhesion and edge strength are resolved, this class of materials would provide an economically viable substitute for

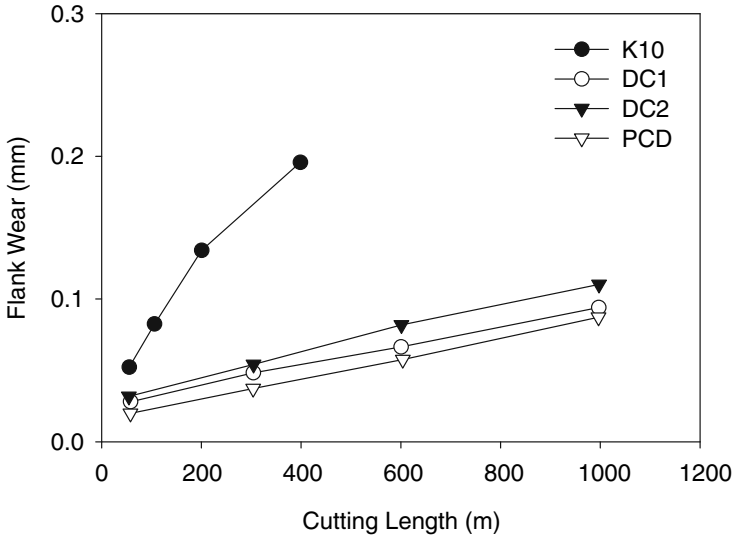

Fig. 5.2 Progression of flank wear of different tool materials in turning CFRP under wet cutting conditions. Cutting speed 100 m/min, feed rate $= 0.1$ mm/rev, depth of cut $= 0.5$ mm, tool geometry -5, -6, 5, 6, 15, 15, 0.8 [4]

PCD tools. Figure 5.2 shows the cutting performance of various tool materials in turning of CFRP pipe (52 vol% carbon fiber). The cutting tool materials included a standard uncoated carbide grade K10 (WC-6%Co), diamond-coated silicon nitrides, DC1 with 20-μm film thickness and DC2 with 10-μm film thickness, and a PCD tool with 5-μm diamond grain size and cobalt as the binder. The figure shows that the wear rate of the bare-cemented carbide tool is considerably higher than that of the diamond-coated silicon nitrides and the PCD tool. The wear rates of DC1 and DC2 are comparable to that of the sintered diamond. Selecting a tool life criterion of flank wear VB $= 0.1$ mm, the tool life for the PCD tool is found to be more than eight times the tool life for the K10 carbide (11.6:1.4 min). The tool lives for the DC1 and DC2 are found to be comparable, 10.8 and 8.6 min, respectively. The higher tool life for the diamond-coated tool DC1 is attributed to the thicker diamond film. The diamond grains on the diamond-coated tool were smoothed by abrasion, but the cutting edge remained relatively sharp. The thinner diamond film on DC2 abraded faster than the thicker film on DC1 and exposed the substrate to abrasion wear. The sintered diamond tool wore by the breaking away of diamond particles from the cutting edge. It is noted here that the use of silicon nitride as substrate material and the added strength to the cutting edge by incorporating a chamfer $(0.1\,\text{mm} \times 30^\circ)$ and negative rake angles all contributed to a better quality diamond film that was capable of withstanding the cutting conditions [4].

It has been previously stated that the dominant wear mechanism in machining FRPs is abrasion. Other possible wear mechanisms include chipping, adhesion, and tribooxidation. The wear mechanisms are primarily determined by the physical and

the mechanical characteristics of different fiber–matrix systems. For example, glass, carbon, and boron fibers are all extremely abrasive and cause severe abrasive wear. Aramid fibers, on the other hand, are tough and able to evade the cutting action by bending. They inflict damage on the cutting tool because of their low heat conductivity and their ductile characteristics. Abrasive wear manifests itself in the form of rounding of the cutting edge. A relatively flat and irregular flank wear land, and to a lesser extent a curved rake wear land are developed on the two primary faces forming the cutting edge (refer to Fig. 4.7 for illustration) because of rubbing of the fibers on the flank and rake faces. The wear lands may also be marked with shallow grooves that run parallel to the cutting direction. This type of wear is most apparent when machining FRPs with cemented carbide tools. On the other hand, chipping of the cutting edge occurs mostly when machining with more brittle tool materials such as PCD and PCBN. Microchipping is the common form of wear when machining with PCD tools and is caused by the breaking away of individual diamond grains from the cutting edge. Adhesive wear is marked by the presence of carbonized or melted material deposits that settled on the tool surfaces.

Wear is also strongly dependent on the volume fraction of reinforcement fibers and the direction in which these fibers run into the workpiece. Generally, the higher the fiber content the greater the area of abrasive material in contact with the tool and the higher the wear rates. Also, fiber orientations that promote fiber spring back after cutting cause greater rubbing between the tool flank and the fibers and lead to greater flank wear. The tool life curves for several tool materials in machining glass-fiber- and carbon-fiber-reinforced polymers are shown in Figs. 5.3 and 5.4, respectively. The composition and form of the work materials used to generate the

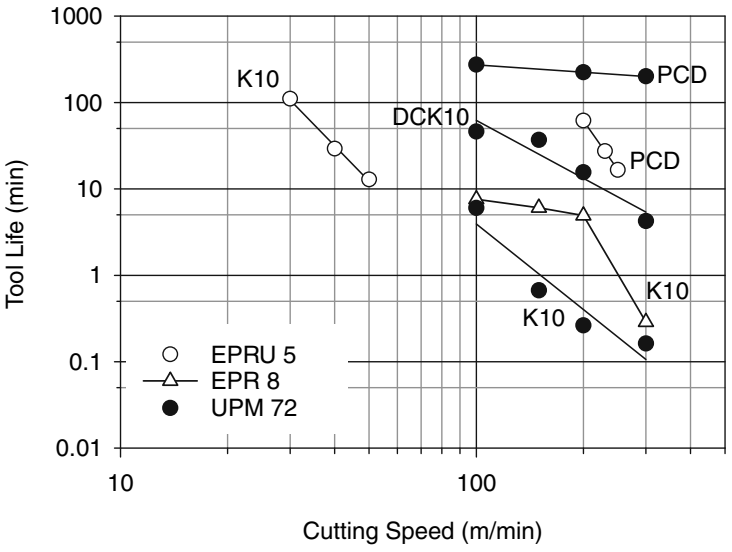

Fig. 5.3 Tool life for various tool materials in turning GFRP. Material composition and form are shown in Table 5.1. Taylor's tool life equation coefficients are shown in Table 5.2 [5]

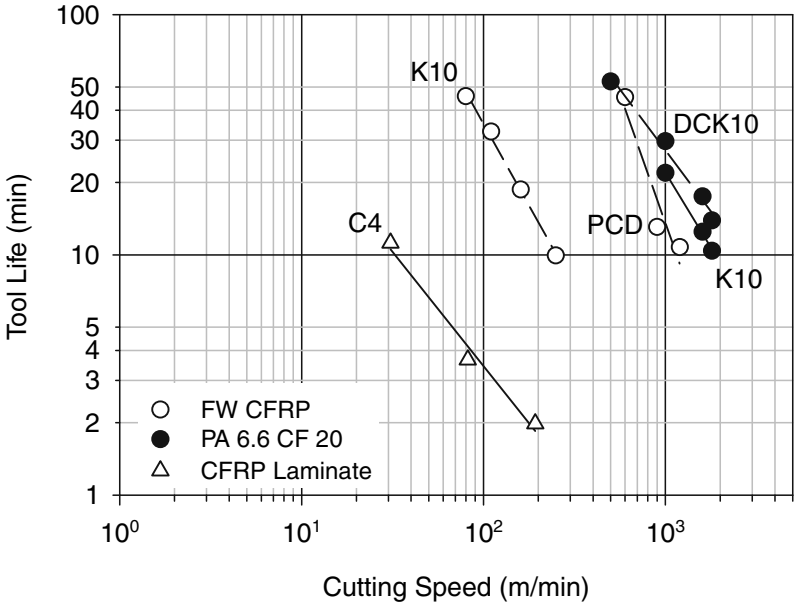

Fig. 5.4 Tool life for various tool materials in turning CFRP. Material composition and form are shown in Table 5.1. Taylor's tool life equation coefficients are shown in Table 5.2 [5, 6]

Table 5.1 Form and composition of FRPs used to generate data in Figs. 5.3 and 5.4 [5, 6]

Material	Matrix	Fiber	Fiber content (wt%)	Reinforcement form
EPRU 5	Epoxy	Glass	70	Unidirectional cloth
EPR 8	Epoxy	Glass	65	Bidirectional fabric
UPM 72	Polyester	Glass	50	Filament mat
FW CFRP	Epoxy	Carbon	40	Filament wound
PA 6.6-CF 20	Polyamide	Carbon	20	Short fiber
Carbon/epoxy [6]	Epoxy	Carbon	60	Laminate

data are shown in Table 5.1. The cutting conditions and constants C and n of Taylor's tool life equation (4.2) for the tool–material pairs are listed in Table 5.2. The constant C represents the cutting speed for a tool life of 1 min. Thus, larger values of C indicate better tool wear performance and better machinability at high cutting speeds. The constant n represents the negative reciprocal of the slope of the tool life curve. Smaller values of n correspond to steeper curves and greater dependence of tool life on cutting speed. Even though a straightforward comparison of the wear data in the figures is not possible because of the lack of common cutting conditions or material compositions, one can draw some general conclusions by comparing the constants C and n. It is apparent that tool wear in machining CFRP is less dependent on cutting speed than when machining GFRP, and thus higher cutting speeds are attainable when machining CFRP. This is attributed to the excellent thermal

Table 5.2 Taylor tool-life equation coefficients for different cutting tool–work material pairs shown in Figs. 5.3 and 5.4

Material	Tool	α (deg)	γ_o (deg)	d (mm)	f (mm)	n	C (m/min)
EPRU 5	K10	0	5	2.0	0.1	0.2364	90.5
EPRU 5	PCD	0	5	2.0	0.1	0.1704	403.4
EPR 8	DC K10[a]	5	6	1.0	0.1	0.3529	250.2
UPM 72	K10	5	6	1.0	0.1	0.3043	151.5
UPM 72	DC K10	5	6	1.0	0.1	0.4497	639.7
UPM 72	PCD	5	6	1.0	0.1	3.5545	–
Carbon/epoxy	K10	6	5	2.0	0.1	0.7358	1373.2
Carbon/epoxy	PCD[b]	0	5	2.0	0.1	0.4665	3377.8
PA 6.6-CF 20	K10	5	6	1.0	0.1	0.9868	26076.8
PA 6.6-CF 20	DC K10	5	6	1.0	0.1	0.7993	11839.6
Carbon/epoxy [6]	C4	−6	5	0.5	0.2	1.0535	368.0

Tool life criterion VB = 0.2 mm unless otherwise stated. α Rake angle, γ_o Clearance angle, d Depth of cut, and f Feed rate [5, 6]
[a]Diamond-coated carbide
[b]VB = 0.1 mm

conductivity of the carbon fibers and their ability to remove heat away from the cutting zone. This leads to lower cutting edge temperatures and lower wear rates. The same phenomenon is also present when machining GFRP with PCD tools and diamond-coated tools. The excellent thermal conductivity of diamond allows heat to be conducted away from the cutting zone through the cutting tool. The small slope and flatter profile in tool life with cutting speed is related to the low temperature developed during machining GFRP with diamond tools.

The influence of fiber content on tool wear is also evident in Figs. 5.3 and 5.4. For example, decreasing the glass fiber weight content from 70 (EPRU 5) to 50% (UPM 72) while machining with PCD tool at 200 m/min results in an increase in tool life from 27 to 223 min. Similarly, decreasing the carbon fiber weight content from 60% (CFRP filament wound tube) to 20% (PA 6.6 CF 20) while machining with K10 carbide at 1,000 m/min results in an increase in tool life from 2 to 20 min. The fiber orientation also critically influences tool wear, in similar ways it influences the chip formation process and cutting forces. Turning experiments on filament wound FRPs have shown that tool wear is minimum when machining unidirectional (polar winding) tubes, and increases with an increase in winding angle to a maximum then drops with further increase in winding angle [7–9]. For carbon-fiber-reinforced polymers, the maximum tool wear occurs at winding angle of 60°, while it occurs at 45° for glass-fiber-reinforced polymers [7]. The influence of fiber orientation (or winding angle) on tool life is shown in Fig. 5.5 for carbon fiber filament wound tubes. The Taylor tool life equation constants for this data are also listed in this figure [8]. It can be seen that tool wear is most sensitive to cutting speed when the winding angle is ±45°. As the winding angle decreases, tool life becomes less dependent on cutting speed. The value of the constant C also decreases with an increase in winding angle. Therefore, machinability of filament wound tubes also decreases with an increase in winding angle.

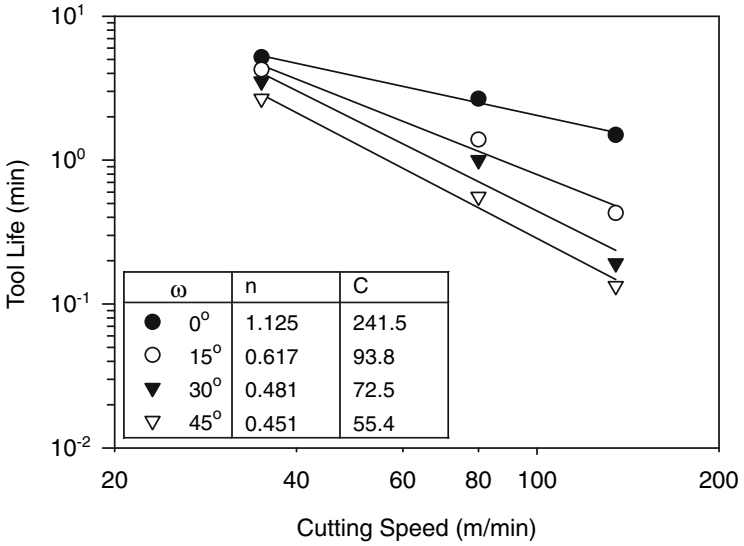

Fig. 5.5 Effect of winding angle on tool life when machining carbon FRP (fiber content 60 vol%) with K10 carbide tool. Side rake angle $= 6°$, VB $= 0.3$ mm [8]

Tool wear is also influenced by turning process parameters, namely cutting speed, feed rate, and depth of cut. Cutting speed has the most significant effect on tool wear, followed by feed rate and depth of cut. Tool wear was found to increase with an increase in cutting speed, an increase in feed rate [9, 10], and a decrease in depth of cut [9]. Figure 4.19 gives an example of the effects of cutting speed and feed rate on tool life for machining CFEP with PCD tool. The major effect of cutting speed on tool life is indicated by the steep slope of the function along the cutting speed axis. The interaction between the effects of speed and feed on tool life is also obvious at high cutting speeds.

5.2.3 Cutting Forces and Specific Cutting Energy

Cutting forces are oscillating and periodic in nature when machining FRPs. The oscillation originates from the repeated cutting tool encounter with the fibers and matrix phases, which produce drastically different magnitudes of cutting forces. The periodic nature of the cutting forces arise from the periodic changes of fiber orientation relative to the cutting speed vector as a result of the continuous turning of the workpiece. The cutting forces generally increase with increasing the feed rate and the depth of cut. The dependence of cutting forces on cutting speed is not uniform across all different types of FRPs. Figure 5.6 and 5.7 show that the cutting (principal) force decreases with an increase in cutting speed when machining GFRP and CFRP, respectively. Further experimental studies in [12] supported these results and showed that the cutting speed only slightly affects the cutting forces when machining GFRP with different tool materials and geometries. However, it

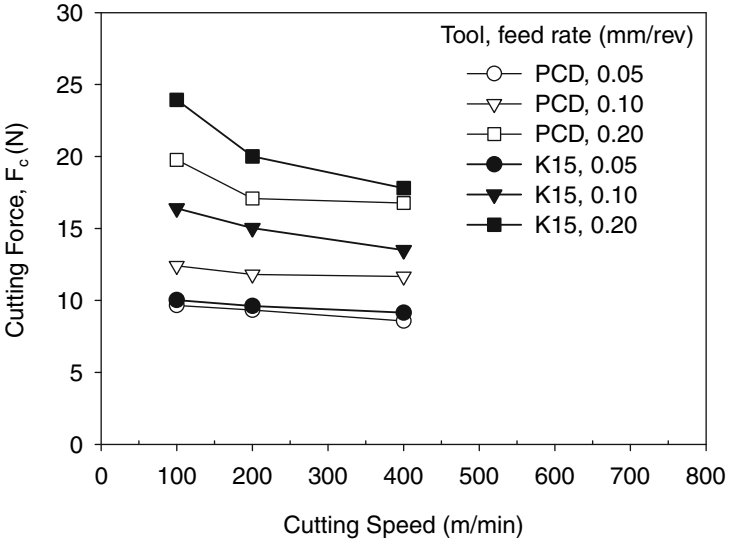

Fig. 5.6 Variation of the cutting (principal) force component with cutting speed and feed rate when machining GFRP manufactured by hand lay-up (unsaturated polyester with 65% glass fibers). Depth of cut = 0.5 mm, rake angle = 6°, clearance angle = 11°, dry cutting [11]

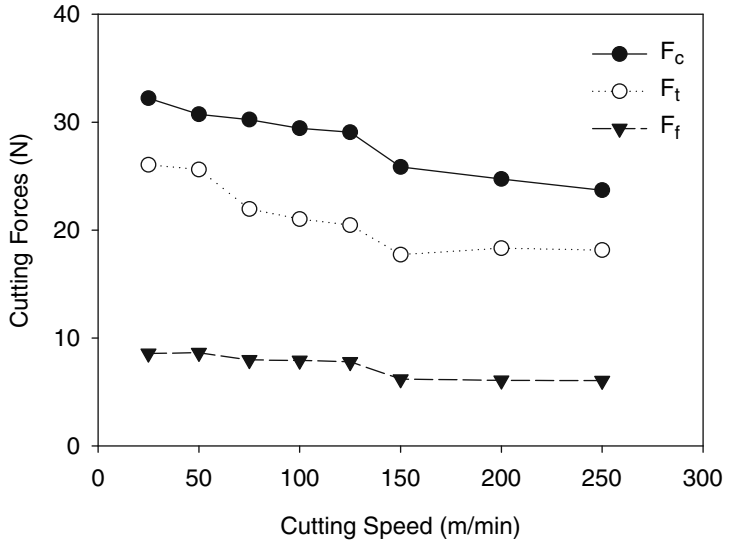

Fig. 5.7 Variation of cutting, feed, and thrust force with cutting speed when machining CFRP. Feed rate = 0.2 mm/rev, depth of cut = 0.5 mm, rake angle = −6°, clearance angle = 5° [6]

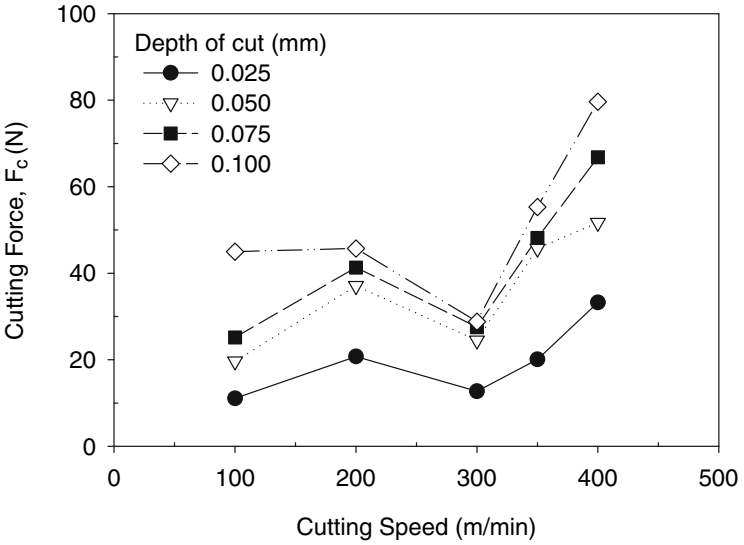

Fig. 5.8 Variation of the cutting force with cutting speed and feed rate when machining CFRP filament wound tube ($\omega = 0^\circ$) with PCD tool. Depth of cut = 1.0 mm, rake angle = 0°, clearance angle = 5°, dry cutting [13]

was shown in [5] that the cutting forces increase with an increase in cutting speed. The rate of change of the cutting forces with cutting speed is believed to be associated with the cutting temperatures. At low cutting speeds the cutting temperatures are not high enough to cause softening or melting of the polymer binder and dry friction predominates. At a critical speed, cutting temperatures lead to melting of the matrix material at the cutting zone and thus to reduction in cutting forces. Figure 5.8 shows that a critical speed is reached at which the cutting force becomes almost independent of cutting speed. Therefore, it was proposed that a cutting speed range from 200 to 300 m/min is the most suited for the machining of carbon/phenolic composites [13].

Figure 5.6 shows that the cutting forces for PCD are lower than those for K15 when machining GFRP, especially at large feed rates. This is attributed to the lower frictional resistance between PCD and GFRP and the better stability of the PCD cutting edge. Figure 5.9 shows that the cutting force is critically dependent on fiber orientation, as determined by the winding angle in filament wound tubes. The cutting force increases with increasing winding angle up to 15° and decreases with further increase in winding angle. The fiber orientation corresponding to the winding angle $\alpha = 15^\circ$ is $\theta = 75^\circ$ (see Sect. 5.2.1). Therefore, this behavior is consistent with the behavior of cutting force with fiber orientation as discussed in Sect. 3.3.2.1.

The specific cutting energy, or specific cutting pressure in turning is defined as the energy required to remove a unit volume of the work material,

$$K_c = \frac{F_c v}{Z_w} = \frac{F_c}{fd}, \tag{5.3}$$

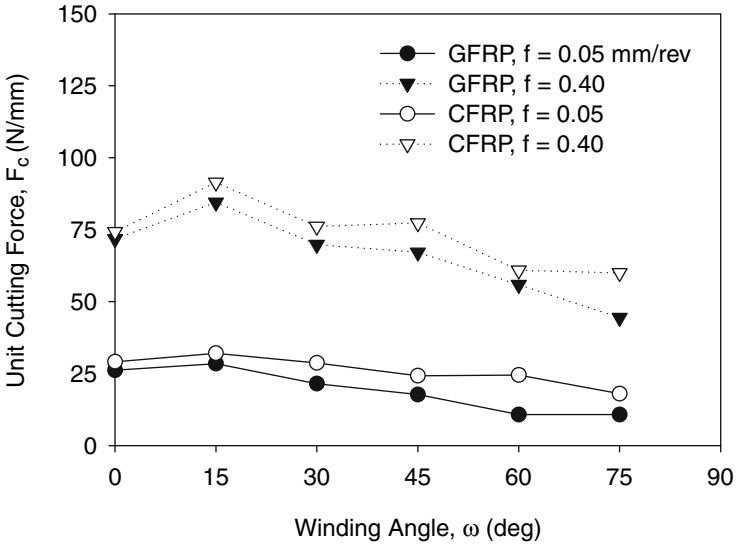

Fig. 5.9 Dependence of the unit cutting force F_c (per 1.0 mm depth of cut) on winding angle when machining glass and carbon FRPs. Cutting speed = 100 m/min, rake angle = 0°, clearance angle = 5° [5]

where Z_w is the material removal rate, f is the feed rate, and d is the depth of cut. The specific cutting energy for machining glass FRP is shown in Fig. 5.10 and for machining carbon/phenolic composites in Fig. 5.11. It is noted here that the specific cutting energy for both glass and carbon fiber composites is well below that of metals ($0.5–60\,kN/mm^2$). The specific cutting energy for PCD is lower than that for K15 carbide tool when machining GFRP. This is most significant at large feed rates. The behavior of specific cutting energy with cutting speed is similar to that of the cutting force. However, it varies considerably with feed rate and depth of cut. Significantly higher specific cutting energy is required for removing small chips (small feed rate and small depth of cut). For a high cutting speed and large chip size the specific cutting energy for a material tends to become constant. Thus, better machinability of FRPs can be obtained at high feed rates and at high cutting speeds. For some materials, such as carbon/phenolic composites, a critical cutting speed is observed at which the specific cutting energy decreases with further increase in cutting speed (Fig. 5.11) as discussed before.

5.2.4 Cutting Temperatures

The heat generated during the cutting process is dissipated through the cutting tool, chip, and workpiece according to the energy balance (5.4). Neglecting energy spent in breaking the fibers and making new surfaces, this heat is equivalent to the

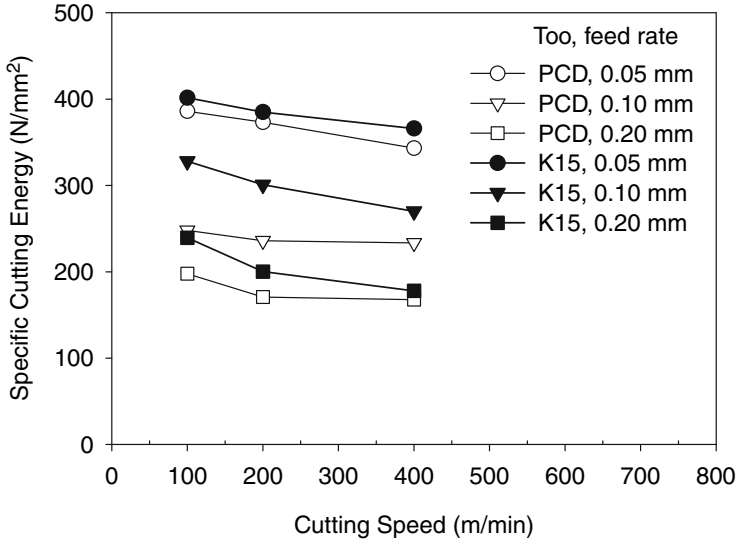

Fig. 5.10 Variation of the specific cutting energy with cutting speed and feed rate when machining GFRP. Cutting conditions are the same as in Fig. 5.6 [11]

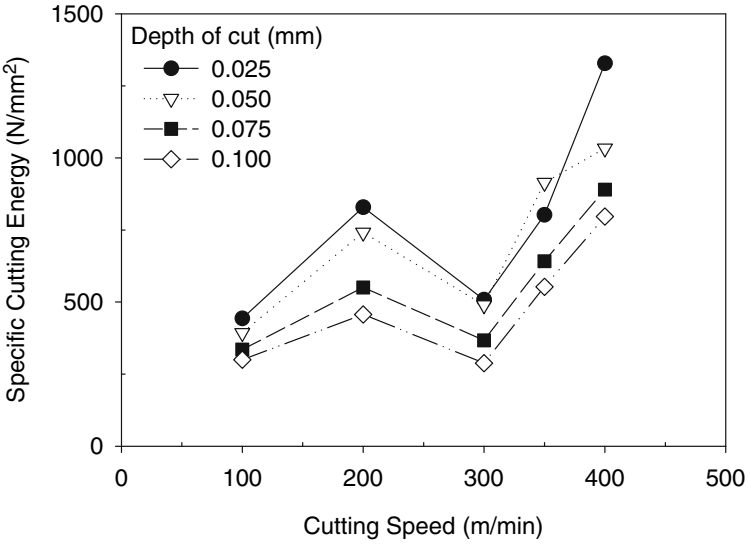

Fig. 5.11 Variation of the specific cutting energy with cutting speed and feed rate when machining CFRP. Cutting conditions are the same as in Fig. 5.9 [13]

machining power as determined by the product of the cutting speed and the cutting force F_c,

$$P_m = vF_c = Q_t + Q_c + Q_w. \tag{5.4}$$

Both rake and clearance faces are under friction when turning FRPs, hence the heat generated increases mainly with cutting speed as shown in Figs. 5.12 and 5.13.

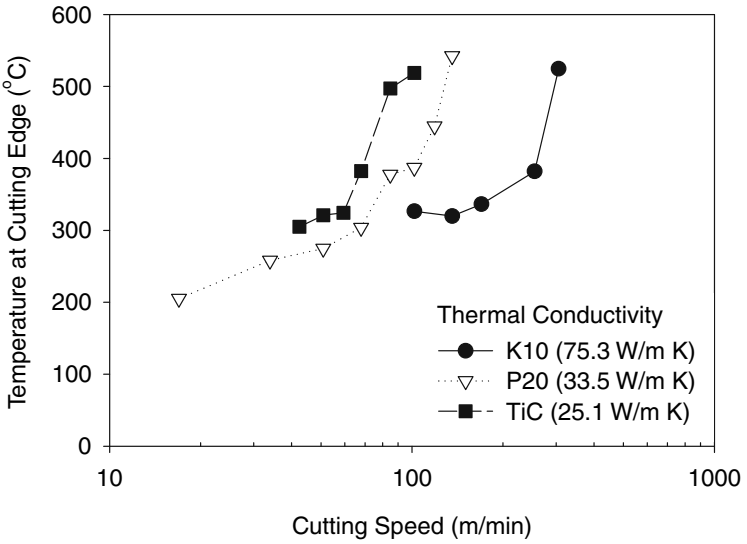

Fig. 5.12 Dependence of cutting edge temperature on cutting speed and tool material when machining GFRP. Depth of cut = 1.0 mm, feed rate = 0.1 mm/rev, rake angle = −5°, clearance angle = 5°, dry cutting [14]

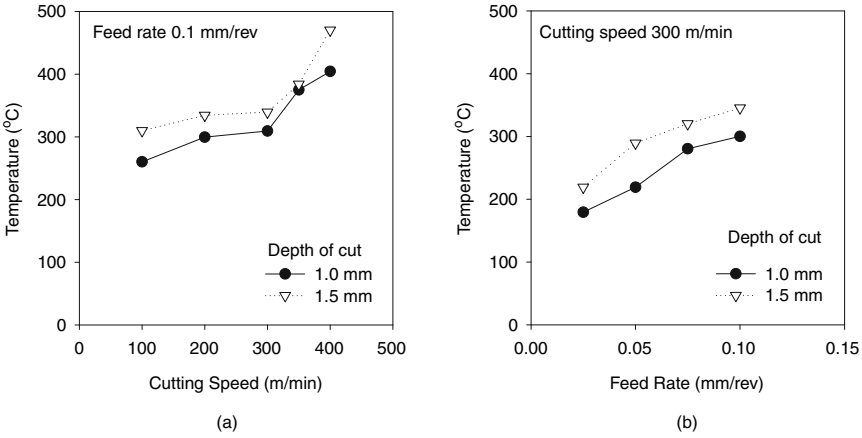

Fig. 5.13 Variation of cutting temperatures (**a**) with cutting speed and (**b**) with feed rate when machining carbon/phenolic composites. Cutting conditions are the same as in Fig. 5.11 [13]

Cutting temperatures are also affected by depth of cut, feed rate, tool and workpiece materials. Figure 5.13 shows that the cutting temperature is proportional to depth of cut and feed rate. The effect of speed, however, is the most pronounced. The share of heat absorbed by the chip, Q_c, increases with increasing material removal rate. At high material removal rates, the largest share of heat is absorbed by the chip. This behavior becomes more obvious with lower thermal conductivity of the tool and the workpiece. Hence, high material removal rates should be obtained by increasing feed rate rather than cutting speed. The portion of heat conducted into the workpiece is related to the thermophysical properties of the tool and work materials as well as the cutting parameters. Carbon fibers transfer more heat than glass fibers and thus the cutting tool temperature is lower for the composite carbon fiber due to its higher thermal conductivity. In the case of low material removal rates, the heat is absorbed equally by the chip and the tool. With increasing material removal rates, the chip transports much more heat from the active area, whereas at low material removal rates the portion of the heat conduction into the tool plays more significant role. The temperatures generated during machining may be high enough to cause melting or decomposition of the polymer matrix. The cutting temperatures at high cutting speeds may also be high enough to cause thermally activated tool wear [14]. The cutting tool temperature is generally lower for cutting tools with higher thermal conductivity as shown in Fig. 5.12. A transitional speed exists beyond which the rate of increase in cutting temperature with speed becomes very high [13, 14]. This transitional speed shifts toward higher cutting speeds with the increased thermal conductivity. This explains the excellent capability of PCD tools to perform well at high cutting speeds as discussed earlier. The machinability of FRPs is improved tremendously when machining at cutting speeds lower than the transitional speed. The transitional speed is 300 m/min for carbon/phenolic composites, 60 m/min for GFRP when cutting with TiC tool, but increases to 150 m/min when cutting with P20 carbide.

5.2.5 Machining Quality

Machined surface quality is often characterized by surface morphology or texture and surface integrity. Surface morphology is concerned with the geometrical features of the generated surface. It is a function of the tool geometry, kinematics of the machining process, and machine tool rigidity. Surface integrity describes the physical and chemical changes of the surface layer after machining. This includes fiber pullout, fiber breakage, delamination, matrix removal, and matrix melting or decomposition. Both surface morphology and integrity depend on process and workpiece characteristics such as cutting speed, feed rate, fiber type and content, fiber orientation, and matrix type and content. The reliability of machined components, especially of high strength applications, is critically dependent on the quality of the surfaces produced by machining. The condition of the surface layer of the machined edge may drastically affect the strength and the chemical resistance of the component [15]. It is necessary, therefore, to characterize and quantify the quality of the machined surface and the effect of process parameters on surface quality.

Surface roughness, which is often used to describe surface morphology, may be described by one of many average roughness height measures such as arithmetic average height, R_a, peak to valley height, R_t, peak to mean height, R_p, mean to valley height, R_v, or ten-point average height, R_z. However, it has been shown that these parameters reveal little about the true surface characteristics of the composite. Most often, these parameters are used in combination with visual inspection to reveal surface features such as matrix smearing, fiber pullout, and delamination. Furthermore, it is found that R_a and R_q are least sensitive to surface topography changes with fiber orientation while R_y and R_z are most sensitive when machining inhomogeneous materials such as FRPs. The differences between machined surfaces may also be better described by statitical parameters of the surface profile such as skewness and kurtosis [15].

Surface roughness is critically dependent on fiber orientation because of the significant effect of the latter on the chip formation mode, as explained in Sect. 3.1. Figure 5.14 shows the influence of fiber orientation on surface roughness when machining glass FRP cylinder made of unidirectional laminates in which the fibers are running perpendicular to the workpiece axis [16]. The surface morphology around the workpiece circumference depends on the fiber orientation angle (the angle between the cutting velocity vector and the fibers), which is directly related to the circumferential angle, φ as shown in Fig. 5.1a. At circumferential angle $\varphi = 0°$, the fibers are parallel to the cutting velocity vector and the fiber orientation angle

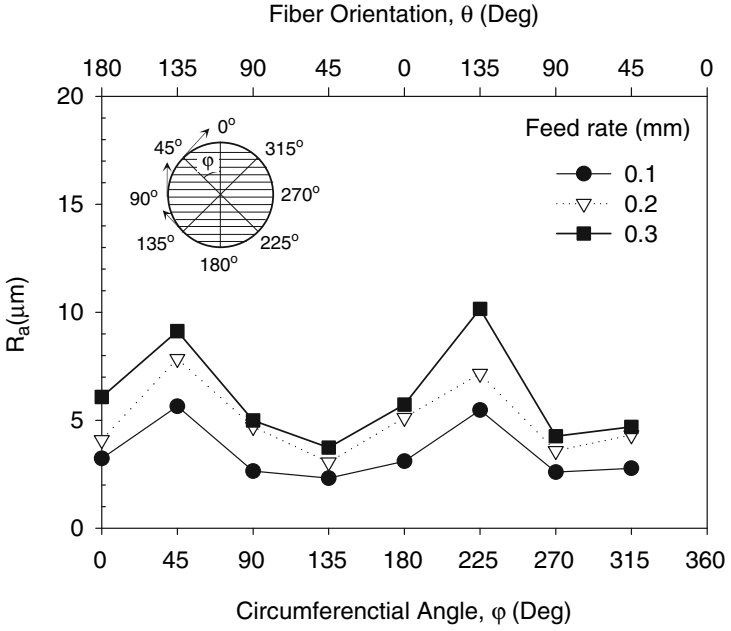

Fig. 5.14 Variation of surface roughness with circumferential position when machining laminate tube at different feed rates [16]

$\theta = 180^\circ$ (or 0°). As φ increases to π, the fiber orientation angle decreases according to the relation $\theta = \pi - \varphi$. Further increase in the circumferential angle, $\varphi > \pi$ leads to a decrease in fiber orientation angle according to the relation $\theta = 2\pi - \varphi$ as shown in Fig. 5.14. The figure shows that surface roughness approximately follows a sinusoidal shape with distinctive maxima at circumferential angles 45° and 225°, both corresponding to fiber orientation 135°. The surface roughness is lowest at circumferential angles 135° and 315°, both corresponding to fiber orientation 45°. This behavior in surface roughness is closely correlated to the chip formation mode as shown in Sect. 3.1. At fiber orientation 45° the fibers are subjected to slight bending and tensile loading which causes the fibers to break in tension and causes little subsurface delamination. At fiber orientation 135° the fibers are subjected to severe bending and compression loading, which causes the fibers to break in compression shear. Significant subsurface delamination and cracking in the fibers take place in this mode of chip formation. Surface roughness also increases with an increase in feed rate, but the effect of fiber orientation is magnified at higher feed rates.

Similar behavior of surface roughness is observed when machining filament wound tubes. Figure 5.15 shows the surface roughness for machining carbon and glass filament wound tubes using the same cutting tool geometry and at constant cutting speed [7]. The best surface quality is obtained when machining tubes with winding angle $\omega = 0^\circ$ (unidirectional or polar reinforcement). The surface roughness increases with an increase in winding angle. For carbon FRPs the maximum surface roughness is obtained at winding angle of 75°. The maximum surface roughness is obtained at about 60° for glass FRPs. Surface roughness is generally lower

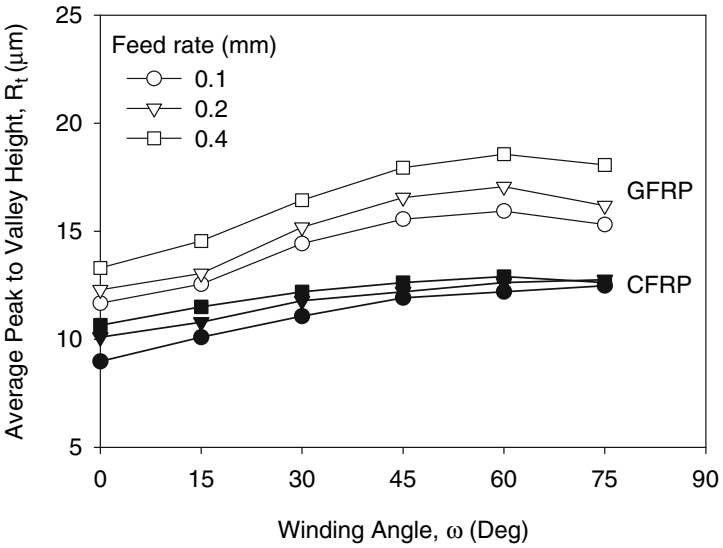

Fig. 5.15 Variation of surface roughness with winding angle when machining filament wound tubes. Fiber content 50%. Cutting speed = 100 m/min, depth of cut = 1.0 mm, rake angle = 0°, clearance angle = 5° [7]

for CFRP than GFRP due to the higher thermal conductivity of carbon fiber and the higher adhesive force between fiber and matrix. The surface roughness for both materials increases with the increase in feed rate. The effect of feed rate is greater for glass FRPs and at small winding angles. Surface roughness data from [8] also support the above-mentioned findings. Furthermore, it was shown that the effect of cutting speed on surface roughness is marginal as compared to the effect of feed rate and winding angle. In both the works, the increase in measured surface roughness with an increase in feed rate was lower than the theoretical increase predicted by kinematics calculations. This was attributed to the initially high surface roughness at low feed rates and the occurrence of localized damage such as pull out of individual fibers or fiber groups and poor surface quality in general. A parametric study of the surface roughness in machining fiber glass filament wound tubes found that feed rate is the most significant factor affecting surface roughness, followed by cutting speed, depth of cut, and winding angle. The interactions between feed rate and depth of cut were the most significant. Better surface roughness was obtained by lowering the cutting speed, the feed rate, and the depth of cut [17].

Typical damage to the machined surface includes matrix chipping and small pits (for brittle thermosets), fiber breakage, fiber pullout, fiber fuzziness (aramid fibers), cracks, delamination and smearing of the matrix material (for thermoplastics). Factors affecting surface damage include fiber orientation, feed rate, cutting speed, and fiber material. The influence of fiber orientation is obvious as it controls the chip formation mode and the ensuing delamination that may result. Matrix damage also increases with increasing fiber orientation. The cutting speed mainly affects the cutting temperatures, which in turn affect the matrix. Combustion of the thermoset matrix or melting of the thermoplastics may occur if localized temperatures exceed the decomposition or melting temperatures of the matrix. The higher thermal conductivity of the carbon fiber is a disadvantage because it increases the portion of heat conducted to the workpiece, and thus increases the thermal damage. Due to the magnitude of the cutting forces, the adhesion strength between fiber and matrix can be exceeded, so that fibers either peel (delamination) or are removed by the expansion of matrix parts. Transverse loading of the laminate, caused by excessive cutting forces, creates an expansion of the matrix, and to interlaminar cracks at the fiber–matrix interface. Tool wear and unsuitable cutting parameters cause thermomechanical damage that can lead to various damage phenomena [7].

5.3 Milling and Trimming of FRPs

Milling is one of the most frequently used material removal processes in manufacturing parts made of FRPs. However, unlike the milling of metals which is characterized by high material removal rates, milling of FRPs is conducted at much lower scale. The reason for this is that FRP components are largely made near net shape and any subsequent milling is limited mainly to deburring and trimming as well as to achieving contour shape accuracy. In milling, as opposed to turning, the

cutting tool is rotating and quite often more than one cutting edge are engaged in cutting at the same time. This adds complexity to the milling process in terms of fiber orientation, chip size, and cutting forces that continuously vary with tool rotation. The machinability of FRPs in milling is mainly characterized by tool wear, surface roughness, and delamination. Measurement of the cutting forces and temperatures are not easy because of the rotation of the tool and hence milling less utilized in studying machinability.

5.3.1 Fiber Orientation in Milling Unidirectional FRPs

Kinematics of the milling process has been discussed in Sect. 2.4, and is shown schematically in Fig. 5.16a, b for up milling and in Fig. 5.16c, d for down milling. The peculiar aspect of cutting with a rotating tool such as in milling, drilling, and abrasive cutting, as opposed to linear orthogonal machining is that the fiber orientation angle, θ, is not constant, but varies continuously with cutting edge position around the cutter axis. In milling and abrasive cutting the chip thickness also varies with cutting edge position. Consider for example Fig. 5.16a for up milling of a unidirectional laminate with fiber orientation $\psi < 90^\circ$. The cutting edge position is indicated by engagement angle ϕ, measured from the vertical line. The uncut chip thickness as given by (2.20) varies with $\sin\phi$ and thus has a maximum value at tool

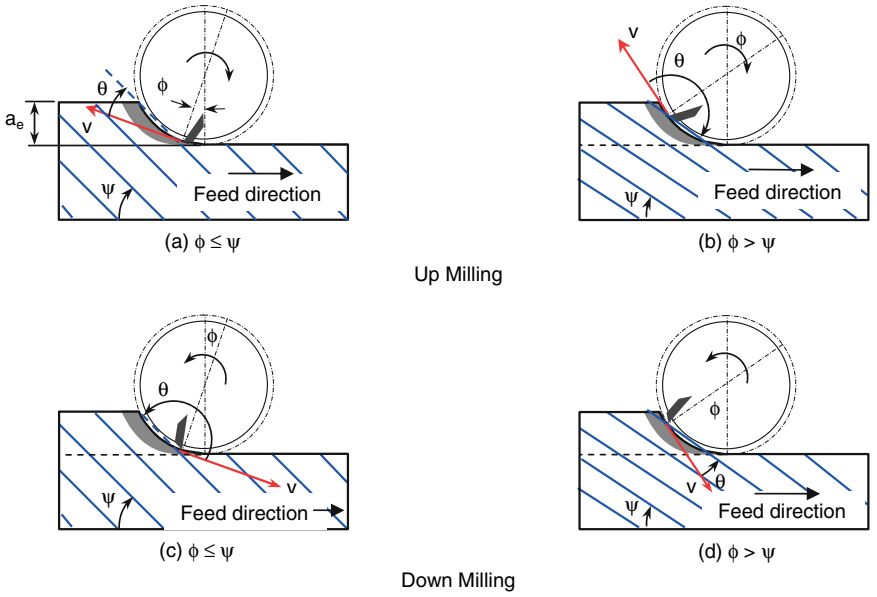

Fig. 5.16 Fiber orientation convention in milling of unidirectional laminates: (**a, b**) up milling and (**c, d**) down milling

exit from the cut. At the current cutting edge position, the fiber is subjected to tensile and bending stresses and the chip formation mode would be of Type III as shown in Fig. 3.8c. The fiber orientation angle, θ, is measured clockwise from the cutting velocity vector (see Fig. 3.7 for convention). Then for the case in Fig. 5.16a and for $\phi \leq \psi$ it can be shown that

$$\theta = \psi - \phi \quad \text{for} \quad \phi \leq \psi. \tag{5.5a}$$

As the engagement angle increases and becomes equal to the laminate orientation, $\phi = \psi$, the chip formation mode will change to Type I and the fiber orientation angle becomes equal to zero. With further increase in the engagement angle so that $\psi > \phi$ as shown in Fig. 5.16b, the fibers will be subjected to compression and bending and the chip formation mode will become of Type V as shown in Fig. 3.8f. The fiber orientation angle for this case is given by

$$\theta = \pi + (\psi - \phi) \quad \text{for} \quad \phi > \psi. \tag{5.5b}$$

Similarly, for down milling (Fig. 5.16c, d) it can be shown that:

$$\theta = \begin{cases} \pi + (\phi - \psi) & \phi \leq \psi \\ \phi - \psi & \phi > \psi \end{cases}. \tag{5.6}$$

Because of this continuous evolution of the fiber orientation angle and the associated chip formation modes, the characteristics of the instantaneous cutting forces (frequency and magnitude) will vary from one cutting edge position to another as shown in Figs. 3.15 and 5.16. The change in uncut chip thickness will also affect the magnitude of the cutting forces. The quality of the machined surface would depend on the fiber orientation at cutting edge entry for up milling and at cutting edge exit for down milling. Since $\phi = 0$ for both of these positions, the quality of the machined surface is a function of the angle ψ for up milling and the angle $(\pi - \psi)$ for down milling.

5.3.2 Tool Wear

Abrasion is the primary wear mechanism when milling and trimming FRPs. In addition, because of the interrupted nature of milling, tool microfracture and chipping are also prevalent, especially for cutting tools of insufficient toughness and mechanically weak cutting edges. Therefore, a great deal of resistance to abrasive wear and high fracture toughness are required in cutting tools for milling. Thermal conductivity is also an important property of the cutting tool because most of the heat generated in cutting has to be dissipated through the cutting tool. The tool materials that meet these two requirements are fine-grained cemented carbides, PCD, and diamond-coated carbides.

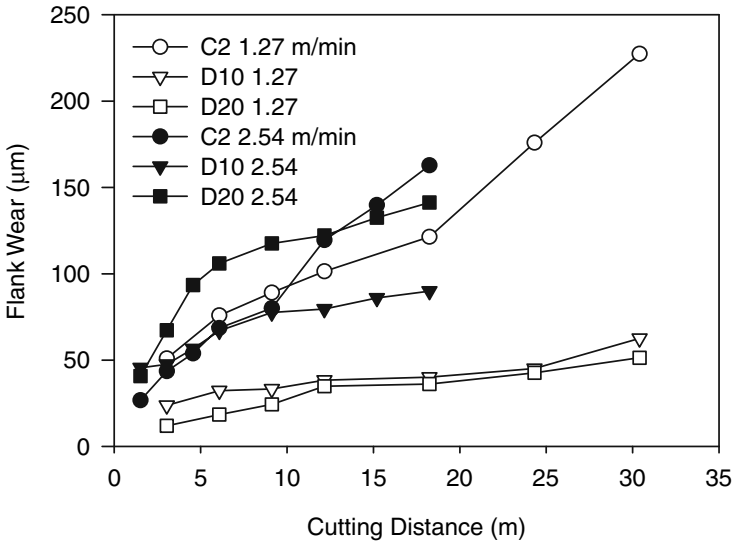

Fig. 5.17 Tool wear in climb milling of CFRP with four fluted C2 carbide end mill. Tool diameter = 7.9 mm, spindle speed = 2,500 rpm, radial depth of cut = 1.0 mm [18]. Reprinted with permission from SAE Paper # 2002-01-1526 © 2002 SAE International

Figure 5.17 shows the performance of diamond coated and uncoated tools in terms of flank wear in milling CFRP at two feed rates, 1.27 m/min and 2.54 m/min. The cutting tool is a general-purpose C2 carbide, four fluted end mill with 30° helix angle, 15° rake angle, and 65° cutting edge angle. The diamond coating was produced by hot filament CVD at two coating thicknesses, 10 μm (D10) and 20 μm (D20). Figure 5.18 shows the wear characteristics of the cutting edges of both uncoated and coated tools after a lineal cutting distance of 31 m. The amount of flank wear generally increases with increasing cutting distance and feed rate for all milling cutters. At the low feed rate, the uncoated tool exhibited significant amounts of flank wear as compared to the diamond-coated tools. After a cutting distance of 31 m, the flank wear on the C2 carbide is more than 4.5 times higher than that of the coated tool D20 and more than 3.5 higher than that of D10. This is indicative of the effectiveness of the diamond coating in combating the abrasive wear commonly associated with machining CFRP. The amount of flank wear for D10 was slightly higher than that for D20 because of the earlier attrition and removal of the diamond film for the thin coating. Rounding of the cutting edge because of abrasion is evident in Fig. 5.18. Severe rounding is seen on the clearance face of the uncoated tool (Fig. 5.18a). The diamond-coated tool D20 is worn by uniform abrasion of the diamond film (Fig. 5.18c) while the tool D10 is worn by gross delamination of the diamond film and rounding of the substrate (Fig. 5.18b). At the high feed rate, the coated tools exhibited high rates of wear at the beginning and then the wear progressed slowly. This is a result of severe chipping and delamination of the diamond film caused by impact at the early stages of cutting. After this premature failure, uniform wear by abrasion of both the diamond film and substrate

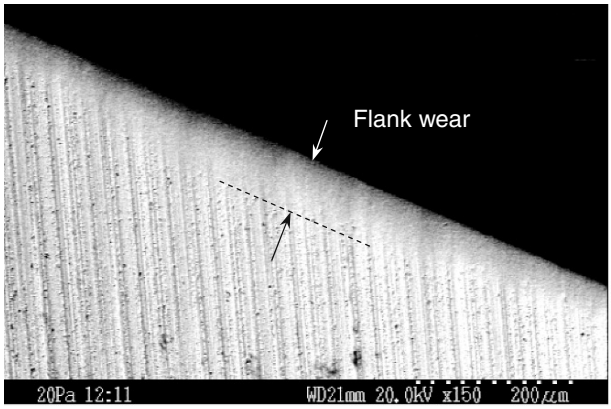

(a) Uncoated

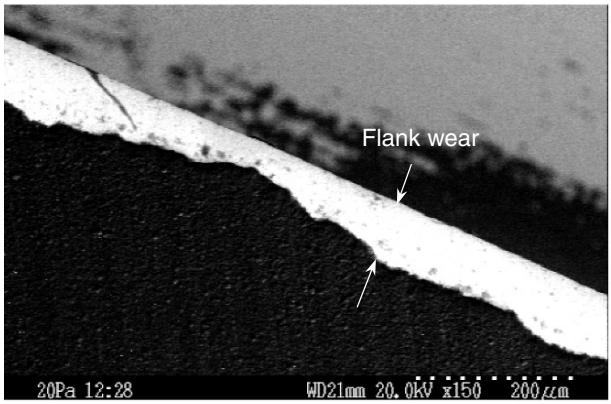

(b) Diamond coated D10

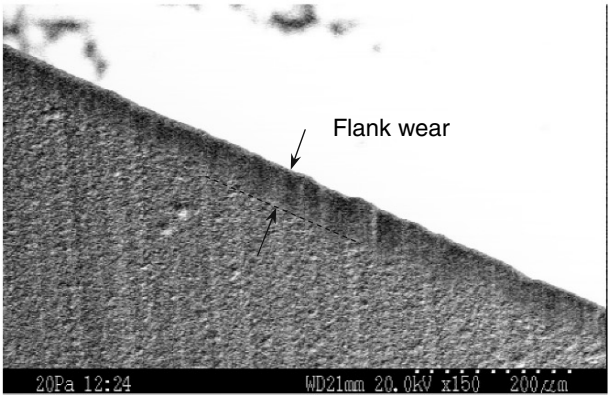

(c) Diamond coated D20

Fig. 5.18 SEM photomicrographs showing the clearance side of the worn cutting edge after machining 31 m of CFRP at 1.27 m/min. (**a**) uncoated, (**b**) D10, and (**c**) D20 [18]. Reprinted with permission from SAE Paper # 2002-01-1526 © 2002 SAE International

took place. The advantage of diamond coating at higher feed rate is not realized until later when the wear of uncoated tool progresses at high rate. The gain in wear resistance is only half of that exhibited for the low feed rate. It is evident from this figure that significant improvement to the machinability of CFRP can be attained by using diamond-coated tools at low feed rates. The low feed rate produces a smaller chip per tooth and thus lower cutting forces and less severe impact on the cutting edge. This results in prolonging the diamond film life by reducing its chipping and delamination.

Figure 5.19 shows the tool life of four flute TiN-coated carbide end mills in machining CFRP laminate panel [19]. The coefficients of Taylor tool life equation are also shown in the figure for a tool life criterion of $V_B = 0.1$ mm. It can be seen that both coefficients n and C decrease with an increase in feed rate. A smaller coefficient n indicates greater dependence of tool life on cutting speed and a smaller coefficient C indicates that lower cutting speeds can be used for obtaining a tool life of 1 min. These trends in the figure indicate that the highest tool life is obtained at low cutting speed and low feed rate. High-speed machinability in terms of tool wear

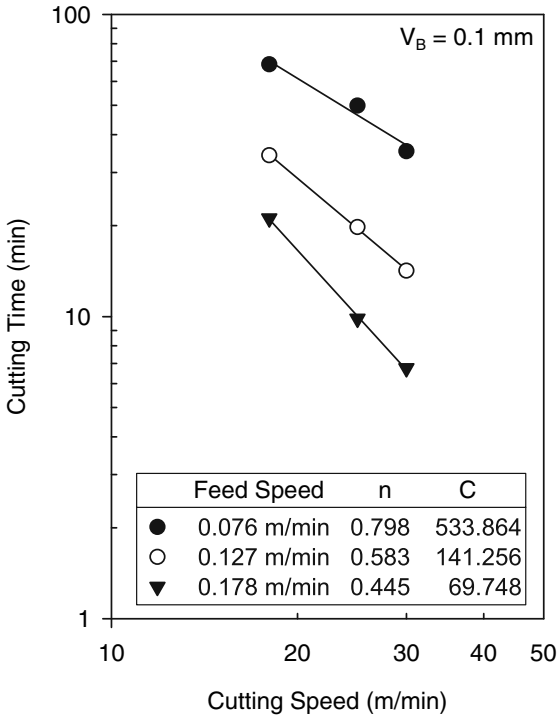

Fig. 5.19 Tool life in edge milling of CFRP using a TiN coated four-flute end mill. Workpiece material IM6/R6376 carbon fiber/epoxy with fiber volume fraction of 63%. Laminate layup $[90,\ (+45/-45)_3,\ (-35/+45)_3,\ 90]_s$. Cutting configuration is up-milling. Tool diameter = 11.11 mm, helix angle = 30°, radial depth of cut = 1 mm, axial depth of cut = 4 mm [19]

can be improved by reducing the feed rate. As the feed rate increases, its effect on tool life becomes more prominent. Keeping in mind that the tool-life criterion used in this figure is lower than normal, higher tool life can be obtained for a tool-life criterion of $V_B = 0.2\,\text{mm}$.

Burr tools such as diamond interlocked solid carbide burr are often used to improve machinability, especially at conditions of high spindle speeds and feed rates common in CNC routing [20]. This tool is comprised of intersecting up and down helix, which generate many diamond-shaped cutting points (see Fig. 5.40e) that shear the fiber in the composites while providing pulling action at the same time. The tool has an uneven count of spirals, up vs. down, to make the points overlap so that they do not make grooves on the machined edge. Two types of wear are observed when burr router bits are used in trimming. These are fracture of the tips of the pyramid tooth and the usual flank wear as shown in Fig. 5.20. The number of teeth that fracture during the trimming operation of CFRP panels is shown in Fig. 5.21 and is influenced by the feed rate and cutting speed, or more precisely the chip thickness. Because of the many teeth engaged in the cut at the same time, the chip geometry is not well defined and an equivalent chip thickness, similar to that defined in abrasive machining, is used instead. The equivalent chip thickness is defined as the product of the radial depth of cut and the ratio of the feed rate to the linear cutting speed,

$$h_q = a_e \left(\frac{v_f}{v} \right). \tag{5.7}$$

It is shown that except for the chip thickness of 0.163 mm, the average number of teeth fractured generally increases with an increase in equivalent chip thickness, which corresponds to an increase in feed rate, a decrease in cutting speed, or both. This may be directly related to the increase in forces required to remove the larger chip thickness. It is also noted that the number of teeth fractured does not change significantly with the increase in cutting distance. This may be accounted for by the

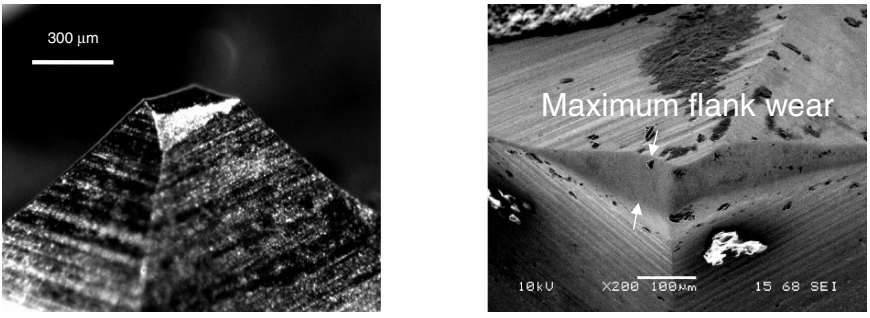

(a) (b)

Fig. 5.20 (**a**) View of fractured tooth from clearance face. (**b**) The presence of nonuniform flank wear as viewed under a scanning electron microscope. The flank wear land, as viewed in a direction normal to the pyramid base, varies with distance from the tip of the tooth (maximum at the tip and minimum at the root of the tooth) [20]. Reprinted with permission from SAE Paper # 2006-01-3173

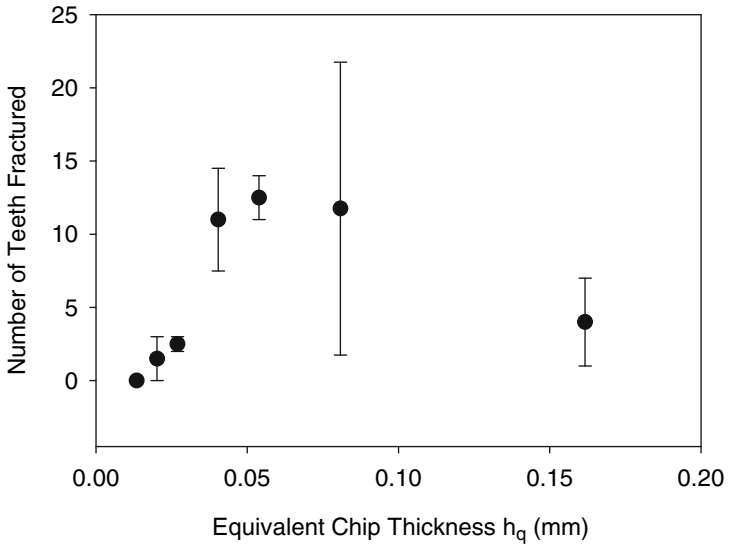

Fig. 5.21 Variation of the number of teeth fractured with equivalent chip thickness during trim routing of CFRP laminate panel under up-milling configuration. Spindle speed range: 5,000–15,000 rpm, feed rate range: 2.54–10.16 m/min, radial depth of cut = 1.6 mm (25% of tool diameter), cutting distance = 26 m [20]. Reprinted with permission from SAE Paper # 2006-01-3173 © 2006 SAE International

fact that the cutting tool became fairly stable once the fragile teeth were fractured at the very beginning of tool engagement. Figure 5.22 shows the relationship between maximum flank wear and equivalent chip thickness after a total cutting distance of 26 m. From the figure it is seen that flank wear decreases with an increase in equivalent chip thickness (i.e., an increase in feed rate, a decrease in cutting speed, or both). The great scatter in the flank wear data is due to the uncertainty in the measurements of flank wear because of the presence of fracture and self-sharpening. Nevertheless, the results in Figs. 5.21 and 5.22 indicate that significant improvements in machinability in terms of tool wear can be achieved by decreasing the equivalent chip thickness.

5.3.3 Cutting Forces and Specific Cutting Energy

The cutting forces in milling and trimming are critically dependent on fiber orientation and uncut chip thickness, both of which are functions of the cutting engagement angle as shown in Fig. 5.16. As the relative angle between the fibers and the direction of cutting changes continuously during cutting, the cutting edge is subjected to cyclic forces as demonstrated by the figures below. Figure 5.23 shows the cutting forces for edge trimming of CFRP laminate orientations 45, 90, and 135° with a single straight cutting edge (orthogonal cutting) under up-milling configuration. The cutting forces acting on the workpiece are typically measured by a tool force

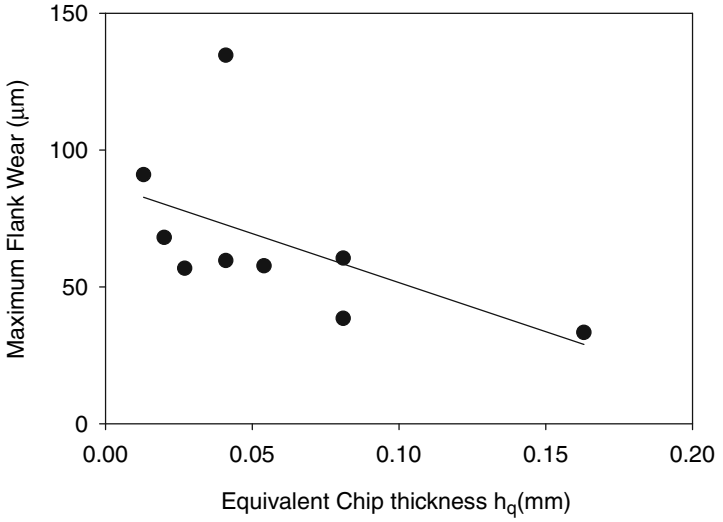

Fig. 5.22 Variation of maximum flank wear with equivalent chip thickness during trim routing of CFRP laminate panel under up-milling configuration. Same conditions as Fig. 5.21 [20]. Reprinted with permission from SAE Paper # 2006-01-3173 © 2006 SAE International

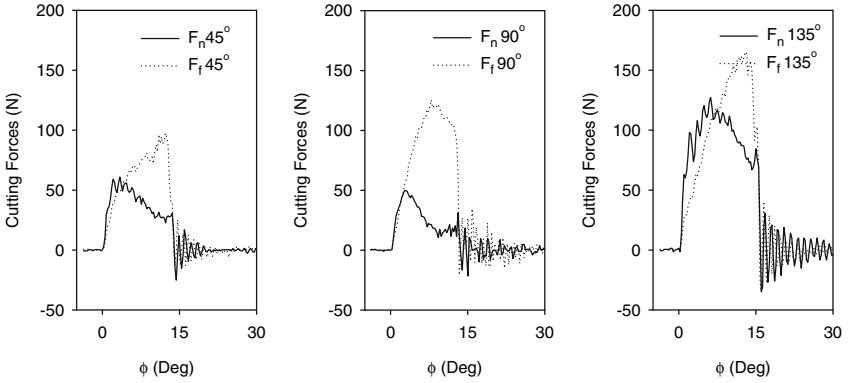

Fig. 5.23 Cutting forces in up-milling of unidirectional CFRP laminates (IM6/Epoxy, $V_f = 0.62$). Cutting tool diameter = 19 mm, rake angle = 15°, clearance angle = 20°, spindle speed = 500 rpm, feed rate = 152 mm/min, radial depth of cut = 1 mm, axial depth of cut = 2.8 mm

dynamometer in the feed direction, F_f, and normal to the feed direction, F_n, as shown. Both forces vary with cutting edge position depending on chip thickness and fiber orientation. The magnitude of the maximum force and degree of oscillation clearly varies with laminate orientation. The highest cutting forces and greatest amplitude of oscillation are produced for laminate orientation 135° because of the severe bending of the fibers before cutting by compression shear. The lowest cutting forces are produced for laminate orientation 45° while the smallest amplitude of oscillation is produced for laminate orientation 90°.

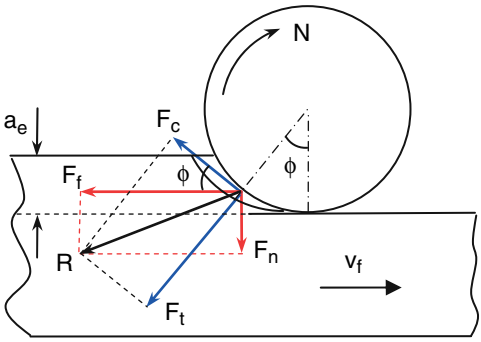

Fig. 5.24 Cutting forces in up-milling configuration

To better understand the relationship between the cutting forces and the cutting edge position, it is required that the forces are resolved in the tangential and radial directions (representing the principal, F_c, and thrust, F_t, forces). Figure 5.24 shows a schematic of the up-milling operation and the transformation coordinates used for force resolution. The feed and normal forces may be related to the principal (cutting) and thrust (radial) forces by the transformation equations

$$\begin{aligned} F_f &= F_c \cos\phi + F_t \sin\phi \\ F_n &= -F_c \sin\phi + F_t \cos\phi \end{aligned} \tag{5.8}$$

and

$$\begin{aligned} F_c &= F_f \cos\phi - F_n \sin\phi \\ F_t &= F_f \sin\phi + F_n \cos\phi. \end{aligned} \tag{5.9}$$

Figure 5.25 shows the transformed cutting and thrust forces for the same setting in Fig. 5.23. For the purpose of clarity, an additional axis showing the instantaneous fiber orientation is added on the top of the figure. It is noted here that both the engagement angle, ϕ, and the chip thickness, a_c, are equal to zero at the beginning of the tool engagement. Hence the cutting forces are zero. In addition, the fiber orientation angle at the beginning of tool engagement is equal to the laminate orientation. As the tool engagement angle increases, the chip thickness also increases, leading to an increase in the cutting forces. For a homogeneous material, the variation of the cutting forces would follow a sinusoidal function, as indicated by (5.2). For unidirectional composites, however, the fiber orientation changes with engagement angle and the cutting forces would change accordingly. Hence, the variation of cutting forces in Fig. 5.25 is a result of two factors, the increase in chip thickness and the change in fiber orientation angle. The effect of fiber orientation on cutting forces has been explained in Sect. 3.3.2.1. The combined and simultaneous effects of chip thickness and fiber orientation angle on the cutting and thrust forces may explain the deviation of the force signals in Fig. 5.25 from the usual sinusoidal wave shape.

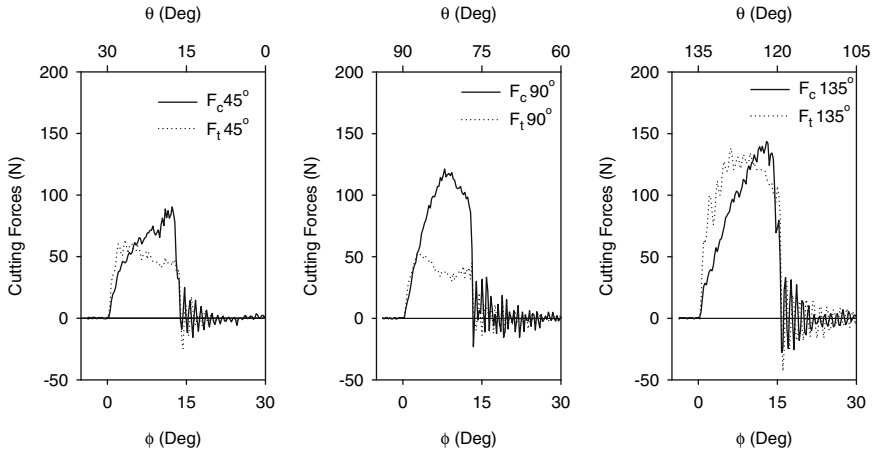

Fig. 5.25 Cutting and thrust forces in cutting unidirectional CFRP laminates. Same conditions as Fig. 5.23

5.3.3.1 Effect of Process Parameters

Tool wear results in changing the cutting edge geometry and thus affects the cutting forces. Therefore, the cutting forces in milling of FRPs are expected to vary with cutting process parameters, such as cutting speed, feed rate, depth of cut, and cutting edge geometry. Figure 5.26 shows the variation of feed force and normal force with cutting speed and feed rate in edge milling of laminate CFRP panel with four flute helical end mill [19]. Both force components decrease with an increase in cutting speed and a decrease in feed rate. Similar behavior of the cutting forces to that shown in Fig. 5.26 has also been reported in [21] for machining unidirectional GFRP with a 5 mm, two-flute helical end mill and in [22] for end milling of carbon short fiber-reinforced PEEK. Geometrically, the chip per tooth, a_f, as described by (2.14) decreases with an increase in spindle speed and a decrease in feed rate. Thus, the behavior of the cutting forces with process parameters can be explained in relation to the thickness of the uncut chip. The relationship between the cutting forces and the process parameters is also determined by regression analysis as in (5.10). It is indicated by this equation that the cutting speed affects only the feed force, but has no significant effect of the normal force. On the other hand, the feed rate has a profound effect on the normal force, but has no effect on the feed force. The cutting speed effect on the normal force and the feed rate effect on the feed force are shown only in terms of the interaction between the two process parameters.

$$\begin{aligned} F_f &= 23.1639 - 0.5460v + 1.2909vv_f, \\ F_n &= 10.1065 + 217.4841v_f - 5.7114vv_f. \end{aligned} \tag{5.10}$$

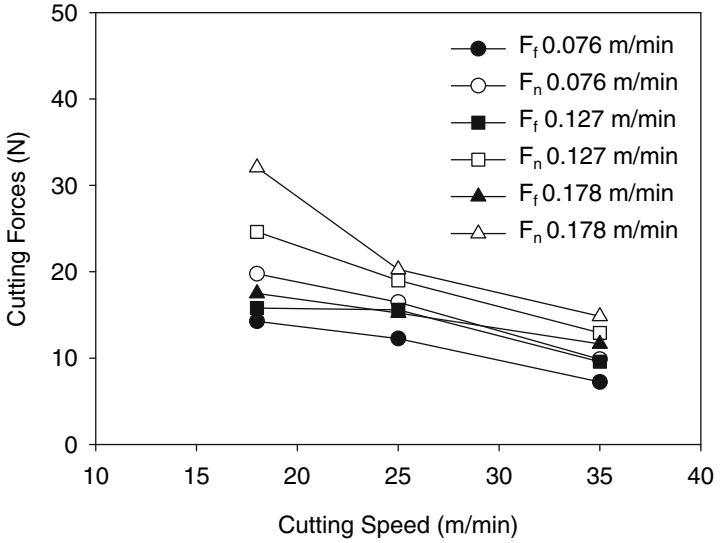

Fig. 5.26 Variation of feed force, F_f, and normal force, F_n, with cutting speed and feed rate in edge milling CFRP laminate. Same conditions as Fig. 5.19 [19]

In addition to the feed and normal forces, a helical end mill will also produce an axial force component perpendicular to the plane of the two other forces. The axial force is only a fraction of the feed force and its magnitude and direction depend primarily on the helix angle. Its response to changes in process parameters is similar to that of the feed and normal forces.

The slight influence of cutting speed on the feed force suggests that an advantage may be gained in terms of productivity and surface finish improvement by utilizing high-speed machining at no cost of increasing the cutting forces. This idea has been investigated by [23] and the results are shown in Fig. 5.27 for a glass-fiber-reinforced laminate that was machined with a PCD tool. It is seen that at a low and moderate feed per tooth, only slight increases in the normal force occur over a cutting speed range from 1,200 to 2,400 m/min. However, significant rise in the feed force occurs over a speed range from 800 to 2,400 m/min. The feed force rise is higher for the higher feed per tooth. This increase in the feed force leads to significant increases in cutting temperatures and undesirable thermal stresses in the tool and the workpiece. A maximum cutting temperature of 44 °C was reported at cutting speed of 35 m/min and feed rate of 0.178 m/min [19], whereas a temperature of 250 °C was reported at a cutting speed of 200 m/min [22]. This temperature exceeds the glass transition temperature of most polymer matrices. Thus, machining at very high cutting speeds may lead to deterioration of the polymer matrix and mechanical damage to the machined surface. Care must be taken when high-speed machining so that the cutting temperatures are kept at safe levels.

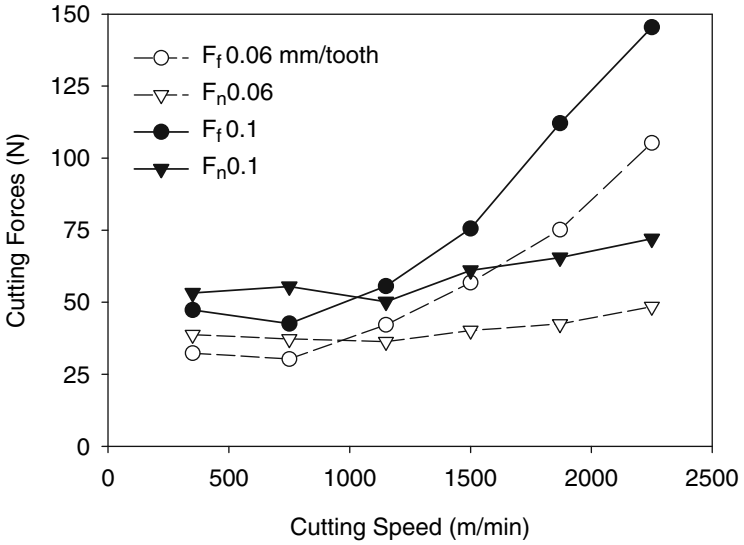

Fig. 5.27 Effect of cutting speed and feed per tooth on cutting forces in end milling of GFRP. Cutting tool is 8-mm PCD edged cutter, with two cutting edges, rake angle $= -2^\circ$, clearance angle $= 7^\circ$. Radial depth of cut $= 8$ mm. Workpiece fiber orientation $0^\circ/90^\circ$, $V_f = 0.50$, thickness $= 3.5$ mm [23]

5.3.3.2 Specific Cutting Energy

The specific cutting energy in milling changes with tool position along the cutting circle. The reasons for these changes are that both undeformed chip thickness and fiber orientation continuously change with cutter position. The specific cutting energy can be obtained from the instantaneous cutting and thrust forces using (3.45):

$$K_c(a_c, \theta) = \frac{F_c}{a_c a_w}, \qquad K_t(a_c, \theta) = \frac{F_t}{a_c a_w}. \tag{3.45}$$

Here, F_c, F_t, and a_c are functions of the cutting edge position, ϕ, which is interrelated to the fiber orientation, θ, by (5.5) and (5.6). For a given depth of cut, a_e, and laminate orientation, ψ, specific cutting energy can be obtained for a range of chip thicknesses and fiber orientations. For example, the data in Fig. 5.25 are used to obtain specific cutting energies for the three laminate orientations 45°, 90°, and 135° using (3.45). The results are shown in Fig. 5.28. The figure shows that the maximum specific cutting energy is required at the beginning of the cut for removing the smallest chip. As cutting continues and the engagement angle increases, the uncut chip size increases and the specific cutting energy rapidly decreases. Unlike homogeneous metals where K_c is always greater than K_t, the results in Fig. 5.28 show that K_t is generally greater than K_c for small uncut chip thickness and for very large fiber orientations. The figure also shows the variation in fiber orientation

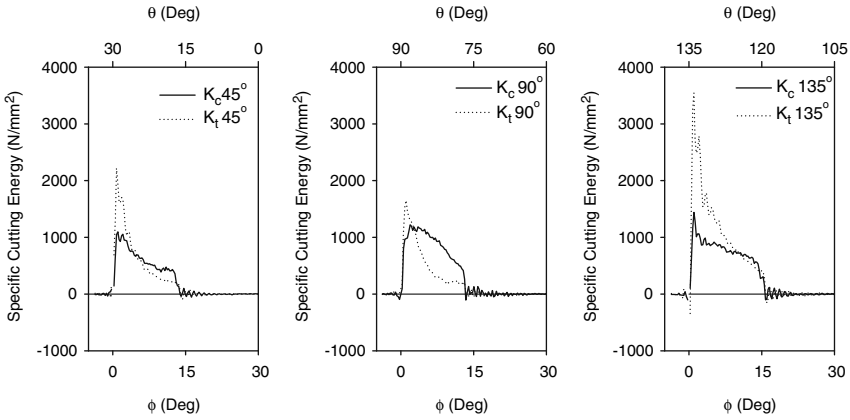

Fig. 5.28 Variation of specific cutting energy with cutting edge position and fiber orientation angle for laminate orientations 45°, 90°, and 135°. Data is obtained from Fig. 5.25

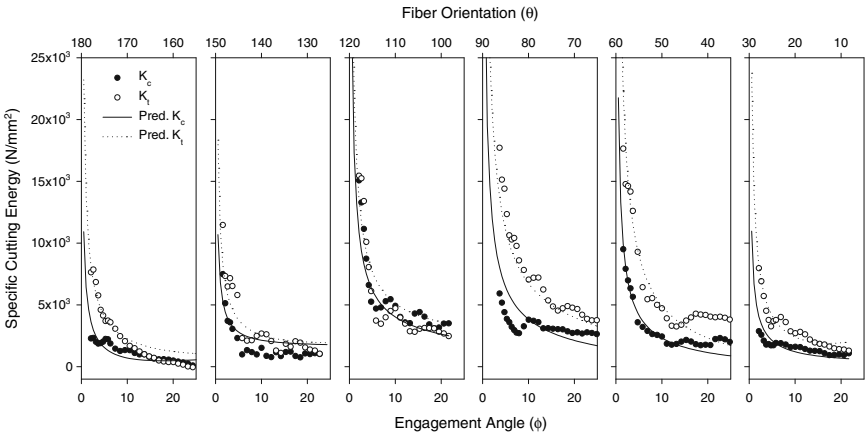

Fig. 5.29 Variation of specific cutting energy with fiber orientation and chip thickness for different laminate orientations. Workpiece material: IM6/Epoxy, $V_f = 0.62$. Cutting tool diameter = 19 mm, rake angle = 15°, clearance angle = 20°, spindle speed = 1,500 rpm, feed rate = 50.8 mm/min, radial depth of cut = 1 mm, axial depth of cut = 2.8 mm

angle with cutting edge position for each laminate. Because both uncut chip size and fiber orientation angle vary with cutting edge position, this figure only demonstrates the combined effect of these two parameters on the specific cutting energy. In order to examine the effects of these parameters individually, one has to study selected sections of the graphs for which the chip thickness is common but the fiber orientation is different. This is demonstrated below for laminate orientations 30°, 60°, 90°, 120°, 150°, and 180°.

The specific cutting energy behavior for the six laminates with varying chip thickness and fiber orientation is shown in Fig. 5.29. The data in this figure has

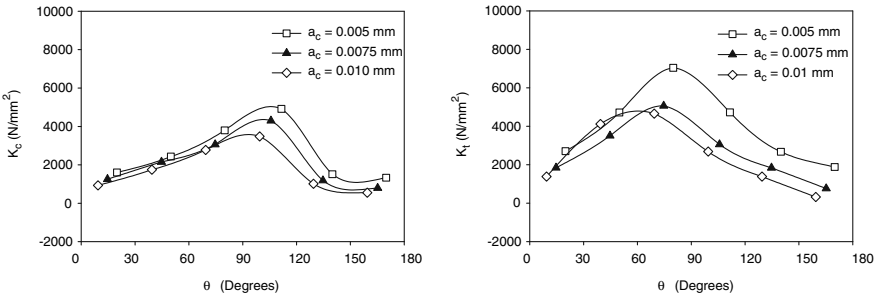

Fig. 5.30 Variation of specific cutting energy with fiber orientation at specific uncut chip thickness levels. Data is extracted from Fig. 5.29

been truncated to remove the abrupt rise and fall in the signal at the beginning and ending of the cut, respectively. The plots are also arranged in such a way that the instantaneous fiber orientation angle increases from approximately 5 to 180° from right to left. Thus, each plot when followed from right to left describes the variation of specific cutting energy with an increase in fiber orientation angle and a decrease in uncut chip thickness. The rapid increase in specific cutting energy with the decrease in uncut chip thickness is evident. Also evident, but not clearly, is the influence of fiber orientation on specific cutting energy. There are apparent upward and downward shifts in the data as you move from one laminate to another. Now, consider a specific tool engagement angle, ϕ and examine the value of K_c and K_t at this angle for all laminates. Take for example $\phi = 9°$ corresponding to uncut chip thickness $a_c = 0.005$ mm. The fiber orientation angles at this instant for the laminates from right to left are 21°, 51°, 81°, 111°, 141°, and 171°. The specific cutting energies K_c and K_t corresponding to these fiber orientations and at this uncut chip thickness are shown in Fig. 5.30. In a similar way, the values for K_c and K_t for uncut chip thickness of 0.075 and 0.01 mm were determined and plotted in the figures. The behavior of specific cutting energy with variation in fiber orientation is clearly shown in this figure and is consistent with the behavior previously discussed for orthogonal machining of unidirectional FRPs (Fig. 3.33a), at least for the component K_c. The specific cutting energy rises gradually with an increase in fiber orientation and reaches a maximum at fiber orientations between 90 and 110°, depending on uncut chip thickness. The increase in uncut chip thickness results in reducing the specific cutting energy and in shifting the maximum to a lesser angle. The effect on K_t is similar, but unlike the trend reported for orthogonal cutting (Fig. 3.33a). One distinct difference between the two is the size of uncut chip. The size of a_c dealt with here is extremely small as compared to both the fiber diameter and the cutting edge nose radius, both of which are in the order of 10 μm. At this scale, the cutting mechanism is dominated by pressing of the fibers below the tool nose and bouncing against the clearance face once the tool has passed, rather than cutting the fibers, as suggested by the model of Zhang et al. [24] and discussed in Sect. 3.5.2. This gives rise to the thrust force as shown in Fig. 5.30b.

Table 5.3 Coefficients of (5.11)

Coefficient	K_c (N/mm^2)	K_t (N/mm^2)
a_o	30.5840	137.1059
a_1	–	−536.5678
a_2	–	1,115.3522
a_3	109.6388	−786.1277
a_4	−76.3806	224.6042
a_5	13.2425	−22.5474
n	−0.6937	−0.7329

Nonlinear regression is used to fit a parametric mathematical function to the data in Fig. 5.29. The mathematical function was based on the physical behavior of the composite material in cutting and consisted of two product terms; a power term to account for the dependence of the specific cutting energy on chip thickness (as demonstrated in Fig. 5.29) and a polynomial to account for the dependence on fiber orientation (as demonstrated in Fig. 5.30). A reasonable form of this function was found by trial and error and is shown in (5.11)

$$K_{c,t} = a_c^n(a_0 + a_1\theta + a_2\theta^2 + a_3\theta^3 + a_4\theta^4 + a_5\theta^5), \tag{5.11}$$

where a_0, a_1, a_2, a_3, a_4, a_5, and n are regression model coefficients and are given in Table 5.3. The fiber orientation angle in this equation is in radians. Comparisons of the regression models and experimental data are also shown in Fig. 5.29. It is apparent from these comparisons that the regression models for K_c and K_t are reasonably good for 30 and 180° laminates, corresponding to shallow fiber orientation angles (0° to ±30°). The regression models are less accurate for the 60°, 90°, and 150° laminates. One possible reason for this poor fit is that the chip formation process is more regular and is characterized by interlaminar shear for fiber orientations up to 60°, but is more irregular and characterized by out plane shear for orientation angles above 60°, as pointed out by Wang et al. [25]. The breakdown of the regression model also demonstrates the limited capabilities of a parametric mathematical modeling in capturing the entire trend of the experimental data. Such limitation is a known weakness in regression analysis using parametric models and has been avoided by utilizing more capable data fitting tools such as Artificial Neural Networks [26].

5.3.3.3 Cutting Force Prediction in Milling FRPs

Prediction of cutting forces in trimming can be easily performed once the specific cutting energy functions and the cutting geometry are known [26]. For an engagement angle, ϕ, the cutting and thrust forces are calculated using (5.12)

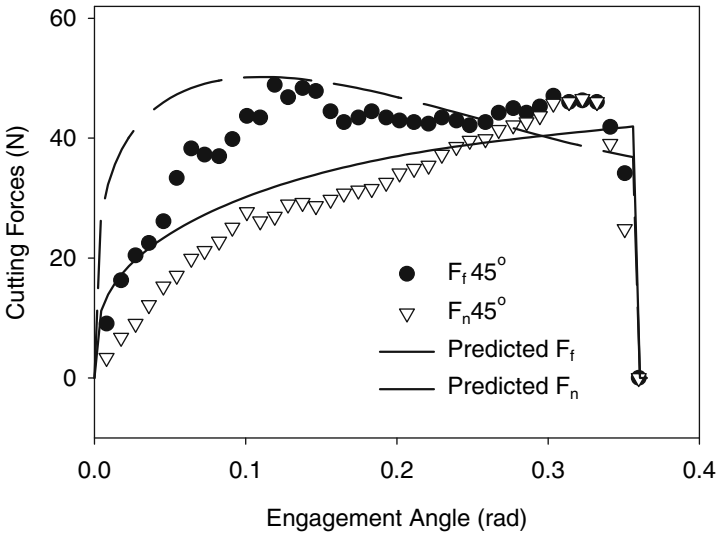

Fig. 5.31 Predicted feed and normal forces in edge milling unidirectional laminate of 45°. Cutting conditions are the same as in Fig. 5.29

$$\begin{aligned} F_{\mathrm{c}}(\phi) &= K_{\mathrm{c}}(a_{\mathrm{c}}, \theta) a_{\mathrm{c}}(\phi) a_{\mathrm{w}} \\ F_{\mathrm{t}}(\phi) &= K_{\mathrm{t}}(a_{\mathrm{c}}, \theta) a_{\mathrm{c}}(\phi) a_{\mathrm{w}}, \end{aligned} \tag{5.12}$$

where the specific cutting energy function is evaluated using (5.11). The feed and normal forces are then calculated from (5.8). An example of predicted forces for milling unidirectional laminate orientation 45° is shown in Fig. 5.31. Force prediction can also be easily extended for multidirectional composites using the principle of superposition. For a laminate with ply stack up sequence $[\psi_1, \psi_2, \ldots, \psi_i, \ldots, \psi_n]$, the fiber orientation for each ply corresponding to an engagement angle, ϕ, can be calculated from (5.5) and (5.6) as $[\theta_1, \theta_2, \ldots, \theta_i, \ldots, \theta_n]$. The instantaneous cutting and thrust forces are then calculated by adding the force contribution from each ply using the equation

$$\begin{aligned} F_{\mathrm{c}}(\phi) &= \sum_{i=1}^{n} [K_{\mathrm{c}}(a_{\mathrm{c}}, \theta_i) a_{\mathrm{c}}(\phi) a_{\mathrm{t}}]_i \\ F_{\mathrm{t}}(\phi) &= \sum_{i=1}^{n} [K_{\mathrm{t}}(a_{\mathrm{c}}, \theta_i) a_{\mathrm{c}}(\phi) a_{\mathrm{t}}]_i, \end{aligned} \tag{5.13}$$

where a_{t} here is the ply thickness and n is the number of plies in the laminate structure. The principle of superposition is used here under the condition that the adhesive strength between the different plies plays an insignificant role in the machining behavior of the individual plies and that these plies will behave under the condition of milling as if they were single separate plies. The validity of such condition has been supported by the findings of [27, 28], and is attributed to the inferior strength of the epoxy polymer as compared to the fiber material.

5.3.4 Machining Quality

Machining quality in milling and trimming is defined by surface finish and surface integrity, which include mechanical and thermal damage to the surface as well as delamination of the top and/or bottom ply of the laminate structure. Surface finish is affected by feed rate, cutting speed, tool nose radius, and tool wear. Surface roughness is generally increased with an increase in feed rate. The response of surface roughness to cutting speed, however, is not consistent with the kinematics prediction of surface roughness as given by (2.55). Figure 5.32 shows the variation of surface roughness R_z with cutting speed for two chip per tooth values when cutting with PCD milling tool [23]. The surface roughness decreases with an increase in cutting speed up to 1,130 m/min, then further increases in cutting speed lead to slight increases in surface roughness. The behavior of surface roughness before the critical speed is explained by the kinematics definition of surface roughness. An increase in cutting speed for a fixed feed and cutter results in a decrease in chip per tooth, a_f, which in turn results in a decrease in surface roughness as described by (2.55). An increase in the feed per tooth (resulting from increasing the feed rate) causes a significant rise in surface roughness. This may be attributed to the heat generated as a result of higher friction. The increase in the feed rate causes a sharp rise in the feed force (Fig. 5.27) which in turn causes higher friction. The critical speed for machining carbon/PEEK composites was found to be much lower at 75 m/min [22]. The cutting temperature corresponding to the critical speed is in the

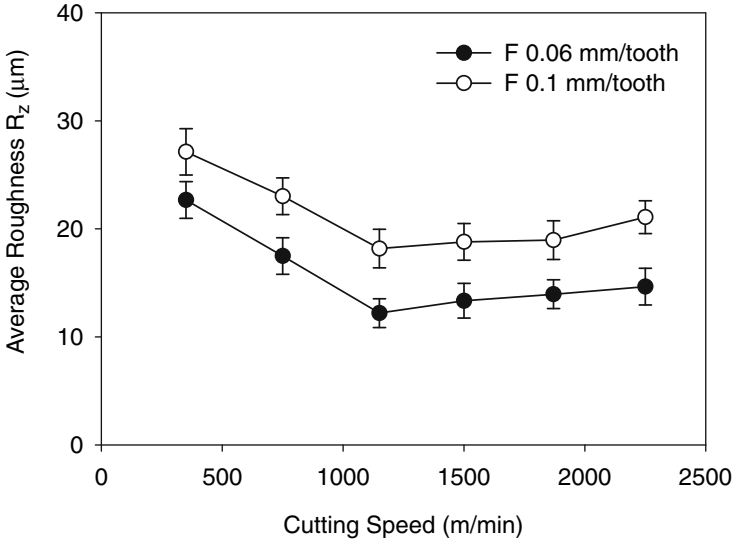

Fig. 5.32 Variation of surface roughness with cutting speed and feed per tooth when machining glass-fiber-reinforced polymer with PCD milling tool. Cutting conditions are the same as Fig. 5.27 [23]

range of 150–175 °C, which exceeds the glass transition temperature of PEEK. The results in [19] and [21] confirm that surface roughness decreases with an increase in cutting speed, but no critical speed could be identified. This could be due to the fact that the cutting speed range used in these studies was below the critical cutting speed. All of these works agree that feed rate is the most influential factor in determining surface roughness.

The surface roughness variation with tool wear, as well as the cutting speed and the feed rate, is shown in Fig. 5.33 for edge trimming of CFRP laminate with a burr

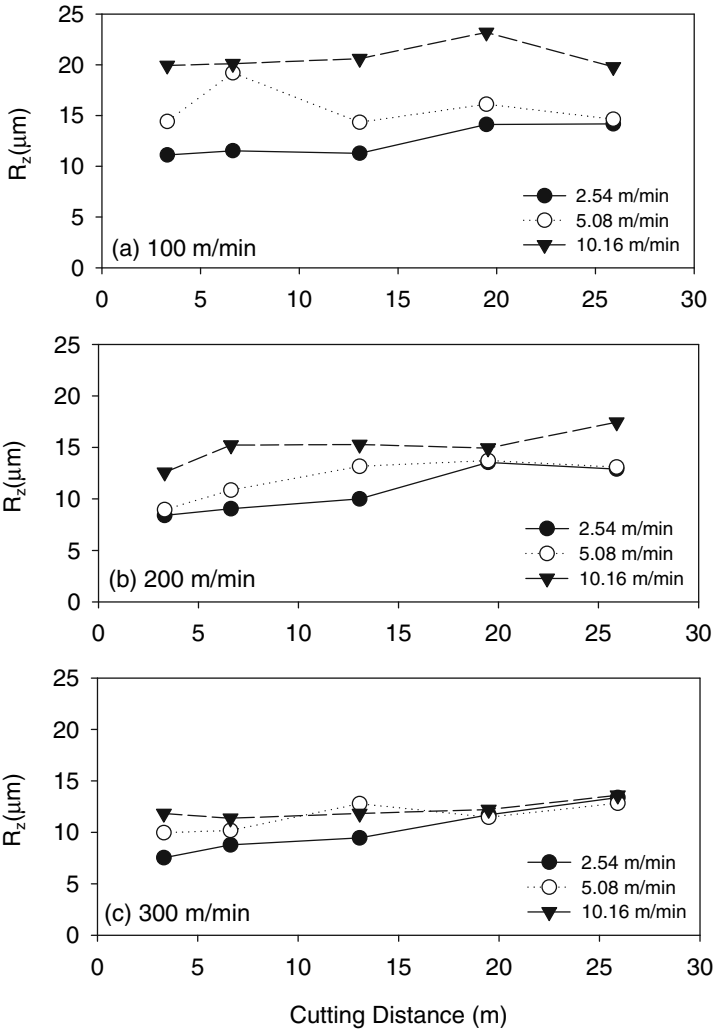

Fig. 5.33 Variation of surface roughness with tool wear (as implied by the cutting distance) at different cutting speeds and feed rates. Tool diameter = 6.35 mm, radial depth of cut = 1.6 mm [20]. Reprinted with permission from SAE Paper # 2006-01-3173 © 2006 SAE International

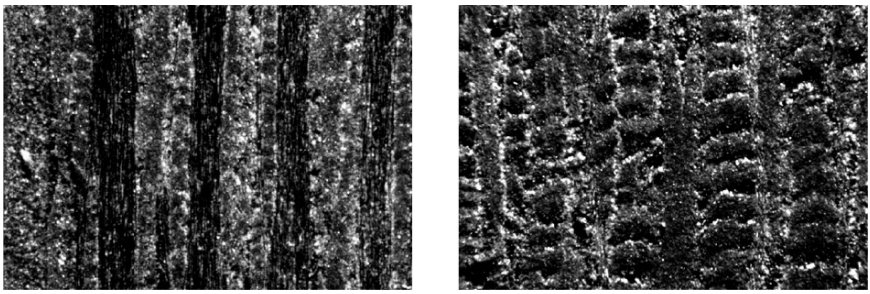

Fig. 5.34 Topography of the machined surface after end milling of CFRP with four flute helical cutter. Direction of cutting is from bottom to top of pictures. Tool diameter = 7.9 mm, spindle speed = 2,500 rpm, depth of cut = 1.0 mm [18]. Reprinted with permission from SAE Paper # 2002-01-1526 © 2002 SAE International

tool of 6.35 mm diameter. Tool wear is implicitly shown in these figures as only the cutting distance, L_c, is shown and assuming that tool wear eventually increases with cutting distance. Analysis of this data by statistical means reveals that surface roughness depends mainly on feed rate and the interaction effect between cutting speed and feed rate. Because of this interaction, the effect of feed rate is more pronounced at low cutting speeds. Equation (5.14) describes the relationship between surface roughness and process parameters

$$R_z = 7.8956 + 1.4745 v_f + 0.1285 L_c - 4.2344 \times 10^{-3} v v_f. \tag{5.14}$$

Topography of the machined surface after milling CFRP with helical tool is shown in Fig. 5.34 for two different feed rates. The surface generated at the low feed rate appears to be smooth and is almost free of cracks. Two different fiber orientations, parallel and perpendicular to the machined surface are clearly recognized. Greater roughness and small pits are characteristics of the regions with perpendicular fibers. Increasing feed rate resulted in an increase in the average chip thickness, and consequently the forces required for chip removal. Higher tool forces, especially the frictional (tangential) force, caused visible cracking of the surface layer. The two fiber orientations are not easily resolved, but it appears that cracking is most severe in the layers having perpendicular fibers. The spacing between the cracks on the machined surface is approximately equal to the feed per tooth and they are inclined at an angle, approximately equal to the cutter helix angle, with respect to the cutting direction. The direction of cut is from top to bottom of the pictures shown. This indicates that these cracks are caused by the individual cutting edges on the milling cutter as they rubbed and pressed against the workpiece surface approaching exit. The presence of these cracks gave rise to the surface roughness at high feed rate. Smearing of the polymeric matrix is also evident for both feed rates, but is more apparent at the high feed rate.

Delamination is another important feature of a machined edge. It is being considered here because of the rise of an axial force component during milling and

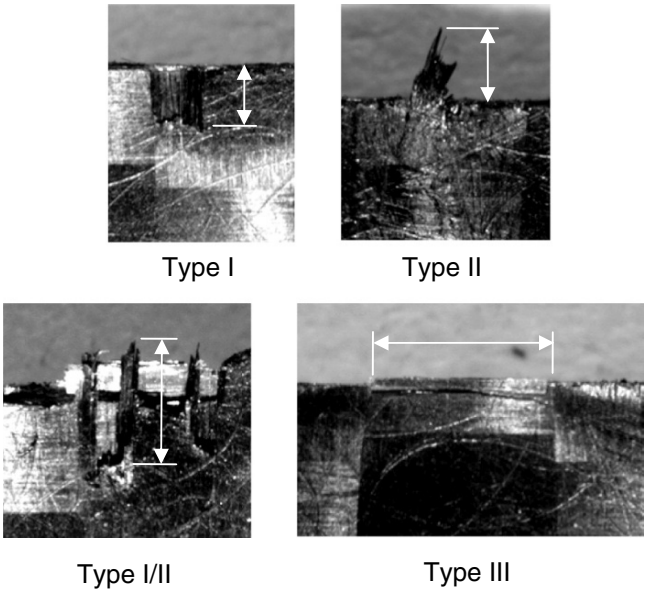

Fig. 5.35 Delamination appearance, types, and measurements

trimming with helical cutting tools. The axial force acts in a direction normal to the stacking plane of the composite laminate and hence may cause interplay separation. This effect is most observed at the top or bottom surfaces of the machined edge because the surface plies are not supported on one side. In conventional helical cutters, the axial force acts in an upward direction and most delamination damage will be seen in the top ply. In a downward spiral-milling tool, the axial force acts in a downward direction and most damage will be seen in the bottom ply. The type of delamination that occurs during milling and its frequency of occurrence depend heavily on the surface ply orientation. A classification of the types of delamination was first proposed in [29] and is explained below. Figure 5.35 shows the appearance of three different types of delamination and how their length or depth is measured. Type I delamination describes areas where the surface fibers have been broken and removed some distance inward from the machined edge. Type II delamination consists of uncut fibers that protrude outward from the machined edge, whereas Type I/II delamination is some kind of a combination of both previous types. Type II delamination is caused by the fibers being able to bend or move away from the path of the advancing tool and then spring back to its original orientation. This may occur most likely for fibers in a ply below the surface ply. Type III delamination describes fibers that are partially attached, or cracks that are parallel to the machined surface [29]. Both Type I and Type III delamination create loose fibers attached to the machined edge and cause a fuzzy appearance.

The effect of surface ply orientation on the occurrence of delamination and its type is shown in Fig. 5.36 for PCD and carbide cutters [29]. The PW and PX surface plies consisted of plain weave fiber at orientation $(0^\circ/90^\circ)$ and $(+45/-45)$ with the cutting direction, respectively. In general, Type II delamination is the most common

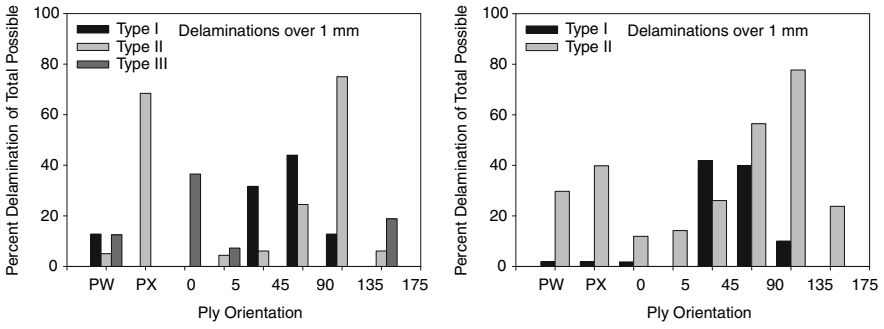

Fig. 5.36 Delamination frequency in relation to surface-ply orientation for (**a**) PCD cutter and (**b**) carbide cutter [29]

when machining with both types of cutters and for all orientations. It is also shown that for the PCD cutter maximum Type I delamination tendency is associated with 90° surface plies, Type II with the PX and 135° plies and Type III with the 0° plies. For the carbide cutter maximum Type I delamination tendency is associated with the 45° and 90° plies and Type II is associated mainly with the PW, PX, 90° and 135° surface plies but appears for all other ply orientations. This is perhaps a result of the severe wear of the carbide cutter. Type III delamination was not observed with the carbide cutter. These results point out the strong relationship between surface ply orientation and delamination and are helpful in making design decisions as to which ply orientation should be used on the surface of a laminate structure in order to decrease delamination.

The occurrence of delamination is also dependent on process parameters such as cutting speed, feed rate, depth of cut, and tool wear [20, 21, 29, 30]. Figure 5.37 shows the variation of average delamination length (cumulative average for all types of delamination) with cutting distance at different levels of cutting speed and feed rate. The delamination depth rises slightly with an increase of cutting distance as a result of tool wear and the effect of feed rate appears to be more significant than that of the cutting distance. Regression analysis of the data revealed that delamination depth mainly depends on individual effect of the process parameters and not on the interaction effect of the parameters. The effect of cutting speed on delamination appears to be slightly more than that of the feed rate. An increase in cutting speed by 100% at feed rate of 5.08 m/min produces 13% decrease in delamination length, while the increase in feed rate by 100% at cutting speed of 200 m/min causes the delamination length to increase by approximately 10%. Equation (5.15) gives the relationship between all these parameters and the average delamination depth

$$\mathrm{DEL} = 0.9545 - 1.1579 \times 10^{-3} v + 0.0379 v_{\mathrm{f}} + 7.8014 \times 10^{-3} L_{\mathrm{c}}. \qquad (5.15)$$

A delamination factor was defined in [21, 30] as the ratio of the maximum width damage on the surface of workpiece to the width of cut, which is equal to tool diameter under full engagement of the cutting tool. It was found that delamination factor in machining GFRP and CFRP with helical cutter is affected by the cutting speed

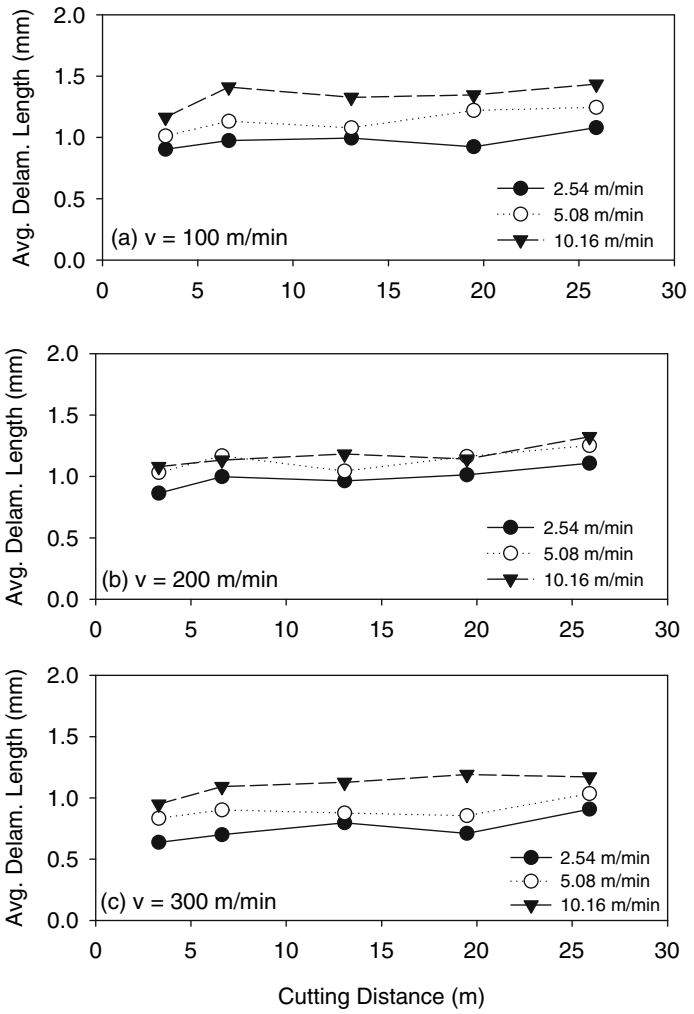

Fig. 5.37 Variation of average delamination length with tool wear (as implied by the cutting distance) at different cutting speeds and feed rates. Tool diameter = 6.35 mm, radial depth of cut = 1.6 mm [20]. Reprinted with permission from SAE Paper # 2006-01-3173 2006 SAE International

and the feed rate. An increase in cutting speed and feed rate generally lead to an increase in the delamination factor. Furthermore, feed rate was found to be the most important factor influencing delamination width. Milling with a six flute straight edge cutting tool was also found to generate more delamination when compared to the helical tool in machining CFRP [30].

Ultimately, delamination tendency is associated with the cutting forces applied to the machined edge, the axial component in particular. It has been shown previously that the cutting forces are proportional to the chip thickness, which in turn is a function of the cutting speed, feed rate, and number of cutting teeth on the cutter. The

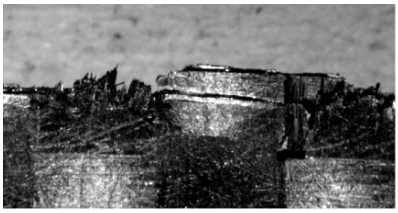
(a) h_q = 0.16 mm

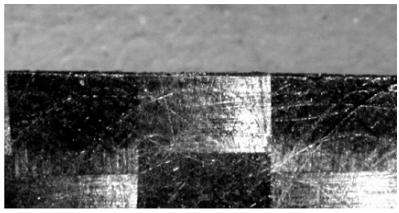
(a) h_q = 0.014 mm

Fig. 5.38 Delamination of machined edge under two different sets of cutting parameters. (**a**) $v = 100\,\mathrm{m/min},\ v_f = 10.16\,\mathrm{m/min},\ h_q = 0.16\,\mathrm{mm}$; (**b**) $v = 300\,\mathrm{m/min},\ v_f = 2.54\,\mathrm{m/min},\ h_q = 0.014\,\mathrm{mm}$

equivalent chip thickness for a burr tool has also been defined in (5.7). Figure 5.38 shows the appearance of the machined edge for two different equivalent chip thickness when edge trimming PW surface ply laminate with a burr tool. It is clear that severe delamination occurs with the largest chip thickness (corresponding to the smallest cutting speed and largest feed rate) and that delamination is almost absent for the smallest chip thickness. This means that great improvement in machinability in terms of delamination is obtained by machining at high spindle speeds and low table feed.

5.3.5 Recommended Practices

Different reinforcement fibers behave differently in response to the action of the advancing cutting edge. The fracture behavior of glass and carbon fibers is brittle in nature and the fibers are not able to sustain high deformations in bending or compression. The fibers therefore fracture due to compression shear and/or bending stress, depending on fiber orientation. Aramid fibers, on the other hand, can sustain large deformations in bending. They evade the advancing cutting edge and bounce back once the edge has passes, creating a fuzzy appearance of the machined edge. This characteristic response of the fibers requires special cutting edge geometry for each fiber type. Furthermore, the relationship between the fiber diameters to that of the radius of the cutting edge has significant implications on the mechanics of cutting. For most practical applications the tool nose radius is greater than the fiber diameter and clean shaving of the fibers by direct shear may not be possible. It is required that the cutting tool maintains a sufficient level of edge sharpness in order to achieve a clean cut. This can be facilitated by selecting tool materials of high wear resistance and edge integrity such as fine and ultrafine grain size carbides and polycrystalline diamond. The submicron grain sizes used for making these tools provide the high abrasive resistance required in this environment, but also cause the tool to be brittle and more susceptible to fracture. The behavior of the matrix binder is also dependent on the cutting edge angles and sharpness. Negative rake angle tools cause the matrix to elastically deform in front of the cutting edge and

significant bouncing takes place behind the cutting edge, leading to poor surface quality and extensive flank wear. Also important is the size of uncut chip relative to the nose radius of the tool. Too small size of uncut chip gives rise to pressing the fibers and matrix under the tool nose and causes poor surface finish and excessive tool wear. The size of uncut chip is controlled by manipulating the cutting process parameters such as cutting speed, feed rate, and number of cutting edges on the milling cutter. The following sections gives recommendations for quality machining of FRPs based on operator control of cutting configuration, process parameters, and proper selection of cutting tools.

5.3.5.1 Selection of Cutting Tools

A variety of cutting tool materials and geometries are available for machining FRPs. One reason for this diversity in tooling is the diverse characteristics of the FRP products stemming from the various forms, types of reinforcement and matrix, and volume fraction of reinforcement fibers that are utilized for various applications. It is also known that tooling for machining FRPs has much benefited from the know how of the woodworking industry. Similarities in macrostructure and machining properties between wood-based composites and man-made fiber-reinforced composites made it feasible to transform, sometimes without any modification, the practices and tooling of wood machining to FRPs machining. This is evident from examining the cutting tool geometries shown in Figs. 5.39 and 5.40.

Solid carbide router bits shown in Fig. 5.39 represent a group of cutting tools available for milling and trimming of composite panels. A straight flute cutter is the simplest and the most versatile tool geometry. Because of the simple straight cutting edge design, this cutter is also available with PCD tips. The straight flute cutter

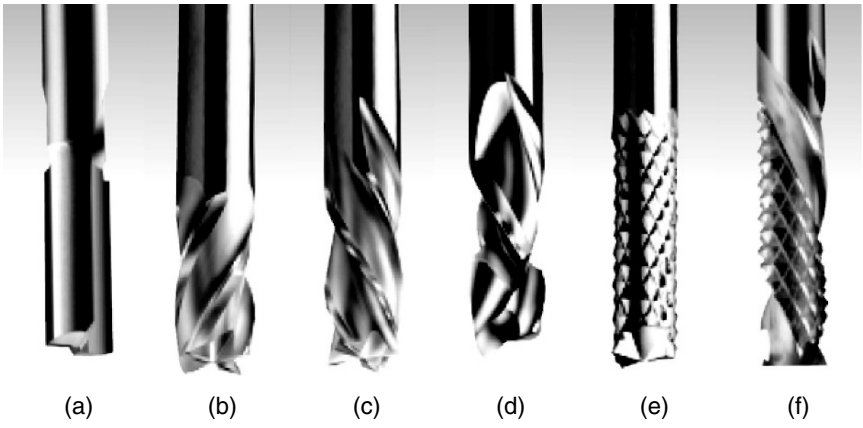

Fig. 5.39 Geometry of cutting tools for milling composite materials (**a**) straight flute, (**b**) upcut helical tool, (**c**) downcut helical tool, (**d**) double spiral compression tool, (**e**) burr tool, (**f**) fluted bur (courtesy of ONSRUD tool company)

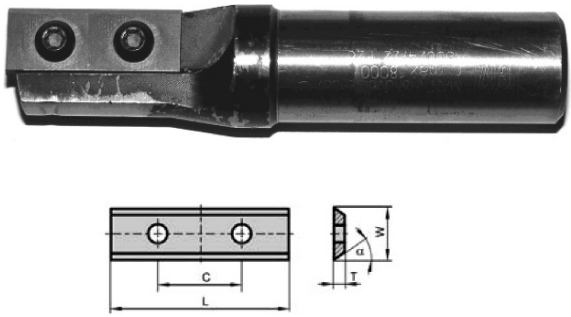

Fig. 5.40 CNC router inserted milling tool

(Fig. 5.39a) provides clean shaving action and good surface finish. It, however, has poor ability of chip disposal and tends to clog very shortly after use. This results in compression of the surface layer and poor surface finish. The unidirectional helical cutters in Fig. 5.39b, c generate an axial force which acts normal to the stacking direction of the laminate. The direction of the force depends on the direction of the spiral. This force in turn causes delamination and fuzzing in the surface ply that is not supported in the force direction. This problem is avoided by utilizing a double helix or compression cutter shown in Fig. 5.39d. The two opposing helix generate forces that act in compression from both sides of the laminate panel, and thus prevent delamination. The burr tools (Fig. 5.39e, f) have been used for many years for cutting and trimming fiberglass due to their high wear resistance and ability to produce a clean cut at relatively high cutting speeds and feed rates. The opposing spirals ground in the body of the tool generate many cutting points that shear the fiber in the composites while providing pulling action at the same time. This ensures clean shearing of the fibers. The tool has an uneven count of spirals, up vs. down, to make the points overlap so that they do not make grooves on the machined edge. The apparent disadvantages of this tool are premature fracture of the tip of the cutting points (Figs. 5.20 and 5.21) and ease of clogging. Both of these shortcomings can be avoided by proper selection of sufficiently small uncut chip thickness.

Aramid fibers are considerably tougher than glass and carbon fibers and resist shearing and bending stresses. Therefore, machining aramid FRP with conventional tool geometries results in poor surface quality in terms of fuzzing. Axial splitting of the fibers due to weak molecular strength transverse to the fiber axis further aggravates the fuzzing problem. The fibers may be sheared more effectively if they are subjected to tension at the same time to prevent bending ahead of the advancing cutting edge. Variations of the tool geometries in Fig. 5.39d, f have proven to be effective in machining aramid FRPs. A high degree of cutting edge sharpness and a small cutting edge radius are also required.

Clogging is a serious problem in all cutting tool designs shown because of the small tool diameter and small gullet size. The clogging is further aggravated by high cutting temperatures which cause the polymer matrix to soften and adhere to the cutting edge. The detrimental effects of this condition are severe damage to the

machined surface and poor surface finish. The use of compressed air in combination with proper selection of speeds and feed rates help in alleviating the clogging problem. Utilization of relatively larger diameter tools such as the one shown in Fig. 5.40 is also beneficial. Selection of the tool wedge angles is also important for controlling tool wear and surface finish. Tool wedge angles of approximately 75° with rake angle of 7° have proved favorable for PCD cutting tips. Keener cutting edge angles and sharper cutting edges are possible when submicron carbide grades are utilized. Reduction in the wedge angle offers only a short-term advantage, which is offset by increased wear. When the clearance angle selected is too small, extensive wear occurs at the flank, resulting in a tendency for the polymer material to become deformed rather than fractured.

5.3.5.2 Selecting Process Parameters and Cutting Configuration

The process parameters important for good machining quality are cutting speed and feed speed, which when combined with the number of teeth on the cutter define the size of uncut chip as given in (2.14). It was shown before that the size of uncut chip influences the cutting forces, surface roughness, and delamination. It is generally the case that better machining quality is obtained with smaller uncut chip thickness, which can be attained by increasing the cutting speed, decreasing the feed speed, increasing the number of teeth on the cutter, or any combination of the three. Because milling and trimming of FRPs is done as a finishing procedure, no substantial material removal is required. There is therefore a benefit in reducing the size of uncut chip because it is characteristic of finish machining and is well suited for high-speed machining. Reducing the chip per tooth by increasing the cutting speed (spindle speed) results in reducing of the cutting forces, improving surface roughness and reducing clogging. For improving production rates, high feed rates are used but result in increasing the chip per tooth. The increase in feed rate in this case should be augmented by a proportional increase in spindle speed so that a small chip per tooth is maintained. However, some precautions are warranted when machining at high speeds. High cutting temperatures are associated with high-speed machining and precautions should be made so that the glass transition temperature of the polymer matrix is not exceeded. Increasing the cutting tool temperatures results in accelerated tool wear and shorter tool life. Because of the small size of chip and the poor thermal properties of the FRPs, the chip is not an effective mean for removing the heat generated from cutting and the tool becomes the preferred path for the heat to dissipate. The use of PCD cutters and diamond-coated carbides is extremely beneficial in high-speed machining because of their excellent thermal conductivity and wear resistance. High spindle speeds are also associated with dynamic instabilities and increased tool and workpiece vibration. This leads to deteriorating machined surface quality and is extremely detrimental to the health of PCD and diamond-coated tool. Only good quality spindles and dynamically stiff machine tools should be utilized in high-speed machining.

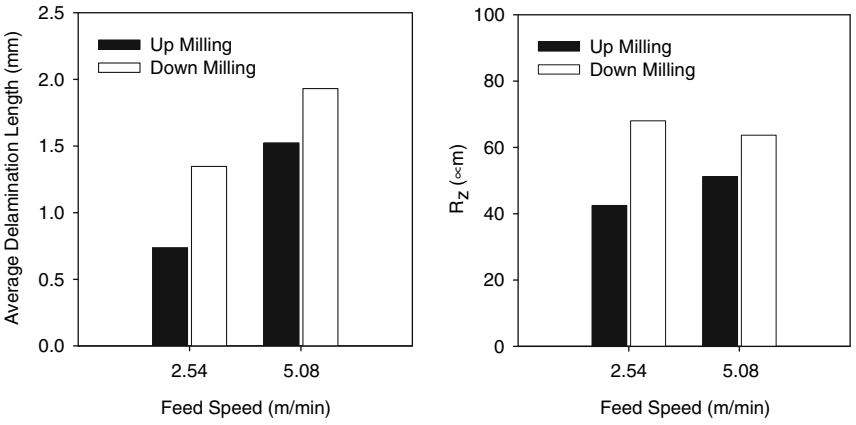

Fig. 5.41 Effect of cutting configuration on machining quality (**a**) Delamination length, (**b**) Surface roughness. Cutting speed = 100 m/min, cutting tool = 6.35 mm burr [20]

The surface integrity is also dependent on the milling configuration. Figure 5.41 demonstrates the difference in average delamination depth and surface roughness in up milling and down milling configurations. The results are for edge trimming of CFRP panels with burr tools and are shown for two feed rates. It is evident that machining quality in up milling is far more better than in down milling for both feed rates [20]. Similar results were also shown for surface roughness when machining CFRP with PCD straight flute cutter [23]. This is likely to be caused by differences in the chip formation mechanics as determined by the fiber orientation relative to the cutting velocity in up milling and down milling (see Fig. 5.16). It is also likely that debris from chips clogs the flute and obstructs the cutting in down milling [23].

5.4 Drilling of FRPs

Drilling represents one of the most important machining operations that are carried out on composites. Drilling, counterboring, and countersinking are often required processes for preparing composite parts for joining and assembly. Despite its extensive use, drilling also remains as one of the most challenging machining operations. Among the key issues to be considered are thermal management, tool wear, and delamination. Poor thermal conductivity of the fiber and the matrix favors heat buildup at the cutting region and majority of the heat generated has to be conducted away through the tool. Because the heat generated during drilling is affected by the cutting speed and the feed rate, FRPs are machined only in a limited range of process parameters in order to avoid heat damage. In some cases, approved coolant can be used in order to reduce the cutting temperatures and control machining dust. Furthermore, different thermal expansion coefficients between fiber and matrix

make it difficult to attain dimensional accuracy of the drilled holes. The holes may shrink after drilling causing poor assembly tolerance. Reinforcement fibers cause severe wear by abrasion of the cutting edges. Wear of the cutting edge in turn increases the thrust force. Thrust force was found to be the most controlling factor of the onset of delamination. The following sections provide a comprehensive treatment of the drilling process in terms of its process parameters and their effect on process outcomes and machining quality.

5.4.1 Fiber Orientation in Drilling

The relationship between fiber direction and the direction of cutting velocity vector is similar to that in milling. Both drilling and milling involve material removal by a rotating cutting edge. Figure 5.42 shows a schematic of the fiber orientation convention for a two-flute drill. The geometry of a two-flute twist drill and the kinematics of drilling are shown in Fig. 2.9. Material removal is primarily performed by the major cutting edges. The chisel edge also contributes to the material removal process, but to a much lesser extent. It is customary in the analysis of drilling unidirectional composites to measure the angular position of the cutting edge relative to the fibers [23, 31, 32]. This is because unlike milling, the chip thickness in drilling is independent of angular position and the center of rotation of the cutting tool is always fixed relative to the workpiece. Only rotation of the cutting edge around the center brings about differences in fiber orientation. As shown in Fig. 5.42, the cutting edge angular position is zero when the cutting edge is lined up with the fibers. At this instant the cutting velocity vector is perpendicular to the fibers and the fiber orientation angle is 90°. As the angular position increases the fiber orientation decreases and reaches zero when the angular position is equal to 90°. This is sim-

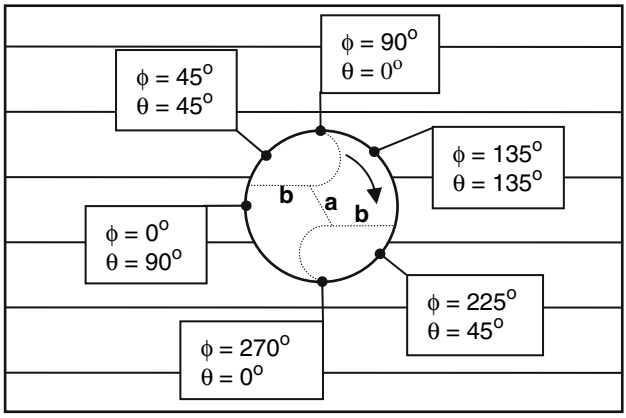

Fig. 5.42 Fiber orientation definition in drilling unidirectional composites (**a**) chisel edge, (**b**) major cutting edge

ilar to milling a laminate with $\psi = 90^\circ$ and the fiber orientation in this case is described by (5.5a). Further increase in the angular position makes $\phi > \psi$ and the fiber orientation is then calculated by (5.5b). Note that at any given moment, the two diagonally opposing cutting edges have the same fiber orientation angle. This makes their cutting behavior identical as will be shown next.

5.4.2 Drilling Thrust Force and Torque

Drilling is a complex mechanism because the chip formation process is caused by multiple cutting edges of varied rake angles and cutting speed. The tool forces generated in drilling are the thrust force (along the direction of the feed) and torque. When drilling metals, these forces are fairly uniform with time because the uncut chip thickness is constant. The two major cutting edges (lips) remove the bulk of the chip and thus affect the drilling torque, thrust force, and radial force. The chisel edge acts as a blunt wedge with a large negative rake angle. In a small region at the center of the chisel edge, material is removed by an extrusion or smearing action. Away from this center region, the chisel edge removes a very thin chip by orthogonal cutting with highly negative rake angle [1]. The chisel edge is thus a major contributor to the thrust force. In drilling unidirectional composites, the drilling forces are cyclic due to the instantaneous changes in the fiber orientation angle. Figure 5.43 shows

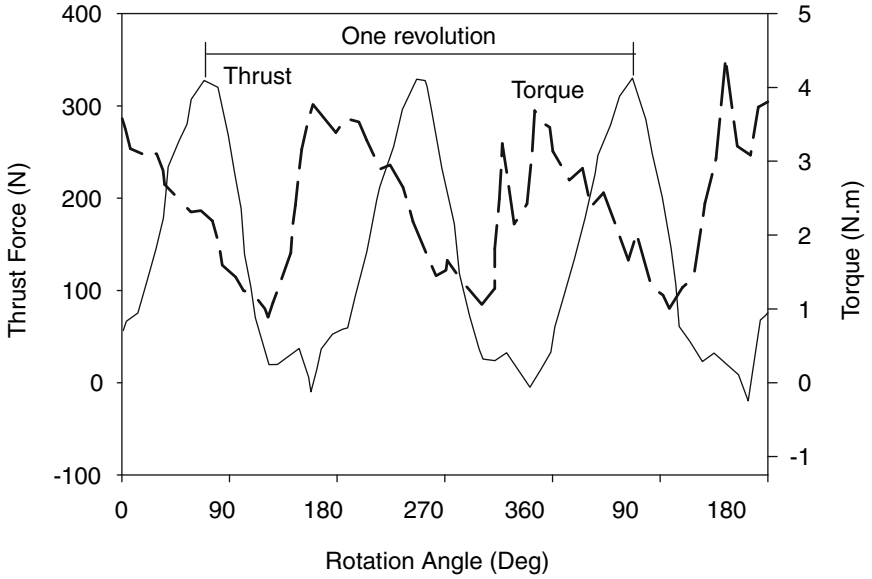

Fig. 5.43 Changes in thrust force and torque with cutting edge position when drilling unidirectional T-300/SG89-3 CFRP ($V_f = 0.62$), feed = 162 mm/min, rotational speed = 88 rpm, 12.7 mm diameter conical carbide drill, 80° point angle [31]

the evolution of the thrust force and torque with cutting edge position during the drilling of CFRP with two-flute twist drill [31]. The figure demonstrates the cyclic and repeated natures of the feed force and torque that is caused by fiber orientation. Similar force cycles were also reported in [32, 33]. The maximum magnitude of the thrust force is in interest to us because delamination propagates by the thrust force. The thrust force is generated by the cutting action of the two primary cutting edges (lips) and the chisel edge, and the latter is found to be a major contributor to the thrust force [33]. The amplitude of the thrust force is significantly decreased and its frequency is increased when the number of flutes is increased [33] or when drilling cross-ply and quasi-isotropic laminates [34].

The cycling of the thrust force and torque is closely related to the fiber orientation. The thrust force reaches a maximum near angular position 90° where the cutting direction is parallel to the fibers ($\theta = 0°$). Past this point the forces fall sharply reaching a minimum at 135° ($\theta = 135°$). As the rotation angle continues to increase, the thrust force increases gradually to a maximum near 270°, corresponding to the engagement of the second major cutting edge. This behavior of the thrust force is somewhat similar to that shown in Fig. 3.15a for orthogonal machining of unidirectional composites where the maximum thrust force occurs at shallow fiber orientations. Deviations in the behavior of thrust force in drilling from that of orthogonal machining is caused by the complexity of the drilling process and the influence of the chisel edge cutting action.

The drilling torque is caused by the cutting force couple acting on the major cutting edges and its magnitude is determined by the magnitude of the cutting force and the drill diameter

$$M = 2F_c \frac{r}{2} = F_c \frac{d}{2}, \tag{5.16}$$

where F_c is the cutting force on the major cutting edge, r is the drill radius, and d is the drill diameter. It is assumed here that F_c is an equivalent cutting force that acts at the center of the uncut chip area and that the chisel edge width is negligible. The torque reaches a maximum near angular position 0°, corresponding to fiber orientation 90°. Further increase in fiber orientation causes the torque to decrease to a minimum at approximately 135°. Again, this is a characteristic behavior of the cutting force as demonstrated in Fig. 3.15a. The dissimilar slopes of the torque curve on both sides of the maximum are caused by dissimilar behavior of the cutting force for fiber orientations smaller than and greater than 90°, which is caused by different modes of chip formation as demonstrated in Figs. 3.7 and 5.16.

Typical behavior of the average thrust and torque during drilling of a unidirectional CFRP laminate is shown in Fig. 5.44 [31]. At the beginning of drilling the chisel edge is penetrating the laminate, which causes the thrust force to rise quickly. The torque rises slowly because of the smaller cutting forces at the chisel edge and the proximity of these forces to the center of the drill. The torque starts to increase rapidly as the cutting edges (lips) engage in cutting the laminate. There is a gradual drop in the thrust force during the full engagement of the drill in the laminate. This might be a result of the softening of the matrix due to the heating generated by drilling and/or the increased reduction in flexural rigidity of the laminate material

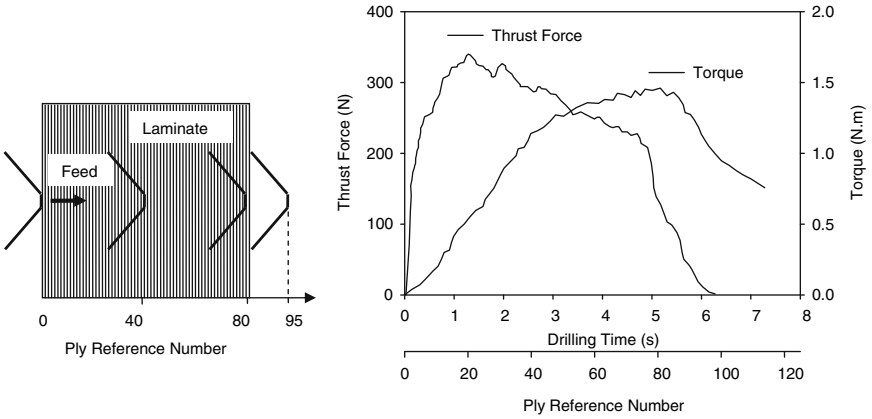

Fig. 5.44 Drilling forces vs. time for the entire drill cycle. Drilling speed = 400 rpm, drill diameter = 6.4 mm carbide drill, UD carbon/epoxy (80 plies), feed = 102 m/min [31]

supporting the drilling point as the hole depth increases. The thrust force and torque decrease rapidly as the drill emerges out of the laminate. The thrust force reaches zero when the drill cone fully emerges out of the laminate but the torque reaches a nonzero value because the flutes of the drill are still engaged in the workpiece.

5.4.2.1 Influence of Process Parameters

The drilling thrust force and torque are affected by the cutting speed, feed rate, and drill geometry. Both thrust force and torque increase significantly with increasing feed rate due to its direct influence on uncut chip size. The effect of cutting speed on thrust force and torque is not significant [35–39]. The standard twist drill geometry parameters that influence thrust force and torque include drill point angle, chisel edge width, web thickness, and drill diameter. These parameters are shown for a conventional drill in Fig. 5.45 and the effects of some of them are shown in Fig. 5.46. An increase in the drill point angle leads to an increase in the thrust force and a decrease in the torque. The torque decrease is associated with the increase of the orthogonal rake angle at each point on the primary cutting edge with the increase in point angle. The standard point angle of 118° was found to be optimum in drilling AS4/PEEK CFRP [39] while the effect of the point angle was found to be marginal in drilling T300/5208 CFRP. The thrust force was maximum for the standard point angle [33]. An increase in web thickness leads to an increase in both thrust force and torque. This is because the larger the web thickness, the longer the chisel edge length and the smaller the orthogonal rake angle at each point on the primary cutting edge. The chisel edge was also found to contribute 40–60% of the total thrust force under normal feed rates.

The combined effect of feed rate and drill diameter on thrust force and torque was found to be more significant than the separate effect of either one of the parameters

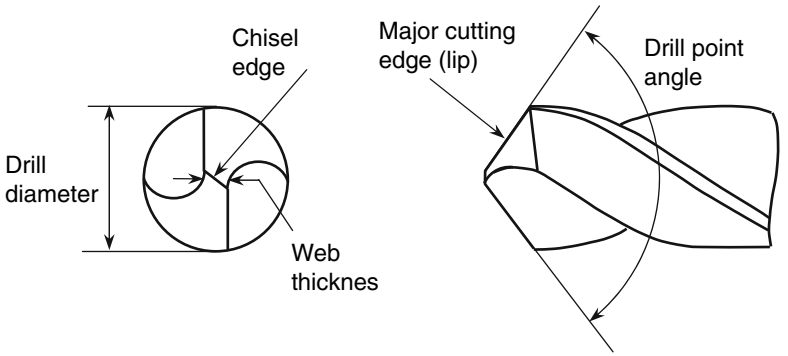

Fig. 5.45 Conventional twist drill geometry parameters most influencing drilling thrust force and torque

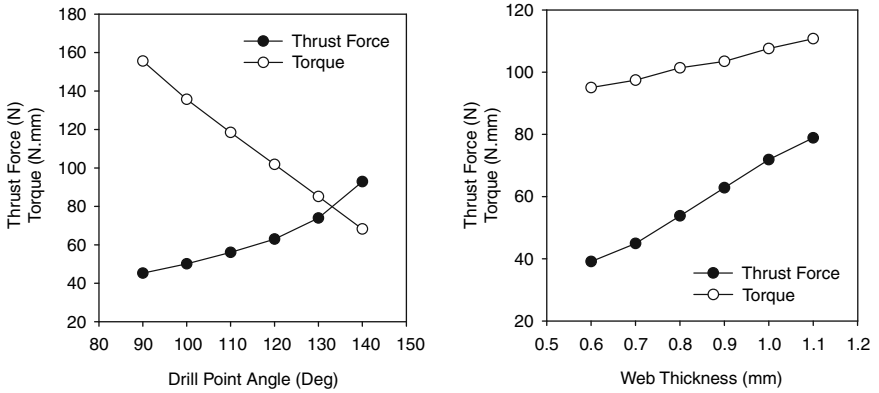

Fig. 5.46 Effect of drill point angle (*left*) and web thickness (*right*) on drilling force and torque. Workpiece is unidirectional CFRP, cutting conditions: 5.0 mm HSS drill, 1,370 rpm, 0.1 mm/rev [36]

[39]. For metals, using conventional twist drill, the thrust force is correlated with the feed rate and drill diameter by an empirical relationship of the form

$$F_{\mathrm{A}} = d^2 H_{\mathrm{B}} \left[K_1 \frac{f^{0.8}}{d^{1.2}} + K_2 \left(\frac{c}{d} \right)^2 \right], \tag{5.17}$$

where H_{B} is the workpiece Brinell hardness in $\mathrm{kg/mm^2}$, f is the feed rate in mm/rev, c is the chisel edge length, and K_1 and K_2 are empirical constants that depend on the workpiece material, thickness, and drill point geometry [3]. Similar equations were also reported for drilling unidirectional and multidirectional composites as listed in Table 5.4. Such a relationship is extremely useful in predicting the machinability of FRPs because they allow the prediction of cutting conditions for free delamination as will be explained next.

Table 5.4 Empirical relationships for thrust force and torque in drilling FRPs

Drilling parameters	Thrust force F_z (N), Torque M (N m)
Workpiece: unidirectional CFRP T300/5208, ply thickness = 0.228 mm, laminate thickness = 20 plies, $H_B = 98\,\mathrm{kg/mm^2}$. Standard HSS twist drill, diameters = 6.35, 12.7 mm, drill point = 118°, chisel length = $0.2d$, feed rate up to 0.12 mm/rev [33, 34]	$F_A = d^2 H_B \left[\frac{1.91 f^{0.4}}{d^{1.2}} + \frac{0.101}{d}\right]$ $F_A = 0.136 H_B d^{0.78} f^{0.4}$ (simplified)
Workpiece: CFRP T300/5208 laminates of different configuration. Cross ply laminate thickness = 20 plies, quasi-isotropic laminate thickness = 24 plies, ply thickness = 0.125 mm. Standard HSS twist drill, diameter = 6.35, drill point = 118°, chisel length = $0.2d$, feed rate up to 0.2 mm/rev [34]	$F_A = 56.3 f^{0.4}$ (unidirectional) $F_A = 41.8 f^{0.32}$ (crossply) $F_A = 43.1 f^{0.22}$ (quasi-isotropic)
E-glass UD GFRP, ply thickness = 0.228, total laminate thickness = 4mm, $V_f = 0.4$. Trepanning tool and twist drill diameters = 8, 10, 14, and 16 mm, feed rates = 0.01–0.2 mm/rev, cutting speed = 50 m/min [37]	$F_A = 48.98 d^{0.783} f^{0.410}$ (twist drill) $F_A = 48.98 d^{0.242} f^{0.37}$ (trepanning/saw drill) $M = 0.039 d^{1.529} f^{0.52}$ (twist drill) $M = 0.039 d^{1.571} f^{0.59}$ (trepanning/saw drill)
E-glass chopped fiber mat, laminate thickness = 10 mm, $V_f = 0.63$, carbide coated drill bit, drill diameters = 6, 10 mm, spindle speed 400 rpm, feed rates = 0.1–0.7 mm/rev [38]	$F_A = 35.004(fd)^{1.3844} - 0.23 d^2$ $M = 0.0064 f^{1.3844} d^{2.3844} + 0.0091 d^2$
Quasi-isotropic layup $[0/45]_{39s}$ of woven CFRP (Toray 300/Fiberite 934), ply thickness = 0.125 mm, laminate thickness = 9.9 mm, $V_f = 0.63$. Drills: carbide tipped HSS, diameters = 6.35, 7.9 mm, spindle speed = 1,000 rpm, feed rates 0.1–1.0 mm/rev [40]	$F_A = 40.77(fd)^{0.66} - 0.36 d^2$ (w/o pilot holes) $F_A = 3.5(fd)^{0.66} + 0.11 d^2$ (with pilot holes) $F_c = 14.12(fd)^{0.66}$, $M = F_c \frac{d}{2}$
Quasi-isotropic layup $[0/45]_{43s}$ of woven AFRP (Kevlar 49/Fiberite 7714) 8.1-mm total thickness. $V_f = 0.6$. Drills: carbide tipped HSS, diameters = 6.35, 7.9 mm, spindle speed = 300 rpm, feed rates 0.1–1.0 mm/rev [41]	$F_A = 35.84(fd)^{0.50} - 0.09 d^2$ $F_c = 30.81(fd)^{0.50}$, $M = F_c \frac{d}{2}$

5.4.2.2 Specific Cutting Energy

The specific cutting energy or pressure has been defined as the cutting force per unit area of the uncut chip and is given by (2.9). In drilling with conventional twist drill the uncut chip area is given by

$$A_c = a_w a_c = \frac{d}{2\sin\kappa}\frac{f\sin\kappa}{2} = \frac{df}{4}. \tag{5.18}$$

Furthermore, the cutting force is related to the drilling torque by the equation

$$F_c = \frac{2M}{d}. \tag{5.19}$$

Combining the above two equations, the specific cutting energy in drilling is given as

$$K_c = \frac{F_c}{A_c} = \frac{8M}{fd^2}. \tag{5.20}$$

Similarly, the specific cutting energy or pressure for the thrust force is given by

$$K_t = \frac{2F_A}{fd}. \tag{5.21}$$

The specific cutting energies for the FRP composites described in Table 5.4 are shown in Fig. 5.47 as a function of $f \cdot d$. The specific cutting energy increases with a decrease in the product $f \cdot d$, which corresponds to smaller uncut chip area, according to the power law relationship

$$\begin{aligned} K_c &= A(f \cdot d)^m, \\ K_t &= A'(f \cdot d)^{m'}, \end{aligned} \tag{5.22}$$

where m and m' are the slopes of the regression lines K_c and K_t, respectively and A and A' are the specific cutting energies for $f \cdot d = 1$. Table 5.5 shows values of the empirical constants for the relationships in (5.22) for several FRPs. It has been shown previously in the case of trimming that the specific cutting energy also increases according to a power law with the decrease in chip thickness. Similar to homogeneous materials, the specific cutting energy term K_c is generally higher than K_t for GFRP and AFRP. The two terms are very close in value for CFRP. The order of magnitude of the specific energy in drilling is comparable to that in turning, but it is substantially smaller than that in trimming. One reason for this is the occurrence of very small chip thicknesses in trimming, which require higher specific cutting energy.

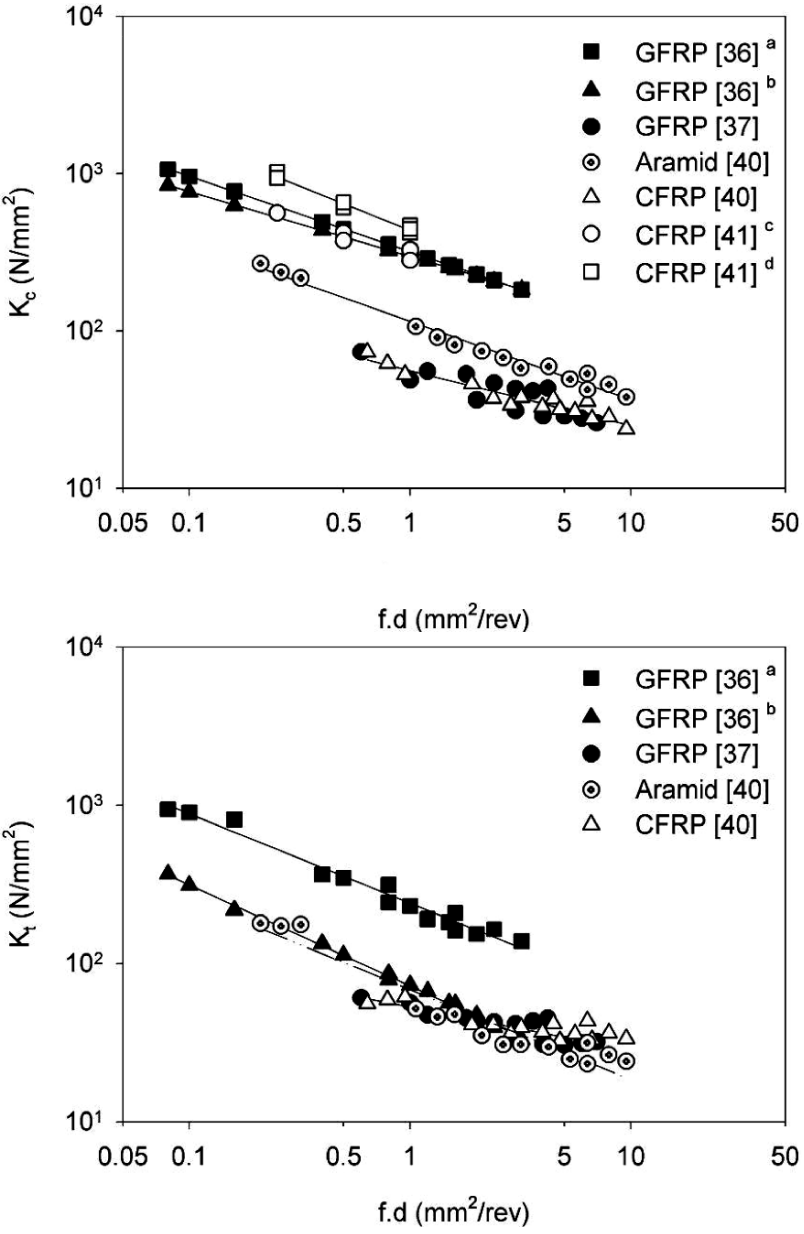

Fig. 5.47 Relationship between specific cutting energy K_c (*top*) and K_t (*bottom*) and the combined parameters $f \cdot d$

Table 5.5 Coefficients of the empirical relationships in (5.22)

Ref	Material	Tool	A	M	A'	m'
[37][a]	UD GFRP	Twist drill	298.062	−0.411	240.247	−0.565
[37][b]	UD GFRP	Trepanning tool	318.827	−0.479	72.002	−0.639
[38]	Chopped E-glass mat	Coated carbide drill	56.151	−0.350	53.170	−0.274
[41]	Aramid CFRP $[0/45]_{43s}$	Twist drill	115.026	−0.501	68.342	−0.570
[41]	CFRP $[0/45]_{39s}$	Twist drill	56.151	−0.350	52.288	−0.211
[42][c]	CFRP [0/90]	Carbide drill	318.827	−0.479	–	–
[42][d]	CFRP [0/90]	Brad and Spur drill	437.407	−0.561	–	–

5.4.3 Cutting Temperatures

Heat generated during drilling of composite materials is distributed differently than when drilling metal parts. In metal cutting a large amount of the heat generated is carried away by the chip. In drilling FRPs a large amount of the heat generated is dissipated by the workpiece and the tool. The spatial and temporal temperature gradients are strongly affected by the thermal conductivity of the workpiece and tool materials. Smaller temperature gradients are observed in carbon–epoxy than in glass–epoxy or aramid–epoxy composites under the same conditions. The cutting temperature in drilling is strongly dependent on cutting speed and feed rate. The upper limit of the cutting speed is limited by the risk of introducing thermal damage to the workpiece material.

The flank surface temperature in drilling CFRP was measured using embedded thermocouples on the flank face behind the cutting edge of double flute twist drills [36, 43]. In this arrangement, the drill is held stationary while the workpiece is rotated by the spindle. This allows inserting thermocouples in miniature holes machined on the flank surface of the drill. Figure 5.48 shows the influence of process parameters on average flank face temperatures. It is apparent that the temperature generated in drilling may reach the melting or decomposition temperature of the polymer matrix. Flank surface temperature increases with an increase in cutting speed. Even though the cutting speed does not have significant impact on the drilling forces, increasing the cutting speed at constant feed causes more heat generation by friction processes and allows less time for heat dissipation through the tool. The influence of feed rate on flank surface temperature varied drastically according to cutting speed and depth of drilled hole. At low cutting speed and for a shallow hole the flank temperature decreased with an increase in the feed rate. A major reason for this is the fact that the higher the feed rate the shorter the cutting time, and hence the lower rise in flank surface temperature. For deeper holes and for high cutting speed the increase in feed rate leads to an increase in flank temperature. Here, the deeper hole drilling and the higher cutting speed provided more time for contact between the cutting tool and the heat source, overriding the effect of feed rate.

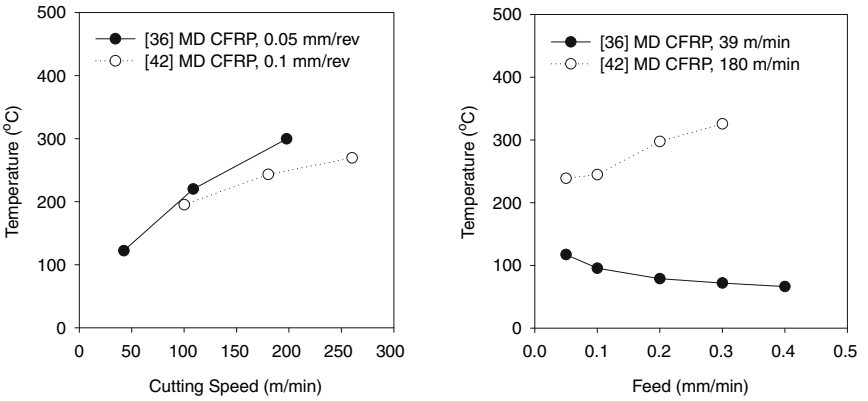

Fig. 5.48 Effect of process parameters on flank face temperature in drilling FRPs. Cutting conditions used in [36]: 2 mm thick multidirectional CFRP panel, carbide drill, drill diameter = 9 mm. Cutting conditions used in [43]: multidirectional (weave) CFRP, $V_f = 0.7$, carbide drill, drill diameter = 8 mm, through hole drilling length 20 mm

5.4.4 Machining Quality

Machining quality in drilling is characterized by the extent of delamination damage, surface roughness, hole edge quality, and roundness. Delamination is an intrinsic problem in drilling layered materials because the drill feed motion and the resulting thrust force acting normal to the stacking plane tend to separate the plies along the weak epoxy layer in between. In addition, different drill point geometries behave differently in terms of delamination response. Delamination leaves cracks between the plies in the drilled component, which may result in degradation of its mechanical performance. Hole surface roughness is measured on the walls of the hole in the direction of the feed. It is influenced by the fiber orientation around the periphery of the hole. It has been shown previously that the chip formation mechanism and the resulting surface roughness are critically dependent on fiber orientation. The drilled edge quality, roundness, and dimensional accuracy are influenced by delamination, tool wear, and cutting temperatures. Distortions to the hole may occur due to the different thermal expansion coefficients along and transverse to the fiber directions and between the polymer matrix and the reinforcement fibers. This may lead to residual stresses and dimensional variations in the hole diameter. Previous studies have shown that proper selection of the drilling parameters and practices is a good strategy for reducing or eliminating some of the problems prone to drilling. The following sections are devoted to the details of the drilling quality and the influencing factors.

5.4.4.1 Delamination

Among the many undesirable features produced by drilling, interlaminar delamination is considered to be the most important one. Delamination is a major concern

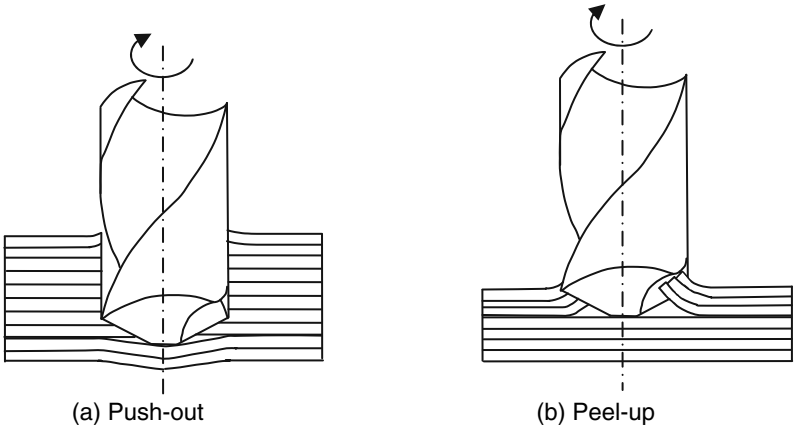

Fig. 5.49 Schematic of push-out delamination at exit and peel-up delamination at entry

in drilling FRPs because it may severely affect the structural integrity and long-term reliability of the machined component [44]. Drilling-induced delamination occurs at the entry and exit planes of the workpiece as illustrated schematically in Fig. 5.49. These are called push-out and peel-up delamination. Two different mechanisms are responsible for delamination on each side of the laminate. The push-out type of delamination has been investigated by video data acquisition in [31] and the damage growth phenomenon has been described in detail. The drill point exerts compressive force on the uncut plies below causing them to bend elastically. As the drill approaches the exit, the number of uncut plies supporting it reduces and the resistance to bending decreases. At a critical thickness the bending stress becomes greater than the interlaminar strength between the plies and an interlaminar crack is initiated around the hole. Further pushing down by the drill point causes the crack to propagate and the flexural rigidity of the supporting plies becomes weaker. This leads to fracturing the material below the drill point as the chisel edge proceed exiting the laminate. The fracture of the bottom surface plies occurs by both Mode I and Mode III fracture. The damage at exit plies is shown as spalling that extends beyond the hole diameter. Peal-up delamination occurs by sliding the pierced plies up the flutes of the drill similar to the action of a power screw. This tends to separate and severely bend the surface plies leading to its fracture under Mode III loading.

The visualization and assessment of delamination damage is a difficult and challenging task because damage is internal and external. Obtaining the size, shape, and location of delamination is necessary for the assessment of machining damage. Optical microscopy and image analysis are often used for measuring the extent of delamination damage at the entry and exit surface plies [42, 45]. Ultrasonic C-Scan has been used to characterize internal delamination damage nondestructively [46]. A delamination factor is defined as the ratio of the maximum diameter of the damage zone to the hole diameter

$$F_{\mathrm{d}} = \frac{d_{\max}}{d} \tag{5.23}$$

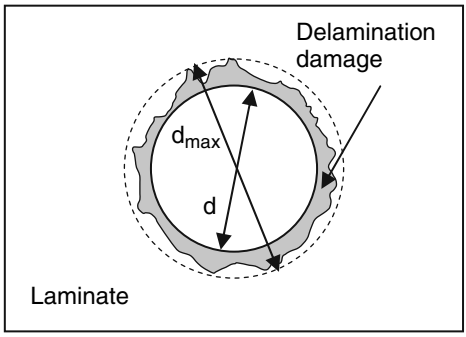

Fig. 5.50 Schematic representation of the delamination factor

is often used to characterize drilling damage and to quantify the effect of process parameters on the extent of delamination. Figure 5.50 shows a schematic explaining the delamination factor.

The onset of delamination and the extent of delamination damage are affected by several process parameters such as feed rate, spindle speed, drill diameter, drill point design, and material configuration. Several studies have pointed out that feed rate is the most influencing parameter to control delamination because of its direct influence on the thrust force. A number of empirical relationships has been developed for several drill geometries to relate the delamination factor F_d and process parameters. A summary of these relationships is given in Table 5.6. These relationships demonstrate the influences of feed rate, drilling speed, and drill diameter on delamination damage. Delamination on the outer surface plies generally increases with an increase in both feed rate and cutting speed. Statistical analysis of the data indicated that cutting speed has the highest statistical and physical significance on F_d [42, 47]. On the other hand, similar studies on glass-fiber-reinforced polymers have shown that feed rate followed by cutting speed have the most statistical and physical significance on F_d [48, 49]. The Brad and Spur carbide drill has the lowest delamination damage, followed by the helical flute carbide drill, the straight flute carbide drill, and the HSS twist drill. This is because delamination is strongly correlated with thrust force, which is in turn dependent on the drill point geometry. The conventional twist drill has a large chisel edge as compared to the Brad and Spur drill (or candle stick drill) and the straight flute drill. Thus it induces higher thrust force and higher tendency for delamination. In addition, HSS twist drill wears much more rapidly than the carbide and the wear-induced thrust force is higher. Statistical analysis of internal damage as measured by ultrasonic C-Scan indicated that feed rate and drill diameter make the largest contribution to delamination damage. The candle stick drill and saw drill were found to cause smaller delamination factor than the twist drill [46].

The thrust force increases with wear to a large extent and delamination damage becomes more prominent with the increase of tool wear. Figure 5.51 below demonstrates the progression of wear and delamination factor with the increase in number of holes drilled. The strong correlation between delamination damage and wear is

Table 5.6 Empirical relationships for delamination factor, F_d in drilling FRPs

Drilling parameters	Delamination factor
Plain weave CFRP with $0/90^\circ$ layup, $V_f = 0.55$, 16 layers with thickness of 4 mm, drill geometry: carbide two-flute helical drill, Brad and Spur drill, 5 mm diameter, feed rates 0.05, 0.1, 0.2 mm/rev, cutting speeds 30, 40, and 50 m/min [42]	Helical flute carbide drill $F_d = 0.923 + 3.463 \times 10^{-3} v + 1.559 f$ (entrance) $F_d = 0.966 + 1.085 \times 10^{-3} v + 0.134 f$ (exit) Brad and Spur carbide drill $F_d = 0.991 + 4.65 \times 10^{-4} v + 0.097 f$ (entrance) $F_d = 1.006 + 1.980 \times 10^{-4} v + 0.021 f$ (exit)
Woven carbon fiber fabric (WFC200)/epoxy matrix, $[0/90]_{12s}$ laminate 5 mm thick, $V_f = 0.55$, all HSS drills, diameters = 6, 8, 10 mm, feed rates 0.01, 0.02, 0.03 mm/rev, spindle speeds 800, 1,000 and 1,200 rpm [46].	HSS twist drill $F_d = 1.961 - 1.81 \times 10^{-4} \mathrm{N} - 10.955 f - 1.77 \times 10^{-2} d$ HSS candle stick drill (Brad and Spur) $F_d = 1.539 - 7.81 \times 10^{-6} \mathrm{N} - 2.274 f - 1.7 \times 10^{-2} d$ HSS saw drill $F_d = 1.508 + 8.681 \times 10^{-6} \mathrm{N} - 3.385 f - 1.49 \times 10^{-2} d$
Material is the same as [42], drill geometry: HSS twist drill, carbide two-flute helical drill, straight four flute carbide drill, 5 mm diameter, point angle 118°, feed rates 0.04, 0.08, 0.15 mm/rev, cutting speeds 16, 24, and 32 m/min [47]	HSS twist drill $F_d = 1.021 + 1.31 \times 10^{-3} v + 0.117 f$ Helical flute carbide drill $F_d = 1.010 - 1.16 \times 10^{-4} v + 0.097 f$ Straight flute carbide drill $F_d = 1.037 + 1.0 \times 10^{-3} v + 0.158 f$

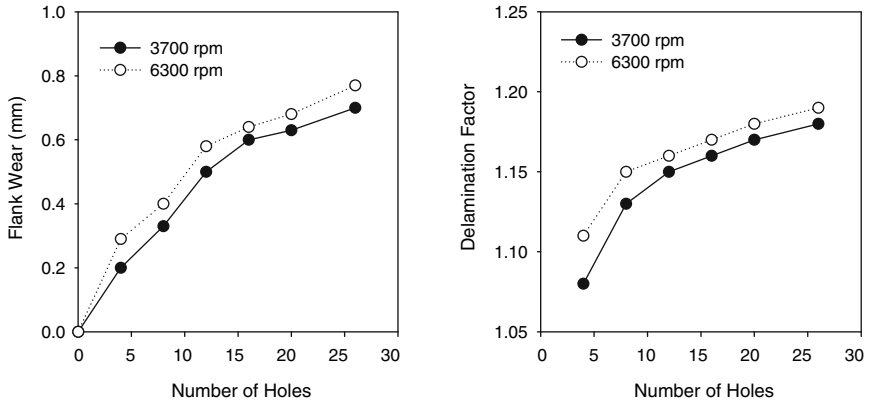

Fig. 5.51 Relationship between delamination factor and flank wear [36]

evident. Delamination becomes serious as the wear rate of the drill rises with the number of drilled holes. The figures also show that delamination becomes more serious as the cutting speed is increased.

5.4.4.2 Surface Roughness

Surface roughness of the wall of the drilled hole is highly dependent on fiber orientation as shown in Fig. 5.52 [23]. The maximum surface roughness occurs at cutting edge positions 135° and 315°, which correspond to fiber orientation $\theta = 135°$ (see Fig. 5.42). At this fiber orientation the fibers are loaded in compression and bending and fail due to compression shear. The bent fibers then bounce back after the cutting edge passes, which creates fuzziness and higher surface roughness. The tangential force and the resulting torque also reach their maximum at this fiber orientation.

Surface roughness is mildly affected by cutting speed and rises slightly with the increase of feed rate in machining CFRP [23, 50]. The arithmetic average surface roughness for thermoplastic CFRP was found to be less than 1 µm for a wide range of cutting speeds and feed rates, which is comparable to the grinding surface of steels. This was attributed to something of the hole surface due to the formation of a recast layer of the matrix. The surface roughness of thermosets was higher (less than 3 µm) due to the brittle fracture of the fibers and matrix. Feed rates below 0.3 mm/rev were recommended for producing finer surface finish. Drilling studies on glass FRPs indicated that surface roughness increases with an increase in feed

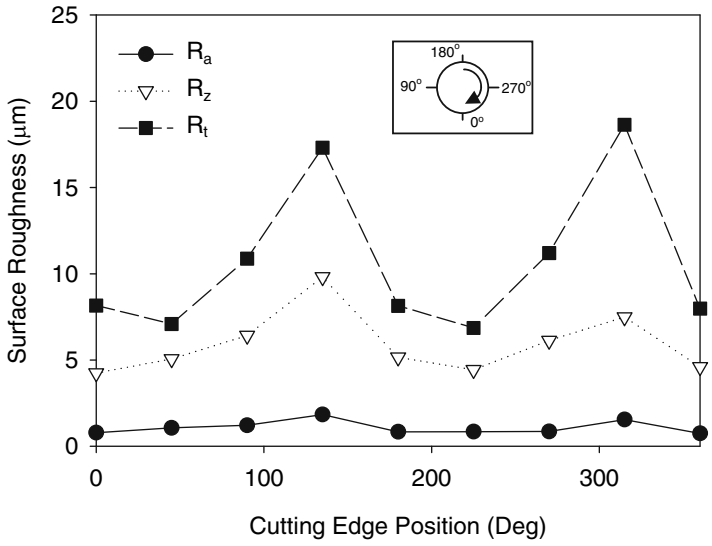

Fig. 5.52 Influence of fiber orientation on surface roughness for drilling unidirectional CFRP laminate ($V_f = 0.6$). Drill diameter = 8.0 mm, cutting speed = 100 m/min, feed rate = 0.08 mm/rev. R_a = centerline average, R_z = average peak to valley height, R_t = peak to valley height [23]

rate and a decrease in cutting speed. Statistical analysis of the arithmetic average surface roughness data also indicated that cutting speed and feed rate have statistical and physical significance on surface roughness. The surface roughness values obtained were in the range from 4 to 8.1 μm, which are considerably higher than those of CFRP [48, 49]. Different tools also produce significantly different results in terms of surface roughness. The Brad and Spur drill produces the lowest surface roughness followed by the carbide drill and the HSS twist drill [49, 50].

5.4.5 Mechanics of Delamination

Delamination occurs during drilling by two distinguishable mechanisms: peeling up of the top layer of the laminate and punching out of the uncut layer near exit as explained earlier. A sharp decrease in the thrust force as the bit enters the workpiece is always associated with the occurrence of delamination by mechanical action of the tool peeling up the top layer of the laminate. Delamination near the exit side is introduced as the tool acts like a punch, separating the thin uncut layer from the remainder of the laminate. This action is associated with an almost instantaneous drop in thrust force from its steady-state value to zero. Several authors have proposed analytical models for delamination mechanisms based on the theory of linear elastic fracture mechanics (LEFM) [32, 33, 40, 51, 52]. In these models, a critical thrust force to the onset of delamination is predicted as a function of the elastic properties of the composite laminate and the drill point geometry. Combining knowledge of the critical force for delamination and existing relationships between feed rate and thrust force allows controlling delamination by controlling the feed rate during the drilling process. In the following sections, predictive models of the onset of delamination are reviewed and their predictions are compared with experimental results.

5.4.5.1 Push-Out Delamination of an Isotropic Laminate

A LEFM model for predicting the onset of exit delamination due to the applied thrust force was first introduced by Hocheng and Dharan [51]. Several simplifications are made in order to perform the analysis. In this model (Fig. 5.53), the laminate structure of thickness H consists of a number of isotropic plies. The modulus of elasticity of the isotropic ply is considered to be the highest modulus of a unidirectional laminate, E_{11}. This allows the analysis to be on the conservative side. The drill is approximated as a cylindrical punch of diameter d and the applied load is assumed to be a concentrated load at the center of the punch. A circular crack of radius $(0.5d + a)$ pre-exists in the structure ahead of the drill point. It is assumed that the crack growth is coplanar and is confined to the plane of the crack. These are conditions that must be met in order for the LEFM theory to be applicable. When drilling a laminate a crack initiates and spreads at the binder interface between the plies, which is a plane of symmetry for the material. Thus, the conditions for LEFM

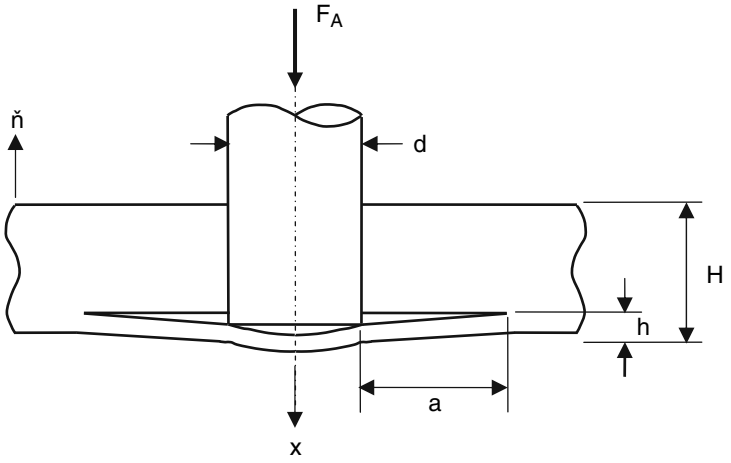

Fig. 5.53 Circular plate model for delamination analysis [52]

are met. The uncut thickness h ahead of the punch is modeled as an isotropic circular plate clamped on its contour to the cut portion of the laminate, which is assumed to be rigid. As the drill cuts downward, this plate is deformed elastically by the action of the applied load F_A at its center. Crack propagation occurs when the elastic strain at its tip goes beyond a critical value.

The energy balance equation from LEFM assuming Mode I crack propagation is given by

$$G\pi(d+2a)\mathrm{d}a = F_A\mathrm{d}x - \mathrm{d}U, \tag{5.24}$$

where G is energy release per unit area. The term on the left side describes the energy required to extend the crack by a distance da. The first term on the right side is the work done by the thrust force F_A as it moves a distance dx and the second term is the elastic energy stored in the circular plate and is given by

$$U = \frac{8\pi M x^2}{\left(a+\frac{d}{2}\right)^2}, \tag{5.25}$$

where M is the flexural rigidity of the plate and is given by

$$M = \frac{Eh^3}{12(1-\nu^2)}. \tag{5.26}$$

The displacement x is expressed as

$$x = \frac{F_A\left(a+\frac{d}{2}\right)^2}{16\pi M}. \tag{5.27}$$

Substituting these equations in the energy balance equation and solving for F_A, the critical load at the onset of delamination is obtained

$$F_A^* = \pi \sqrt{\frac{8 G_{IC} E h^3}{3(1-\nu^2)}} = \pi \sqrt{32 G_{IC} M}, \tag{5.28}$$

where G_{IC} is the critical strain energy release rate in plane strain conditions and Mode I fracture. Plane stain G_{IC} is used instead of G (plane stress) because it can be easily measured. Because G_{IC} is lower than G, this also gives conservative estimates of the critical load for delamination. It is apparent that the thrust force at the onset of delamination is independent of drill diameter when a concentrated load is assumed. The concentrated load condition is best applied to twist drills with narrow chisel point. Experimental validation of (5.28) has shown good agreement with delamination data for twist drills [51].

5.4.5.2 Effect of Drill Point Geometry on Delamination

The model of Hocheng and Dharan [51] was extended by Hocheng and Tsao [52] to include various drill point geometries. Following is a summary of the relationships for critical thrust at the onset of delamination. The reader is referred to [52] for derivation of these relationships.

Saw Drill

A saw drill has cutting teeth around its periphery and thus its thrust force is distributed in such a manner. This allows for better machining quality in drilling. The critical thrust force at the onset of delamination is given as

$$F_S = F_A^* \frac{1}{\sqrt{(1-2s^2+s^4)}}, \tag{5.29}$$

where s is the ratio of drill diameter to circular crack diameter, $s = d/(2a+d)$, and F_A^* is the critical thrust force predicted by (5.28). When the delamination size grows larger than the drill diameter, the ratio s is less than 1 and the critical thrust force predicted for a saw drill (applying circular force to the laminate) is much larger than that predicted for twist drill (applying concentrated load).

Candle Stick Drill

The candle stick drill, also known as Brad and Spur drill, is a modified version of the twist drill where the chisel edge is ground to a point (Fig. 5.56b). The thrust force is applied to the laminate as a concentrated center load plus a peripheral circular load.

The thrust force at the onset of delamination for this drill is given as

$$F_{\mathrm{c}} = F_{\mathrm{A}}^{*} \frac{1+p}{\sqrt{1+p^2(1-2s^2+s^4)}}, \tag{5.30}$$

where $p = p_2/p_1$ is the ratio of the peripheral circular force to the central concentrated force. Since the total thrust force is distributed to the periphery at a ratio p, it is expected that the candle stick drill will allow a larger force at the onset of delamination. The larger the thrust force distribution to the periphery (larger p), the larger the critical thrust force allowed. Physically, the candle stick drill is an intermediate stage between the twist drill and the saw drill. In fact, (5.30) reduces to (5.28) for $p = 0$ (i.e., completely concentrated force).

Core Drill

A core drill is made of a metallic tube of outside diameter d and thickness t, which is impregnated with diamond grit at its end. The thrust force applied by a core drill is a circular force annulus of diameter d and thickness t. The critical force at the onset of delamination is given by

$$F_{\mathrm{R}} = F_{\mathrm{A}}^{*} \frac{1}{\sqrt{1-As^2+Bs^4}}, \tag{5.31}$$

where

$$A = (2-2\beta+(3\beta^2/2)) + (4(1-\beta)^2/\beta(2-\beta))\ln(1-\beta), \tag{5.32}$$

$$B = ((2-4\beta+5\beta^2-3\beta^3+\beta^4)/2) + (2(1-\beta)^2(2-2\beta+\beta^2)/\beta(2-\beta))\ln(1-\beta) \tag{5.33}$$

and $\beta = 2t/d$ is the ratio between the thickness t and the drill radius $d/2$. Since the thrust force is distributed over an annular area rather than concentrated at the center, the core drill provides a higher critical force for delamination than the twist drill.

Step Drill

The step is composed of two stages of twist drill, a primary stage of diameter c and a secondary stage of diameter d, where c is less than d. The thrust force of a step drill after penetration of the primary stage is a circular load that is applied by the lips of the secondary stage. The critical thrust force to the onset of delamination is given by

$$F_{\mathrm{T}} = F_{\mathrm{A}}^{*} \frac{\sqrt{2}}{1-\nu} \times \left[\frac{\{(1-\nu)+2(1+\nu)\xi^2\}^2}{(1+\nu)\{2(1-\nu)(1+2\nu^2)-(12-4\nu+3\nu^2+3\nu^3)\xi^2-8(1+3\nu)\xi^2\ln\xi\}} \right]^{1/2}, \tag{5.34}$$

where $\xi = c/d$ is the primary to secondary stage diameters ratio. The critical thrust increases with an increase in the diameter ratio.

The validity of the above models was checked by comparing their predictions to experimental data in [53] as shown in Fig. 5.54 and Table 5.7. The data was obtained for woven fabric (WFC200) carbon fiber/epoxy prepregs with stacking sequence $[0/90]_{12s}$. The laminate consisted of 24 plies and was 6 mm thick. The fiber volume fraction was 0.55, the Young's modulus was 18.4 GPa, Poisson's ratio was 0.3 and the strain energy release rate was $140\,\mathrm{J/m^2}$. The figure shows that the extent of delamination damage for a given drill point geometry correlates well with the thrust force. A critical thrust force exists below which delamination does not occur. The critical thrust force at the onset of delamination can be experimentally determined by linear extrapolation as shown in the figure and its values are shown in Table 5.7 along with the values predicted by (5.28)–(5.34). It can be seen that

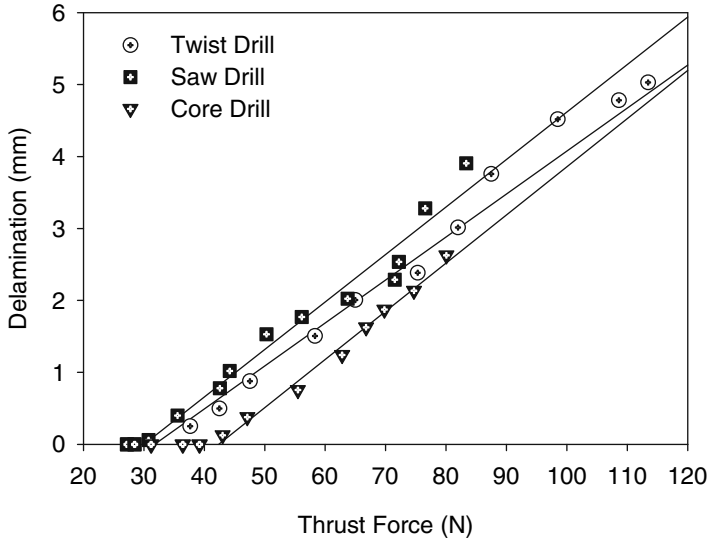

Fig. 5.54 Dependence of delamination on thrust force for three different drill geometries. The twist drill and saw drill were both 10 mm in diameter. The core drill was plated with diamond of 60 grit size at the front end. [53]

Table 5.7 Critical thrust force and feed rate for delamination [52, 53]

Drill bit	Theoretical critical thrust force (N)	Experimental critical thrust force (N)	Critical feed rate ($\times 10^{-3}$ mm/rev)
Twist drill	34.1	31.8	4.7
Saw drill	38.8	30.5	5.1
Candle stick drill	36.2	26.4	6.9
Core drill	48.4	42.7	7.5
Step drill	31.4	29.1	4.9

model predictions are good for the twist drill, core drill, and step drill. The step drill provides a relatively low critical force for delamination, followed by the twist drill while the core drill provides the highest. Corresponding critical feed rates above which delamination will occur have also been determined experimentally and shown in Table 5.7. It can be seen that the core drill provides the highest feed rate for safe drilling without delamination. Once the critical thrust force is known, the critical feed rate for delamination can also be determined from empirical relationships listed in Table 5.4.

5.4.5.3 Push-Out Delamination of Anisotropic Laminate

The previous analysis assumed isotropic properties of each ply in the composite laminate. In reality, the unidirectional ply is highly anisotropic and the crack geometry in reality may not be circular. Jian and Yang [33,33] introduced a LEFM model for delamination in unidirectional laminates with an elliptical crack geometry. The principal directions of the laminate are aligned with the major and minor axes of the elliptical crack. The critical thrust force at the onset of delamination is found to be a function of elipticity of the crack and is given by

$$F_{\mathrm{A}}^{*} = 3\pi \left(\frac{b}{a}\right) \sqrt{2G_{\mathrm{IC}} D^{*}}, \tag{5.35}$$

where a and b are half major and minor axes of the elliptical crack that are aligned along the longitudinal and transverse directions, respectively. D^{*} is an expression of the stiffness of the laminate and is given by

$$D^{*} = D_{11} + \frac{2(D_{12} + 2D_{66})}{3} \left(\frac{a}{b}\right)^{2} + D_{22} \left(\frac{a}{b}\right)^{4} \tag{5.36}$$

and in turn Ds are the bending stiffness matrix terms for pure bending due to an out-of-plane load and are given by

$$\begin{aligned} D_{11} &= \frac{E_{11} h^{3}}{12(1 - \nu_{12}\nu_{21})}, \quad D_{22} = \frac{E_{22} h^{3}}{12(1 - \nu_{12}\nu_{21})} \\ D_{12} &= \frac{\nu_{12} E_{22} h^{3}}{12(1 - \nu_{12}\nu_{21})} \quad \text{and} \quad D_{66} = \frac{E_{66} h^{3}}{12}. \end{aligned} \tag{5.37}$$

The critical thrust force is a function of elipticity ratio a/b, and minimizing F_{A}^{*} with respect to a/b results in a value of $a/b = (D_{11}/D_{22})^{1/4}$. Higher values of thrust force result in higher values of a/b. Since the goal is to eliminate delamination altogether, the minimum value of a/b is substituted in (5.35) and the expression for critical thrust force for delamination becomes

$$F_{\mathrm{A}}^{*} = 3\pi \sqrt[4]{\frac{D_{22}}{D_{11}}} \sqrt{2G_{\mathrm{IC}} D c^{*}}, \tag{5.38}$$

where

$$Dc^* = 2D_{11} + \frac{2(D_{12} + 2D_{66})}{3}\sqrt{\frac{D_{11}}{D_{22}}}.$$

Combining (5.38) with the appropriate equation for feed rate from Table 5.4, an expression can be found for the critical feed rate for delamination. For example, the empirical relationship for T300/5208 unidirectional composite drilling with twist drill is given by:

$$F_A = 0.136 H_B d^{0.78} f^{0.4}. \tag{5.39}$$

When this equation is combined with (5.38) the corresponding critical feed for delamination is obtained as

$$f^* = \left\{ \frac{3\pi}{0.136 H_B d^{0.78}} \sqrt[4]{\frac{D_{22}}{D_{11}}} \sqrt{2 G_{IC} Dc^*} \right\}^{2.5}. \tag{5.40}$$

5.4.6 Recommended Practices

The analytical models discussed above imply that delamination is likely to occur at the interfaces near the exit side of a drilled hole when the applied thrust force exceeds a critical value. A strategy is often used to avoid introducing delamination is to reduce the thrust force (by reducing the feed rate) as the tool reaches the exit side so that the thrust force remains below the critical value. Using variable feed rate to slow the feed at entry and exit while drilling in between at the highest possible feed rates allows for delamination free drilling and high productivity. It was shown in [33] that manipulating the feed rate provides good results for twist drill diameters below 6 mm. Figure 5.55 shows an example of CNC programming used to drill a hole using variable feed rate strategy. The feed rate for each step was calculated using the analytical models shown above so that the thrust force is always below the critical thrust force for delamination at the particular thickness of the step. For larger drill diameters, modifying the drill point geometry by reducing the chisel edge width becomes necessary for delamination control to become possible [40]. Another approach to delamination control is to increase stiffness of the bottom ply of the laminate. Increasing thickness of the bottom ply and using a support plate have been shown to be effective in reducing delamination. The thicker the last ply thickness the larger the critical thrust force allowed. Thus, whenever possible, thicker plies must be used at the bottom of the laminate.

Delamination in thick composite parts may also be avoided by drilling from both sides of the laminate with a diamond tipped hole saw (core drill). The laminate is drilled half way through the thickness from one side then cut through from opposite side. All the cutting forces acted at the center of the laminate and there is no resultant force pushing out the bottom of the hole. This process may be accomplished as an N/C operation and with using coolant. While this practice is not practical for small

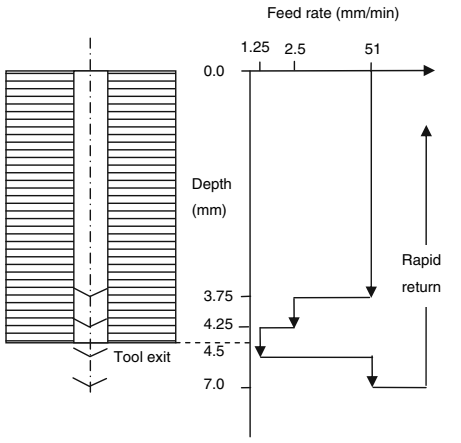


```
*** Sample program to cut  a hole with variable ***
*** feed rate in 4.5 mm CFRP laminate ****

G90 G92 X0.0 Y0.0 Z2.0;   Sets up the tool start position
G00 Z0.02 M03 S40;        Spindle rotates at 1200 rpm,
                          tool rapidly moves to 0.5 mm
                          from workpiece
G01 Z-0.15 F2.0;          Tool drills to a distance of
                          3.75 mm at 51 mm/min
G01 Z-0.17 F0.1;          Tool drills to a distance of
                          4.25 mm at 2.5 mm/min
G01 Z-0.22 F0.05;         Tool drills to a distance of
                          5.5 mm at 1.25 mm/min
G01 Z-0.28 F2.0;          Tool continues to 7mm depth
                          at 51 mm/min
G00 Z2.0;                 Tool rapidly returns to
                          starting position
M05;                      Spindle stops
M30;                      Program ends
```

Fig. 5.55 Variable feed rate strategy and associated CNC program for delamination free drilling of unidirectional laminate [33]

diameter holes, it is a reasonable solution for larger holes. However, this operation inevitably leaves a little material at the center of the hole to be removed with a finish operation if required.

Thrust force is closely correlated to drill wear and care must be taken to ensure good control of drill wear. This is done by selecting proper tool materials and drill point geometry that will result in reducing the rate of tool wear. Drill bits made of HSS fail after drilling just a few holes when drilling GFRP and CFRP because of the high abrasiveness of these materials. Tungsten carbide drills, particularly submicrometer grades possess adequate tool life because of their higher rupture resistance and hardness. Wear resistance is also increased by applying diamond coating and PCD-tipping. However, these drills can be easily chipped, particularly when used with portable drills. Best results are obtained when drilling with solid carbide straight flute drill or diamond-coated twist drill.

Drill wear is also closely related to tool temperature, and hence control of the cutting temperature is extremely important for controlling tool wear and reducing thermal damage to the machined part. Parts have been scrapped because of damage due to extreme heat build up deep in the laminate. It is recommended that approved coolants be used whenever possible. In addition, a peck cycle can be used to drill thick composite laminates on computer-controlled machines. Selection of tool material for better heat channeling out of the drilled hole may also be considered. This includes PCD-tipped and diamond-coated drills which provide high thermal conductivity.

Proper selection of drill point geometry is also extremely important for controlling the thrust force. Analytical models discussed above and supported by experimental data have shown that higher critical thrust force at the onset of delamination is achieved by distributing the forces away from the center of the drill

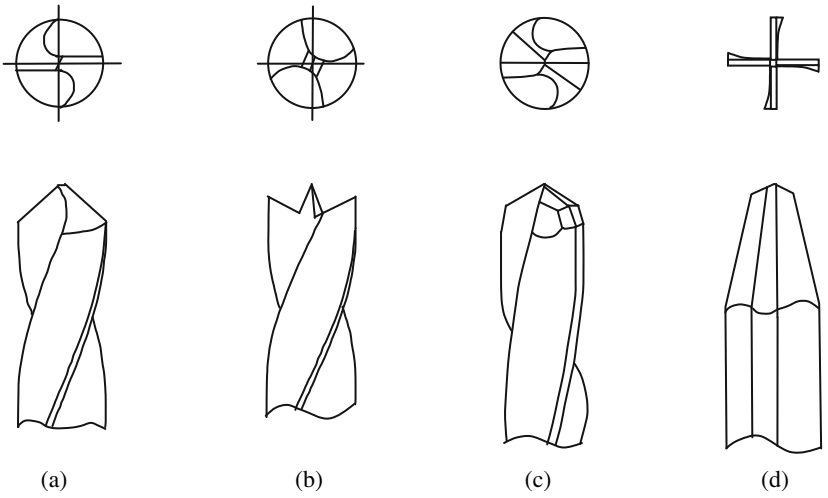

Fig. 5.56 Different drill point designs (**a**) standard twist drill, (**b**) candle stick drill, (**c**) multifaceted drill, (**d**) straight flute drill

(i.e., avoiding concentrated force). Among the drill point designs shown in Fig. 5.56, the candle stick drill (b) and the straight flute carbide drill (d) produce the lowest delamination damage, where the style (b) drill works best in thin laminates. This is because both drills have smaller chisel edge width which results in significantly reducing the thrust force. It was shown in [33] that the chisel edge contribution to the thrust force is as high as 40–60%. Large reduction in thrust force is also achieved when a pilot hole is used [40]. A solid carbide drill with an eight-facet split point (c) has also been proved effective. The success of the eight-facet drill is attributed to the long taper angle at the shoulder, which tends to minimize fiber breakout.

5.5 Abrasive Machining and Grinding

Abrasive machining and grinding remove material by the action of the motion of small hard particles attached to a relatively rigid body. The hard phase is typically aluminum oxide, silicon carbide, cubic boron nitride, or diamond particles. Grinding is a major manufacturing process and has received much attention by the scientific community. Abrasive machining, to the contrary, is a relatively new practice and has received very little attention. However, the similarities between grinding and abrasive machining might in many instances be sufficient to bridge the gap in knowledge and facilitate the transfer of experience from grinding to abrasive machining. Abrasive machining has particular aspects that make it somewhat different than grinding. Differences between the two processes fall mainly in three process

Table 5.8 Comparison between typical ranges of process parameters in abrasive machining and grinding

Parameter range	Abrasive machining	Grinding
Typical cutter/wheel diameter (mm)	6–25	Up to 1,000
Cutting speed, v (m/min)	100–500	1,500–5,000
Workpiece feed rate, v_f (m/min)	0.25–1.00	5.0–50.0
Radial depth of cut, a_e(mm)	1.00 – Full tool diameter	0.01–0.05
Equivalent chip thickness, h_q (μm)	2.00–50	0.01–0.1
Material removal rate, Z_w (cm^3/min)	10–100	1.00×10^{-5}–2.50×10^{-4}

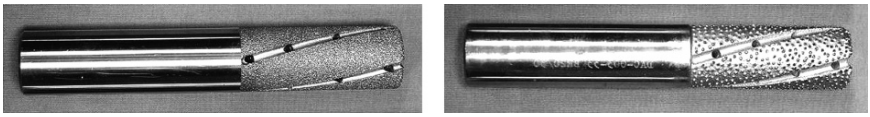

Fig. 5.57 Typical diamond abrasive cutters with fine 80 grit (*left*) and coarse 30 grit (*right*). Flutes and coolant holes are incorporated in the cutter for ease of debris removal and cooling

parameters: depth of cut, wheel or cutter diameter (and the resulting velocity), and workpiece feed rates. Table 5.8 lists some of the common ranges of parameters for grinding and abrasive machining. Straight surface grinding utilizes depths of cut in the range from 10 to 50 μm. Typical wheel velocities are 1,800 m/min, although faster velocities up to 7,000 m/min are used in some cases. The workpiece velocity is much slower than the wheel velocity, with a typical ratio of 100–200 is used [54]. Abrasive cutters have small diameters as compared to grinding wheels and are used for more massive material removal. The cutting speed and the workpiece feed are relatively lower but the depth of cut is higher. As a result, abrasive machining equivalent chip thickness is considerably larger, the material removal rate is higher, and the surface roughness is higher than those for grinding.

5.5.1 Abrasive Machining

Abrasive machining is used in edge trimming and bulk machining (milling) of FRP components instead of machining with a defined edge cutter. The primary motives being an almost complete elimination of delamination and an improved surface finish [55, 56]. Figure 5.57 shows typical diamond abrasive cutters used in edge trimming and machining of FRPs. The abrasive particles are diamond grit of various sizes attached by metallic bond to the tool shank. The 30 grit cutter is a general purpose cutter used for roughing applications since it has large diamond grains and wide gain spacing, allowing for better chip disposal. The 80 grit cutter has denser concentration of small diamond particles and is better suited for finishing applications. There are two techniques for bonding the diamond grit to the tool shank,

namely electroplating and brazing [57]. In both methods a single layer of diamond particles is attached to the tool shank with a metal bond. Electroplating involves immersing a steel tool shank in a nickel plating solution with suspended diamond particles. The nickel ions build up on the steel shank between the diamond particles, tacking a single layer of particles to the surface of the tool. The tool is then overplated with nickel until approximately 50–70% of the diamond particle is covered by the bond matrix. Electroplating results in high density of diamond particles with low grain exposure. This reduces the clearance required for chip disposal and causes heat build up and rapid tool wear. In the brazing technique, diamond grit and a nickel-chrome braze alloy are applied to the surface of the steel shank. The tool/diamond combination is then heated to melt the braze alloy. The braze alloy bonds to the steel substrate and to the diamond particles, individually setting each diamond particle and bonding it to the steel shank. Brazing allows greater control of the diamond particles density and distribution. This results in high grain exposure and allows for maximum clearance for chip disposal.

The mechanics of cutting with abrasive particles is similar to edge trimming with multiple-edge cutting tools. The kinematics of machining with fixed abrasives has been discussed in Sect. 2.6. Each abrasive grit on the cutter acts as a single point cutting edge with a large negative rake angle and a wide edge angle (see Fig. 2.11). An equivalent chip thickness, h_q, as given by (5.7) is used to characterize the uncut material size. For an abrasive cutter of 25 mm diameter rotating at 5,000 rpm and trimming 2 mm off a workpiece at a feed rate of 2 m/min the equivalent chip thickness obtained is 0.01 mm. When edge trimming with a single-edge cutter at the same cutting parameters, the maximum chip thickness obtained is significantly higher at 0.217 mm. Because the specific cutting energy is power law proportional to the reciprocal of the chip thickness, the specific cutting forces in abrasive machining are significantly greater than those in edge trimming with an end mill. However, the cutting forces are distributed over many small abrasive particles that are engaged in the cut at the same time and the influence of each individual grit on the workpiece is minimized. This allows for less mechanical damage to the workpiece and better surface finish.

5.5.1.1 Cutting Forces and Specific Cutting Energy

The cutting forces in abrasive machining are measured in the feed direction and normal to the feed direction as shown in Fig. 5.58. The axial force is almost absent because of the arbitrary distribution of the grit on the tool periphery and the absence of organized oblique cutting. Each individual grit may have oblique faces engaged in cutting, but these are randomly oriented and their net effect in oblique terms is negligible. And even though a helical flute may be incorporated in the cutting tool design as shown in Fig. 5.57, there is no continuous cutting edge along the flute direction that would act as an inclined cutting edge, and hence the absence of oblique cutting. Cutting forces in abrasive machining are dependent on feed rate and grit size as shown in Fig. 5.58. The cutting forces generally increase with an increase

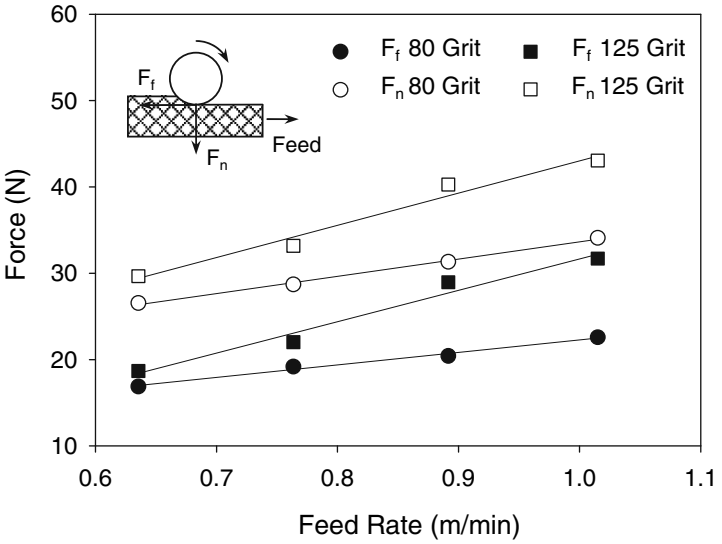

Fig. 5.58 Dependence of cutting forces on feed rate and grit size when machining CFRP multidirectional laminate. Workpiece: woven carbon fibers/epoxy IM-6/3501-6, workpiece thickness = 8.71 mm, tool diameter = 12.7 mm, spindle speed = 10,000 rpm, radial depth of cut = 0.51 mm, water soluble synthetic coolant used [55]

in feed rate and a decrease in grit size (an increase in grit number). Increasing the feed rate while holding the cutting speed and radial depth of cut constant results in a proportional increase in equivalent chip thickness and a proportional increase in the forces required to remove the chip. Cutting tools with finer grit have greater particle density and lower particle clearance for chip disposal. This results in a greater number of particles engaged in cutting, and greater depth of engagement for each individual particle. Also, the frictional forces are higher because of the grain shallow clearance. This explains the higher dependence of cutting forces on feed rate for the finer 125 grit cutting tool. For both cutting tools, the normal force is substantially higher than the feed force. This is characteristic of FRP machining at small depths of cut because frictional forces dominate the cutting mode. As the depth of cut is increased, the feed force becomes higher than the normal force [55, 56].

The specific cutting energy in abrasive machining is defined by the relationship [54]

$$u = \frac{P}{Z} = \frac{F_f v}{a_e a_w v_f}, \tag{5.31}$$

where P is the cutting power, F_f is the feed force, v is the cutting speed, Z is the volumetric material removal rate given by the product of the radial depth of cut, a_e, the width of cut, a_w, and the feed rate, v_f. This expression represents an overall cutting energy quantity, as opposed to K_c, the instantaneous specific cutting energy defined for milling operations, because the instantaneous cutting force for each grit cannot be easily determined. Typical specific cutting energy values for abrasive machining

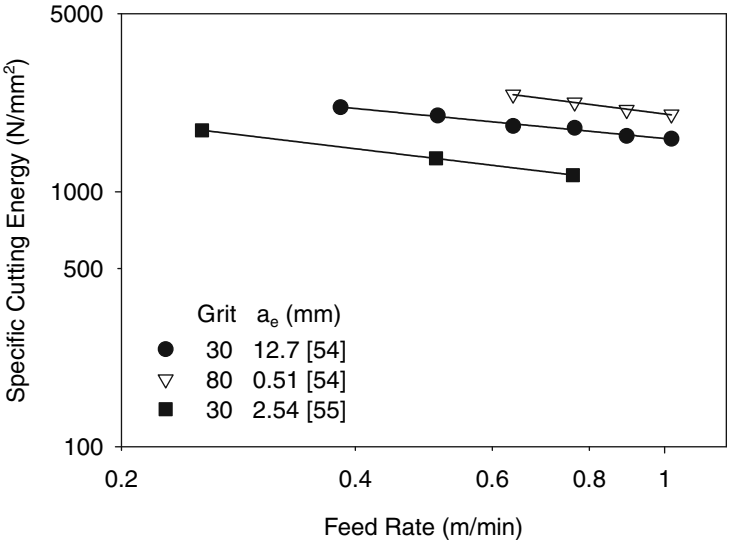

Fig. 5.59 Dependence of cutting forces on feed rate and grit size when machining CFRP multidirectional laminate. Cutting conditions for [55] depth of cut for 30 grit tool = 12.7 mm, depth of cut for 80 grit tool = 0.51 mm, other conditions are the same as Fig. 5.58. Spindle speed for [56] = 4,000 rpm, all other parameters are the same as [55]

of CFRP are shown in Fig. 5.59. Similar to the behavior in milling and drilling, the specific cutting energy decreases with an increase in feed rate according to a power law relationship. However, it is apparent that the specific cutting energy required for abrasive cutting is significantly higher in magnitude than that required for drilling and milling. This is particularly due to the smaller equivalent chip size involved and explains the higher specific cutting forces and temperatures involved in abrasive machining.

5.5.1.2 Machining Quality

The surface topography in abrasive machining is generated by the traces of the individual abrasive particles on the machined surface. Therefore, surface roughness in abrasive machining is critically dependent on grit size and not highly dependent on feed rate [55]. The machined surface has a pattern of parallel groves that run along the machined surface in the direction of feed speed. The size of grooves, and thus the resulting surface topography generally correlates with the abrasive grain size as shown in Fig. 5.60.

Feed rate does not appear to have a significant effect on surface roughness for small depth of cut and for fine grit cutters [55, 56]. Also for fine grain size the cutting configuration has no influence on surface roughness [55]. For larger depth of cut and for large grit size up cutting consistently produces better surface finish

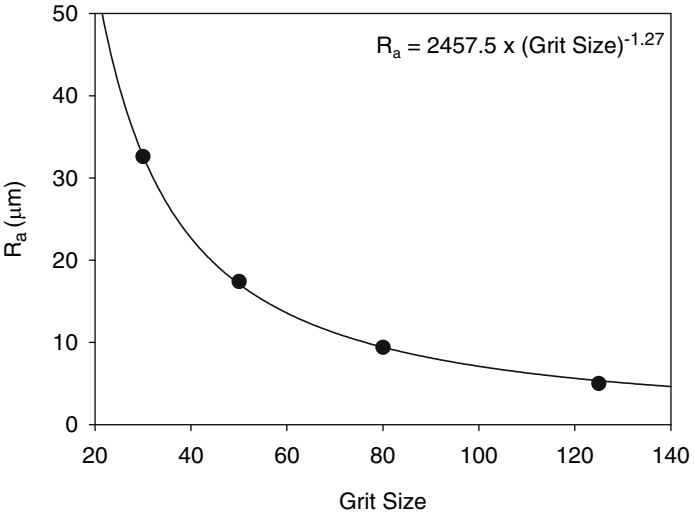

Fig. 5.60 Relationship between surface finish and abrasive cutter grit size [55]

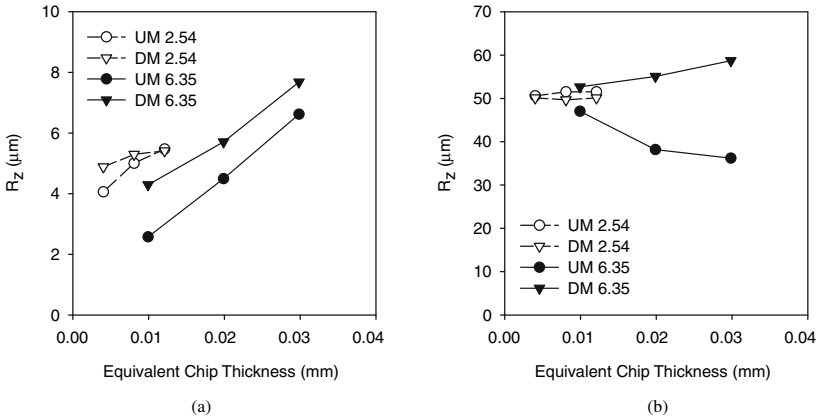

Fig. 5.61 Effect of equivalent chip thickness and cutting configuration on surface finish in abrasive machining of CFRP, (**a**) longitudinal direction, (**b**) transverse direction. Cutting tool grit size 30, tool diameter = 12.7 mm, spindle speed = 4,000 rpm, UM = up (conventional) cutting, DM = down (climb) cutting [56]

than down cutting. The influence of these cutting parameters on surface roughness may be interpreted by considering the interaction between maximum equivalent chip thickness, chip size per abrasive grain, and grain clearance for chip disposal. Figure 5.61 shows the effect of equivalent chip thickness and cutting configuration on surface roughness in abrasive machining of CFRP multidirectional laminate with 30 grit cutter. Surface roughness is measured along the cutting direction and in the transverse direction. For a given spindle speed, the effective chip thickness is proportional to the product of the radial depth of cut and feed rate. Thus, increasing

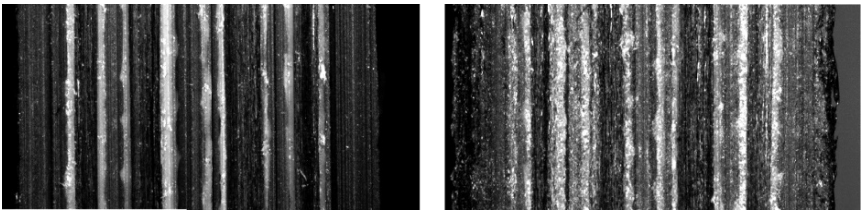

(a) (b)

Fig. 5.62 Topography of the machined surface for CFRP multidirectional laminate. Cutting tool diameter = 12.7 mm, grit size = 30, depth of cut = 6.35 mm, spindle speed = 4,000 rpm, machining direction is from *top* to *bottom*, (**a**) feed rate = 0.254 m/min, $h_q = 0.01$ mm, (**b**) feed rate = 0.762 m/min, $h_q = 0.03$ mm

either one produces proportionally larger effective chip thickness. It is shown that surface roughness in the longitudinal direction is much smaller than that in the transverse direction and is strongly influenced by effective chip thickness. Up cutting also produced better surface finish than down cutting. This is in agreement with the kinematics interpretation of surface roughness (2.55) where h_q in abrasive machining is analogous to a_f in end milling. Surface roughness in the transverse direction is probably controlled by the grooves left behind by the abrasive grains and is less dependent on effective chip thickness. This is the case for down cutting and for small depth of cut, whereas for up cutting the transverse surface roughness decreases with an increase in effective chip thickness.

Topography of the machined surface at two different feed rates is shown in Fig. 5.62. The surface topography is marked by grooves that run along the cutting direction. For the smaller feed rate (smaller h_q) the surface appears to be smoother and the different plies making the laminate are easily resolved. Both left and right edges of the machined surface are neatly cut and are free of damage. For the higher feed rate (larger h_q) the surface is showing considerable fuzziness and smearing of the matrix. The plies making up the laminate are not easily resolved and evidence of damage to the left and right edges of the workpiece is clear. Except of the damage to the edges, the machined surface is free of delamination. The low values of surface roughness and good quality of the machined surface make abrasive machining superior to edge trimming for finish and rough machining of FRPs. Care must, however, be exercised to ensure proper disposal of the chips in order to reduce cutter loading and frictional heat build up. It is recommended in most abrasive machining applications that light cuts are taken and plenty of coolant is used to flush out the debris and to cool machined surface.

5.5.2 Grinding

Grinding is a finishing abrasive machining process whereas the depth of cut to tool diameter ratios are typically very small (in the order of 0.0001) and the cutting

speeds are typically much higher than the workpiece feed rate (typical ratios of 100–200). As a result, the size of chip removed by each abrasive grain is extremely small (smaller than the fiber diameter) and the length and radius of curvature of the chip are very large as compared to its thickness. In essence, the shape of the undeformed chip is almost triangular and the action of each abrasive grain in removing the chip is similar to linear machining with very large rake angle. Furthermore, the angle of engagement of the wheel is very small in comparison to milling and abrasive machining. Therefore, the fiber orientation relationship to the cutting grain motion is almost constant throughout the latter engagement in the workpiece. Consequently, the chip formation mechanism and cutting forces during grinding of a given laminate will vary only as a function of the chip thickness. Due to the small size of the chip, specific grinding forces are relatively high and the generated temperatures due to sliding friction are significant. The use of coolant in grinding is therefore necessary to keep the material temperature below the maximum operating temperatures of the polymer matrix. Kinematics of grinding is discussed in Chap. 2 and for more in depth treatment of the grinding process the reader is referred to [54].

5.5.2.1 Cutting Forces and Specific Cutting Energy

Grinding forces are mainly dependent on chip thickness and fiber orientation of a laminate. For a given wheel speed and workpiece feed rate, the chip thickness is proportional to the wheel depth of cut. Figure 5.63 shows the grinding forces per unit width of cut in the feed (also called tangential) direction and normal to the feed direction in down grinding of unidirectional and multidirectional CFRP laminates. The multidirectional laminate has 24 plies with stacking sequence $[(0^\circ/90^\circ/45^\circ/-45^\circ)_3]_s$. The fiber orientation convention in this figure is the same as that in Fig. 3.7. For the purpose of comparison, the figure also shows the cutting and thrust forces for orthogonal machining with -20° rake angle single point cutting tool [58, 59]. The horizontal grinding force increases with an increase in fiber orientation from 0 to 60° and then decreases with further increase in fiber orientation. The normal grinding force exhibits a somewhat similar behavior for the two lowest grinding depths of cut where a maximum in the normal force is obtained at approximately 90°. On the other hand, the horizontal force for orthogonal machining reaches its maximum at fiber orientation of 120° while the normal force reaches a maximum at approximately 60°. For the same depth of cut, the grinding forces for multidirectional laminate are slightly higher than the maximum grinding forces for laminate orientation of 60°. The reason may be that plies with different fiber orientations support each other more strongly and provide more resistant to grinding [59]. The behavior of grinding and cutting forces is closely related and in both cases is influenced by fiber orientation. For shallow positive fiber orientations the fibers are broken by buckling and fracture due to bending stress. The forces required for buckling the fibers are relatively low. Examination of the chips produced from grinding parallel to the fibers reveals the existence of long and short fiber segments that may have been produced by this type of fracture. As the fiber orientation angle

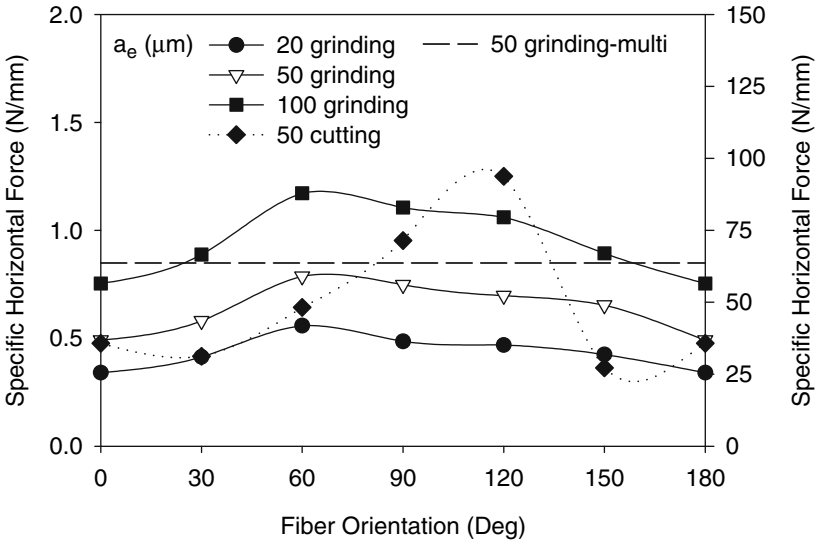

(a)

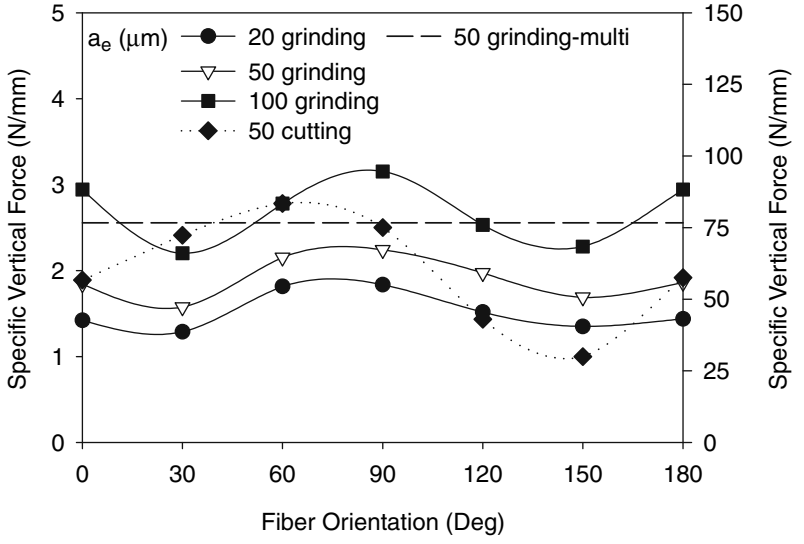

(b)

Fig. 5.63 Variation of horizontal grinding force (**a**) and vertical grinding force with fiber orientation. Cutting forces from orthogonal machining are shown for comparison. Grinding wheel designation BWA36HVAA, $v = 25\,\mathrm{m/s}$, $v_f = 4\,\mathrm{m/min}$. Orthogonal cutting speed = 1 m/s [58, 59]

increases, the fibers become subjected to tensile loading and fracture due to tension and compression shear. This mode of fracture requires the greatest forces and produces powdery dust containing small fragments of fibers. Further increase in the fiber orientation angle subjects the fibers to severe bending and fracture occurs due to bending stress and the forces for fracture become smaller. This influence of the fiber orientation on grinding forces becomes more profound with increasing depth of cut and almost fades away at very small depth of cut. This is apparently because material removal at the small depth of cut is most likely dominated by noncutting mechanisms such as plowing and smearing.

There is an apparent shift in the location of the maximum horizontal grinding force in comparison to that in orthogonal cutting. This shift is perhaps due to differences in rake angle. The rake angle of an abrasive grit is believed to be very large ($> -60^\circ$) as compared to the -20° rake angle used in orthogonal cutting. The effect of rake angle on fiber deformation and fracture is better understood by considering the angle between the tool rake face and the fibers. This angle is called the effective fiber orientation angle and was found to have a significant effect on the mode of chip formation in orthogonal cutting of unidirectional GFRP [60]. The effective fiber orientation angle is defined as

$$\theta_e = 90 - \theta + \alpha. \tag{5.32}$$

In essence, cutting a 30° unidirectional laminate with -20° rake angle tool produces similar effects to cutting a 10° laminate -40° rake angle tool because in both cases the effective fiber orientation angle is 40°. Thus, increasing the magnitude of negative rake angle has similar effect on chip formation to reducing the fiber orientation.

The depth of cut in grinding has a significant effect on the forces generated. It is noted that the normal grinding force is several orders of magnitude (3–4 times) higher than the horizontal grinding force. The difference between the normal force and the horizontal force become smaller as the depth of cut is increased. In addition, the normal force in orthogonal cutting is only slightly higher than the horizontal force. The effect of depth of cut on grinding forces is better understood when put in the context of equivalent chip thickness, which is proportional to the depth of cut and the feed rate to wheel speed ratio as given by (5.7). Figure 5.64 shows the relationship between horizontal and normal tool forces and equivalent depth of cut for abrasive machining, grinding, and cutting of CFRP. It is evident that both horizontal and vertical tool forces increase according to a power law with an increase in equivalent chip thickness. A critical chip thickness exists below which the normal force is greater than the horizontal force. The difference between the normal and horizontal forces is proportional to the distance either way from the critical chip thickness. It is believed that this critical chip thickness represent the transition in chip formation mode from noncutting to fiber cutting mechanisms.

The specific cutting energy calculated by (5.31) is shown in Fig. 5.65 for the same horizontal force data in Fig. 5.64. It is shown that the specific cutting energy increases according to a power law with a decrease in the equivalent chip thickness

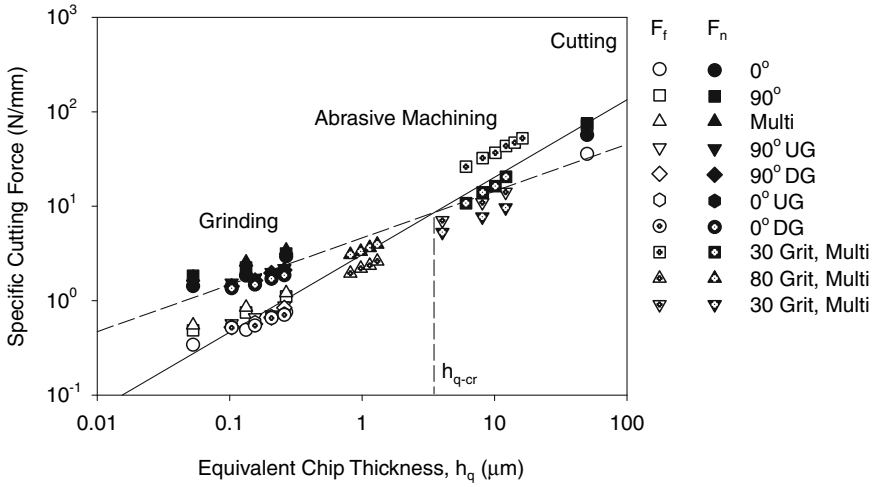

Fig. 5.64 Effect of equivalent chip thickness on horizontal and vertical specific cutting forces in orthogonal cutting, abrasive machining and grinding of CFRP. Data from [55, 56, 58, 59, 61]

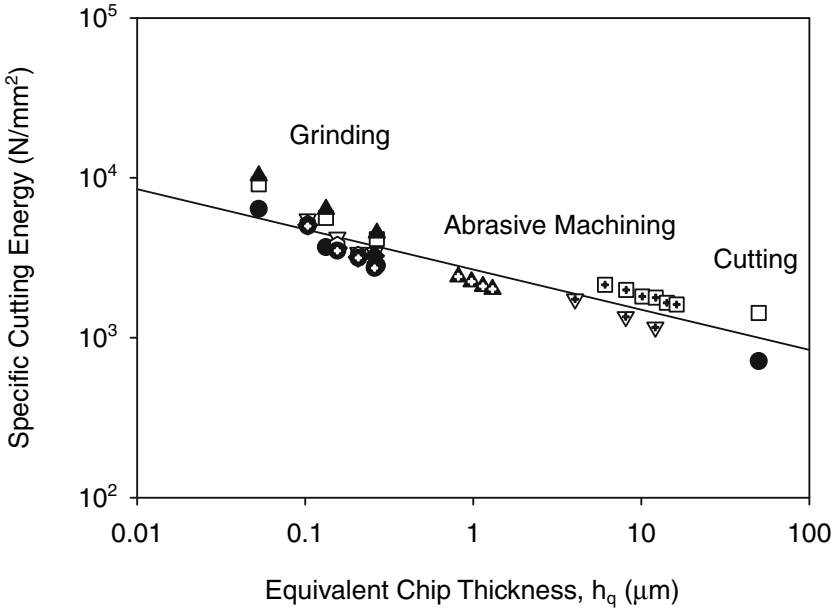

Fig. 5.65 Effect of equivalent chip thickness on horizontal specific cutting energy in orthogonal cutting, abrasive machining, and grinding. Symbols in this figure have the same meaning as Fig. 5.64

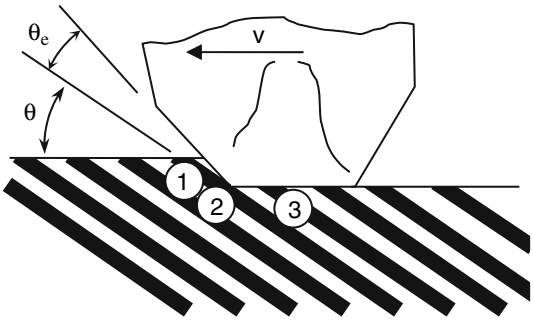

Fig. 5.66 Energy expenditure in cutting with an abrasive particle. (1) cutting zone, (2) pressing zone, and (3) sliding zone

(i.e., smaller depth of cut, smaller feed rate, and large wheel speed). Furthermore, the specific cutting energy for grinding is much larger (as high as ten times) than that required for cutting. Similar phenomenon is described when grinding metals and is believed to account for energy expenditure in noncutting mechanisms. For example, the specific energy in grinding steels is 2–6 times higher than the melting energy per unit volume of the metal. Since the melting energy per unit volume is the limiting energy for plastic deformation (which accounts for chip removal in metals), it is believed that other mechanisms besides plastic deformation are responsible for this energy consumption. Two secondary mechanisms are proposed to explain this anomaly, namely sliding and plowing [54].

Figure 5.66 illustrates the different zones of energy expenditure when cutting with an abrasive grain. The exact partition of the total cutting energy between the three zones is not known and only qualitative assessment of the influencing factors can be made at this point. The cutting zone accounts for energy expenditure due to fiber cutting by microfracture due to one or more of several loading configurations, depending on the effective fiber orientation angle, which include direct or compression shear, bending, and tensile loading. This accounts for the bulk of energy expenditure when cutting with a sharp tool and a large depth of cut to tool nose radius ratio. In grinding, however, this energy might be only a small fraction of the total energy expenditure because of the small chip thickness and shallow effective fiber orientation angle. Energy expenditure in region 2 occurs because of pressing of the fibers and matrix under the wear flat without material removal. Such a mechanism has been discussed in Sect. 3.3.1.1 in relation to cutting with a nose-radiused tool. Its contribution to the total energy expenditure is dependent on the elastic properties of the FRP and the coefficient of friction. Energy expenditure in region 3 occurs because of the existence of wear flats on the abrasive grain sliding against the workpiece surface without removing any material. Limited experimental work has shown so far that the horizontal and normal grinding forces increase linearly with the increase in the area of wear flats on the grinding wheel [56]. The sliding forces are influenced by the grit size and amount of wheel wear. The rise in the normal force and specific cutting energy at values of equivalent chip thickness much

smaller than the critical chip thickness indicates the dominance of pressing and sliding mechanisms over the cutting mechanism. As the chip thickness is increased above the critical value, significant penetration of the grains into the workpiece is achieved and fiber cutting becomes dominant.

5.5.2.2 Grinding Temperature

Virtually all the energy spent in grinding is converted to heat. Because of the unusually high specific cutting energy for grinding and the high grinding speeds involved, the rate of heat generation is higher than that in abrasive machining and cutting. The time for heat conduction is also much less and the thermal conditions of grinding may approach adiabatic conditions. Burning of the workpiece surface is very likely if coolant is not properly applied. Figure 5.67 shows the temperature rise in cut-off grinding of unidirectional CFRP under dry and wet conditions [62]. The temperature

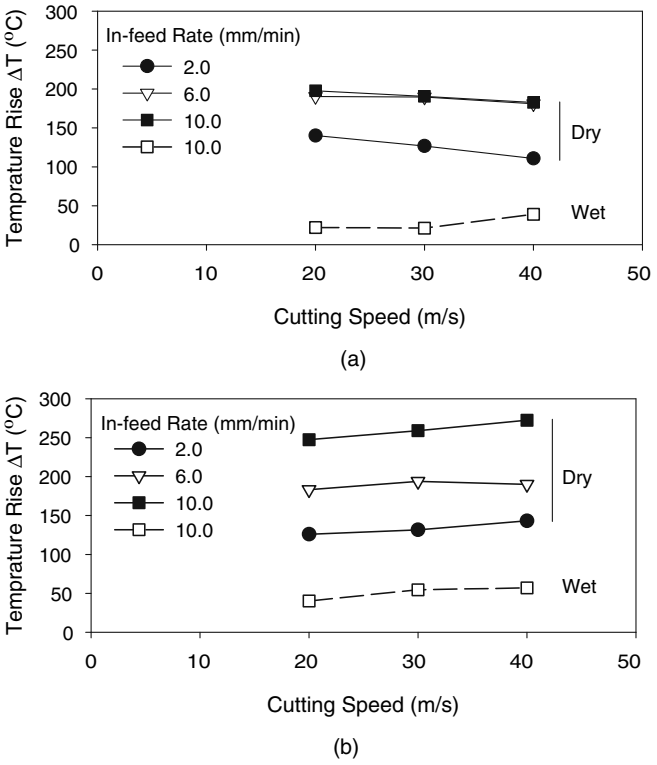

Fig. 5.67 Temperature rise on the surface of CFRP laminate due to cut-off grinding (**a**) parallel to the fibers and (**b**) perpendicular to the fibers. Workpiece: unidirectional CFRP, $V_f = 0.6$, grinding wheel is metal bonded diamond abrasive with diameter = 150 mm, width = 1 mm and mesh number = 140 [62]

rise on the surface of the workpiece is generally high, and under certain conditions well exceeds the glass transition temperature of the polymer matrix. The grinding temperatures are affected slightly by the cutting speed but the effect of in-feed rate is very pronounced, particularly for grinding perpendicular to the fibers. The temperature rise generally increases with an increase in the in-feed rate. At the highest in-feed rate of 10 mm/min, the temperature rise for grinding perpendicular to the fibers is significantly higher than that for grinding parallel to the fibers. This was found to be well correlated with the horizontal grinding forces which were higher for grinding perpendicular to the fibers. The grinding power, which is converted to heat, is proportional to the product of the horizontal grinding force and the cutting speed. Numerical and experimental analysis in [62] has shown that greater amount of heat (20–70%) is conducted away from the cutting zone by the fibers in comparison to 10–30% in parallel grinding. The grinding temperatures in wet grinding are far less than those in dry grinding, which indicates the effectiveness of using grinding fluids for heat management. Wet grinding should be used whenever possible to prevent the polymer matrix from heat degradation.

5.5.2.3 Grinding Quality

Grinding surface roughness is generally better than that of other material removal processes. This is due to the small size of chip removed and the action of multiple cutting points engagement at the same time in smoothing the surface. Surface roughness in grinding is dependent on fiber orientation and depth of cut. As explained earlier, the fracture process by which the material is removed is critically dependent on fiber orientation and depth of cut and is the primary influence on surface roughness. The surface topography in grinding is influenced by both grit size, depth of cut, and fiber orientation. The depth of cut and grit size determine the number of active grains and the actual depth of engagement of the active grains on the wheel and thus the depth of grooves left on the ground surface by the abrasive grains. Finer grit penetrates less in the workpiece and produces shallow grooves.

Figure 5.68 shows surface topography in grinding unidirectional CFRP with aluminum oxide wheel of mesh size 36. Figure 5.69 shows surface roughness measurements along the feed direction and transverse to the feed direction [59]. For grinding parallel to the fibers the surface topography clearly reveals grooves running parallel to the grinding direction. Wide grooves are traces of the abrasive particles scratching the surface while other narrow grooves are places where the fibers once existed (Fig. 5.68a). Cross section of the machined edge (Fig. 5.68b) shows evidence of debonding along the fiber/matrix interface below the surface. This is apparently caused by the large shear force along the interface. Inspection of the chips produced reveals numerous long and short fibers, which suggests that fibers were debonded from surface by buckling due to rubbing and friction against the wheel and the chip formation mechanism in this case is likely to be buckling induced fracture. The polymer matrix is smeared over the surface creating the appearance of a smooth surface ($R_a \cong 1\,\mu m$ in the longitudinal direction). Surface roughness measured in

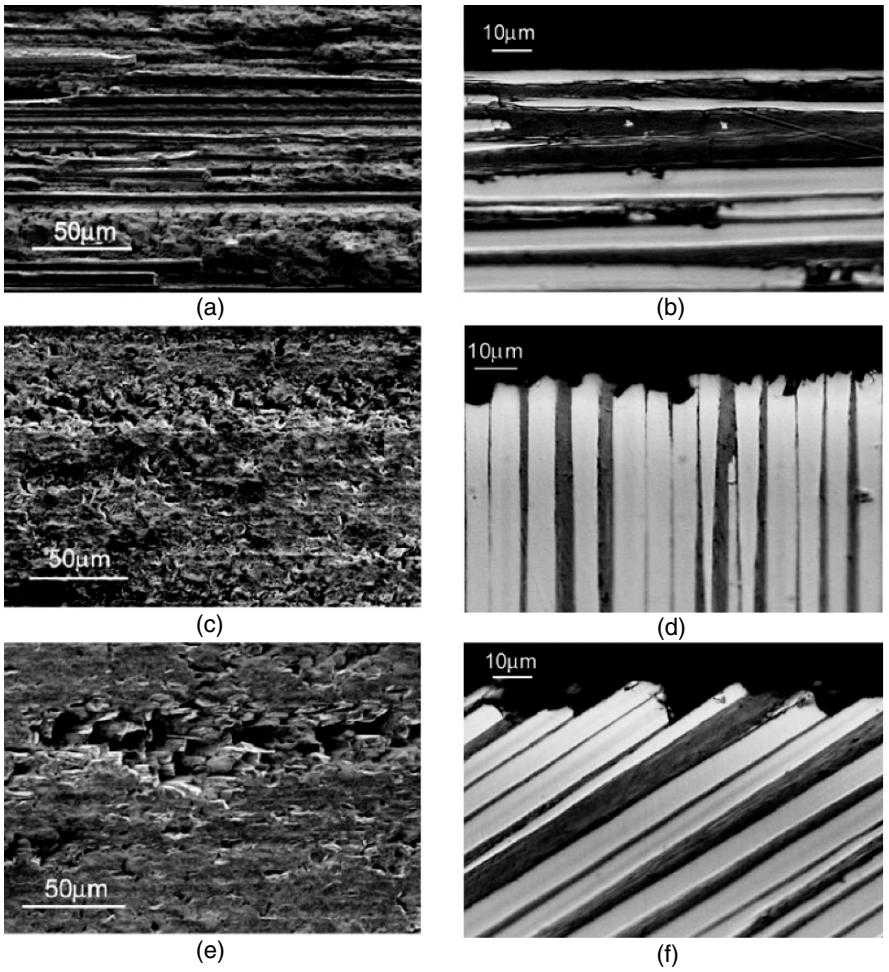

Fig. 5.68 Surface topography resulting from grinding unidirectional CFRP (**a**) 0°, (**c**) 90°, and (**e**) 150°. Photographs (**b**), (**d**), and (**f**) show cross sections of the ground surface for the same fiber orientations. Grinding wheel designation BWA36HVAA, $a_e = 20\,\mu m$, $v = 25\,m/s$, $v_f = 4\,m/min$ [59]

the transverse direction is slightly higher than that in the longitudinal direction as shown in Fig. 5.69. Also, surface roughness slightly increases with an increase in depth of cut.

The effect of fiber orientation on surface roughness is small for fiber orientations $30° < \theta < 120°$ and the overall surface roughness is lower than that for 0°. In this range of fiber orientations, the cutting mechanism evolves from buckling induced fracture to tension loading and compression shear induced fracture at shallow fiber orientations. As the fiber angle increases, the loading change into compression and fracture occurs by compression shear. Figure 5.68c shows the machined surface

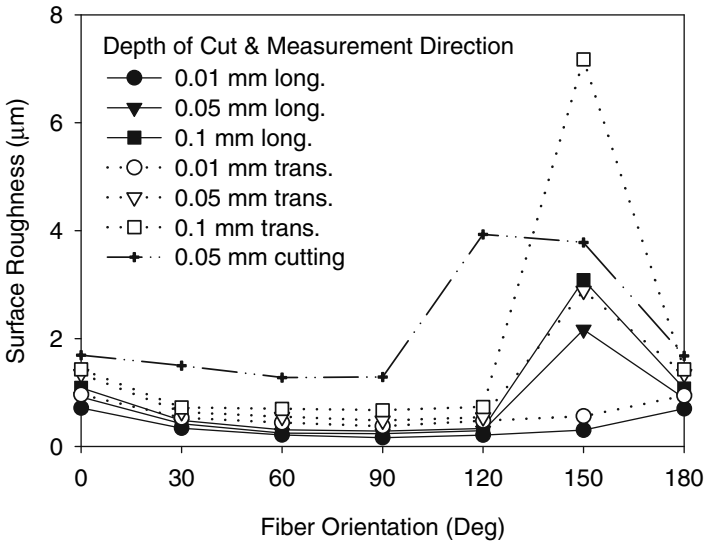

Fig. 5.69 Dependence of surface roughness on fiber orientation in down grinding unidirectional CFRP. Grinding conditions are the same as in Fig. 5.68. Cutting rake angle $= -20^\circ$, cutting speed $= 1$ m/s [59]

topography and Fig. 5.68d shows a polished cross section of the machined edge for fiber orientation 90°. The surface topography reveals several shallow pits where fiber fracture has occurred slightly below the surface. Cross section of the machined surface shows that the fracture surface of the fibers is irregular and inclined to the fiber direction, indicating failure by shear. The surface finish obtained in this range of fiber orientations is best. As the fiber orientation increases beyond 120°, the fibers become more subjected to severe bending and fracture due to bending stress takes place at a point below the machined surface and almost normal to the fiber direction. Figure 5.68e, f show the deeper extent of damage penetration below the machined surface that results from this type of fracture. Surface roughness corresponding to this type of fracture is the highest and is most sensitive to depth of cut. It is noted here that similar behavior of surface roughness is exhibited by orthogonal machining as shown in Fig. 5.69. The peak surface roughness, however, occurs at smaller fiber orientation angle of 120°. This is probably due to the effect of rake angle and sliding friction of the abrasive particle. The rake angle in grinding is much higher than that in cutting and a larger wear flat is contact with the fibers as shown schematically in Fig. 5.66. This gives rise to the buckling mode of fracture over a very wide range of fiber orientations.

Surface roughness was found to increase with an increase in feed rate for both grinding parallel and perpendicular to the fibers. Increasing the wheel speed resulted in decreasing surface roughness when grinding parallel to the fibers but has only marginal effect when grinding perpendicular to the fibers [61]. Because both feed rate and cutting speed affect the equivalent chip thickness, it is of interest to

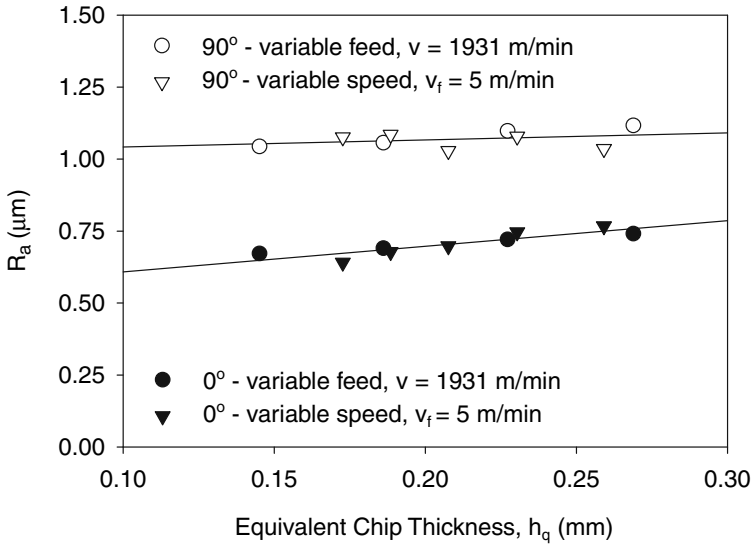

Fig. 5.70 Dependence of surface roughness on equivalent chip thickness in grinding unidirectional CFRP [61]. Grinding wheel WA4618V, grinding depth = 80 μm

investigate the effect of the latter on surface roughness. Figure 5.70 shows a compilation of surface roughness data against equivalent chip thickness for various cutting speeds and feed rates. It is shown the equivalent chip thickness only slightly affects surface roughness when grinding perpendicular to the fibers, and its effects are more profound when grinding parallel to the fibers. This is because an increase in the equivalent chip thickness leads to an increase in number of active grains and the depth of engagement of the active grains [63]. This leads to deeper grooves and higher surface roughness.

5.6 Summary

The machinability of FRPs by conventional means is primarily assessed by the extent to tool wear, delamination, and to a lesser extent by cutting forces and cutting temperatures. The latter is due to the fact that their direct measurement is more difficult, especially for processes where the cutting tool is in rotation or being concealed inside the workpiece. Better machinability in general is achieved by minimizing tool wear and delamination while maintaining high production rates. This is often very difficult simply because of the fact that tool wear increases with an increase in cutting speed and feed rate (i.e., an increase in production rate).

5.6.1 Turning

Machinability was found to be critically influenced by fiber orientation, fiber content, cutting speed, and to a smaller degree by feed rate. Tool wear generally increases with an increase in fiber content, an increase in cutting speed, and an increase in feed rate. In turning filament wound tubes, tool wear also increases with an increase in winding angle. Tool wear is less in turning CFRP than that in turning GFRP, and it is less when turning with PCD and diamond-coated tools than when turning with uncoated carbides. This is most likely a result of the effective heat dissipation capabilities of carbon fibers and diamond, both of which assist in lowering the temperature at the cutting region and thus reducing tool wear and allowing better machinability at high cutting speeds. The cutting temperatures also affect the cutting forces through softening of the polymer matrix. The cutting forces in turning decreased with an increase in cutting speed up to a transitional cutting speed beyond which further increase in cutting speed results in increasing the cutting forces. The transitional speed corresponds to cutting temperatures around 300 °C, which roughly correspond to the melting temperature of thermoplastics and decomposition temperature of thermosets. The viscous behavior of polymers at high strain rates associated with higher cutting speeds may explain the rise in cutting forces. The transition cutting speed was found to increase with an increase in thermal conductivity of the cutting tool material. This underlines the significance of higher thermal conductivity materials (such as PCD and diamond-coated tools) in improving high-speed machinability. The surface roughness in turning is closely related to fiber orientation. For filament wound tube turning, surface roughness increases with an increase in winding angle.

5.6.2 Milling and Trimming

Cutting tools made of PCD, diamond-coated carbides, and solid carbide burr tools were found to provide good solution to the problem of tool wear in milling and trimming applications. Similar to turning, tool life decreased with an increase in cutting speed and an increase in feed rate. Because of the intermittent nature of the milling and trimming processes, it was found that cutting tools perform better for smaller values of equivalent chip thickness, which is determined by the product of the radial depth of cut and the feed rate to cutting speed ratio. This is due to the significant reduction in impact forces on the cutting edge due to the reduction in chip thickness. Delamination, which is a major concern in milling and trimming operations, is also proportional to effective chip thickness. This means that better machinability of FRPs is achieved by using smaller radial depth of cut, smaller feed rates, and higher cutting speeds, which is a combination typical of finishing operations. The extent of delamination is also influenced by the surface ply orientation. Generally, ply orientations of 135°, 90°, 45°, and $(+45°/-45°)$ plain weave were found to promote delamination while ply orientation 0° and plain weave $(0°/90°)$ produced

the lowest delamination in edge trimming. Therefore, delamination can be reduced by designing laminates with 0° and $(0^\circ/90^\circ)$ surface plies. Delamination is also reduced by proper selection of cutting tool geometry and proper cutting configuration. Straight flute cutters and double spiral compression tools are most suitable because they eliminate the axial force component acting normal to the ply. Down milling (climb) was also found to be more suitable than up milling (conventional) for reducing delamination and improving surface roughness.

5.6.3 Drilling

Delamination is the most serious limitation to machinability in drilling FRPs. This is due to the fact that all drilling operations are associated with a thrust force that acts normal to the ply. This force tends to separate the plies in a laminate by interlaminate cracking, even though intralaminate cracking is also possible. Therefore, the key to reducing delamination in drilling lies in the effort to reduce or distribute the thrust force component. This is achieved by a combination of strategies that include proper scheduling of the feed rate in a drilling cycle, proper selection of drill point geometry, and the use of core or saw drills for distributing the feed force. There is also a direct relationship between drill point wear and delamination because tool wear also increases the thrust force. Extensive research in drilling has pointed out that the thrust force is proportional to the product of feed rate and drill diameter. Therefore, a direct relationship between the extent of delamination and feed rate is found. Moreover, there exist a critical feed rate below which delamination will not occur. Knowledge of this critical feed rate and the relationship between feed force and feed rate allows the selection of proper feed rates for avoiding delamination. Analytical modeling of the delamination problem using LEFM has be performed for different drill point–laminate combinations and expressions for predicting the critical thrust force for delamination have been found. These expressions were found to be in good agreement with experimental data. Another major concern in drilling is the temperature generation at the cutting point. Due to the confinement of the drill point, dissipation of the heat generated at the cutting region takes place primarily through the cutting tool. Therefore, high thermal conductivity through the cutting tools and through the tool cooling is recommended.

5.6.4 Abrasive Machining and Grinding

The machinability of FRPs in abrasive machining and grinding is critically dependent on the equivalent chip thickness. Specific horizontal and normal forces, surface roughness, and surface temperature all increase with an increase in equivalent chip thickness. Specific cutting energy on the other hand decreases with an increase in equivalent chip thickness. It is therefore desirable to adjust the grinding parameters so that the equivalent chip thickness is very small. On the other hand, reducing the

chip thickness gives rise to noncutting mechanisms such as pressing and sliding, which are responsible for much of the heat generation and surface damage in grinding. Experimental results have shown that a critical chip thickness exists beyond which cutting energy expenditure becomes more significant than noncutting energy expenditure. This critical chip thickness is found to be well within the range of abrasive machining parameters. It is therefore conceivable that better machinability of FRPs would be obtained by abrasive machining with very low equivalent chip thickness than by grinding. Because abrasive machining and grinding generate greater amount of heat than milling and trimming, it is recommended that all of these operations use an approved flood coolant.

Review Questions and Problems

1. Discuss the role of fiber orientation in determining the chip formation mechanism and the resulting surface topography in milling and abrasive cutting of unidirectional composites. Consider laminate orientations of 0, 30, 90, and 120°.
2. Discuss the role thermal conductivity of the cutting tool and workpiece in affecting tool life and thermal damage.
3. Explain why PCD tool life exhibits less dependence on cutting speed than carbide and CBN tools when machining GFRP.
4. Which of the tool materials K10 carbide, CBN, and PCD would you recommend for the high speed machining of GFRP? Why?
5. Discuss the effects of cutting speed and feed rate on cutting forces when machining GFRP and CFRP by turning.
6. Discuss the effects of cutting speed and feed rate on cutting temperatures in turning FRPs.
7. It is always desirable to increase material removal rate without decreasing machinability. Given the situation in turning, the material removal rate is given by the product of cutting speed, feed rate, and depth of cut. Which of these parameters should be increased in order to increase material removal rate without affecting machinability?
8. Consider milling of unidirectional FRP parallel to the fibers with a single-edge cutting tool. Assuming that the radial depth of cut is 25% of the tool diameter and that down milling configuration is utilized. Discuss the evolution fiber orientation angle and its effect on the chip formation mode as the cutting edge moves from entry to exit.
9. Repeat Question 8 for up milling of 90° unidirectional laminate.
10. In a turning application of a glass/epoxy composite, an unsatisfactory surface roughness was produced. Which one of the following actions would you recommend in order to improve surface roughness? Justify your answer by reference to pertinent material in class notes.

(a) Increase cutting speed
(b) Increase feed speed
(c) Increase both cutting speed and feed speed
(d) Decrease cutting speed
(e) Decrease feed speed
(f) Decrease both cutting speed and feed speed
(g) Other action – explain

11. Suppose that in a trimming operation of multidirectional FRP's you are getting high surface roughness. Which action(s) would you take to improve surface roughness?

(a) Reduce spindle speed
(b) Increase spindle speed
(c) Reduce feed speed
(d) Increase feed speed
(e) Increase number of teeth on cutter
(f) Decrease number of teeth on cutter
(g) Decrease cutter diameter

12. Suppose you are designing a laminate structure that has to be trim machined in order to achieve a desired contour. Assuming that you have the freedom in selecting fiber orientations of the surface plies, what fiber direction relative to the trimming direction would you select for the surface plies in order to reduce delamination?
13. Explain how abrasive machining and grinding are similar, how different.
14. Discuss the effect of equivalent chip thickness on tool forces, surface roughness, and specific cutting energy in abrasive machining and grinding of FRPs.
15. Why is the specific cutting energy in grinding is several orders of magnitude higher than that in cutting?
16. Consider a milling operation of unidirectional CFRP with a cutter diameter of 20 mm, and one cutting edge on the cutter. The cutter speed is 500 rpm, the feed speed is 100 mm/rev, and the depth of cut is 3 mm. The thickness of the workpiece is 4.0 mm. A schematic of the cutting configuration is shown below.

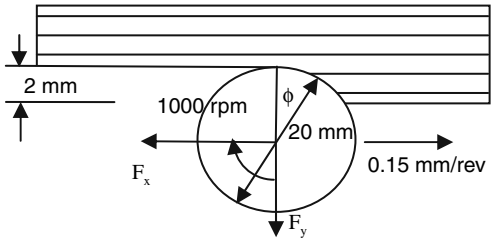

(a) Determine the total engagement angle ϕ.
(b) Using the fiber orientation convention in used in Chap. 3, determine the instantaneous fiber orientation angle θ_i at instant i as a function of the instantaneous engagement angle ϕ_i. Evaluate the fiber orientation angle for

the entire range of engagement, using an angular increment of 2°, starting from zero.

(c) Using specific energy K_c and K_t as given by (5.11), determine the instantaneous cutting and thrust force on the chip. Evaluate these forces for the entire range of engagement, using an angular increment of 2°.

(d) Determine the instantaneous feed and normal forces F_x and F_y for the same angular engagement in part c. Plot F_x and F_y vs. engagement angle ϕ_i.

17. It has been shown in Table 5.4 that the thrust force in drilling is proportional to the feed rate. The delamination model of Hocheng and Dharan [50] gives an expression for the critical thrust force at which delamination would occur in drilling, and it is given by (5.28). Using this information, derive an expression for the critical feed rate for delamination for the following materials and drill geometries:

(a) Unidirectional CFRP T300/5208, ply thickness = 0.228 mm, laminate thickness = 20 plies, standard HSS twist drill [32, 33].

(b) Quasi-isotropic CFRP T300/5208 laminate, thickness = 24 plies, ply thickness = 0.125 mm, standard HSS twist drill [33].

(c) E-glass UD GFRP, ply thickness = 0.228, total laminate thickness = 4 mm, standard twist drill [36].

18. The thrust force in drilling of unidirectional T300-5208 laminate with a HSS drill of diameter 6.25 mm is correlated to the feed rate by the relationship

$$F = 56.3 f^{0.4},$$

where v_f is the feed rate in 10^{-3} mm/rev and F is in Newton. Properties of this composite material are given in the table below:

Mechanical properties of T300-5208

	Unidirectional	Multidirectional
E_{11}	153.0 GPa	75.6 GPa
E_{22}	10.9 GPa	75.6 GPa
ν_{12}	0.3	0.214
G_{IC}	250 J/m^2	250 J/m^2
Ply thickness	0.228 mm	0.228 mm

(a) Determine the critical thrust force for delamination for this material.

(b) Determine the maximum feed rate that can be used to drill this material without delamination and where across the laminate thickness this feed rate should be applied. Assume a laminate thickness of 10 mm.

(c) What strategy would you device to drill this material at maximum production rate while avoiding delamination?

19. The thrust force-feed rate relationship for a quasi-isotropic laminate T300-5208 is given by $F = 43.1 f^{0.22}$. Assuming that the delamination analysis

for unidirectional laminates apply to this laminate, determine the critical feed force for delamination. Use the data in Problem 19. Discuss the validity of the assumption used above.

20. The bending stiffness coefficients for T300/5208 unidirectional laminate of 5.0 mil ply thickness (0.125 mm) are given below [33]. Other relevant data for this laminate are given in Problem 19.

    (a) Using this date, calculate the critical feed force at the onset of delamination using (5.35)–(5.37).
    (b) Calculate the critical force at the onset of delamination using (5.28) assuming isotropic laminate and circular crack. Compare the results for the two approaches.

Ply no. from bottom	D_{11}	D_{22}	D_{12}	D_{66}	D_c^*
1	1.00×10^{-1}	5.67×10^{-3}	1.59×10^{-3}	3.95×10^{-3}	0.390
2	8.00×10^{-1}	4.56×10^{-2}	1.27×10^{-2}	3.15×10^{-2}	3.316
3	2.70	1.54×10^{-1}	4.29×10^{-2}	1.06×10^{-1}	10.584
4	6.38	3.65×10^{-1}	1.02×10^{-1}	2.52×10^{-1}	25.088

21. The bending stiffness coefficients for T300/5208 unidirectional laminate of 9.0 mil ply thickness (0.228 mm) are given below [33]. Other relevant data for this laminate are given in Problem 19.

    (a) Using this date, calculate the critical feed force at the onset of delamination using (5.35)–(5.37).
    (b) Calculate the critical force at the onset of delamination using (5.28) assuming isotropic laminate and circular crack. Compare the results for the two approaches.

Ply no. from bottom	D_{11}	D_{22}	D_{12}	D_{66}	D_c^*
1	2.96×10^{-2}	1.68×10^{-3}	4.72×10^{-4}	1.17×10^{-3}	0.067
2	2.37×10^{-1}	1.35×10^{-2}	3.77×10^{-3}	9.34×10^{-3}	0.537
3	7.99×10^{-1}	4.55×10^{-2}	1.27×10^{-2}	3.15×10^{-2}	1.809
4	1.89	1.08×10^{-1}	3.02×10^{-2}	7.47×10^{-2}	4.288

References

1. Stephenson, D.A., Agapiou, J.S., Metal Cutting Theory and Practice, Marcel Dekker, New York, NY, 1997.
2. Trent, E.M., Wright, P.K., Metal Cutting, 4th Edition, Butterworth-Heinemann, Boston, MA, 2000.
3. Shaw, M.C., Metal Cutting Principles, 2nd Edition, Oxford University Press, New York, NY, 2005.

4. Usuki, H., Narutaka, N., Yamane, Y., A study of the cutting performance of diamond coated tools – tool wear of diamond coated tools in machining of CFRP. International Journal of the Japan Society for Precision Engineering 25(1), 35–36, 1991.
5. Spur, G., Lachmund, U., Turning of fiber-reinforced plastics, in Jahanmir, S., Ramulu, M., Koshy, P. (eds), Machining of Ceramics and Composites. Marcel Dekker, New York, NY, 1999, pp. 209–248.
6. Masuda, M., Kuroshima, Y., Chujo, Y., Failure of tungsten carbide-cobalt alloy tools in machining of carbon materials. Wear 169, 135–140, 1993.
7. Spur, G., Wunsch, U.E., Turning of fiber-reinforced plastics. Manufacturing Review 1, 124–129, 1988.
8. Kim, K.S., Lee, D.G., Kwak, Y.K., Namgung, S., Machinability of carbon fiber-epoxy composite. Journal of Materials Processing Technology 32, 553–570, 1992.
9. Palanikumar, K., Paulo Davim, J., Mathematical model to predict tool wear on the machining of glass fibre reinforced plastic composites. Materials and Design 28(7), 2008–2014, 2007.
10. Ramulu, M., Faridnia, M., Garbini, J.L., Jorgensen, J.E., Machining of graphite/epoxy materials with polycrystalline diamond (PCD) tools, in Ramulu, M., Hashish, M. (eds), Machining Characteristics of Advanced Materials. ASME, New York, NY, MD-Vol. 16, 1989, pp. 33–40.
11. Davim, J.P., Mata, F., New machinability study of glass fiber reinforced plastics using polycrystalline diamond and cemented carbide (K15) tools. Materials and Design 28, 1050–1054, 2007.
12. An, S-.O., Lee, E-.S., Noh, S-.L., A study on the cutting characteristics of glass fiber reinforced plastics with respect to tool materials and geometries. Journal of Materials Processing Technology 68, 60–67, 1997.
13. Sreejith, P.S., Krishnamurthy, R., Malhotra, S.K., Narayanasamy, K., Evaluation of PCD tool performance during machining of carbon/phenolic ablative composites. Journal of Materials Processing Technology 104, 53–58, 2000.
14. Sakuma, K., Seto, M., Tool wear in cutting glass-fiber-reinforced-plastics (The relation between cutting temperature and tool wear). Bulletin of the JSME 24, 748–755, 1981.
15. Ramulu, M., Characterization of surface quality in machining of composites, in Jahanmir, S., Ramulu, M., Koshy, P. (eds), Machining of Ceramics and Composites. Marcel Dekker, New York, NY, 1999, pp. 575–648.
16. Cupini, N.L., Ferreira, J.R., Turning of Carbon and Glass Fiber Hybrid Cloth Composite Material. NIST Special Publication No. 847, Gaithersburg, 1993, pp. 447–453.
17. Palanikumar, K., Karunamoorthy, L., Karthikeyan, R., Optimizing the machining parameters for minimum surface roughness in turning of GFRP composites using design of experiments. Journal of Materials Science and Technology 20, 373–378, 2004.
18. Sheikh-Ahmad, J., Sirdhar, G., Edge trimming of CFRP composites with diamond coated tools: edge wear and surface characteristics, in Proceedings of the SAE General Aviation Technology Conference and Exhibition, Wichita, KS, Paper No. 2002-01-1526, April 2002.
19. Ucar, M., Wang, Y., End-milling machinability of a carbon fiber reinforced laminated composite. Journal of Advanced Materials 34, 46–52, 2005.
20. Janardhan, P., Sheikh-Ahmad, J., Cheraghi, H., Edge trimming of CFRP with diamond interlocking tools, in Proceedings of Aerospace Manufacturing and Automated Fastening Conference, Toulouse France. ASE Publication 2006-01-3173, 11–14 September 2006.
21. Davim, J.P., Reis, P., Multiple regression analysis (MRA) in modelling milling of glass fiber reinforced plastics (GFRP). International Journal of Manufacturing Technology and Management 6, 185–197, 2004.
22. Rahman, M., Ramakrishna, S., Thoo, H.C., Machinability study of carbon/PEEK composites. Machining Science and Technology 3, 49–59, 1999.
23. Konig, W., Wulf, Ch., Grab, P., Willerscheid, H., Machining of fibre reinforced plastics. Annals of CIRP 34, 537–547, 1985.
24. Zhang, L.C., Zhang, H.J., Wang, X.M., A force prediction model for cutting unidirectional fiber-reinforced plastics. Machining Science and Technology 5, 293–305, 2001.

25. Wang, D.H. Ramulu, M. Arola, D., Orthogonal cutting mechanisms of graphite/epoxy composite. Part I: unidirectional laminate. International Journal of Machine Tools and Manufacture 35, 1623–1638, 1995.
26. Sheikh-Ahmad, J., Twomey, J., Kalla, D., Lodhia, P., Multiple regression and committee neural network force prediction models in milling FRP. Machining Science and Technology 11(3), 391–412, 2007.
27. Wang, D.H., Ramulu, M., Arola, D., Orthogonal cutting mechanisms of graphite/epoxy composite. Part II: multi-directional laminate. International Journal of Machine Tools and-Manufacture 35, 1639–1648, 1995.
28. Yadav, R., Force Prediction Model for Milling CFRP, Masters Thesis. Wichita State University, Wichita, KA, 2005.
29. Colligan, K., Ramulu, M., Delamination in surface plies of graphite/epoxy caused by the edge trimming process. Processing and Manufacturing of Composite Materials, PED-Vol. 49/MD-Vol. 27, ASME, New York, NY, 1991, pp. 113–125.
30. Davim, J.P., Reis, P., Damage and dimensional precision on milling carbon fiber-reinforced plastics using design experiments. Journal of Materials Processing Technology 160, 160–167, 2005.
31. DiPaolo, G., Kapoor, S.G., DeVor, R.E., An experimental investigation of the crack growth phenomenon for drilling of fiber-reinforced composite materials. Journal of Engineering for Industry. ASME Transaction 118, 104–110, 1996.
32. Petrof, R.C., On the dynamics of drilling glass reinforced plastic with different drill point geometries. SME Technical Paper EM86-363, 1986.
33. Jian, S., Yang, D.C.H., Effects of federate and chisel edge on delamination in composites drilling. Journal of Engineering for Industry. ASME Transaction 115, 398–405, 1993.
34. Jian, S., Yang, D.C.H., Delamination-free drilling of composites laminates. Journal of Engineering for Industry. ASME Transaction 116, 475–481, 1994.
35. Malhorta, S.K., Some studies on drilling of fibrous composites. Journal of Materials Processing Technology 24, 291–300, 1990.
36. Chen, W.-C., Some experimental investigation in the drilling of carbon fiber-reinforced plastic (CFRP) composite laminates. International Journal of Machine Tools and Manufacture 37, 1097–1108, 1997.
37. Mathew, J., Ramakrishnan, N., Naik, N.K., Trepanning on unidirectional composites: delamination studies. Composites: Part A 30, 951–959, 1999.
38. Mohan, N.S., Ramachandra, A., Kulkarni, S.M., Machining of fiber-reinforced thermoplastics: influence of feed and drill size on thrust force and torque during drilling. Journal of Reinforced Plastics and Composites 24, 1247–1257, 2005.
39. Mohan, N.S., Ramachandra, A., Kulkarni, S.M., Influence of process parameters on cutting force and torque during drilling of glass-fiber polyester reinforced composites. Composite Structures 71, 407–413, 2005.
40. Won, M.S., Dharan, C.K.H., Chisel edge and pilot hole effects in drilling composite laminates. Journal of Manufacturing Science and Technology 124, 242–247, 2002.
41. Won, M.S., Dharan, C.K.H., Drilling of aramid and carbon fiber polymer composites. Journal of Manufacturing Science and Technology 124, 778–783, 2002.
42. Davim, J.P., Reis, P., Drilling carbon fiber reinforced plastics manufactured by autoclave – experimental and statistical study. Materials and Design 24, 315–324, 2003.
43. Weinert, K., Kempmann, C., Cutting temperatures and their effects on the machining behaviour in drilling reinforced plastic composites. Advanced Engineering Materials 6, 684–689, 2004.
44. Person, E., Eriksson, I., Hammersberg, P., Propagation of hole machining defects in pin-loaded composite laminates. Journal of Composite Materials 31, 383–409, 1997.
45. Khashaba, U.A., Delamination in drilling GFR-thermoset composites. Composite Structures 63, 313–327, 2004.
46. Tsao, C.C., Hocheng, H., Taguchi analysis of delamination associated with various drill bits in drilling of composite material. International Journal of Machine Tool andManufacture 44, 1085–1090, 2004.

47. Davim, J.P., Reis, P., Study of delamination in drilling carbon fiber reinforced plastics (CFRP) using design experiments. Composite Structures 59, 481–487, 2003.
48. Davim, J.P., Reis, P., Antonio, C.C., Drilling fiber reinforced plastics (FRPs) manufactured by hand lay-up: influence of matrix (Viapal VUP 9731 and ATLAC 382-05). Journal of Materials Processing Technology 155–156, 1828–1833, 2004.
49. Davim, J.P., Reis, P., Antonio, C.C., Experimental study of drilling glass fiber reinforced plastics (GFRP) manufactured by hand lay-up. Composites Science and Technology 64, 289–297, 2004.
50. Hocheng, H., Puw, H.Y., On drilling characteristics of fiber-reinforced thermoset and thermoplastics. International Journal of Machine Tools and Manufacture 32, 583–592, 1992.
51. Hocheng, H., Dharan, C.K.H., Delamination during drilling in composite laminates. Journal of Engineering for Industry 112, 236–239, 1990.
52. Hocheng, H., Tsao, C.C., Comprehensive analysis of delamination in drilling of composite materials with various drill bits. Journal of Materials Processing Technology 140, 335–339, 2003.
53. Hocheng, H., Tsao, C.C., Effects of special drill bits on drilling-induced delamination of composite materials. International Journal of Machine Tools and Manufacture 46, 1403–1416, 2006.
54. Malkin, S., Grinding technology: theory and applications of machining with abrasives. Society of Manufacturing Engineers, Dearborn, MI, 1989.
55. Colligan, K., Ramulu, M., Edge trimming of graphite/epoxy with diamond abrasive cutters. Machining of Advanced Composites, MD-Vol. 45/PED-Vol. 66, ASME, New York, NY, 1993, pp. 97–115.
56. Sheikh-Ahmad, J., Unpublished data, Wichita State University, 2005.
57. Peterman, L.M., Diamond Tooling: Productivity Key to RP Fabrication. Technical Sessions of the 41st Annual Conference – Reinforced Plastics/Composites Institute, Atlanta, GA, 27–31 January 1986. The Society of the Plastics Industry. http://www.abrasive-tech.com/pdf/trpfab.pdf, cited December 2007.
58. Hu, N.S., Zhang, L.C., A study of the grindability of multidirectional carbon fibre-reinforced plastics. Journal of Materials Processing Technology 140, 152–156, 2003.
59. Hu, N.S., Zhang, L.C., Some observations in grinding unidirectional carbon fibre-reinforced plastics. Journal of Materials Processing Technology 152, 333–338, 2004.
60. Ramulu, M., Kim, D., Choi, G., Frequency analysis and characterization in orthogonal cutting of glass fiber reinforced composites. Composites: Part A 34, 949–962, 2003.
61. Tso, P-.L., Chang, J.-W., Study on the grinding of continuous carbon fiber reinforced plastics. Machining of Advanced Composites, MD-Vol. 45, ASME, New York, NY, 1993, pp. 89–96.
62. Lee, D.G., Kim, P.J., Temperature rise and surface roughness of carbon fiber epoxy composites during cut-off grinding. Journal of Composite Materials 34, 2061–2080, 2000.
63. Hecker, R.L., Ramoneda, I.M., Analysis of wheel topography and grit force for grinding process modeling. SME Technical paper MR03-184. Proceedings of NAMRC XXXI, May 20–23, 2003, Hamilton, Ontario, Canada.

Chapter 6
Nontraditional Machining of FRPs

As the demand on high performance composites increases, stronger, stiffer, and harder reinforcement materials are introduced into modern advanced composite structures. This makes the secondary machining of these materials increasingly difficult. Traditional machining of composites is difficult because of its heterogeneity, anisotropy, low thermal conductivity, heat sensitivity, and high abrasiveness. The stacked nature of most fiber-reinforced composites makes them also susceptible to debonding between the individual plies as well as within the same ply. Under certain circumstances traditional machining may become extremely difficult even when diamond cutting tools are utilized. Therefore, tool geometry, tool materials, and operating conditions must be adapted in order to reduce heat generation, tool wear, and the mechanical and thermal damages to the workpiece. This may lead to operating conditions that are impractical because of tool low material removal rates (MRRs), frequent tool changes, or unacceptable levels of delamination. Under these circumstances, nontraditional machining process may become the only viable and economical method for machining difficult-to-machine composites. Nontraditional machining processes include waterjet (WJ), abrasive waterjet (AWJ), abrasive suspension jet (ASJ), laser and laser-assisted machining, ultrasonic machining, and electrical discharge machining (EDM). Among this wide range of processes, only AWJ, laser, and EDM of FRP composites have received considerable attention in the literature. This chapter provides an overview of the technology used in each one of these processes, its influencing parameters, and its feasibility for machining FRPs.

6.1 Abrasive Waterjet Machining

High-velocity waterjets have been used since the early 1970s in cutting a variety of materials, including corrugated board, paper, cloth, foam, rubber, wood, and granite. Abrasive waterjets expand the capabilities of high-velocity waterjets by introducing abrasive particles as the cutting medium. First introduced in the late 1980s, this technology allows harder and more exotic materials to be machined

J.Y. Sheikh-Ahmad, *Machining of Polymer Composites*.
DOI: 10.1007/978-0-387-68619-6,

efficiently at reasonable speeds. Currently AWJs are used to cut a wide range of engineering materials including ceramics, metal alloys, and composites. There are many distinct advantages of AWJ cutting which makes it desirable over other traditional and nontraditional machining processes. AWJ can virtually cut any material without any significant heat damage or distortion. Because the cutting forces are very small and no cutting tools are required, the setup time is shorter than traditional machining processes and fixturing requirements are either very minimal or not required at all. Depending on the CNC machine tool capabilities, it is possible to cut two-dimensional contours and even complex three-dimensional shapes with AWJ. Finally, AWJ is one of the most environmentally friendly material removal processes. It requires no cutting fluids and generates no fumes or harmful waste as compared to traditional machining. The used water and abrasives can be either recycled or disposed off naturally. Nevertheless, there are some limitations to cutting with AWJs. The initial capital investment is generally high in comparison to other nontraditional and conventional machine tools. The operating cost is high as well. This includes the cost of abrasives and other expensive wear parts that are routinely replaced, such as the orifice and mixing tube. The waterjet traveling at supersonic speeds generates considerably higher noise than other nontraditional machining processes such as laser cutting and EDM. Being a modern manufacturing process, AWJ machining is not yet well developed so that it can be exploited to its fullest potential. The following sections discuss the capabilities of AWJ systems and their application in machining FRPs.

6.1.1 Technology Overview

An AWJ system utilizes a high-speed waterjet to accelerate abrasive particles at extremely high speeds (450–720 m/s) so that it will erode the workpiece material at impact. A typical AWJ system layout is shown in Fig. 6.1. To form a waterjet, water is pressured up to 400 MPa and expelled through a sapphire or diamond nozzle (0.1–0.4 mm in diameter) to form a fine waterjet at a speed that approaches 900 m/s. At this speed, this plain waterjet can be used to cut materials such as plastics, paper products, cloth, wood, and some advanced composites. To enhance its cutting performance, abrasives are mixed in the waterjet in a special mixing chamber as shown in Fig. 6.2. The waterjet creates a vacuum which sucks the abrasives from the abrasive ports and mixes it in the mixing chamber. The abrasive particles are accelerated by the waterjet but to the exchange of momentum energy, and a focused AWJ is produced, whose diameter is in the order of the nozzle diameter.

At the heart of an AWJ system is a reciprocating plunger pump, also called intensifier, which is driven by pressurized oil from a hydraulic pump. The intensifier increases the water pressure ratio between the low pressure oil to the high pressure water by up to 40 times. A high pressure vessel accumulator is used to produce uniform water flow and attenuate output pressure variations. High pressure water is delivered to the nozzle through special high pressure tubing and swivel connectors.

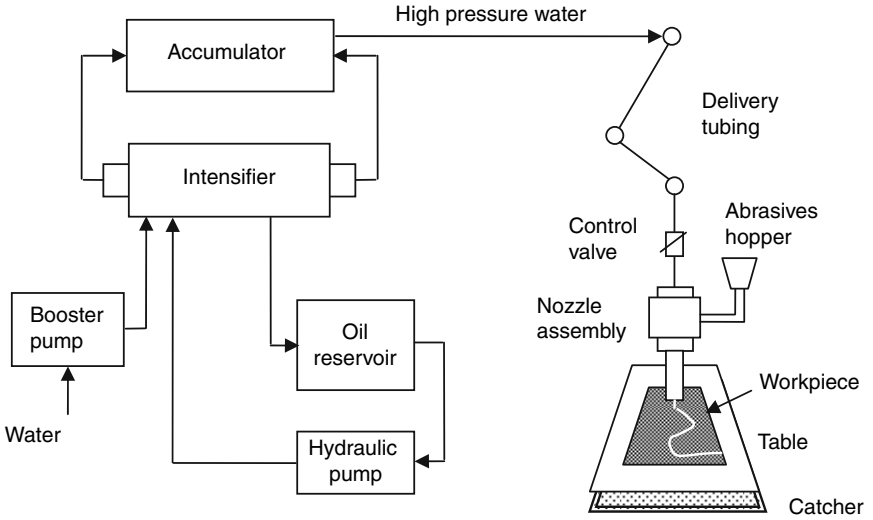

Fig. 6.1 Schematic diagram of AWJ machining system

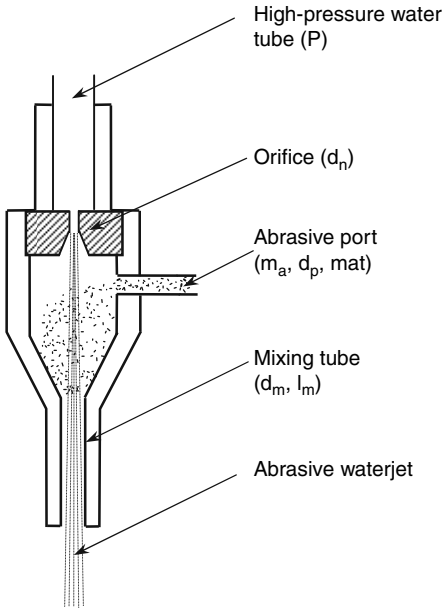

Fig. 6.2 Schematic of AWJ nozzle assembly showing the variables controlling AWJ performance

A nozzle orifice is typically made from synthetic sapphire or diamond in order to provide adequate wear resistance. The most common mechanisms of failure of the orifice are chipping from foreign particles in the water and plugging from mineral deposits. Both problems are effectively solved by proper water filtration and treatment. At the nozzle, abrasives are introduced and to create an AWJ ready for cutting.

The abrasives most commonly used are garnet of mesh sizes 16–80. Other harder abrasives such as aluminum oxide and silicon oxide are also used to cut exotic alloys and ceramics. AWJ is delivered through a mixing tube that is typically made from a special grade tungsten carbide. This part of the nozzle wears frequently and has to be replaced in order to maintain a cohesive and focused waterjet. The motion of the nozzle is typically handled by CNC-controlled two-axes structure. Robotic arm manipulators are also common for three-dimensional positioning and control. Part of the jet energy is dissipating in cutting the workpiece material. Once the jet has exited the cut, the energy is dissipated into the catch tank, which is usually full of water and debris from previous cuts [1, 2].

6.1.1.1 AWJ Process Parameters

AWJ machining is a complex process that is characterized by a large number of process parameters that determine efficiency, economy, and quality of the whole process. The shear magnitude of these influencing parameters makes it extremely difficult to analyze and predict the performance of AWJ machining. Generally, the parameters that affect an AWJ system are divided into four groups, namely hydraulic parameters (waterjet pressure, water flow rate), mixing parameters (mixing tube diameter and length), abrasive parameters (abrasive particle size and shape, abrasive material, abrasive flow rate) and cutting parameters (traverse speed, standoff distance, inclination angle) [3]. The first three groups are related to the system hardware, while the fourth group is related to the application of AWJ in a particular machining operation. The target most important parameters (outcomes) of the machining process are the depth of cut, cutting rate, kerf width, surface topography and delamination. The significance of AWJ process parameters on machining results is summarized in the Table 6.1. The same parameters are also indicated in Fig. 6.2. The effect of pressure, orifice diameter, and abrasive flow rate on MRR and depth of cut is obvious. Increasing the pressure and reducing orifice diameter result in increasing the jet speed (momentum energy), and hence, when coupled with sufficient abrasive flow rate it would allow for an increased cutting activity of

Table 6.1 Significance of AWJ parameters on machining results [3]

Machining results	AWJ parameters						
	P	d_n	l_m	d_m	m_a	d_a	mat
Volume removal rate	3	3	1	2	3	2	2
Depth of cut	3	3	0	2	3	2	2
Width of cut	1	0	0	3	1	0	0
Surface waviness	2	2	1	1	2	1	1
Surface roughness	2	2	0	0	1	3	2
Running cost of cutting	1	1	1	1	2	0	0

P Waterjet pressure, d_n Waterjet orifice diameter, l_m Mixing tube length, d_m Mixing tube diameter, m_a Abrasive flow rate, d_a Abrasive particle diameter, Mat Material strength property, 3 Most significant, 2 More significant, 1 Less significant, 0 Not significant

the abrasive particles. Like any abrasive machining process, the surface roughness is directly related to the abrasives mass flow rate and particle diameter. The width of cut is directly related to the AWJ diameter, which is a function of the mixing tube diameter.

6.1.1.2 Process Capabilities

Today's AWJs can cut through a wide range of materials and thicknesses and obtain reasonable tolerances and surface roughness. Quality of the cut surface in terms of kerf width, taper, and surface roughness depends on cutting (traverse) speed, abrasive flow rate, and workpiece material. Figure 6.3 shows the relationship between cutting speed and workpiece thickness for several aerospace materials [4, 5]. The general trend for the materials shown is that at sufficiently small jet traverse speeds large thickness of the material can be cut. The thickness rapidly decreases with an increase in cutting speed. Although it is technically possible to cut steel as thick as 250 mm, this cutting is not practical because the cutting time is very long and the cut quality is poor. The practical limit for cutting steel and titanium in production is about 50 mm [6]. The dimensional tolerances and surface finishes also depend on thickness and cutting speed. The tolerance range that can be held on small parts

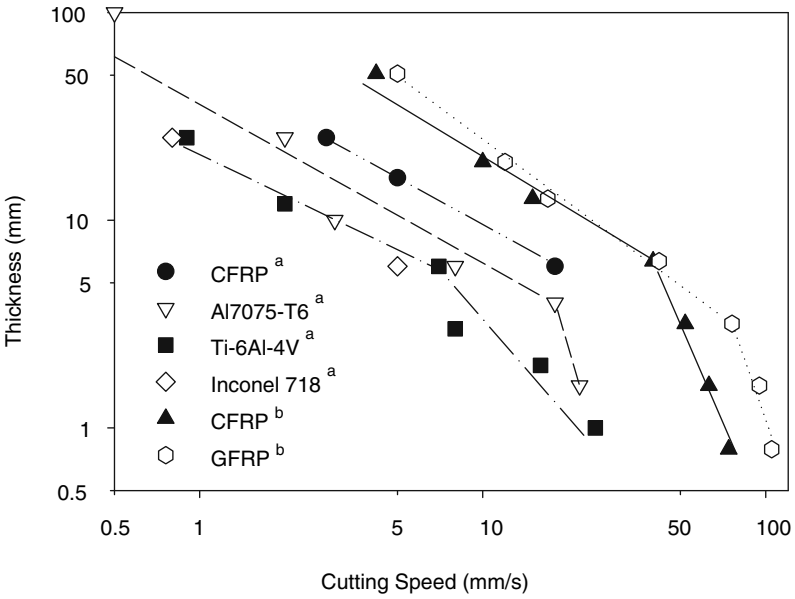

Fig. 6.3 Relationship between cutting speed and material thickness in AWJ cutting of aerospace materials [4,5]. Cutting conditions (**a**): $P = 138,\ 207$ MPa, standoff distance = 2.5 mm, garnet size = 50, 100, abrasive flow rate = 10 g/s. Cutting conditions (**b**): P = 345 MPa, $d_n = 0.229$ mm, $d_m = 0.762$ mm, garnet mesh 80

is about ±0.025 mm and on large parts is about ±0.125 mm. Tighter tolerances are possible with tighter control of the machine axes and nozzle motion. Nevertheless, these tolerances do not compare with the tolerance ranges of traditional machining processes (e.g. ±0.002 mm for rough milling and ±0.001 mm for finishing). The typical surface roughness obtained with AWJ cutting is similar to that of sanding, sand blasting, and rough grinding and is in the range from R_a 1.5 to 8.0 μm. Kerf width on the top surface is typically in the order of the jet diameter. A slight taper is produced because the jet loses its energy as it cuts deeper into the material. Taper angles in the range of 2–8° may be produced. With fine nozzles a kerf width in the order of 0.5 mm can be obtained [2].

6.1.2 Material Removal Mechanisms

The material removal processes in AWJ machining are considered in two scales, namely micro- and macroprocesses. The microprocesses are concerned with the behavior of abrasive particle as it impacts the target surface at high velocities. Material removal in this scale occurs by solid particle impact erosion which results from one or more of the following processes: microcutting, fatigue, melting, and brittle fracture. The contribution of each particular erosion process depends on several factors, such as impact angle, particle kinetic energy, particle shape, target-material properties, and environmental conditions. Nevertheless, all four mechanisms are observed during the AWJ cutting. On the other hand, macromaterial removal processes are concerned with kerf formation as a result of the jet behavior, its characteristics, and the controlling process parameters. Below a brief discussion of the most relevant material removal processes to our subject will be given. The reader is encouraged to consult the relevant work in the literature for more in-depth consideration of the subject of erosion by AWJ. An extensive discussion of the nature of microprocesses, their experimental verification and analytical modeling is given in [7]. The most accepted theories on kerf formation have been based on the fundamental work by Hashish [8–10].

6.1.2.1 Micromechanisms of Material Removal

The type of erosion mechanism responsible for material removal by solid particle impact is ultimately influenced by the workpiece material and abrasive particle properties. For ductile materials, microcutting and ploughing deformation processes are considered the most significant while brittle materials erosion is believed to occur by brittle fracture. Figure 6.4 is a schematic representation of some erosion processes.

Microcutting (Fig. 6.4a) occurs by the impact of sharp abrasive particle at sufficiently small impact angle. The particle is driven by its momentum energy to indent the particle and then follow a trajectory that results in removing tiny chip (also called lip), in a similar way to single point cutting tools. The lip formed at the end

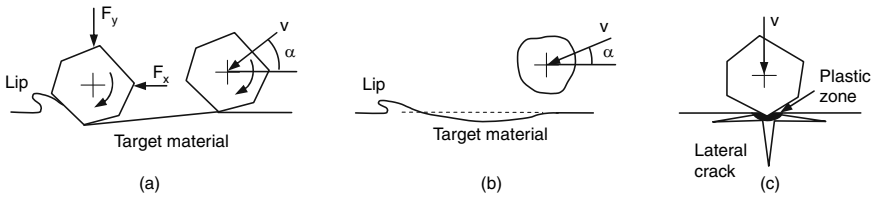

Fig. 6.4 Micromechanisms of material removal by solid particle impact, (**a**) microcutting, (**b**) ploughing deformation, and (**c**) lateral cracking

of the particle track is later removed by other impacting particles. The process is purely a result of plastic deformation of the material ahead of the impacting particle. The volume of material removed by the abrasive particle is a function of its kinetic energy, angle of impact, and the target material's flow stress. It increases by an increase in particle mass and speed and a decrease in the flow stress. This mechanism is more likely to occur at shallow impact angles and for particles with sharp edges. For impact angles approaching 90° a cutting trajectory ceases to exist and only indentation by plastic deformation occurs. For spherical particles, ploughing deformation (Fig. 6.4b) dominates the materials removal process. The erosion mechanism for brittle materials is governed by indentation fracture mechanics through the formation, propagation, and interaction of microcracks (Fig. 6.4c). The MRR is controlled by the depth of particle penetration, crack-formation geometry (depth, length), and interaction. SEM examination of kerf surfaces of aluminum, titanium, and steel alloys have shown evidence of the occurrence of microcutting and ploughing during AWJ machining. Evidence of mixed material-removal modes that consist of brittle fracture and plastic deformation have been identified in AWJ machining of ceramics [7].

6.1.2.2 Macromechanism of Material Removal (Kerf Formation)

The macroscopic interaction of the AWJ with the workpiece material is responsible for kerf formation and ultimately gross material removal and cutting. Geometry of the cutting front, width and depth of the kerf, and topography of the generated surface are the important characteristics of the AWJ erosive process. Figure 6.5 illustrates the general process of AWJ cutting as viewed inside a transparent plastic block by high speed photography [8]. As the jet travels along the x-direction, it undergoes three stages of development. At the beginning, the jet approaches the surface parallel to its axis. With the increase in depth of cut, the local impact angle increases and the jet bends. The initial (or development) stage takes place over a distance x_o before the jet reaches its maximum depth of cut. Beyond this distance, the cutting process proceeds in a cyclic manner. Steady-state cutting occurs to an interface depth h_c, below which a step of the material appears to move under the impact of the jet until it reaches the final depth h. The zone above h_c is termed the cutting wear zone, in which the material is removed primarily by microcutting action

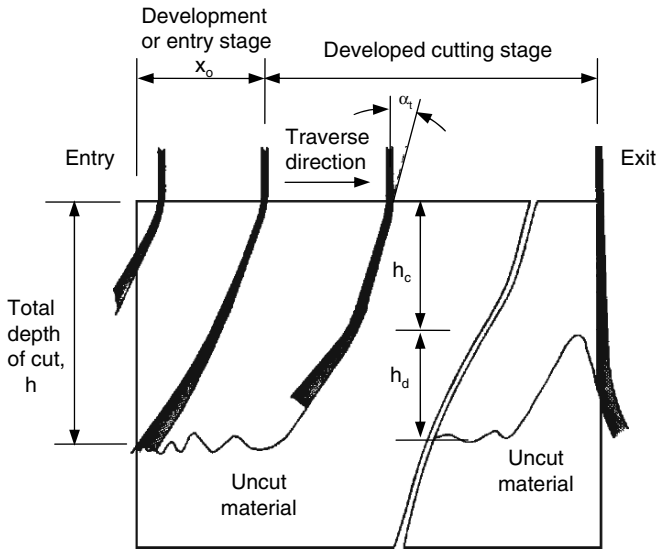

Fig. 6.5 Different zones of AWJ cutting, redrawn from [11]

of particles impacting the surface at shallow angles. In the steady-state zone (cutting wear zone), the MRR equals the jet material displacement rate by traversal. The characteristic property of the generated surface in this zone is surface roughness.

The step formation below h_c is termed the deformation zone, in which material is removed by plastic deformation wear due to impact at large angles. A certain critical impact angle marks the transition from the steady-state cutting wear regime to the deformation wear regime. In the deformation wear zone, marked with depth h_d, the jet penetrates the material at a decreasing rate as the depth is increased. The material removal mode in this zone is caused by plastic deformation, surface hardening, and crack formation that are all associated with particle bombardment. The characteristic feature of the surface is waviness due to striations caused by jet instabilities.

As the jet approaches the exit edge of the workpiece, an uncut triangle is formed. The height of the triangle approximately marks the steady-state zone depth, h_c. For total separation of the workpiece, the workpiece thickness should be equal to or less than h_c. Increasing the traverse speed will decrease the depth of cutting wear zone, and over a critical traverse speed the kerf will be generated only by deformation wear erosion [11].

6.1.2.3 AWJ Kerf Characteristics

The kerf geometry obtained by AWJ cutting is schematically illustrated in Fig. 6.6, and is characterized by kerf surface topography (roughness, waviness), kerf width,

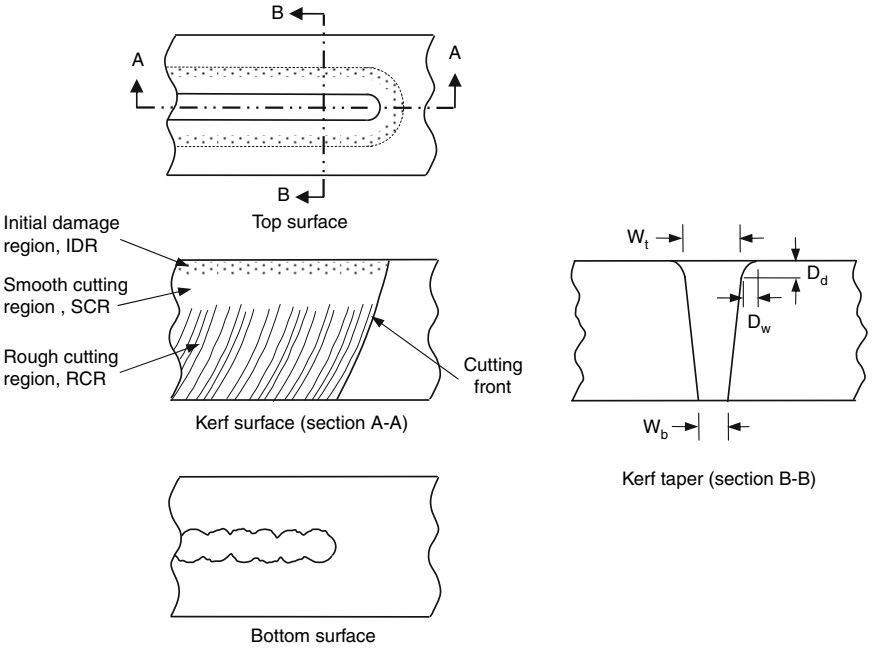

Fig. 6.6 Schematic illustration of kerf geometry and characteristics. Adapted from [11, 13]

and taper. Kerf geometry is an important outcome of AWJ cutting because it limits the process capability for achieving the desired tolerances and surface finish requirements. The previous discussion has pointed out the existence of two distinct zones on the kerf surface, namely the cutting wear zone (also called smooth cutting zone) and deformation wear zone (also called rough cutting zone). Further studies on AWJ cutting of ceramics and fiber-reinforced polymers (FRPs) indicated the existence of a third distinct zone at the top of the kerf, called the initial damage zone. This zone is characterized by roundness of the top corners at the jet entrance. Material removal in this zone occurs by deformation due to the normal impact of stray particles at the jet periphery [12, 13]. Each of the three regions discussed above varies in size depending on the selection of cutting parameters.

The initial damage zone is characterized by the depth and width (D_d and D_w, respectively) of roundness of the top corners of the kerf as shown in Fig. 6.6. Its influenced primarily by standoff distance, pressure, traverse speed, and mesh size. An increase in the standoff distance and a decrease in the pressure result in greater roundness of the kerf corners. This is apparently due to the increase in jet diameter and decrease in jet cohesion with these parameters [13].

Surface waviness is caused by instabilities in the cutting process due to the jet losing its energy with increasing depth of cut. Therefore, the amplitude of waviness increases with an increase in depth of cut. Surface waviness is critically dependent

on the steadiness of the dynamic process parameters such as traverse speed, pressure, and abrasive flow rate. An increase in cutting speed and a decrease in abrasive flow rate generally result in an increase in surface waviness. Waviness is also affected by the machinability of the target material. Hard-to-machine materials such as ceramics are less susceptible to waviness as a result of changes in the dynamic process parameters than soft materials [12].

Kerf width and taper are influenced by the AWJ structure (which is a function of pump pressure and standoff distance), the traverse speed, and to a lesser extent by abrasive flow rate. Cutting speed has the most significant influence on top kerf width where an increase in cutting speeds results in a decrease in kerf width. Increasing pump pressure and standoff distance almost linearly increases top kerf width. This was found to be the general behavior for ductile materials and FRPs [8, 13]. Kerf taper, which is described by the ratio of kerf width at jet entrance (W_t) and exit (W_b) is generated because the jet loses its cutting efficiency with depth. Kerf taper increases with an increase in traverse speed and an increase in grit size. In practice, the traverse speed is used to control the kerf wall straightness. The traverse speed is reduced until straight walls are produced [12].

Surface roughness in the smooth cutting zone is mainly dependent on abrasive particle size. The smaller the particle size, the better is the surface roughness. It was also reported that increasing the traverse speed result in an increase in surface roughness for several target materials. The increased number of impacting particles at low traverse speeds accounts for the improvement in surface roughness [8].

6.1.3 AWJ Machining Characteristics of FRPS

AWJ machining is a widely used process in industry because of its obvious advantages. Some of the advantages include high linear cutting speeds (may reach four times that of traditional cutting) and the absence of heat affected zone (HAZ). Figure 6.3 shows typical cutting speeds (traverse speeds) and thickness relationships for some composites and aerospace materials. It is shown that cutting speeds as high as 2,400 m/min may be used to cut effectively CFRP and GFRP thin parts (6 mm thick). This represents tremendous productivity gains over traditional trimming methods. Some limitations of AWJ machining have also been identified. At high cutting speeds, steady-state cut (cutting wear zone) may not be achieved, delamination are introduced into the workpiece; when composites containing aramid fibers are cut, fraying of the fibers can occur, and in some cases moisture absorption can lead to delamination under load. Several studies have reported on the machining characteristics of fiber-reinforced composites using AWJ [13–17]. These studies describe the machining outcomes in terms of kerf width, taper, surface roughness, and delamination.

6.1.3.1 Material Removal Mechanisms

The material removal mechanism in plain waterjet machining of unidirectional graphite fiber-reinforced epoxy laminates was investigated in [14]. AWJ machining of unidirectional and multidirectional graphite/epoxy was investigated in [13–15]. In these studies, scanning electron microscopy was used to examine the kerf surface and conclusions were made as to the possible mechanisms of material removal. Figure 6.7 shows SEM photomicrographs of plain waterjet machined surfaces for fiber orientations 0°, 45°, and 90°. These pictures reveal the absence of supporting matrix from between the fibers. The fiber ends of the 45° and 90° clearly show evidence of shear fracture. Shear failure was evident from the resin cusps visible on the kerf fibers. Microbending and fracture of fibers was also observed, particularly near the jet exit. This suggests that fracture is the primary mode of material removal in plain waterjet machining of unidirectional composites. Fracture of the fibers occurs after the supporting binder phase is eroded from between the fibers. It is also suggested that this is the mechanism of material removal in all areas of the kerf surface since no distinct differences in wear topography were noted at different depths. In the macroscopic scale (photos not shown) the machined surfaces of the 45° and 90° laminates included striations outlining the bent erosion path of the waterjet. Striations were more pronounced for the 45° laminate and near the exit zone of the jet and were always followed by a high degree of delamination, fiber pullout, and matrix cracking along the fiber/matrix interface. The fiber pullout occurred for fiber bundles at a time leaving large cavities in the machined surface. On the other hand, the 0° laminate did not exhibit striations or large fiber bundles pullout. Fiber rollout instead was the dominant wear form giving the surface a corrugated roof appearance. Fiber rollout appears to be a postmachining phenomena caused by high-pressure jet forces acting on the exposed fibers within the kerf walls. Incident jet pressure dislodges the fibers which have been fractured or partially disbanded from the matrix. Rollout describes the final removal of the fibers from the surface leaving pockets in the matrix. These pockets would occasionally contain resin cusps attributed to shear failure between the fibers and the matrix [14].

Three macroregions were identified along the kerf surface in AWJ machining of graphite/epoxy multidirectional laminates [13, 15]. These regions with distinct

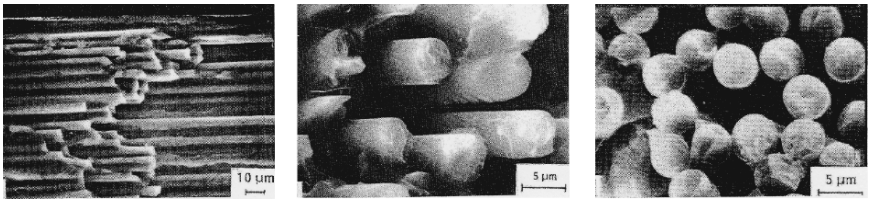

(a) 0° (b) 45° (c) 90°

Fig. 6.7 Appearance of waterjet machined surface of unidirectional graphite/epoxy composite. Material = IM-6/3501-6, $V_f = 0.65$, thickness = 5 mm, pressure = 240 MPa, standoff = 1.0 mm, traverse speed = 1.6 mm/s, nozzle diameter = 1.0 mm [14]

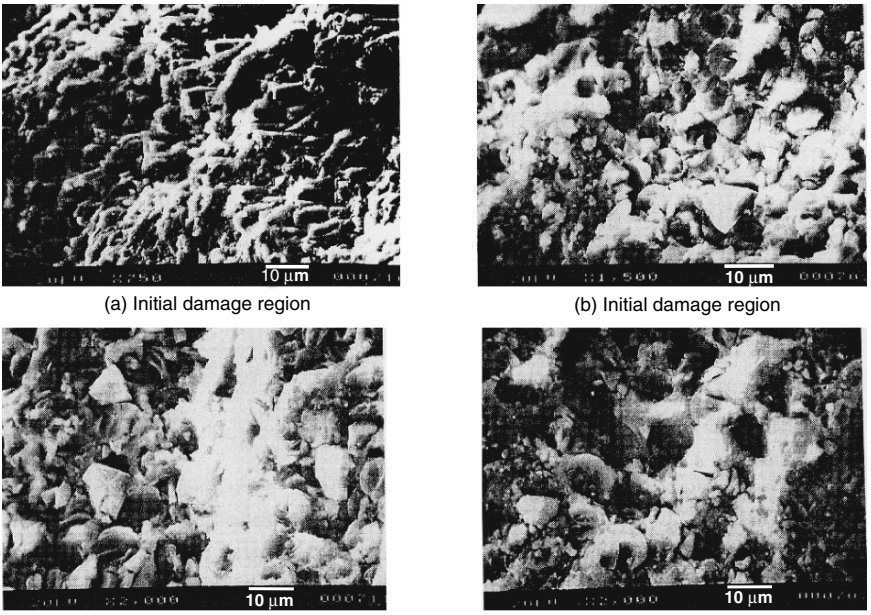

(a) Initial damage region (b) Initial damage region

(c) Smooth cutting region (d) Rough cutting region

Fig. 6.8 Appearance of waterjet machined surface of unidirectional graphite/epoxy composite. Material = IM-6/3501-6, layup = $[(0/90/45/-45)_n]_s$, $V_f = 0.65$ [13]

surface features are shown schematically in Fig. 6.6 and were called the initial damage region (IDR), smooth cutting region (SCR) and rough cutting region (RCR). Discussion of the microfeatures and possible material removal mechanisms in these regions is given next. Their macrofeatures will be discussed in the following sections. Micrographs of typical kerf surfaces resulting from AWJ machining are shown in Fig. 6.8. The machined surface in the IDR (Fig. 6.8a) appeared irregular with broken fibers, fiber pullout, and large pockets of fiber and matrix removed. These damage features are believed to be caused by singular abrasive particles at the periphery of the AWJ. The particle density at the jet periphery is low and their energy is high. Hitting the surface at almost normal angles of attack, these particles are capable of causing greater nonuniform damage as exhibited in the IDR. At greater magnification and at various depths of cut, the machined surface appears smoother and large pockets of material removal disappear. This is evident in micrographs (Fig. 6.8b–d) taken at different depths on the kerf surface. The machined surface is generally dictated by broken fibers and fiber pullout. Selective removal of the binder matrix is not apparent in these surfaces as it was the case in plain waterjet machined surfaces (Fig. 6.7). Both fibers and matrix appear to be removed by the same microcutting action of the abrasive particles in the AWJ. This results in smoother surfaces and the absence of high degree material damage due to delamination [14]. The material removal mode appears to be a combination of micromachining and brittle fracture of the fibers. This appears to be the dominant

material removal mode throughout the entire depth of cut, despite the macrovariations in surface topography that are evident in the RCR and the SCR. This suggests that the formation of macrofeatures in AWJ cutting is solely a product of the inherent energy of the jet [13].

6.1.3.2 Macrofeatures of AWJ Machined Surface

AWJ cut surfaces show three characteristic regions: the rounded IDR, a SCR, and a wavy or striated rough region (RCR) as shown in Fig. 6.6. The relative extents of the three regions are highly dependent on process parameters, and optimization of the AWJ cutting process for a particular material often involves proper selection of process parameters such that the SCR extends almost throughout the entire thickness [5]. Formation of IDR at the top of the kerf is caused by low density particle concentration at the periphery of the jet impacting the surface at almost normal angles. It is characterized by small penetration craters caused by singular particle impact and shallow abrasive wear tracks outlining the path of abrasives along the kerf wall. Standoff distance is the most significant influencing parameter on IDR while the effect of other independent parameters is negligible. In general, specimens machined with a low standoff distance exhibited smaller IDR, whereas higher standoff distance increased the damage width and depth [13].

The primary surface irregularity in the SCR, extending between IDR and RCR, is surface roughness. Waviness may appear randomly, or because of irregularities in the traverse speed and unsteadiness of jet pressure and abrasive feed rate. Surface roughness is due to minute wear tracks caused by the individual abrasive particles impacting the kerf wall. The size of wear tracks depends on the size of abrasive particles and their orientation is parallel to the jet direction. The orientation of wear tracks becomes more random with an increase in depth and a decrease in abrasive flow rate [16]. Figure 6.9 shows variation of the surface profile across the machined surface at different depths from the kerf top for the first 10 mm kerf wall. The surface profiles clearly show a transition from smooth surface in the SCR to wavy surface in the RCR, with waviness amplitude increasing with an increase in depth. Surface roughness is mainly dependent on abrasive particle size and supply pressure. Smaller surface roughness in the SCR was obtained by combinations of small abrasive particle size and low pressure [15]. Similar findings were also reported in AWJ machining of glass/epoxy bidirectional composite laminates (5 mm thick) [17]. It was found that abrasive type is the most significant factor affecting surface roughness followed by hydraulic pressure and traverse speed, which have almost equal significant effects. Standoff distance, abrasive flow rate, and cutting direction relative to fiber orientation were found to have insignificant effects on surface roughness. The optimum cutting conditions (within the range of parameters tested) in terms of average R_a in both SCR and RCR regions were obtained for aluminum oxide abrasive, 276 MPa supply pressure (high level), 1.5 mm/s traverse rate (low level), 1.5 mm standoff distance (low level), and 7.5 g/s abrasive flow rate (high level). The conditions that promote good surface finish are those associated

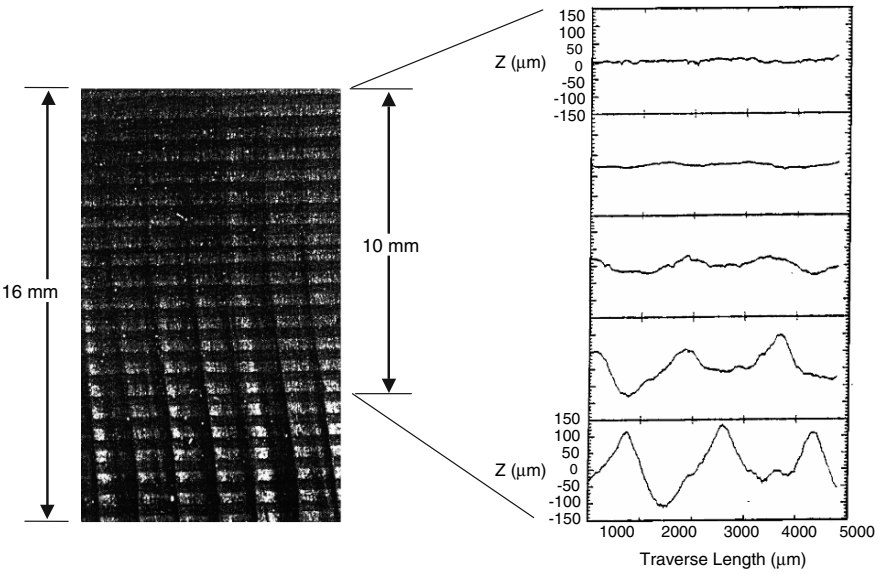

Fig. 6.9 Surface topography and profile of AWJ machined surface. Material = IM-6/3501-6, layup = $[(0/90/45/-45)_n]_s$, $V_f = 0.65$, thickness = 16 mm, pressure = 104 MPa, standoff = 1.0 mm, traverse speed = 1.6 mm, grit # = 100 [13]

with high abrasive kinetic energy and small abrasive size. Low, medium, and high are designated levels of the cutting parameters in a design of experiments study using Taguchi's method [17]. Even though the effect of supply pressure may be in contrast to the findings in [15], this disagreement is apparently attributed to the measurement domain in both studies.

The effect of abrasive flow rate and traverse speed on surface roughness in AWJ cutting of multidirectional graphite/epoxy laminate (4 mm thick) is shown in Fig. 6.10 [16]. The figure shows results of surface roughness measurements 0.5 mm from the jet entrance and exit on the machined surface. It is evident that surface finish is smoother near the jet entrance than the jet exit. At small traverse speeds, the roughness at entrance and exit is similar. But as the traverse speed increases the surface finish near jet exit deteriorates. Abrasive flow rate and traverse speed appear to have slight influence on roughness near the jet exit, but its influence is much greater near the jet exit. Surface roughness near the jet exit increases with an increase in traverse speed and a decrease in abrasive flow rate. Furthermore, the difference between entrance and exit surface roughness increases with an increase in abrasive flow rate.

The length of SCR was most affected by abrasive particle size, jet pressure, and traverse speed. Waviness amplitude in the RCR was affected by a combination of pressure, traverse speed, and grit size while waviness width was primarily affected by the traverse cutting speed. Due to interaction effects, both

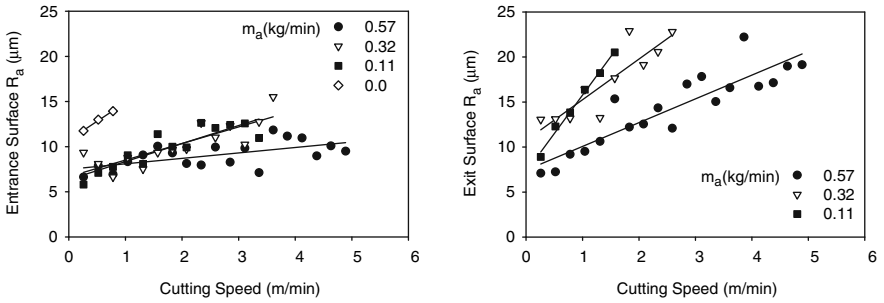

Fig. 6.10 Variation of surface roughness with traverse speed and abrasive flow rate, (**a**) at jet entrance and (**b**) at jet exit. Material = IM-6/3501-6, layup = $[(45/-45/90/0)_2, 45, -45]_s$, $V_f = 0.65$, thickness = 4 mm, pressure = 310 MPa, standoff = 1.0 mm, nozzle diameter = 1.15 mm, orifice diameter = 0.3 mm, abrasive = 60 grit garnet [16]

roughness and waviness height also increased with an increase in measurement depth [13]. Regression models for surface roughness and waviness height were reported in [13, 15].

6.1.3.3 Kerf Width and Taper

Kerf width is highly dependent on the structure of the AWJ and the machinability of the workpiece. The jet spreads out as it exits the mixing tube with the inner region of the jet having higher velocities and is convergent. Thus, it could cause a tapered cut in relatively hard-to-machine materials. For softer materials, a larger portion of the jet will be effective and kerf width will be either divergent–convergent, or only divergent, depending on thickness [11]. The kerf taper may be defined as the ratio of the kerf width at inlet (W_t) to the kerf width at exit (W_b),

$$T_R = \frac{W_t}{W_b}. \tag{6.1}$$

Parametric study of the influence of process parameters on kerf width and taper indicated that standoff distance has the largest influence on kerf width for shallow depths of cut. With an increase in cutting depth, the effect of traverse speed on kerf width increases, as well as the effect of other variables. For material thickness greater than 8 mm, kerf width is affected equally by pressure, traverse speed, and grit size while the effect of standoff distance became insignificant. Kerf taper was controlled primarily by standoff distance for material thickness less than 5 mm. As the cutting depth increased, the effect of grit size on kerf taper became more prominent. At greater depth of cut both standoff distance and grit size have significant influence of kerf taper. A regression model for the profile of the cut kerf in AWJ machining of graphite/epoxy multidirectional laminates is reported in [13]. The model provided good correlation with experimental results ($R^2 = 0.97$). Figure 6.10 shows the influence of standoff distance and traverse speed on kerf width at entrance and exit as

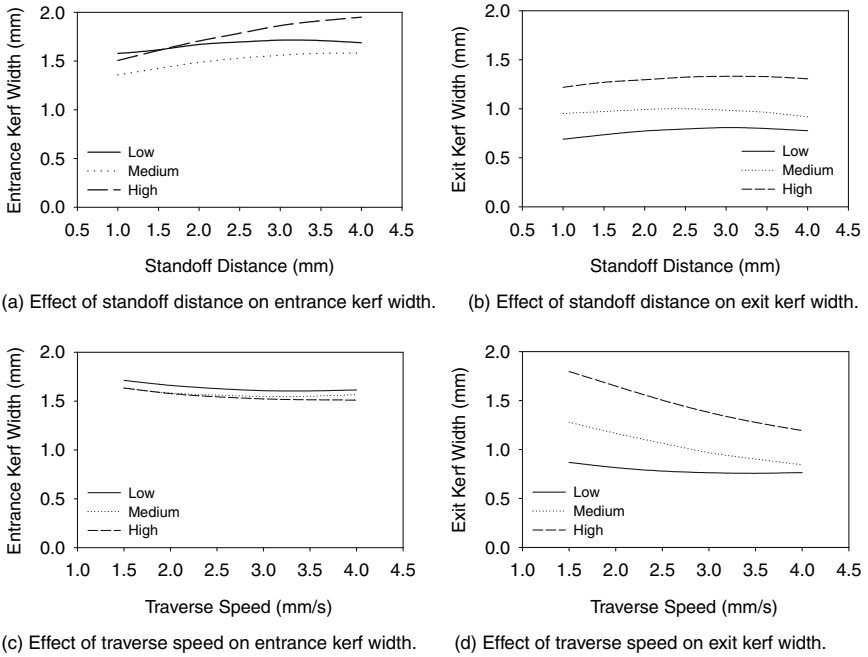

(a) Effect of standoff distance on entrance kerf width. (b) Effect of standoff distance on exit kerf width.

(c) Effect of traverse speed on entrance kerf width. (d) Effect of traverse speed on exit kerf width.

Fig. 6.11 Parametric effects on kerf width in AWJ machining graphite/epoxy multidirectional laminates. Low, medium, and high refer to the level of all cutting parameters as listed in Table 6.2, except for one being considered. Material = same as Fig. 6.9, orifice diameter = 0.3 mm, nozzle diameter = 1.0 mm, $m_a = 10\,g/s$ [13]

Table 6.2 AWJ cutting parameters levels for Figs. 6.11 and 6.12

AWJ parameter	Low	Medium	High
Pressure (MPa)	103	172	241
Standoff (mm)	4.0	2.5	1.0
Traverse speed (mm/s)	1.6	2.9	3.9
Grit size (garnet no.)	150	100	80

evaluated by the regression model. Entrance kerf width increases with an increase in standoff distance, whereas exit kerf width appears to have only slight changes. This is mainly attributed to the divergence of the AWJ with increased distance from the mixing tube exit. The exit kerf width decreases significantly with an increase in traverse speed whereas the entrance kerf width appears to have only slight changes (Fig. 6.11c, d). The limited effect of traverse speed on entrance kerf width is justified by the high energy of the AWJ before penetration. This energy is high enough to cause stable material removal at shallow depths regardless of the traverse speed. As the jet loses much of its energy near exit, its ability to remove material becomes more influenced by the traverse speed.

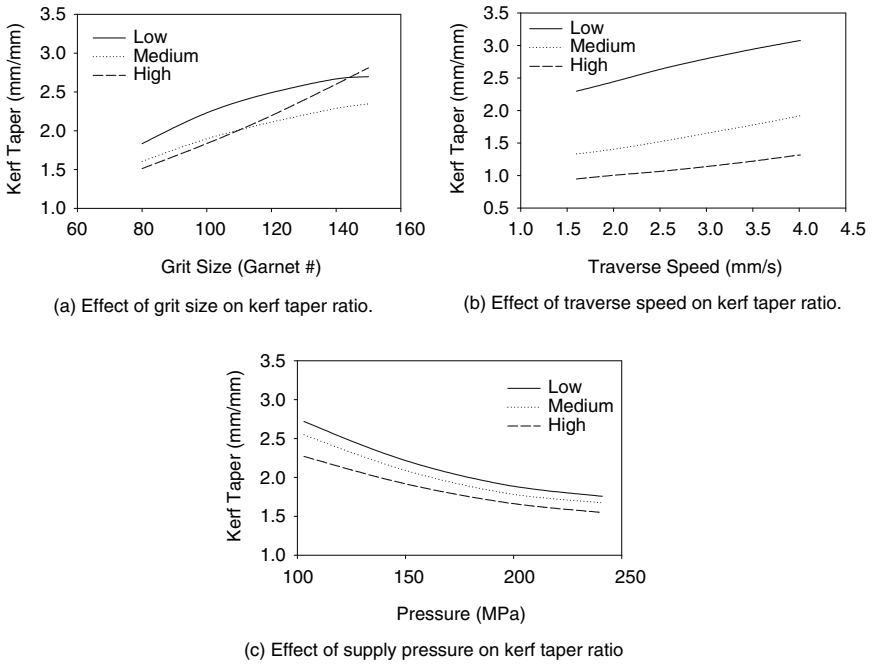

(a) Effect of grit size on kerf taper ratio.

(b) Effect of traverse speed on kerf taper ratio.

(c) Effect of supply pressure on kerf taper ratio

Fig. 6.12 Parametric effects on kerf taper in AWJ machining graphite/epoxy multidirectional laminates. Low, medium, and high refer to the level of all cutting parameters as listed in Table 6.2, except for the one being considered [13]

Figure 6.12 shows the influence of grit size, traverse speed, and pressure on kerf taper ratio as calculated by (6.1). Kerf taper increases with a decrease in abrasive particle size, an increase in traverse speed, and a decrease in pressure. The variation in kerf taper with traverse speed appears to be more significant at low level of the cutting parameters than at medium or high levels. This has to do with the rate of dissipation of jet energy with cutting depth at this level of parameters. The low pressure causes low jet speed and less kinetic energy for the particles. Jet diversion is greater at larger standoff distance and its ability to produce taper increases. Finally, smaller size abrasive particles lose their kinetic energy faster than larger particles because of their small mass. Thus, all of these in combination contribute to a greater rate of energy loss with an increase in depth of cut.

6.1.3.4 Delamination

Delamination generally occurs when cutting layered composites with high-velocity waterjets [14, 16, 18, 19]. Delamination is also observed in AWJ cutting of composites at high traverse speeds and low abrasive flow rate [14, 18]. Shaw and Tseng [20] explained the phenomenon of delamination in terms of linear fracture mechanics

using a similar approach to that discussed in conventional drilling (Sect. 5.4.5). It was assumed that the last supported plies in the structure act as an elastic plate that would deform elastically under the jet pressure. Crack propagation would occur at a critical level of energy release rate. It was suggested that the most likely site for delamination is the bottom of the laminate. It is argued, however, that normal loading of the jet pressure is not the only cause of delamination [11, 18]. Lateral flow of the jet due to jet deflection by previously formed steps on the kerf may also be able to penetrate the weak interface between the composite plies causing delamination. Colligan et al. [16] noted that all severe delaminations have abrasive particles wedged within the delamination space. This may have been caused by lateral jet flow. Konig et al. [19] noted that the occurrence of delamination in waterjet machining is always accompanied by enhanced curvature of the surface grooves and distinct increase in the surface roughness in the middle and bottom sections of the material. A sudden change in penetration rate could also cause delamination. This occurs when cutting coated materials, such as ceramic-coated metal, or workpieces made of layered materials of different hardness (steel-reinforced composites, fiber-reinforced composites). The jet penetrates the ceramic coating material easily, but deflects off the harder-to-penetrate substrate at the ceramic metal interface, resulting in cracking and spalling of the ceramic [11]. The work in [18] have shown that delamination is more closely related to the residual energy in the waterjet, which in turn is a function of the jet pressure. It was found that delamination size increases with an increase in traverse speed and a decrease in hydraulic pressure when cutting 4 mm thick CFRP laminate with waterjet.

Figure 6.13 shows polished cross sections of graphite/epoxy laminates after machining with waterjet (a) and AWJ (b) [16]. It is evident that severe delamination occurs throughout the entire laminate thickness when machining with plain waterjets and it is not confined to the last plies in the structure. The high-deflected

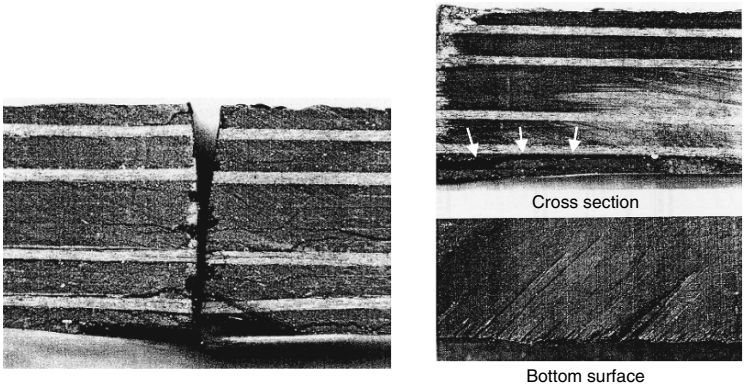

Fig. 6.13 Delamination damage in waterjet and AWJ machining of multidirectional graphite/epoxy laminates [16]

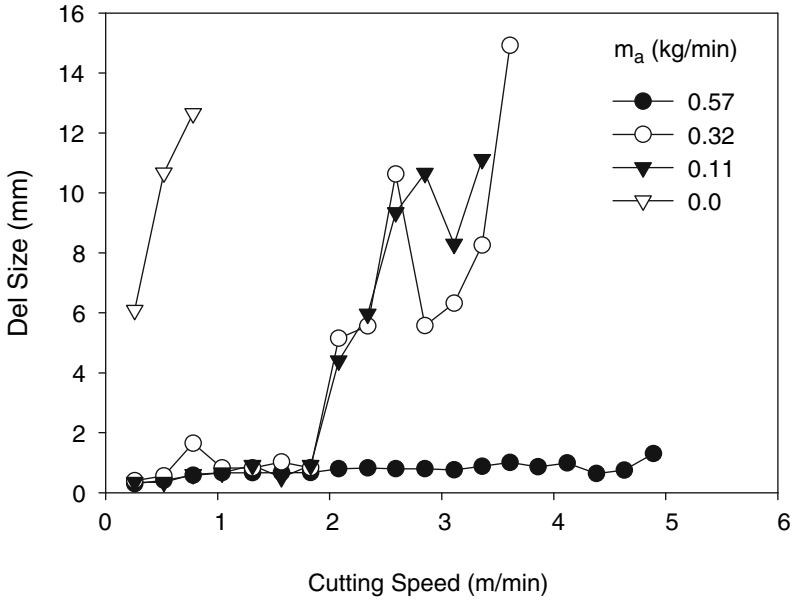

Fig. 6.14 Effects of traverse speed and abrasive flow rate on delamination size in AWJ machining of graphite/epoxy multidirectional laminates. Same conditions as Fig. 6.10 [16]

jet pressure and the lack of cutting mechanisms in plain weterjet generate sufficient loading to separate the composite plies at the fiber–matrix interface. Figure 6.13b shows that both interlaminar and intralaminar delamination of the exit plies occurs when AWJ machining of graphite/epoxy laminate. Abrasive particles wedged in between the delaminated plies resulted in visible out of plane delamination (bottom surface of specimen). The delamination is larger in thick laminates, but is independent of thickness and is always confined to the bottom two or three plies of the laminate. Figure 6.14 shows the relationship between the extent of delamination and process parameters. It is clear that increasing traverse speed and reducing abrasive flow rate increase the severity of exit ply delamination. It is noted that these operating parameters also result in generating waviness patterns on the bottom part of the kerf. Under these conditions the jet loses its ability to effectively cut the material at greater depths due to low exposure time and less active abrasive particles. Figure 6.14 shows that for a given set of cutting conditions delamination occurs at a critical traverse rate. The traverse rate at which delamination occurs appears to be independent of flow rate beyond a threshold flow rate. For flow rates above 0.57 kg/min, delamination occurs at a critical traverse speed of 1.77 m/min for a 4-mm thick laminate and at 0.8 m/min for 28.5-mm thick laminate [16]. Konig et al. [19] have also reported a critical traverse rate at which delamination occurs in waterjet machining of hybrid aramid-glass FRP (thickness, 3 mm; jet pressure, 350 MPa; standoff distance, 2 mm). The critical traverse speed was approximately 1.0 m/min for nozzle diameter of 0.15 mm and 1.5 m/min for nozzle diameters between 0.175 and 0.25 mm.

6.1.4 Modeling of AWJ Cutting

The AWJ cutting process is a complex process that is influenced by several factors and parameters encompassing hardware, process, and target material. It is highly desirable that the influence of these parameters on the performance of AWJ is understood and that predictive models are available to relate inputs and outputs. Such models are essential for the selection of optimum process parameters for a given combination of hardware system and target material. There are a number of models in the literature that attempt to predict the depth of cut achievable in different materials cut by AWJ, kerf geometry, and machining quality. These models are generally based on volume–displacement relationships [9, 21], energy conservation principle [18], or regression analysis of experimental data [13]. Some of these models and their predictive capabilities are discussed here. An extensive discussion of these models and many others is given in [7].

In general, models that are based on energy conservation principles or volume–displacement relationship require that the waterjet velocity and the abrasive particle velocity be known. In AWJ cutting, the abrasive particles are accelerated by exchange of momentum from the high-velocity waterjet. The theoretical velocity of the waterjet accelerating through an orifice is obtained from Bernoulli's law as

$$V_{\mathrm{th}} = (2P/\rho_{\mathrm{w}})^{1/2}, \tag{6.2}$$

where P is the pressure and ρ_{w} is the water density. In practice the actual jet velocity is lower than the theoretical velocity because of loss of momentum due to wall friction and compressibility of water. The actual jet velocity is given by

$$V_{\mathrm{j}} = C_v(2P/\rho_{\mathrm{w}})^{1/2}, \tag{6.3}$$

where C_v is a momentum efficiency coefficient. Typical values for C_v are in the range $0.85 < C_v < 0.95$. The abrasive particle velocity V_{a} can be related to waterjet velocity $\mathrm{V_j}$ using the exchange of momentum principle by

$$V_{\mathrm{a}} = \eta \frac{V_{\mathrm{j}}}{1 + (m_{\mathrm{a}}/m_{\mathrm{w}})}, \tag{6.4}$$

where η is a momentum transfer efficiency, m_{a} is the abrasive particle flow rate, and m_{w} is the waterjet flow rate. The momentum transfer efficiency is a function of several process parameters including pump pressure, abrasive mass flow rate, abrasive particle characteristics, and orifice and mixing tube geometry. The value of η is between 0.65 and 0.85. Experiments have indicated that an optimum momentum transfer occurs in the range of medium pump pressures, small abrasive flow rates, and large mixing tube diameters. The water flow rate is given by

$$m_{\mathrm{w}} = \rho_{\mathrm{w}} C_{\mathrm{d}} \frac{\pi}{4} d_{\mathrm{n}}^2 (2P/\rho_{\mathrm{w}})^{1/2}, \tag{6.5}$$

where C_{d} is a discharge coefficient for the waterjet orifice, whose diameter is d_{n}. This coefficient is typically between $0.6 < C_{\mathrm{d}} < 0.8$. Thus, for example, a pressure

of 310 MPa will produce a maximum waterjet velocity of about 750 m/s and a maximum possible particle velocity of 510 m/s for ratio $m_a/m_w = 0.25$, $C_v = 0.95$, and $\eta = 0.85$.

6.1.4.1 Depth of Cut for Ductile Materials

Hashish [9] developed a model for predicting the possible depth of cut in AWJ cutting of ductile material based on volume–displacement principle. In this principle, it is assumed that cutting is a steady-state process and that the volume removal rate calculated geometrically from the jet displacement is equivalent to the physical removal rate. The model allows the calculation of the depth of the cutting wear zone h_c and the depth of deformation wear zone h_d separately.

$$h_c = \frac{Cd_j}{2.5}\left(\frac{14m_a}{\pi u d_j^2 \rho_a}\right)^{2/5}\frac{V_a}{C_K}, \tag{6.6}$$

$$h_d = \left[\frac{\pi d_j \sigma_f u}{2(1-C)m_a(V_a - V_{thr})^2} + \frac{C_f}{d_j}\frac{V_a}{(V_a - V_{thr})}\right]^{-1}. \tag{6.7}$$

The total cutting depth h is the sum of h_c and h_d. In the above equations, C is a coefficient that depends on the local jet impact angle and it accounts for the termination for the cutting wear mode. The maximum value of C is 1 (when the cutting wear mode occurs) and the minimum value is 0 (when the cutting wear mode is terminated); d_j is jet diameter, for simplicity is replaced by the mixing tube diameter d_m; and u is traverse speed, where C_f is coefficient of wall friction ($C_f = 0.002$ is found adequate for depths up to 50 mm). C_K is an intrinsic velocity that combines particle and material characteristics and it is given by

$$C_K = \left(\frac{3\sigma_f R_f^{3/5}}{\rho_a}\right)^{1/2}, \tag{6.8}$$

where σ_f is the mechanical flow strength of the target material and R_f is the particle roundness factor, which is the average diameter of particle corners to the diameter of maximum inscribed circle. Typical value for roundness of garnet particles mesh 80–150 is 0.40. The strength of the target material is approximated as $\sigma_f = E/14$. V_{thr} is a threshold particle velocity that depends on the abrasive shape and type. Typical values of V_{thr} for common metals where determined experimentally by Hashish [9] as aluminum alloys $= 40$ m/s, stainless steel 304 $= 90$ m/s, alloys steel 4,340 $=$ 90 m/s, titanium 6Al-4V $= 60$ m/s. The prediction procedure for these models is outlined in Fig. 6.15. From the results provided in [9], the models provide good correlation with experimental data for materials thickness below 30 mm ($0.894 < R^2 < 0.988$). Some of the limitations of this model is that it is restricted to ductile behaving materials and that a threshold velocity have to be first determined for the target material. In addition, the particle velocity is hard to measure and approximate values have to be used.

1. Calculate the following nondimensional numbers

$N_c = \frac{h_c}{d_j}$ Cutting wear depth of cut number

$N_d = \frac{h_d}{d_j}$ Deformation wear depth of cut number

$N_1 = \frac{\rho_a u d_j^2}{m_a}$

$N_2 = \frac{\rho_a V_a^2}{\sigma_f}$

$N_3 = \frac{\rho_a V_{thr}^2}{\sigma_f}$ Minimum relative strength number

$N_4 = C_f$ Coefficient of wall drag($C_f \cong 0.002$)

$N_5 = 3R_f^{5/3}$ Particle shape number ($R_f \cong 0.4$ for garnet mesh 60–180)

$N_6 = \frac{V_{thr}}{V_a} = \sqrt{\frac{N_3}{N_2}}$ Threshold velocity number

$N_c = \frac{\sqrt{N_2 / N_5}}{\frac{(\pi / 14)^{0.4}}{C} N_1^{2/5} + \sqrt{N_3 / N_5}}$ Cutting wear depth number

$N_d = \frac{(1 - N_6)^2}{\frac{\pi / 2}{C_1}\left(\frac{N_1}{N_2}\right) + N_4(1 - N_6)}$ Deformation wear depth number, where $C_1 = 1 - C$

2. Determine the particle velocity V_a (equation 6.1)
3. Determine the angle of impact at top of the kerf $_t$ from $\alpha_t = \frac{a_1 N_1^{2/5} + \sqrt{N_3 / N_5}}{\sqrt{N_2 / N_5}}$, where $a_1 = (\pi / 14)^{0.4}$
4. Determine the optimum angle of impact, $_i$ from $\alpha_i = \left[\frac{\pi}{4\gamma_p}\frac{N_5^{1.5}}{N_2}\right]^{1/3}$

   where $\gamma_a = 1 + mr_a^2 / I$, r_a is abrasive particle radius and I is abrasive particle moment of inertia, $I = 0.5mr_a^2$ for particles with high sphericity (>0.7) and $I = 0.3mr_a^2$ for particles with low sphericity. Sphericity for garnet is approximately 0.78.
5. Compare α_t to α_i. If $\alpha_t > \alpha_i$, go to step 9.
6. Compare $V_a \sin \alpha_t$ to V_{thr}. If $V_{thr} > V_a \sin \alpha_t$ go to step 9.
7. Calculate the ratio C from $C = 1 - \frac{\alpha_t}{\alpha_j}$
8. Calculate the depth of cut h_c using $h_c = d_j N_c$
9. Calculate the depth of cut h_d using $h_d = d_j N_d$
10. Add h_c to h_d to obtain the total depth of cut. The value of h_c will equal zero if steps (7) and (8) are bypassed.

Fig. 6.15 Simplified calculation procedure for depth of cut prediction for ductile materials [9]

6.1.4.2 Depth of Cut for Brittle Materials

The depth of cut *h* for brittle materials is given by the Zeng and Kim [21] in the form of power expressions

$$h = \frac{N_m P^{1.25} m_a^{0.343} m_w^{0.687}}{8{,}800 u^{0.866} d_j^{0.618}}, \tag{6.9}$$

where h is in mm, m_a is in kg/s, P is in MPa, d_j is in mm, u is in m/s, and m_w is in kg/s. N_m is a machinability number which defines the material resistance to AWJ machining and is determined experimentally. The machinability number can be approximated by

$$N_m = \left(\frac{1,077}{R_B}\right)^{1.44}, \tag{6.10}$$

where R_B is the hardness of the target material on Rockwell B scale [22]. Experimental verification have shown that this model predicts values higher than experimental depths of cut for relatively soft materials. The predictions for ceramics and for low depth of cut (less than 50 mm) were found to be reasonable.

A similar model to that in (6.9) was obtained for phenolic fabric polymer matrix composite laminates (cotton fibers reinforced phenolic) using conservation of energy principle [23]. The model has the form

$$h = 12.406\frac{m_a^{0.429}P^{1.215}}{d_j u^{0.668}\rho_w}, \tag{6.11}$$

where h is in mm, m_a is in kg/s, P is in MPa, d_j is in mm, u is in m/s, and ρ_w is in $\mathrm{kg/m^3}$. A statistical analysis of the model predictions found that the regression coefficient $R^2 = 0.94$. It is noted that both models in (6.9) and (6.11) point out similar qualitative relationships between the depth of cut (jet penetration) and process parameters. The depth of cut generally increases with an increase in supply pressure and abrasive flow rate and decreases with an increase in traverse speed.

6.1.4.3 Delamination

A semi-empirical model for predicting delamination due to the pressure of waterjet was given in [18]. The underlying assumptions behind the model are similar to those used in the derivation of delamination in drilling by linear elastic fracture mechanics. It is assumed that delamination at a certain depth of laminate composite will occur when the jet energy is sufficient to propagate a circular crack. The layer beneath the waterjet was assumed to behave like a circular elastic plate that is clamped at its periphery. The average delamination damage measured perpendicular to the kerf is related to the specific jet energy, E at the kerf depth by

$$\mathrm{Del} = A\mathrm{e}^{-BE}, \tag{6.12}$$

where A and B are empirical constants and E is the specific energy at the kerf depth (or residual energy on the bottom ply) is defined by

$$E = \left(1 - \frac{h}{Z_{max}}\right)\frac{m(V_j - V_{thr})^2}{2ud_j}, \tag{6.13}$$

Table 6.3 Constants for (6.14)

Output	k	a	b	c	d	R^2
Material removal rate, $\frac{Z_w}{uS^2}$	0.018	1.9	0.3	0.5	−0.9	0.98
Depth of cut, $\frac{h}{S}$	0.12	2.4	0.8	0.9	−0.9	0.90
Width of cut, $\frac{W_t}{S}$	0.17	0.06	−0.14		−0.02	0.77
Width/depth ratio, $\frac{W_t}{h}$	1.4	−2.3	−0.95	−0.9	0.9	0.89

where h is the workpiece thickness, Z_{max} is the maximum kerf depth obtained under quasistatic traverse speed, V_{thr} is a threshold velocity, and V_j is the waterjet velocity.

6.1.4.4 Model for Milling CFRP

Hocheng et al. [24] used dimensional analysis to derive a relationship between input parameters and the output of AWJ milling process of CFRP. The mathematical relationship has the form:

$$\text{Output} = k\left(\frac{v_a - v_{thr}}{u}\right)^a \left(\frac{uS^2\rho_a}{m_a}\right)^b \left(\frac{d_a}{S}\right)^c \left(\frac{\sigma_f S^2}{um_a}\right)^d, \tag{6.14}$$

where Output is the output parameter of the AWJ process, S is standoff distance, d_a is abrasive diameter, and the remaining parameters have the same meaning in (6.7). A threshold velocity of 80 mm/s was estimated for this application. The constants a, b, c, and d are listed in Table 6.3 for a number of output parameters. Also listed are the regression coefficients for the different outputs. It is seen that model predictions for MRR and depth of cut are very good, as indicated by the coefficient R^2.

6.2 Laser Machining

Laser machining of FRP composites offers many advantages over traditional machining processes. There is no contact between the tool and the workpiece, and hence there are no cutting forces, no tool wear, and no part distortion because of mechanical loading. Laser cutting is a thermal process and is not influenced by the strength and the hardness of the work material. Therefore it is best suited for cutting heterogeneous materials composed of different phases with contrasting mechanical properties. It provides high machining rates, thin kerf width, and flexibility to cut complex contoured shapes. Drawbacks of laser cutting include material changes and strength reduction due to the formation of a HAZ, the formation of kerf taper and a decrease in cutting efficiency as thickness of workpiece increases. Most of these problems are effectively reduced by proper selection of process parameters

for optimum cutting performance. Another problem in laser machining of composite materials is the generation of hazardous chemical decomposition products. Mass spectrometry and gas chromatography analysis of fumes from laser cutting of graphite/epoxy, aramid/epoxy, and glass/epoxy indicated the presence of fragmented powders of fiber materials and high concentrations of CO, CO_2, and low molecular organic compounds. It has also been shown that laser cutting of aramid/epoxy produces large quantities of hydrogen cyanide, which may pose a considerable health risk [25]. Several studies have reported on the applicability of laser cutting technology in processing FRPs. The following sections give a summary of the major findings.

6.2.1 Technology Overview

Laser machining utilizes the energy from an intense, highly directional coherent beam of infrared light to remove material from the workpiece by localized melt shearing and vaporization. LASER stands for Light Amplification by Stimulated Emission of Radiation, which is the underlying principle for the generation of all types of lasers. This principle states that if an atom or molecule is raised to a high energy level by an outside energy source (e.g., heat, light, chemical reaction, etc.) and is allowed to decay back to its ground state energy level, a photon (unit of light) is released. If that photon contacts another atom or molecule that also has been raised to a high energy level, the second atom or molecule will be triggered to return back to ground state, releasing a second photon along with the triggering photon. The pair of photons released has identical wavelength, phase, direction, and energy (coherent). In a laser generating device, the emitted photons are subjected to multiple reflections by two highly parallel and partially transmitting mirrors. This allows for the light to be highly amplified by stimulating the lasing media. The light then emerges from the partially transmitting mirror as a highly culminated and coherent beam.

Lasers are categorized into solid-state and gas lasers, depending on the lasing media as shown in Table 6.4. Furthermore, all laser types operate in one of two temporal modes: continuous (CW) and pulsed modes. In continuous mode, the laser

Table 6.4 Types of lasers [26]

Laser type	Active media	Mode of operation	Wavelength (μm)
Solid-state	Cr:Ruby	Pulsed	0.6943
Solid-state	Nd:glass	Pulsed	1.06
Solid-state	Nd:YAG	CW or pulsed	1.06
Gas	Heliem–neon	CW or pulsed	0.6328, 1.15, 3.39
Gas	Argon	CW or pulsed	0.4765, 0.4880, 0.5145
Gas	CO_2–N_2–He	CW or pulsed	10.6

beam is emitted without interruption. In pulsed mode, the laser beam is emitted periodically. CO_2 lasers are capable of delivering high power up to 3 kW and their radiation is absorbed well by nonmetals. The solid-state YAG lasers (Yttrium aluminium garnet crystal doped with Nd^{3+}) are operated in the pulse mode and can achieve peak powers of 7–10 kW, with an average power in the order of 400 W. Their radiations are not effectively absorbed by organic materials or glass. Therefore, CO_2 lasers are best suited for machining of composites materials and the YAG lasers are not suitable for cutting glass FRPs.

6.2.1.1 Laser Cutting Systems

Laser cutting systems generally consist of four major groups of components: laser beam generation (CO_2 or Nd:YAG); beam delivery and focusing; workpiece positioning relative to the laser beam; and auxiliary devices such as gas nozzle and safety equipment. Figure 6.16a is a schematic of laser cutting system. There are several variations of the laser beam introduction to the workpiece. The beam could be fixed while the workpiece is moved by a CNC-controlled two-axes table. In other configurations, such as a robotic arm, the workpiece is fixed while the beam is moved in three-dimensional space. In all laser systems, a beam delivery system is used to transport and focus the laser beam for cutting or drilling. The beam delivery system houses reflecting mirrors, a focusing lens, and a coaxial gas nozzle. The beam is focused to a spot diameter in the order of 0.1 mm and intensity in the order of $10\,MW/cm^2$. The gas jet coming through the nozzle assists the laser beam in cutting by generating a secondary heat source (as in the case of exothermic reaction of oxygen with ferrous materials). At low cutting speeds, the gas jet flowing through the kerf enables heat transfer toward the backside of the workpiece. At high jet pressures, the gas provides efficient cooling at the beam entry side and results in reducing beam entry kerf width. The assist gas also helps in the mechanical removal of material from the kerf and in keeping debris from contaminating the focusing lens (Fig. 6.15b).

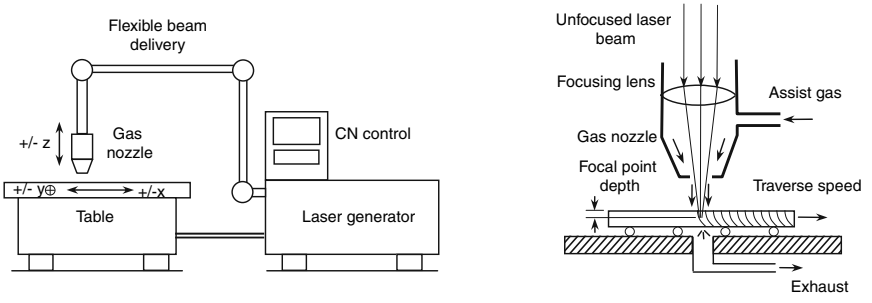

(a) Schematic of 3-axes laser cutting system

(b) Cutaway of the gas nozzle

Fig. 6.16 Schematics of a typical three-axes laser cutting system

6.2.1.2 Laser Cutting Process Parameters

The laser cutting process parameters are grouped into four categories:

1. Laser beam parameters: power density, wavelength of emission, temporal mode (CW or pulsed), spatial mode (TEM mode), and focal spot size
2. Gas parameters: gas mixtures, gas pressure, and nozzle configuration
3. Machine tool parameters: cutting speed (also known as feed or traverse speed)
4. Workpiece parameters: thickness, absorption coefficient of at the given laser beam wavelength, melting and vaporization heat, melting and vaporization temperatures, thermal conductivity, and heat capacity

Laser parameters and workpiece parameters determine the effectiveness of laser machining. The TEM mode (transverse electromagnetic mode) describes the characteristic spatial pattern of the laser beam and determines its propagation and focusing. The subscripts "mm" refer to the number of nulls (zero intensity) in the spatial pattern that occur in each of two orthogonal directions transverse to the direction of beam propagation. The TEM_{00} mode is often used for machining. In this mode, the laser beam intensity follows a Gaussian distribution as a function of spot radius. The smallest spot size possible for gas lasers is about 0.1 mm in diameter. Part of the incident beam is reflected by the surface of the workpiece. The amount by which the beam is reflected depends on the wavelength of the beam and the surface condition of the workpiece. Generally, the longer the wavelength of the laser beam, the higher the reflectivity of the surface. Laser energy which is not reflected is absorbed by the surface of the workpiece. Energy transfer to the workpiece takes place in two ways: at low values of specific power, absorption typically takes place in a superficial layer of the material less than 1 μm deep and it penetrates further into the material by conduction; at specific powers high enough to vaporize the material, a vapor column surrounded by the melted material is formed. Due to the multiple reflections of the beam within the hole and the energy absorbed through the entire thickness of the workpiece, more efficient heat transfer occurs. Deep penetration occurs in composite materials at specific powers in the order of 10^2–$10^3\,W/cm^2$. The size of the hole and the efficiency of heat transfer are influenced by the laser beam diameter, the assist gas pressure, absorption coefficient, and vaporization temperature of the material.

6.2.1.3 Process Capabilities

Laser cutting is a highly flexible-high productivity process with a wide range of equipment commercially available. Many different kinds of materials can be cut, regardless of hardness. The flexibility of the laser system and computer numerical control of the machine tool provide dimensional tolerances that are typically between 0.05 and 0.1 mm. The kerf width is typically in the order of the laser beam diameter (0.1–1.0 mm) and surface roughness is comparable to AWJ machining (1–10 μm). A major drawback of laser cutting is the formation of a HAZ and

Table 6.5 Representative data for laser cutting of FRP composites [27]

Material	Laser power (W)	Cutting speed (m/min)	Thickness/kerf depth (mm)	Kerf width (mm)
Kevlar/epoxy	150–950	2.0	3.2–9	0.1
Aramid/polyester	800	0.5	2.0	0.6
Glass/epoxy	1000	2.0	5.0	0.5
Glass/polyester	800	0.5	2.0	–
Graphite/epoxy	300	0.3	1.0	0.1
Graphite/epoxy	1,000–2,000	0.9–7.2	1.0–4.0	–
Graphite/polyester	800	0.5	2.0	0.5

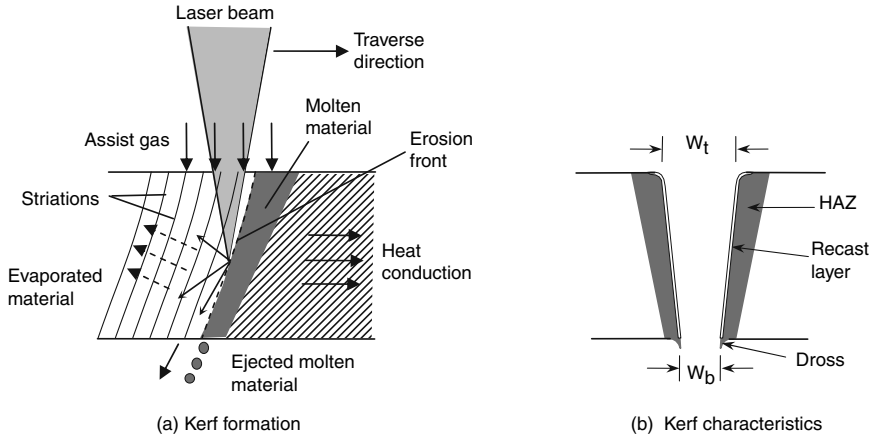

Fig. 6.17 Erosion front in laser cutting

striations on the machined surface. Both phenomena are controlled by the process parameters (cutting speed and beam power) and may be significantly reduced or eliminated. In general, laser cutting provides higher cutting speeds than AWJ machining. Table 6.5 lists representative cutting data of common FRP composites.

6.2.2 Mechanisms of Material Removal

Material removal in laser cutting takes place by creating and moving an erosion front in the direction of cutting as shown in Fig. 6.17a. As a focused laser beam impinges on the surface of the workpiece, a certain amount of heat is absorbed by the material at the surface and subsequently conducts into the workpiece. The interaction of the absorbed heat with the assist gas and the workpiece material causes material to be removed and a kerf or slot is formed to a certain penetration depth. Deep penetration in most metals occurs at laser power density of $10^6\,\mathrm{W/cm^2}$, and for composites it occurs at much lower power densities (10^2–$10^3\,\mathrm{W/cm^2}$) [28]. Material removal from the kerf takes place by one or more of the following mechanisms: inert gas

melt shearing, reactive gas melt shearing, vaporization, chemical degradation, and scribing [29]. For materials that melt when heated with a laser beam, such as metals and thermoplasitcs, the focused heat forms a penetration cavity of molten metal which is subsequently removed by the shearing action of a high-pressure assist gas. Air is most commonly used when oxidation is not a concern. Inert gas such as nitrogen and argon are used when oxidation is not tolerated. The edge of the laser cut material shows a regular pattern of striations as shown in the figure. These are believed to be caused by cutting front instabilities. Active gas melt shearing is used to cut ferrous metals by replacing the inert gas with oxygen or air. An additional heat source is generated from exothermic reaction of the active gas with the metal. This allows for higher cutting speeds than with inert gas melt shearing. Vaporization takes place when the material is heated rapidly to the vaporization temperature and subsequently ejected with molten material by the action of the assist gas. This mechanism is more common for some polymers, polymer composites, and wood. Because of the absence of melting, the surface roughness produced is better than that of melt shearing. However, the cutting speeds are comparatively lower. Chemical degradation relies on material disintegration by breaking of chemical bonds due to the action of the laser beam. This mechanism is most common for aramid composites, thermoset polymers, elastomers, and wood. Scribing is the mechanism most common in machining ceramics and involves creating grooves on the surface of the workpiece which later become locations of high stress concentration and fracture.

Kerf formation in laser cutting is a predominantly thermal process and its characteristics are closely related to this process. Figure 6.17b is a schematic of the laser cutting kerf. Because of the melting of the material and subsequent cooling as the cutting front moves away a thin recast layer is formed by solidification. Solidification of molten metal droplets may also occur at kerf exit forming dross. This may require deburring subsequent to laser cutting. Striations on the machined surface result from propagation of a cyclic erosion front. The frequency of striations depends on traverse speed and laser power. Depending on the severity and frequency of striations, the surface finish of the laser cut edge may not be acceptable and further smoothing may be required. Heat conduction away from the cutting front creates a HAZ of different characteristics than the parent material. The size of the HAZ depends on workpiece thermal conductivity, laser beam power, and cutting speed. Kerf taper is also affected by the feed rate and laser beam power. In general, it is desirable to obtain a laser cut that is taper and striations free and with the minimum size of HAZ. This requires an optimization of the cutting process parameters leading to a set or a range of acceptable levels process parameters for a given material thickness [30].

6.2.3 Laser Machining Characteristics of FRPS

Laser cutting of FRPs is a complicated process because the constituents of these materials have greatly different physical and thermal properties, and thus behave

Table 6.6 Typical thermal properties of matrix and fiber materials

Material	Conductivity s [W/(m K)]	Heat capacity [J/(kg K)]	Vaporization temperature (°C)	Thermal diffusivity $(cm^2/s) \times 10^{-3}$	Heat of vaporization (J/g)	Density (g/cm^3)
Epoxy	0.10	1,100	400–440	0.76	1,100	1.20
Polyester	0.20	1,200	350–500	1.33	1,000	1.25
Aramid fiber	0.05	1,420	950	0.24	4,000	1.44
Glass fiber	1.0	850	2,300	4.61	31,000	2.55
Graphite fiber	50	710	3,300	380.66	43,000	1.85

differently when exposed to the high energy laser beam. Table 6.6 below shows various thermal and physical properties of polymer matrix and reinforcing fiber materials. Polymers in general have a very high absorption coefficient for infrared radiation, low thermal conductivity, low diffusivity, and very low heat for vaporization when compared to the reinforcing fibers. When the composite material surface is hit by the laser beam the matrix is first affected by the heat. Most cutting of thermoplastic matrix material in FRPs takes place by shearing of a localized melt formed by the laser beam. Epoxy matrix materials are removed by chemical degradation, which requires higher energy and higher temperatures than melt shearing of thermoplastics. The reinforcing fibers require higher temperatures and longer exposure time to vaporize. Aramid fibers have thermal properties that are close to the polymer matrix and they will be affected by the heat in a similar manner. This is why aramid-reinforced polymers are the most suitable for laser cutting. Glass fibers have much higher vaporization temperature and thermal diffusivity. Their cutting by laser beam may occur by melting or vaporization. Carbon fibers require the highest vaporization temperature and their thermal conductivity is the highest. This leads to great dissipation of the heat into the workpiece creating a large HAZ. Therefore, CFRPs are the least suitable for high-power CO_2 laser cutting. However, reasonable improvements in cutting quality may be achieved by using pulsed Nd:YAG lasers [31, 32]. The higher beam intensity, less interaction time, and better focusing behavior of these lasers give a smaller thermal load and consequently a smaller HAZ than a continuous CO_2 laser.

The laser cut surface is characterized by uneven material removal of the matrix and the fibers because of differences in heat for vaporization, the formation of a charred layer near the kerf surface, slope of the kerf surface, and the formation of a HAZ. These characteristics are shown schematically in Fig. 6.18 [33]. Laser cutting quality is strongly influenced by material properties such as laminate layup, thermal diffusivity, and vaporization temperature and by cutting speed, laser power, and the assist gas type and pressure. Charring is typically caused by chemical decomposition of the epoxy matrix and in the case of aramid FRPs, by chemical decomposition of the fibers. A layer of protruding fibers is exposed when the charred material is removed and is caused by the selective removal of the binder matrix by decomposition, vaporization, or melt shearing. In addition, heat conduction into the workpiece causes heat damage and deterioration of the material properties to a certain depth or

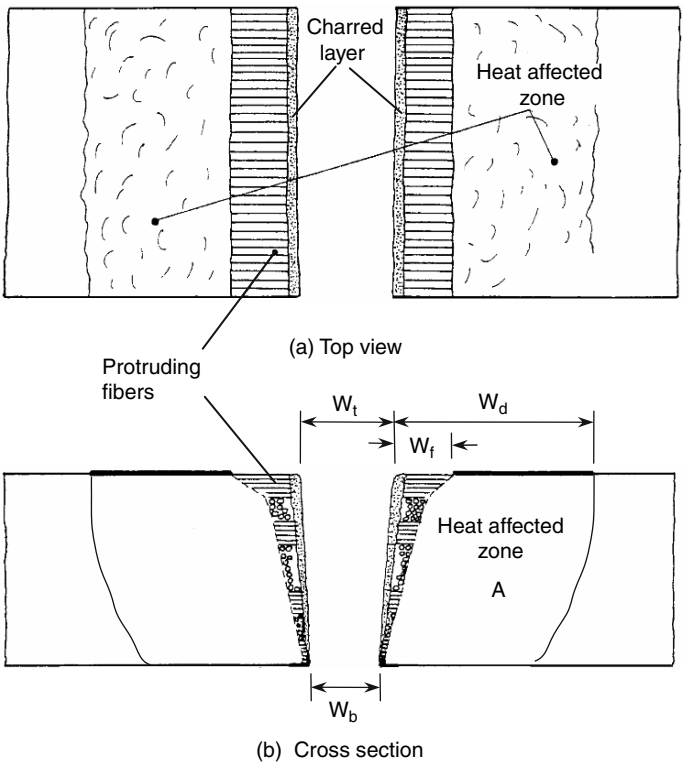

Fig. 6.18 Schematic of FRP composites laser cutting characteristics [33]

area. The boundaries of the HAZ are associated with isotherms of the matrix char temperature. The size and shape of HAZ are closely related to the fiber orientation relative to the travel direction of the laser beam and the thermal conductivity of the fibers. Cutting unidirectional CFRPs perpendicular to the fibers has been reported to produce larger area of HAZ than when cutting parallel to the fibers [34]. This is apparently due to the channeling of heat away from the cutting zone by the excellent heat conducting carbon fibers. Craters and delamination may also result from laser cutting because of thermal stresses and the pressure of the assist gas.

6.2.3.1 Surface Morphology

Material removal in laser cutting of FRPs takes place by chemical degradation, vaporization, and to a lesser extent by melt shearing. Generally, the energy needed to vaporize the fibers is higher than that required for the matrix. Therefore, the matrix is first disintegrated by the action of the laser beam. The morphology is therefore dependent on the constituents of the composite and arrangement of fibers. It is also dependent on the cutting speed and the laser beam power. Striations, similar to those

observed in laser cutting of metals, were visible on the cut surface when machining of woven aramid fiber-reinforced polyesters with continuous CO_2 laser at low cutting speeds. Increasing the cutting speed, the striations became less pronounced and eventually disappeared at a critical cutting speed [28]. Striations were also reported at all cutting speeds, and seemed to be fairly independent of the cutting speed when machining carbon-fiber-reinforced laminate with pulsed Nd:YAG laser [31]. Uneven surface appearance in laser cutting was also caused by nonuniform loss of material from the surface. Remarkable loss of the matrix is evident, particularly near the beam entry. The presence of longitudinal grooves (parallel to the laminate) as well as the scanty presence of longitudinal fibers suggested that many fibers in the longitudinal direction are removed together with the matrix. Nonuniform material loss appears to be a function of the matrix and the fiber materials selected. Aramid fibers have thermal characteristics similar to the polymer matrix materials, so material behavior during beam/material interaction is similar to that of homogeneous materials. SEM micrographs of the kerf surface for aramid FRP shows a relatively smooth surface between fiber and matrix regions. Graphite fibers, however, exhibit matrix loss between the laminates that is much higher than that observed for other fiber materials. In all cases, the cut surface is covered with a charred layer and resolidified matrix residues. Charring is more pronounced at low cutting speeds and/or high laser beam power. In addition, delamination between the 0° and 90° laminates and debonding of the fibers from the matrix were occasionally detected [28, 31].

Microscopic examination of the machined surface is possible once the charred layer is removed by mechanical polishing. Figure 6.19 shows SEM micrographs of the machined surface of aramid, glass, and carbon FRPs after the charred layer has been removed [28]. It is evident from these pictures that the matrix material has been removed from between the fibers, creating an appearance of fibers standing alone or protruding from the surface. The length of the protruding fibers decreases with an increase in the cutting speed, but is independent of the assist gas pressure [33]. The end of the aramid fibers are carbonized to a considerable length (Fig. 6.19a) while the glass fibers appear to be partially melted and cut at different lengths (Fig. 6.19b). For glass fibers near the beam entry no signs of melting could be detected but a central cavity was present at the fiber end. This distinctive appearance may be a result of fiber disintegration by vaporization. The carbon fibers are cut at the same length and appear to be covered by carbonized residues (Fig. 6.19c).

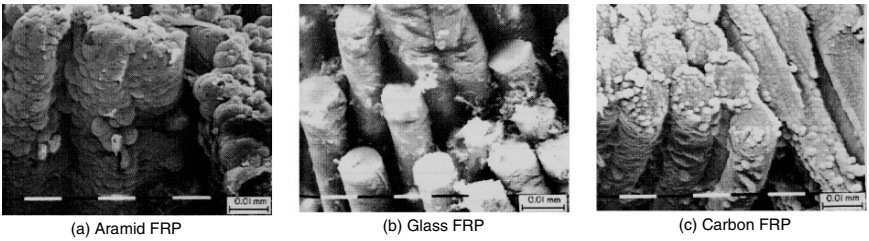

(a) Aramid FRP (b) Glass FRP (c) Carbon FRP

Fig. 6.19 SEM photos of the laser machined surface after cutting with 500 W continuous laser [28]

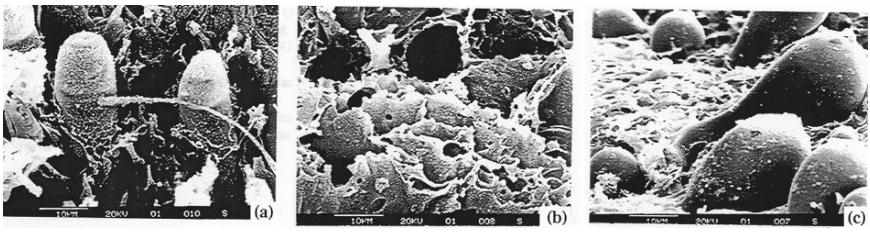

Fig. 6.20 SEM photos of Nd:YAG laser drilled hole in glass/epoxy composite. (**a**) bottom, (**b**) mid-height, and (**c**) mouth regions [35]

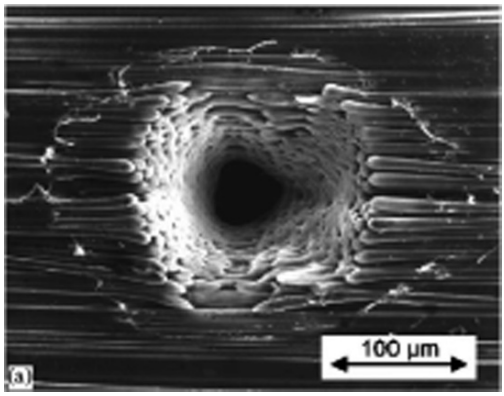

Fig. 6.21 Fiber swelling in T300 carbon-fiber-reinforced polymer drilled with Nd:YAG laser [36]

Distinctly different microscopic surface appearances were reported after drilling glass and carbon FRPs with pulsed Nd:YAG laser as shown in Fig. 6.20 [35, 36]. At the hole entry glass fiber ends resembled mushroom heads sticking out of the matrix (Fig. 6.20c). This is likely because prolonged exposure to laser radiation caused the matrix to disintegrate and recede to a considerable depth, but the energy was only high enough to melt the fibers into droplets. For locations in the middle of the hole, the surface morphology shows both fibers and matrix disintegrated to the same level (Fig. 6.20b). As for the surface near the bottom of the hole fractured glass fibers were found imbedded in the molten polymer matrix (Fig. 6.20a). This was attributed to the low level of laser power at the bottom of the hole, which was only high enough to disintegrate the matrix and leave the fibers standing alone. Subsequently the protruded fibers were fractured due to the stresses generated by the assist gas jet pressure or thermal loading [35].

The Nd:YAG laser cut ends of PAN based T300 carbon fibers exhibited considerable swelling close to the hole and extends around 100 µm from the hole as shown in Fig. 6.21 [36]. The hole is slightly elongated parallel to the fiber direction. This is due to the higher thermal conductivity along the fibers. The fiber swelling which was attributed to internal gas pressure generated by the rapid volatilization of impurities within the fibers, occurring simultaneously with the structural ordering when high temperatures in the order of 1,300–2,000 °C are attained. Untreated PAN based T300 fibers are low modulus fibers containing 92–95% carbon. The fibers

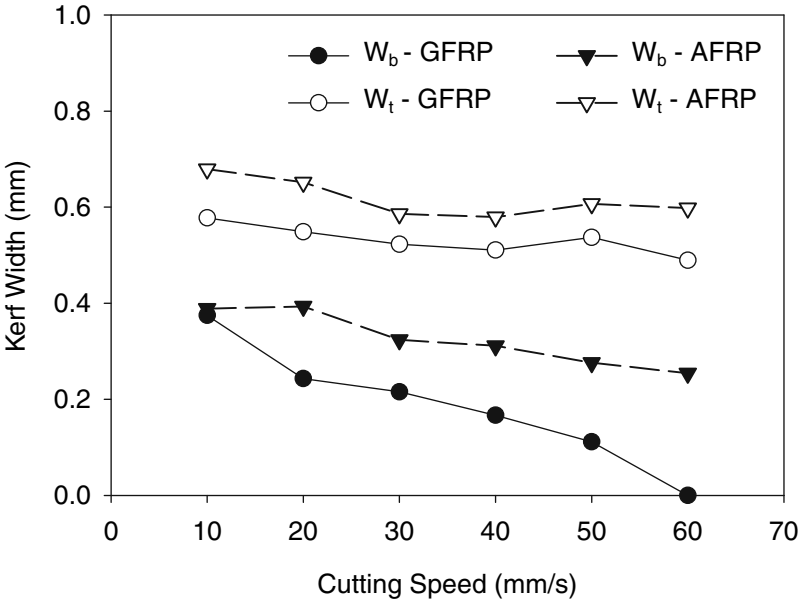

Fig. 6.22 Variation of kerf width at top and bottom of workpiece with cutting speed for CO_2 laser cutting of AFRP and GFRP. Thickness = 4 mm, laser power = 800 W, mode = CW, spot radius = 0.1 mm [37]

incorporate a high level of structural disorder and volatile noncarbon impurities that can be removed by heat treatment. It was shown that subjecting the carbon fibers to a heat treatment at 2,000 °C results in more ordered fiber graphitic structure, with much reduced swelling during laser cutting [36].

6.2.3.2 Kerf Width and Taper

The top kerf width at the beam entry side (W_t) and bottom kerf width at the beam exit (W_b) decrease as the cutting speed is increased as shown in Fig. 6.22 [37]. A limiting cutting speed exists for which the kerf width at the bottom becomes equal to zero and a through cut is no longer possible. It is suggested that the kerf formation is more sensitive to the interaction time of the beam and the workpiece material, which is inversely proportional to the cutting speed. The slower the cutting speed the longer the interaction time and the more energy absorption and conduction into the workpiece. This leads to a larger volume of material to be removed and a wider kerf. The kerf width was also found to be less sensitive to power, thickness, and assist gas pressure. An increase in the laser beam power and a decrease in the assist gas pressure generally resulted in an increase in kerf width [33]. The kerf width for aramid FRP is shown to be more than that for glass FRP and is less dependent on cutting speed at the bottom side of the workpiece. This is attributed to the lower

heat for vaporization and more homogeneous thermal behavior of aramid FRP. In pulsed Nd:YAG laser cutting of CFRP it was found that the top kerf width is dependent on pulse frequency. The top kerf width decreased with an increase in pulse frequency up to a critical value then increased with further increase in pulse frequency. The bottom kerf width showed only a decreasing trend with an increase in pulse frequency [32].

Usually the kerf width at the beam entry is larger than that at the beam exit, even though under some conditions due to interactions with the assist gas, the bottom kerf width may be larger [28, 32, 33]. This creates an inclination or taper of the cut surface. The decrease in kerf width with the increase in depth is due to the decrease in the beam energy absorbed by the material. With the decomposition of constituent materials starting at the top surface, a keyhole is formed and a vapor column grows and acts as a blackbody for the laser beam. The incident radiation which falls into the keyhole loses some power due to reflection and absorption by the vapor. In addition, diversion of the beam beyond its focal point leads to decreasing power density along the keyhole [28]. The difference between the top kerf width and the bottom kerf width, which also defines kerf taper, increases with an increase in cutting speed. This is more pronounced for the glass FRP. The kerf taper for aramid FRP appears to be almost constant while that of glass FRP increases with an increase in cutting speed. This is because the limiting speed for through cutting has been reached. In pulsed Nd:YAG laser cutting of CFRP it was found that kerf taper was decreased with an increase in pulse frequency to a minimum, then increased with further increase in pulse frequency. Higher pulse duration, higher cutting speed, and lower pulse energy were also found to reduce kerf taper [32].

6.2.3.3 Heat Affected Zone

Laser cutting forms a HAZ, which is bound on the kerf side by charred matrix residues and protruding fibers, and extends into the workpiece to a point at which the material temperature reaches the decomposition temperature of the matrix. Since heat conduction is the primary mode for energy transfer from the cutting zone to the surrounding material, the size of HAZ is dependent on process parameters that would facilitate or impede heat conduction. These include interaction time (or cutting speed), thermal conductivity (as influenced by fiber properties and fiber layup), and laser beam power. The size of HAZ increases as the difference between the vaporization temperatures of the fibers and that of the matrix become larger. Small size of HAZ is obtained when thermal properties of the fiber are closest to those of the matrix (e.g., aramid fibers and organic matrix). Carbon fibers, on the other hand, have much higher vaporization temperature than the matrix. Therefore, much higher temperatures are required for cutting the fibers and more heat is conducted away from the laser beam, creating a wider HAZ [28]. The size of HAZ also decreases with an increase in cutting speed, because of the smaller interaction time, and increases with an increase in laser power. The ratio of laser power to cutting speed is called specific laser energy, E_s, which defines the energy input per unit

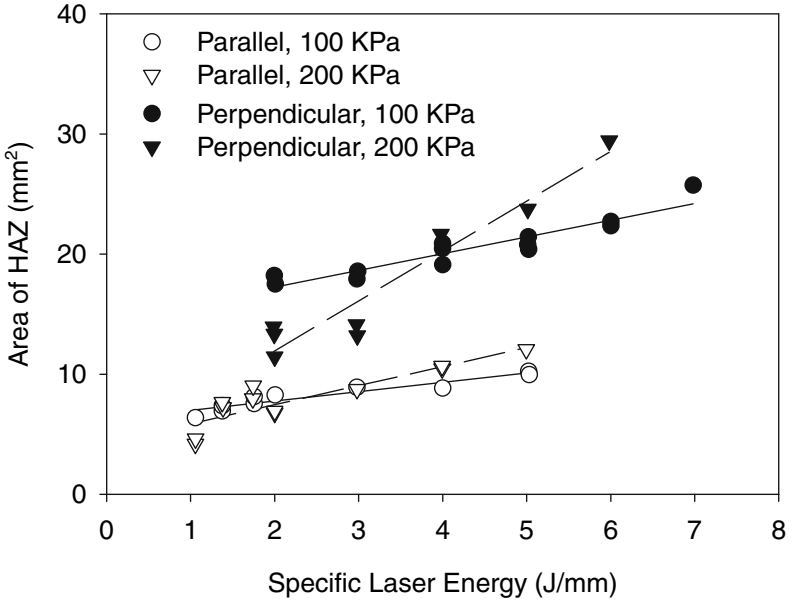

Fig. 6.23 Effect of specific cutting energy and assist gas pressure on the section area of HAZ in laser cutting of carbon/PEEK. Laser power levels from 350 to 650 W, frequency = 300 Hz. N_2 coaxial jet was used as assist gas [34]

length of the material along the cut,

$$E_s = \frac{PQ}{v}, \tag{6.15}$$

where P is the laser beam peak power, Q is the pulse duty, and v is the cutting speed. For continuous lasers the pulse duty is 1.0, and it is less than 1.0 for pulsed lasers. Figure 6.23 shows the influence of specific laser energy on the cross-sectional area of HAZ in machining carbon/PEEK unidirectional composites with pulsed CO_2 laser [34]. It is shown that the size of HAZ generally increases with an increase in the laser specific energy. Furthermore, the size of HAZ for cutting perpendicular to the fibers is considerably larger than that for cutting parallel to the fibers. This is because carbon fibers have much higher thermal conductivity than the matrix which causes greater amounts of heat to dissipate when cutting perpendicular to fibers, and thus the size of HAZ is larger. The influence of assist gas pressure on the size of damage is also shown in the figure. The interactions between the assist gas pressure, specific energy, and fiber orientation are apparent in the results whereas increasing the assist gas pressure results in reducing the heat damage below a certain level of specific laser energy. Increasing the assist gas pressure was also found to decrease the size of heat damage in laser machining of aramid/epoxy composites [33]. This may be attributed to efficient cooling effects of the assist gas. Beyond the critical energy level increasing the assist gas pressure results in an increase in the size of

heat damage. This effect may be attributed to the role the assist gas plays in heat transport through the thickness of the workpiece and to the rise in flow turbulence and less effective cooling at high pressure. Furthermore, the effect of assist gas on thermal damage is more pronounced when cutting perpendicular to the fibers. Statistical analysis of the results in Fig. 6.23 indicated that specific laser energy is the most influencing factor, followed by first-order interaction between gas pressure, specific laser energy, and fiber direction relative to the cutting speed. An empirical equation relating these parameters to the area of HAZ is given as

$$\text{HAZ}\ (\text{mm}^2) = 5.5522 + 1.3797E_\text{s} + 1.5037 \times 10^{-4} pE_\text{s}\theta, \tag{6.16}$$

where E_s is specific laser beam energy in J/mm, p is assist gas pressure in kPa, and θ is fiber orientation in degrees (0° or 90°).

The size of HAZ was found to be most influenced by pulse frequency and cutting speed in Nd:YAG laser cutting of CFRP [32]. At high pulse frequency the laser behaves like a continuous beam and the cut surface does not have sufficient time to cool down. This leads to heat conduction to a greater depth and hence a larger heat damages zone. The size of HAZ was also found to depend on pulse intensity. When pulse duration is longer, the average pulse power would be lower, leading the power intensity to drop. Hence, longer pulse duration and lower pulse frequency produce smaller HAZ. Unlike the behavior shown in Fig. 6.23, it was found that the size of HAZ decreases with an increase in the pulse energy to cutting speed ratio up to a certain level and then increases with further increase in this ratio. For the cutting conditions and materials used, an optimum level of pulse energy to cutting speed ratio from 2 to 4 J/mm/s was identified for which the size of HAZ is minimum.

6.2.4 Modeling and Analysis

The laser cutting process is a complex three-dimensional heat flow phenomena that is affected by laser beam and process parameters. Optimization of the cutting process enables selecting the most appropriate parameters for minimum size of HAZ and smallest kerf width. There is therefore interest in formulating models for quantitative prediction of the effects of material properties and laser cutting conditions on the size and shape of the kerf and the surrounding HAZ. There are several factors that complicate the analysis laser cutting of FRPs. The workpiece material is anisotropic and its thermal conductivity is critically dependent on fiber orientation. The laser beam is a moving heat source which causes transient changes in the temperature field. Furthermore, complications also arise from the different response of the constituent materials to the heat from the laser beam. The matrix material melts or evaporates at much lower temperatures than the reinforcing fibers. Several models are proposed in the literature based on making simplifying assumptions

regarding material thermal conductivity, energy balance, boundary conditions, and heat transport mechanisms [37–43].

The governing equation of heat conduction can be written as

$$k\nabla^2 T + q = \rho c \frac{\partial T}{\partial t}, \tag{6.17}$$

where k is the thermal conductivity, T is the temperature, q is a heat source term, and c is the specific heat capacity. For a semi-infinite anisotropic body with orthotropic material properties coinciding with the axes of the coordinate system this equation can be written as [38]

$$k_x \frac{\partial^2 T}{\partial x^2} + k_y \frac{\partial^2 T}{\partial y^2} + k_z \frac{\partial^2 T}{\partial z^2} + q = \rho c \frac{\partial T}{\partial t}. \tag{6.18}$$

Considering the laser beam as a moving heat source moving along the x-direction at a constant speed $v = \mathrm{d}x/\mathrm{d}t$, and with the absence of heat generation, (6.18) is written as

$$k_x \frac{\partial^2 T}{\partial x^2} + k_y \frac{\partial^2 T}{\partial y^2} + k_z \frac{\partial^2 T}{\partial z^2} = \rho c v \frac{\partial T}{\partial x} \tag{6.19}$$

subject to the boundary conditions

$$T = T_o \quad \text{at } x = \pm\infty,\ y = \pm\infty,\ z = \infty, \tag{6.20}$$

where T_o is the ambient temperature and

$$\eta PQ(\hat{\boldsymbol{n}} \cdot \hat{\boldsymbol{k}}) = -Ak(\hat{\boldsymbol{n}} \cdot \nabla T) \tag{6.21}$$

at $z = 0$, where PQ is the heat emitted at the origin per unit time for $t > 0$, P is the laser beam power, Q is the pulse duty, and η is a coefficient of laser absorption. Solution of (6.18) provides the transient temperature distribution in the laser cut workpiece from which predictions of the kerf geometry and boundaries of the HAZ can be made. For evaporative material removal, the kerf geometry is determined by isotherms of the vaporization temperature. The boundaries of the HAZ are determined by isotherms of the charring temperature of the polymer matrix.

Analytical and numerical solutions of (6.18) and (6.19) can be obtained by making simplifying assumptions. Tagliaferri et al. [28] assumed that heat conduction is unidirectional and perpendicular to the cut. The workpiece was also assumed to be semi-infinite in the direction perpendicular to the cut and the thermal properties were assumed to be independent of temperature. The problem of laser cutting is then reduced to one directional heat conduction equation

$$\frac{\partial^2 T}{\partial x^2} = \alpha \frac{\partial T}{\partial t} \tag{6.22}$$

for which a solution was obtained by the finite difference method. For a one-dimensional array of n nodes with uniform spacing perpendicular to the cut, (6.22)

becomes

$$T_n^{t+1} = T_n^t \left(1 - \frac{2\alpha\,\Delta t}{\Delta x^2}\right) + \frac{\alpha\,\Delta t}{\Delta x^2}\left(T_{n-1}^t - T_{n+1}^t\right), \tag{6.23}$$

where T_n^t is the temperature at node n and time t, α is the thermal diffusivity of the material, and Δt is the time increment. In solving this equation, it was assumed that the temperature at the edge of the kerf is equal to the vaporization temperature. Predictions of the HAZ size were made for cutting unidirectional fiber-reinforced polyesters. The analysis indicated that higher cutting velocities result in less thermal damage and predicted that graphite/polyester composites exhibit the greatest degree of thermal damage due to the high thermal conductivity of graphite fibers.

Chen et al. [39] developed an explicit three-dimensional finite difference solution for (6.18). The analysis was applied to laser drilling of carbon/PEEK composites. It was assumed that the laser beam has a Gaussian distribution, material removal takes place by vaporization and that heat loss due to radiation is negligible. The upper and lower surfaces of the workpiece were assumed to exchange heat with the environment by heat convection. The governing finite difference equation and the heat convection boundary condition are given by (6.24) and (6.25), respectively,

$$k_x \frac{T_{i-1,j,k}^t - 2T_{i,j,k}^t + T_{i+1,j,k}^t}{\Delta x^2} + k_y \frac{T_{i,j-1,k}^t - 2T_{i,j,k}^t + T_{i,j+1,k}^t}{\Delta y^2} + k_z \frac{T_{i,j,k-1}^t - 2T_{i,j,k}^t + T_{i,j,k+1}^t}{\Delta z^2} + q = \rho c \frac{T_{i,j,k}^{t+1} - T_{i,j,k}^t}{\Delta t}, \tag{6.24}$$

$$\frac{T_{i,j,k-1}^t - T_{i,j,k}^t}{\Delta z} = \frac{h}{k_z}(T_o - T_{i,j,k}^t), \tag{6.25}$$

where $T_{i,j,k}^t$ is the temperature at node nodal position (i, j, k) and time t. Material removal was assumed to take place by vaporization and the kerf boundary was determined by isotherms of the material evaporation temperature. The model results were found to be in good agreement with experimental results relating to hole shape and size.

Pan and Hocheng [40] provided analytical solution for (6.19) as applied to the laser grooving of unidirectional CFRP under different conditions. Mirror image method is used for specimen of finite thickness. Anisotropic thermal conductivities that are also temperature dependent were used in order to improve the analysis. The analysis and supporting experiments revealed that grooving parallel to fiber orientation produces the smallest HAZ, while perpendicular to the fiber orientation produces the largest one.

Chryssolouris et al. [41] developed an analytical model for multipass grooving of unidirectional composites. The analysis is based on the energy balance of a small control volume at an arbitrary point of the groove surface. The energy absorbed by the material is balanced against heat conduction into the material and material ablation. Material properties were determined by volume fraction averaging. The laser beam was assumed to have a continuous wave Gaussian intensity distribution.

Prediction of the groove depth was based on the contours of vaporization temperature and is given by the equation

$$\ln\left(\frac{d}{D}\right) = \ln\left(\frac{PN}{vD}\right) + \ln\left(\frac{2A\rho}{\sqrt{\pi}}[c(T_s - T_o) + L_v]\right), \tag{6.26}$$

where d is the groove depth, D is the laser beam diameter, N is the number of passes by the laser, v is the laser scanning velocity, A is the material absorptivity, T_s is the erosion front temperature, and L_v is the latent heat for vaporization. The above equation was extended in [42] to determine the extent of HAZ by determining the location of the char temperature isotherm. The material situated between the erosion front and the char temperature isotherm is defined as the HAZ. The width of this damage zone is estimated as

$$W_d = \frac{\alpha}{v\beta}\ln\left(\frac{T_s - T_o}{T_c - T_o}\right), \tag{6.27}$$

where β is a function of the position of the erosion front and T_c is the char temperature.

Caprino et al. [43] developed a model for predicting the depth of cut in laser cutting of unidirectional GFRP based on the energy required for vaporization of a volume V of the material,

$$V = \frac{\eta P t_i}{Q_v}, \tag{6.28}$$

where t_i is beam–workpiece interaction time defined as $t_i = v/D$, and Q_v is material vaporization energy, approximated by the rule of mixtures as

$$Q_v = (Q_f - Q_m)V_f + Q_m, \tag{6.29}$$

where Q_f and Q_m are vaporization energies for fibers and matrix, respectively, and V_f is the fiber volume fraction in the composite. Substituting (6.29) in (6.28) gives

$$d = \delta\frac{DP}{v[(Q_f - Q_m)V_f + Q_m]}, \tag{6.30}$$

where δ is a material parameter that is dependent on laser beam absorptivity and intensity. It has been shown that the model predictions agree well with experimental results in laser cutting of aramid, glass and carbon FRPs [43].

6.3 Electrical Discharge Machining

EDM is a thermal process that uses spark discharges to thermally erode electrically conductive materials. Microscopic bits of the workpiece material are melted or vaporized by the very intense and localized heat of the spark discharge. The shape of the electrode defines the area in which spark erosion will occur, thus determining

resulting cavity. EDM does not depend on material hardness but requires that electrical receptivity of the workpiece be lower than 100 Ω cm [44]. Therefore, in addition to metals, EDM can process carbon FRPs, intermetallic compounds of certain carbides, borides, nitrides, the composites containing them, and other nonconducted ceramics. Advantages of EDM include high accuracy of cutting, fine surface finish, the absence of direct contact between electrode and workpiece (no forces), the ability to process extremely fragile workpiece without damage, and its ability to process materials independent of hardness or strength. On the other hand, EDM provides only very low MRRs, and similar to other thermal processes it generates recast layer and HAZ at the cut surface. However, the HAZ produced by EDM is significantly smaller than that produced by laser cutting [31].

6.3.1 Technology Overview

There are two main types of EDM systems, the plunge (or die sinker) type and the wire type. Both use the same concept of discharge spark generation between the electrode and the workpiece in order to microscopically remove material from the workpiece. The difference between the two types is in the shape of the electrode. The die sinker EDM uses an electrode that is a mirror image of the required cavity to be cut. The electrode is slowly plunged or sunk into the workpiece, maintaining a gap all the times for the electric discharge sparking to take place. A wire EDM uses a moving continuous wire electrode to produce a cut in the workpiece, in a way similar to that of a band saw. The wire is held taught between two heads which guide it through the workpiece, while marinating a gap. Since the wire electrode is eroded in the process, a new wire is always fed from a spool wound onto another spool.

All EDM systems consist of four major subsystems: a DC power supply, dielectric system, electrode, and servosystem. Figure 6.24 is a schematic of a die-sinker

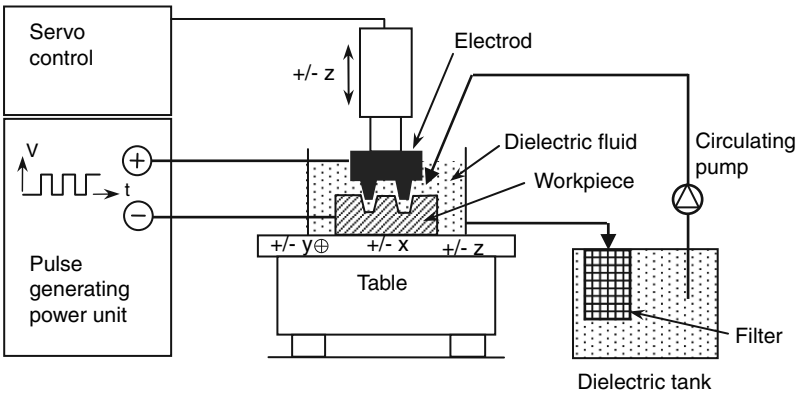

Fig. 6.24 Schematic of a die sinker EDM system

EDM illustrating the four main subsystems. The power supply generates pulsed DC power and controls its voltage, current, duration, duty cycle, frequency, and polarity. The dielectric system consists of dielectric fluid, delivery devices, pumps, and filters. The dielectric fluid insulates the electrode form the workpiece, acts as coolant, and flushes away debris from the spark gap. The most important characteristic of a dielectric fluid is surface tension. A high surface tension provides a slow plasma spreading velocity, thus concentrating the heat source to erode the material. The dielectric must also deionize quickly to act as an insulator and have a low enough viscosity for easy circulation [45]. Common dielectric fluids include hydrocarbon oil, silicon-based oil, and deionized water. The electrode function is to transmit the charge to the workpiece so it can be eroded by melting and/or vaporization. The electrode also wears in the process, and therefore it is important to select electrode materials with low wear rates. Electrodes are typically made from copper, brass, tungsten, and graphite. Graphite electrodes provide the lowest wear rate for the highest MRR, but they are more difficult to make than copper and brass electrodes because of their abrasivity and the dust generated from machining. Metallic electrodes usually work best with low melting point materials while graphite and tungsten electrodes are used with high melting point materials. A servosystem controls the infeed of the electrode or workpiece and maintains the required gap for discharge sparking to take place.

6.3.1.1 Process Parameters

Independently controlled EDM process parameters include open circuit voltage, frequency, electrode material, polarity, and servo drive gap sensitivity. Dependent variables and results include average current, spark gap, overcut, MRR, wear ratio, surface roughness, depth of recast and heat affected zone, corner radius, and taper. For typical cutting operations, a 120 V DC power and current values from 0.5 to 10 A are applied. Pulse duration of 10–100 μs are common for die sinker EDM, whereas for wire EDM durations are generally less than 2 μs [44]. Low current and high frequency (short pulse duration) are typically used for the best surface finish, but at the expense of low MRRs. Increasing current, while holding all other parameters constant causes the spark to remove larger crater of material from the surface of the workpiece. This results in increasing MRR and increasing surface roughness. Increasing spark frequency, while holding all other parameters constant, results in a decrease in surface roughness. This is because the energy available for material removal is shared by a number of sparks. Each spark removes a small crater from the surface. The gap between the electrode and the workpiece is controlled by the spark voltage and the current. The smaller the gap, the closer the accuracy with a better finish and slower MRR. Efficient flushing also becomes difficult. Increasing the pulse duration has the effect of increasing MRR, increasing surface roughness, and decreasing electrode wear. Electrode materials can be metallic or graphite. Brass, copper, tungsten, and zinc are the most common metallic materials. Studies have shown that graphite provides the higher rate of material removal in relation to

electrode wear. This is because of its high resistance to heating since graphite does not melt when heated but evaporates at about $3,500\,^{\circ}$C. Polarity refers to the direction of current flow relative to the electrode. Generally, positive electrode polarity causes less wear rates while negative polarity causes higher MRR.

6.3.1.2 Process Capabilities

EDM is very suitable for machining complex shapes in electrically conductive hard-to-machine metals, alloys, and composites. Hardness and mechanical strength of the workpiece are not the limiting factor. Examples of EDM operations include small hole drilling at shallow angles and on curved surfaces, slots, cavities, and complex die geometries. Process accuracy of ± 0.0025 to ± 0.127 mm can be easily achieved. Volumetric MRRs range from 0.016 to $1.6\,\text{cm}^3/\text{h}$. MRR is strongly affected by power, dielectric, and electrode material. Surface finish obtained ranges from 0.04 to $3.1\,\mu$m [46].

6.3.2 Material Removal Mechanisms

Thermal erosion of the workpiece and the tool takes place in a sequence of steps that are driven by the electric power pulse. The workpiece and the electrode are initially insulated by the dielectric flowing in the gap between them. As a pulse of DC current is delivered to the electrode and the workpiece, an intense electrical field is created. At first, no current flows in the gap because of the insulation. The intense electric field, however, causes charged particles in the dielectric to form a high-conductivity bridge across the gap. This causes breakdown and deionization of small portion of the dielectric. This in turn results in the formation of a spark channel and at the onset of sparking the voltage across the gap decreases and the current increases to a level set by the operator. The temperature and pressure increase and a plasma channel grows in the gap. A small amount of material from the surfaces of both the electrode and the workpiece melts and vaporizes and a bubble rapidly forms around the plasma channel. The dielectric around the plasma restricts the plasma growth and the input energy is concentrated in a very small volume. This causes the plasma temperature to reach nearly $4,000\,^{\circ}$K and the pressure rises significantly. When the electric pulse is terminated, the heating effect stops instantly. This causes the plasma channel and bubble to collapse. The rushing dielectric fluid washes away molten metal forming a small crater on both surfaces (Fig. 6.25). This sequence is repeated thousands of times each second causing uniform erosion of the workpiece and the electrode. As the process continues, the electrode is advanced and a constant gap between the electrode and the workpiece is maintained. Proper operating parameters are selected in order to reduce erosion of the electrode. Because input energy is proportional to the voltage, current, and pulse time, these three process parameters are generally used to control the performance of the EDM process.

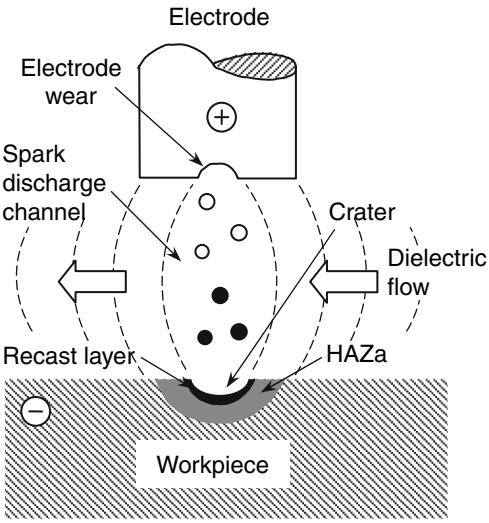

Fig. 6.25 Material and electrode erosion by EDM

The surface produced by EDM process consists of a large number of overlapping, small craters that are formed from the discharge energy. The size of craters, and hence the resulting surface roughness is proportional to the discharge energy and the reciprocal of spark frequency. The machined surface is usually characterized by three types of surfaces layers. The top surface consists of a thin layer of spattered material that is deposited from the melt and vapor debris in the dielectric. This layer is porous and brittle and can be easily removed by mechanical means. Underneath this surface is the recast or white layer, which is caused by melted material that has not been flushed by the dielectric and then rapidly resolidifies. The metallurgical structure of this layer is different than the base material because of rapid solidification. In the third layer, the HAZ, heat is not high enough to cause melting but is sufficiently high to induce microstructural transformation. This layer retains some structural properties of the original material. Recast and heat affected layers occur on all materials and range from 0.002 to 0.13 mm deep. Microcracks are formed at the surface especially at high pulse duration due to fairly different cooling rates at the interface between white and heat-affected layers. In general, the density of cracks depends on the pulse energy and increases as the pulse duration is raised.

6.3.3 EDM Characteristics of FRPS

Glass and Kevlar fiber-reinforced polymers are poor electrical conductors and may not be machined by EDM. But EDM has been utilized for machining carbon/polymer and carbon/carbon composites because the carbon fibers are electrically conductive [47–50]. It is being considered as an alternative machining process because of its versatility, precision, and the absence of contact forces. This allows

it to produce very complex shapes and drill very small holes without mechanically damaging the composite laminate. Because material removal in EDM is a thermal process, heat effects on the workpiece are inevitable, but could be significantly minimized by proper selection of process parameters. The feasibility of EDM is based on the maximum attainable MRR, minimum electrode wear, size of recast layer, and HAZ and surface roughness.

6.3.3.1 Surface Characteristics

Lau et al. [47] investigated die sinker EDM of PAN-based carbon/epoxy multidirectional material with fiber volume fraction of 65%. A voltage of 100 V and peak discharge currents of 0.5–5 A were used. The pulse-on time ranged from 25 to 160 μs and the pulse-off time ranged from 100 to 600 μs. At low currents the material is removed largely by vaporization, the machined surface is characterized by small craters and the fiber ends appear undisturbed and clearly recognized. At high currents (above 1.0 A), high temperatures are produced which cause severe melting of the composite surface. The molten material resolidifies on the surface giving the appearance of a highly heterogeneous surface. This results in lowering electrical conductivity and impeding material removal from the surface. Considerable swelling of the fiber ends takes place, which squeezes the matrix from between the fibers. In addition, debonding between the fibers and the matrix was also detected. The phenomena of fiber swelling was also reported in laser drilling of T300 CFRP, in which the fibers are also PAN based [36]. The PAN-based fibers incorporate a high level of structural disorder and volatile impurities. Fiber swelling adjacent to the machined surface is attributed to internal gas pressure generated by the rapid volatilization of impurities within the fiber, occurring simultaneously with the structural ordering when high temperatures in the order of 1,300–2,000 °C are attained.

Hocheng et al. [48] and Guu et al. [49] investigated the EDM of carbon/carbon composites with 1-mm diameter copper and graphite electrodes, respectively. The electrode polarity was positive and kerosene was used as the dielectric. The gap voltage was held constant at 35 V while the pulse current varied from 0.2 to 10 A. It was hypothesized that material removal occurs by vaporizing the material closest to the electrode surface, while the material beneath is melted and blown away by the dielectric. Some of the melted material that is not blown away resolidifies on the machined surface and forms a recast white layer. At low currents the recast layer is thin and the machined surface is characterized by shallow valleys and craters of roughly honeycomb shape. As the current is increased, the machined surface exhibited irregular valleys and long grooves and the recast layer becomes thicker and more irregular. Microvoids were also detected at the machined surface under large pulse current conditions. Analysis of the surface chemistry revealed transfer of the copper electrode material to the machined surface. The machined surface material is described as an alloy of the base material, the electrode material, and

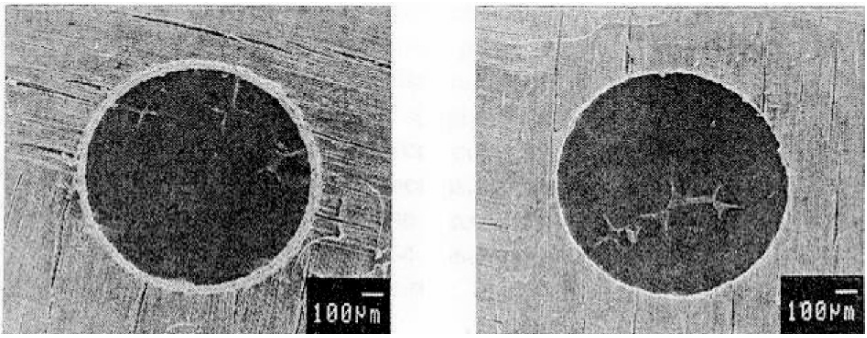

(a) Top Surface (b) Bottom surface

Fig. 6.26 SEM photomicrographs of the top and bottom surfaces of a 1.0 mm diameter hole drilled by EDM in a carbon weave/carbon matrix composite. Graphite electrode, positive polarity, pulse current = 3A, pulse-on time = 20µs [49]

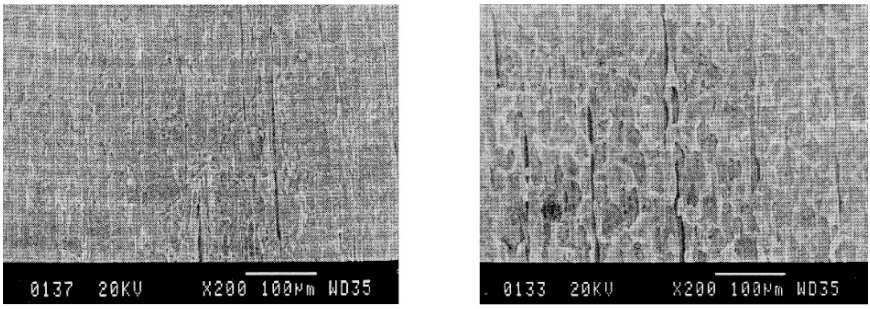

(a) 1 A (b) 5 A

Fig. 6.27 Morphology of the inside surface of the hole after EDM drilling of carbon weave/carbon matrix composite. Graphite electrode, positive polarity, pulse-on time = 100µs [49]

dielectric. The amount of copper diffused to the surface increases with an increase in the pulse current, reaching about 10% at pulse current of 10 A [48].

Figure 6.26 shows the hole quality in a carbon/carbon composite drilled with a graphite electrode [49]. The figure clearly shows a white recast layer formed at the hole surfaces. The size of the recast layer is smaller and the hole quality is better at the bottom surface. Unlike mechanical and AWJ drilling, no burr formation is observed at the hole edges. However, there is evidence of delamination damage that extend beyond the thermally affected zone. Figure 6.27 shows the inside surface of a hole drilled by graphite electrode EDM. The surface is formed by craters and elongated grooves. Craters shape and size are strongly dependent on the fiber direction and the discharge channel position. Thermal expansion of the carbon fibers in the lateral direction and debonding between fiber and matrix are also evident. Surface roughness increases with increasing pulse current. Higher pulse current causes more frequent cracking of the dielectric fluid and more frequent melt explosions.

Excellent surface finish can be obtained by setting the machine parameters at low pulse current and small pulse-on duration. But this will be at the expense of lower MRR.

6.3.3.2 Material Removal Rate

MRRs in EDM are much smaller than those in AWJ and laser machining due to the nature of material removal by spark erosion and the lower energy input. MRRs in the order of $10\,\mathrm{mm}^3/\mathrm{min}$ were reported for carbon/epoxy composites [47] and $1.0\,\mathrm{mm}^3/\mathrm{min}$ for carbon/carbon composites [49, 50]. MRR increases with increasing energy input, which is attained by increasing gap voltage, pulse current, and pulse-on time. However, there exist a limit to this proportionality where the MRR is a maximum. This is particularly the case for pulse-on duration cycles below $100\,\mu\mathrm{s}$. At low pulse-on durations, the EDM process is efficient and increasing the discharge energy by increasing the pulse current and pulse-on duration cycle causes an increase in MRR. At pulse-on duration cycles beyond $100\,\mu\mathrm{s}$ the process becomes inefficient. At high discharge energy levels extremely high temperatures are created and severe melting of the composite surface takes place. Solidified matrix particles and matrix material smeared on the surface reduce electrical conductivity, leading to reduction in MRR. An optimum MRR was reported at a current density of $1\,\mathrm{A}/\mathrm{cm}^2$ for carbon/epoxy composites [47]. Copper and graphite electrodes produced comparable MRR and accuracies but lower electrode wear was observed with the copper electrode. Positive electrode polarity was shown to yield higher MMR and lower electrode wear rates. Empirical relationships between MRR and operating parameters were obtained for EDM of carbon–carbon composites with positive polarity graphite electrode [49]. The range of pulse current is from 0.2 to 5 A and pulse-on time is from 20 to $220\,\mu\mathrm{s}$.

$$\begin{aligned} \mathrm{MRR} &= 0.378 I_\mathrm{p}^{0.216} \tau_\mathrm{on}^{0.041} \quad \text{for } \tau_\mathrm{on} \leq 100\,\mu\mathrm{s} \\ \mathrm{MRR} &= 4.400 I_\mathrm{p}^{0.134} \tau_\mathrm{on}^{-0.428} \quad \text{for } \tau_\mathrm{on} > 100\,\mu\mathrm{s}. \end{aligned} \tag{6.31}$$

EDM of carbon–carbon composites with negative polarity copper electrode did not reveal an optimum in the MRR [50]. ANOVA analysis of the results indicated that the most influencing parameter is pulse current followed by gap voltage and then pulse-on time. The relationship between process parameters and MRR is given as

$$\mathrm{MRR} \times 10^{-3} = 0.139886 + 1.0124 \times 10^{-2} I_\mathrm{p} - 1.99685 \times 10^{-4} \tau_\mathrm{on} + 1.589 \times 10^{-2} V_\mathrm{g}. \tag{6.32}$$

6.3.3.3 Electrode Wear

The electrode material and the wear rate have significant effects on MRR, hole quality, and surface finish. The wear rate of the electrode is sensitive to electrode material and polarity. Lau et al. [47] investigated the performance of copper and graphite

electrodes with positive and negative polarity in EDM of carbon/epoxy composites. It was found the graphite electrode wears out more rapidly than copper electrodes, particularly with negative polarity. In fact, the copper electrode had much lower wear rate at any cutting conditions. Nevertheless, the wear rate for both electrode materials was lower for positive polarity than for negative polarity. The surface finish that could be produced by copper electrode was much better than that produced by graphite electrode. At high levels of pulse current, the graphite electrode produced burnt surfaces which were brittle and had no practical use. George et al. [50] investigated EDM of carbon–carbon composites with negative polarity copper electrode. It was shown that the most significant parameter influencing electrode wear is pulse current. The relationship between process parameters and electrode wear was determined by ANOVA analysis and is given as

$$\begin{aligned}\text{EWR} = &-0.029214 + 3.86 \times 10^{-3} I_\text{p} + 2.3045 \times 10^{-5} \tau_\text{on} \\ &+ 4.8555 \times 10^{-4} V_g (\text{mg/min}).\end{aligned} \tag{6.33}$$

6.3.3.4 Recast Layer

Temperatures close to the electrode in EDM may reach as high as 40,000 K. This causes materials at the vicinity of the electrode to evaporate. Material further away will melt and form a recast layer. The thickness of recast layer increases with increasing pulse current. This is a result of steeper thermal gradients that build up in the material at high energy input. The effect of pulse-on duration is minor as compared to that of the pulse current. A correlation model for the effect of process parameters on recast layer thickness was obtained [49]

$$d_\text{t} = 13.696 I_\text{p}^{0.534} \tau_\text{on}^{0.204}. \tag{6.34}$$

6.3.3.5 Delamination

High pressures and temperatures generated by the spark channel cause delamination at the machined edge. Delamination is more pronounced at places where the fibers are perpendicular to the machined edge and almost absent at places where fibers are parallel to the edge; see Fig. 6.26 [49]. The extent of delamination is measured by delamination factor, F_d, which is the ratio of the maximum diameter of the damage zone to the hole diameter (see Fig. 5.48). The delamination factor increases with an increase in pulse current and pulse duration. The impulse force from the spark channel increases with increasing discharge energy, which is proportional to pulse current and pulse-on time, thus increasing the delamination degree. Proper choice of operating conditions can eliminate delamination damage to the workpiece. An empirical relationship was derived for EDM of carbon–carbon composites as

$$F_\text{d} = 0.815 I_\text{p}^{0.0681} \tau_\text{on}^{0.0579}. \tag{6.35}$$

6.4 Summary

Among the nontraditional processes used to machine fiber-reinforced composites are abrasive waterjet machining (AWJ), laser machining, and EDM, with AWJ being by far the most widely implemented. Nontraditional machining offers certain advantages over traditional machining. These include high production rates, such as in the case of AWJ machining of thin panels, greater flexibility, and the capability to produce complex contours and shapes. In addition, these processes require no cutting tools (as in the sense of traditional processes) and very minimum fixturing, if any. Laser cutting and EDM generate no cutting forces, and hence mechanical distortions and damages are minimum. For some composite materials, such as aramid FRPs, nontraditional machining by laser beam might be the most effective method for producing clean cut edges. Nontraditional machining also has its own limitations. AWJ pressures incident on the workpiece cause delamination and variations in the jet pressure cause waviness in the cut kerf. Laser machining and EDM primarily utilize heat for material removal. This causes undesirable alterations to the local microstructure and properties of the material adjacent to the cut. Furthermore, these processes are relatively new and the know how of their application to FRPs is still under development. This in a way impedes their exploitation to the fullest extent.

6.4.1 AWJ Machining

AWJ machining takes place by particle impact erosion. Abrasive particles accelerated by the momentum energy of a high-velocity waterjet impact the surface of the workpiece and subsequently remove material from the surface by one or more of the following mechanisms: microcutting, ploughing deformation, and microfracture. The dominant mechanism of material removal is determined by the shape of the impacting particle, the impact angle, and properties of the target surface. Microcutting and ploughing deformation are associated with ductile materials and shallow impact angles; where microcutting occurs for sharp particles while ploughing deformation is associated with spherical particles. Microcracking occurs when the particles impact at large angles. Microcutting is believed to be the dominant material removal mechanism in AWJ machining of fiber-reinforced composites. Because the impacting particles lose energy as they travel down the kerf, the AWJ tends to bend and follows a curved trajectory. Material removal is also less efficient deeper into the kerf. Hence the generated kerf is tapered and its surface is characterized by surface roughness at the top region of the kerf and waviness at the bottom region. The process parameters that influence the kerf characteristics include hydraulic pressure, abrasive flow rate, abrasive particles size, standoff distance, and traverse speed. Surface roughness is affected the most by abrasive particle size, followed by hydraulic pressure and traverse speed. Waviness on the other hand is affected primarily by the standoff distance and traverse speed. Kerf taper is affected

by a combination of hydraulic pressure, abrasive particle size, and traverse speed. The kerf taper increases with an increase in abrasive particle size, a decrease in hydraulic pressure, and an increase in traverse speed. These conditions have the net effect of decreasing the kinetic energy of the abrasive particles and hence decreasing their cutting efficiency. Optimization of AWJ cutting requires the selection of cutting conditions that correspond to minimum waviness and minimum taper of the kerf. Delamination is also a major concern when AWJ machining composites and it is caused by cutting conditions that promote water penetration (water wedging) and abrasive embedment between the bottom plies of the laminate. These conditions include high traverse speed and low abrasive particle flow rate.

6.4.2 Laser Machining

Laser machining is a thermal process that removes material by melting and vaporization. As a laser beam impinges on the surface of the workpiece some of the heat is absorbed by the material at the surface and is subsequently conducted deeper into the material. Depending on the material thermal properties and the interaction time, the heated material will melt or evaporate and subsequently be removed with the help of an assist gas. This facilitates deeper penetration of the laser beam and a kerf is formed. Due to the contrast in thermal properties of the polymer matrix and reinforcement fibers, the response of each type of FRP to laser cutting is characteristically different. Carbon FRPs are the most difficult to cut with lasers because of the high vaporization temperature and high thermal conductivity of the carbon fibers. On the other hand, aramid FRPs are the most suitable for laser cutting because of the similarity of its thermal properties to those of the polymer matrix. The laser cut kerf is characterized by its taper and the formation of striations and a charred layer on the surface. When the charred layer is removed, exposed fibers protrude from the surface with no binder in between. Furthermore, because of heat conduction into the workpiece, laser cutting is characterized by the formation of a HAZ, which is an area in the vicinity of the kerf surface where the material has been altered because of the effect of heating. In laser machining of FRPs, the HAZ is marked by the contours of decomposition temperature of the polymer matrix. The process parameters that influence laser cutting include power, traverse speed, assist gas pressure, and workpiece material composition and architecture. Both kerf taper and size of HAZ increase with an increase in laser beam power and a decrease in traverse speed, both of which result in an increase in the specific laser energy. Furthermore, the size of HAZ is larger for cutting perpendicular to the fibers than for cutting parallel to the fibers. This is particularly true for carbon FRPs because of the excellent thermal conductivity of carbon fibers. An increase in the assist gas pressure generally results in a decrease in the size of HAZ as a result of the efficient cooling of the assist gas.

6.4.3 EDM

EDM is another thermal machining process that utilizes spark erosion for material removal. Because of the requirement to conduct electricity through the erosion gap, EDM is only suitable for machining electrically conductive composites such as carbon FRPs and carbon/carbon composites. EDM provides the lowest MRR among the three processes considered. Hence, it is not suitable for bulk material removal. Its advantages, however, are tighter tolerances and the ability to machine complex shaped cavities and very small diameter holes. The surface characteristics of EDM are the formation of recast layer and HAZ. The process parameters that influence these characteristics are polarity of the DC power supply, gap voltage, and current and pulse-on time. At low pulse-on durations, the MRR increases with an increase in the energy input, which is obtained by increasing the gap voltage, current, and pulse-on time. Positive electrode polarity was shown to produce higher MRRs. The formation of recast layer is caused by solidification of the molten material at the kerf surface. The thickness of recast layer increases with an increase in the pulse current. Delamination also occurs in EDM due to the high temperatures and pressures associated with spark erosion and due to the thermal mismatch between the matrix and reinforcement fibers. Delamination is more pronounced at locations where the fiber ends are perpendicular to the machined surface. The extent of delamination increases with an increase on pulse current and pulse duration.

Review Questions and Problems

1. Discuss and compare the micromechanisms of material removal in AWJ, laser and electrical discharge machining of FRPs.
2. List the advantages and limitations of AWJ machining, laser machining, and EDM over traditional routing in trimming and slotting of FRPs.
3. What are the advantages and limitations of thermal removal processes in comparison to AWJ machining?
4. Given the opportunity to choose between traditional and nontraditional machining processes for edge trimming of CFRP, which process would you choose if your main concern is

   (a) High production rates
   (b) Good surface roughness
   (c) Lowest mechanical damage
   (d) Lowest thermal damage
   (e) High accuracy

5. Explain the mechanism of kerf formation in AWJ and laser machining of FRPs.
6. What is the cause of kerf taper in AWJ machining and in laser machining?
7. Explain the phenomena of striation formation in AWJ and laser machining of FRPs.

8. Explain the nature of heat affected zone in laser machining of FRPs. How is different from that in electrical discharge machining?
9. Discuss possible mechanisms for causing delamination at exit when cutting FRPs with AWJ.
10. Discuss the effect of traverse speed on the extent of delamination in AWJ machining.
11. Suppose that in an AWJ trimming operation of multidirectional FRP's you are getting high levels of delamination. Which action(s) would you take to improve the cutting quality?

    (a) Reduce traverse speed
    (b) Increase traverse speed
    (c) Increase jet pressure
    (d) Decrease jet pressure
    (e) Increase abrasive flow rate
    (f) Decrease abrasive flow rate
    (g) Increase mesh number
    (h) Decrease mesh number

12. Suppose that in an AWJ trimming operation of multidirectional FRP's you are getting unacceptable surface roughness. Which action(s) would you take to improve the cutting quality?

    (a) Reduce traverse speed
    (b) Increase traverse speed
    (c) Increase jet pressure
    (d) Decrease jet pressure
    (e) Increase abrasive flow rate
    (f) Decrease abrasive flow rate
    (g) Increase mesh number
    (h) Decrease mesh number

13. Suppose that in a situation of AWJ machining the jet is not able to penetrate the workpiece and a through cut is not obtained, what actions would you take in order to produce through cutting?
14. Which electrode material and polarity are recommended for EDM of carbon-fiber-reinforced composites, why?
15. Explain why aramid FRPs are more amenable to laser machining than glass and carbon FRPs.
16. Explain differences in laser machining characteristics of carbon FRPs with continuous CO_2 and pulsed Nd:YAG lasers.
17. Explain the nature of fiber swelling phenomena in thermal machining of low modulus PAN-based carbon FRPs.
18. Discuss the role of assist gas in laser machining of FRPs.
19. Explain strategies for reducing thermal damage in laser and electrical discharge machining of FRPs.

References

1. Wang, J., Abrasive Waterjet Machining of Engineering Materials, Trans Tech Publications, Switzerland, 2003.
2. AbrasiveJet and WaterJet Machining: Introduction. http://www.waterjets.org/about_abrasivejets.html. Cited in January 2008.
3. Hashish, M., Optimization factors in abrasive-waterjet machining. Journal of Engineering for Industry 113, 29–37, 1991.
4. Hashish, M., Machining of advanced composites with abrasive waterjets. Manufacturing Review 2, 142–150, 1989.
5. Conner, I., Hashish, M., Ramulu, M., Abrasive waterjet machining of aerospace structural sheet and thin plate materials. Proceedings of the 2003 WJTA American Waterjet Conference, Houston, Texas, 17–19 August 2003.
6. Koelsch, J.R., Waterjet vs. EDM. Manufacturing Engineering, 135(4), 2005
7. Momber, A., Kovacevic, R., Principles of Abrasive Waterjet Machining, Springer, New York, NY, 1998.
8. Hashish, M., Visualization of the abrasive-waterjet cutting process. Experimental Mechanics 28, 159–169, 1988.
9. Hashish, M., A model for abrasive-waterjet (AWJ) machining. Journal of Engineering Materials and Technology 111, 154–162, 1989.
10. Hashish, M., Characteristics of surfaces machined with abrasive waterjets. Journal of Engineering Materials and Technology 113, 354–362, 1991.
11. Hashish, M., Hilleke, M., Water jet machining of composites and ceramics, in Jahanamir, S., Ramulu, M., Koshy, P. (eds), Machining of Ceramics and Compsites. Marcel Dekker, New York, NY, 1998.
12. Hamatami, G., Ramulu, M., Machinability of high temperature composites with abrasive waterjet. Journal of Engineering Materials and Technology 113, 381–386, 1990.
13. Arola, D., Ramulu, M., A study of kerf characteristics in abrasive waterjet machining of graphite/epoxy composite. Journal of Engineering Materials and Technology 118, 256–265, 1996.
14. Ramulu, M., Arola, D., Water jet and abrasive water jet cutting of unidirectional graphite/epoxy composite. Composites 24, 299–308, 1993.
15. Ramulu, M., Arola, D., The influence of abrasive waterjet cutting conditions on the surface quality of graphite/epoxy laminates. International Journal of Machine Tools and Manufacture 24, 295–313, 1994.
16. Colligan, K., Ramulu, M., Arola, D., Investigation of edge quality and ply delamination in abrasive waterjet machining of graphite/epoxy. Machining of Advanced Composites, ASME, New York, NY, MD-Vol. 45/PED-Vol. 66, 1993, pp. 167–185.
17. Azmir, M.A., Ahsan, A.K., Investigation on glass/epoxy composite surfaces machined by abrasive water jet machining. Journal of Materials Processing Technology 198, 122–128, 2008.
18. Groppetti, R., Cattaneo, A., A model for hydro and hydro-abrasive jet machining of carbon fiber reinforced plastic composites. NIST Special Publication, 847, 297–405, 1993.
19. Konig, W., Wulf, C., Grab, P., Willerscheid, H., Machining of fibre reinforced plastics. Annals of CIRP, 34, 537–547, 1985.
20. Shaw, D., Tseng, C.N., Analysis of delamination in a laminate drilled by waterjet. Proceedings of the Machining of composite materials symposium, ASM Materials Week, Chicago, Illinois, 1–5 November, 1992, pp. 89–96.
21. Zeng, J., Kim, T.J., Development of an abrasive waterjet kerf cutting model for brittle materials, in Lichtarowicz, A. (ed), Jet Cutting Technology. Kluwer, Dordrecht, 1992, pp. 483–501.
22. Zeng, J., Determination of machinability and abrasive cutting properties in AWJ cutting, in M. Hashish (editor), Proceedings of 2007 American WJTA Conference and Expo, Houston, Texas, 19–21 August 2007, paper 3-B.

23. Wang, J., Guo, D.M., A predictive depth of penetration model for abrasive waterjet cutting of polymer matrix composites. Journal of Materials Processing Technology 121, 390–394, 2002.
24. Hocheng, H., Tsai, H.Y., Shiue, J.J., Wang, B., Feasibility study of abrasive-waterjet milling of fiber-reinforced plastics. Journal of Manufacturing Science and Engineering 119, 133–119, 1997.
25. Flaum, M., Karlsson, T., Cutting of fiber-reinforced polymers with CW CO_2 laser. SPIE-High Power Lasers and Their Industrial Applications, 801, 142–149, 1987.
26. McGeough, J.A., Advanced Methods of Machining, Chapman and Hall, New York, NY, 1988.
27. Schucher, D., Vees, G., Laser material processing of composite materials. Machining of Composite Materials II. Proceedings of the ASM 1993 Materials Congress, Pittsburg, Pennsylvania, 17–21 October 1993, pp. 153–158.
28. Tagliaferri, V., Di Ilio, A., Visconti, I.C., Laser cutting of fibre-reinforced polyesters. Composites 16, 317–325, 1985.
29. Ion, J.C., Laser Processing of Engineering Materials: Principles, Procedures and Industrial Applications. Elsevier Butterworth-Heinrmann, UK, 2005.
30. Rajaram, N., Sheikh-Ahmad, J., Cheraghi, S.H., CO_2 laser cut quality of 4130 steel. International Journal of Machine Tools and Manufacture 43, 351–358, 2003.
31. Lau, W.S., Lee, W.B., A comparison between EDM wire-cut and laser cutting of carbon fibre composite materials. Materials and Manufacturing Processes 6, 331–342, 1991.
32. Mathew, J., Goswami, G.L., Ramakrishnan, N., Naik, N.K., Parametric studies on pulsed Nd:YAG laser cutting of carbon fibre reinforced plastic composites. Journal of Materials Processing Technology 89–90, pp. 198–203, 1999.
33. Di Ilio, A., Tagliaferri, V., Veniali, F., Machining parameters and cut quality in laser cutting of aramid fibre reinforced plastics. Materials and Manufacturing Processes 5, 591–608, 1990.
34. Hocheng, H., Pan, C.T., Section area of heat affected zone in laser cutting of carbon fiber-reinforced PEEK. Machining of Advanced Composites, ASME, New York, NY, MD-Vol. 45/PED-Vol. 66, 1993, pp. 153–165.
35. Zhang, Y.H., Lau, W.S., Yue, T.M., Chiang, L., An investigation into the drilling of glass fibre reinforced liquid crystal polymer using pulsed Nd:YAG laser. Machining of Composite Materials II. Proceedings of the ASM 1993 Materials Congress, Pittsburg, Pennsylvania, October 17–21, 1993, pp. 117–121.
36. Voisey, K.T., Fouquet, S., Roy, D., Clyne, T.W., Fibre swelling during laser drilling of carbon fiber composites. Optical and Lasers in Engineering 44, 1185–1197, 2006.
37. Cenna, A.A., Mathew, P., Analysis and prediction of laser cutting parameters of fibre reinforced plastics (FRP) composite materials. International Journal of Machine Tools and Manufacture 42, 105–113, 2002.
38. Pan, C.T., Hocheng, H., The anisotropic heat-affected zone in the laser grooving of fiber-reinforced composite materials. Journal of Materials Processing Technology 62, 54–60, 1996.
39. Cheng, C.F., Tsui, Y.C., Clyne, T.W., Application of a three-dimensional heat flow model to treat laser drilling of carbon fibre composites. Acta Materialia 46, 4273–4285, 1998.
40. Pan, C.T., Hocheng, H., Prediction of extent of heat affected zone in laser grooving of unidirectional fiber-reinforced plastics. Journal of Engineering Materials and Technology 120, 321–327, 1998.
41. Chryssolouris, G., Sheng, P., Anastasia, N., Laser grooving of composite materials with the aid of water jet. Journal of Engineering for Industry 115, 62–72, 1993.
42. Chryssolouris, G., Sheng Choi, W.C., Three-dimensional laser machining of composite materials. Journal of Engineering Materials and Technology 112, 387–392, 1990.
43. Caprino, G., Tagliaferri, V., Maximum cutting speed in laser cutting of FRP. International Journal of Machine Tools and Manufacture 28, 389–398, 1988.
44. Pterofes, N.F., Gadalla, A.M., Processing aspects of shaping advanced materials by electrical discharge machining. Advanced Materials and Manufacturing Processes 3, 127–154, 1988.
45. Gadalla, A.M., Cheng, Y.M., Recent developments in electrical discharge machining. Machining of Advanced Materials, ASME, New York, NY, MID-Vol. 45/PED-Vol. 66, 1993, pp. 187–205.

46. Sommer, C., Sommer, S., Complete EDM Handbook, Advance Publishing, Houston, Texas, 2005.
47. Lau, W.S., Wang, M., Lee, W.B., Electrical discharge machining of carbon fibre composite materials. International Journal of Machine Tools and Manufacture 30, 297–308, 1990.
48. Hocheng, H., Guu, Y.H., Tai, N.H., The feasibility of electrical-discharge machining of carbon-carbon composites. Materials and Manufacturing Processes 13, 117–132, 1998.
49. Guu, Y.H., Hocheng, H., Tai, N.H., Liu, S.Y., Effect of electrical discharge machining of the characteristics of carbon fiber reinforced carbon composites. Journal of Material Science 36, 2037–2043, 2001.
50. George, P.M., Raghunath, B.K., Manocha, L.M., Warrier, A.M., Modelling of machinability parameters of carbon–carbon composite – a response surface approach. Journal of Materials Processing Technology 153–154, 920–924, 2004.

Chapter 7
Health and Safety Aspects in Machining FRPs

Even though fully cured composites are considered inert, their machining raises concerns about health and safety due to exposure to dust and decomposition compounds. Therefore, it is necessary to evaluate the byproducts of both traditional and nontraditional machining of composites in order to assess the potential of harming the operator's health due to exposure. Assessment of machining byproducts is also necessary for devising effective measures for eliminating hazardous exposures. Both traditional machining and nontraditional machining processes are considered. Among the nontraditional machining methods, laser beam cutting was subject to the most investigation because it poses the greatest potential of exposure to hazards. Abrasive waterjet machining has the advantage of being carried out under water and the water jet entrapping and washing away most of the dust generated. However, exposure to high levels of noise remains a concern that must be addressed.

The intention of this chapter is to make the reader aware of the potential harm to health and safety related to machining fiber-reinforced composites. The chapter will also report on studies that characterize the morphology and chemical composition of machining byproducts, the influence of machining process parameters, and common protection methods against these hazards. It is worth noting that this chapter is not intended as an authoritative and accurate source in the subject of occupational health and safety. For more accurate detailed listing of toxicity, reactivity, and health and safety data for composites and their constituents the reader is advised to consult detailed material safety data sheets (MSDS) provided by the material suppliers. The reader is also advised to consult local and federal government regulations concerning the safe handling of composite materials and the legally accepted exposure levels.

J.Y. Sheikh-Ahmad, *Machining of Polymer Composites*.
DOI: 10.1007/978-0-387-68619-6,

7.1 Hazard Sources and Routes of Exposure

Hazard is the potential that a material, process, or equipment will cause an adverse health effect (injury) under the conditions in which it is produced or used. In machining fully cured and polymerized composites the sources of hazard are associated with direct handling of the material as well as dust and gaseous emissions caused by machining. Since the composites are fully cured, they are considered chemically inert and their direct exposure to skin does not pose a threat. However, glass and carbon fiber ends protruding from a composite part are often stiff and sharp enough to penetrate skin. Aramid fibers do not exhibit these characteristics and therefore pose no danger of skin penetration. In addition, thermal decomposition of cured epoxy produces volatile vapors that are allergic, toxic, or carcinogenic [1–3]. Table 7.1 provides a general listing of the hazards generated from machining composites and the routes of exposure to the human body. It is noted that the major routes of exposure involve both dermal and inhalation, while the major sources of exposure include aerosols, dust, and gaseous compounds.

An aerosol is a group of particles suspended in a gaseous medium. In the context of occupational hygiene the gaseous medium is usually air. Aerosols are frequently classified according to their physical form and source. Aerosols consisting of fibers, fiber fragments, and particulates (e.g., coal, wood, graphite) are designated dusts. Aerosols consisting of liquid droplets (e.g., oil, water, solvents) are called mists. Aerosols containing submicrometer particles that are formed from condensation or combustion processes are generally called fumes or smokes. The actual impact of exposure to these hazards on health and safety depends greatly on their morphology, chemical properties, concentration, and length of exposure.

Dusts are solid particles, ranging in size from below 1 µm up to at least 100 µm, which may be or become airborne, depending on their origin, physical characteristics, and ambient conditions. For most occupational hygiene situations, the particle size is expressed in terms of aerodynamic diameter, defined as the diameter of a hypothetical sphere of density $1\,g/cm^3$ having the same terminal settling velocity in calm air as the particle in question, regardless of its geometric size, shape, and true density. It is generally accepted that particles with aerodynamic diameter greater than 50 µm do not usually remain airborne very long. Dust is further classified according to particle size as inhalable dust, thoracic dust, and respirable dust.

Table 7.1 Hazards and routes of exposure in machining FRPs

Hazard	Operation	Exposure route			
		Inhalation	Skin contact	Eye contact	Injection
Exposed protruding fibers	Handling	–	–	–	x
Dust	Traditional machining	x	x	x	–
Fumes	Laser machining, EDM, traditional machining	x	x	x	–

Inhalable dust is that size fraction of dust which enters the body though the nose and mouth. Particles with median aerodynamic diameter greater than about 30 μm are trapped in the nose, throat, and upper respiratory tract. Thoracic dust is that fraction that can penetrate the head airways and enter the airways of the lungs. The larger size particles of this dust ($>10\,\mu m$) will deposit in the tracheobronchial airway region and may later be eliminated by mucociliary clearance. Respirable dust refers to those dust particles that are small enough to penetrate deep into the alveolar region of the lung, the region where inhaled gases can be absorbed by the blood. Only about 1% of 10 μm particles gets as far as the alveolar region, so 10 μm is usually considered the practical upper size limit for penetration to this region. Insoluble particles that penetrate deep into the alveolar region are engulfed by macrophage cells (phagocytes), which can either then travel to the ciliated epithelium and then be transported upward and out of the respiratory system, remain in the pulmonary space, or enter the lymphatic system. Certain particles, such as silica-containing dusts, are cytotoxic; i.e., they kill the macrophage cells [4].

Today, very little information exists on the toxicological properties of inhaled composite aerosols. Research on the medical hazards of cured composite dust involving investigations into pulmonary toxicity have shown inconclusive evidence of adverse effects on human respiratory system [2, 5]. It has also been shown that the accumulation of large enough burdens of insoluble particles in the lungs leads to impaired clearance. This so-called "dust overload" condition may occur as a result of prolonged occupational exposures, even at relatively low levels [4]. It is widely accepted, however, that composite dust remains a serious irritant to skin, eyes, and lungs. The US Department of Labor, Occupational Safety and Health Administration (OSHA) lists the airborne composite dust as "nuisance dust" [6]. This term suggests that the human body's natural clearance mechanisms will eliminate most of the dust and that the dust has no pathological significance. The American Conference of Governmental Industrial Hygienists (ACGIH) classifies composite dust as Particles Not Otherwise Specified (PNOS). This includes low toxicity particles (i.e., not cytotoxic, genotoxic, or otherwise chemically reactive with lung tissue, not radioactive or a sensitizer, or toxic other than by inflammation or the mechanism of "lung overload") [7].

Permissible exposure levels (PELs) are set by health authorities in order to establish levels of exposure to which the vast majority of workers may be exposed without experiencing adverse health effects. These legally acceptable exposure levels vary from one country to another and over time. As knowledge of the interaction of workplace hazards with the human body is acquired, the permissible exposure limits may be adjusted accordingly. In the United States, the primary sources of environmental evaluation criteria for the work place are OSHA Permissible Exposure Limits (PELs) [6], ACGIH Threshold Limit Values (TLVs) [7], and the National Institute for Occupational Safety and Health (NIOSH) Recommended Exposure Limits (RELs) [8]. ACGIH established TLVs for PNOS is $3\,mg/m^3$ for respirable dust and $10\,mg/m^3$ for inhalable dust. In addition, MSDS provided by the supplier contains essential information for the safe handling of the material. This information includes physical and chemical properties, PELs, toxicity, reactivity, fire and

explosion hazards, and health hazards. The following sections discuss the effects of FRP constituent aerosols on the human body. The phenomena of aerosol generation in mechanical edge trimming and laser cutting are discussed in separate sections.

7.1.1 Matrix Material

Most of the health hazards associated with manufacturing polymer composites involve uncured thermosetting resins, cross-linking agents and other additives. Thermoplastic matrices and fully cross-linked thermoset polymers are basically inert and considered harmless. Their dust is particulate in nature and is thermally stable up to 250 °C. However, excessive heating of the polymer matrix may result in decomposition into airborne and potentially toxic substances that are respirable. Chemical decomposition is one of the material removal mechanisms in laser machining and EDM because the processing temperatures are extremely high. Excessive heating may also result under certain processing conditions during traditional machining. These conditions must be avoided in order to protect the health of the workers and integrity of the machined parts.

The decomposition products from thermal processing depend on processing temperature and pyrolysis mechanisms. The decomposition products may condensate out of the vapor phase or remain gaseous. The condensation particles first form as nuclei out of supersaturated vapor phase. The particle nucleus then grows by processes like coalescence and agglomeration. At the particle surface, further substances like polynuclear aromatic hydrocarbons (PAH) can condense. In most cases particles are solid. However, laser processing of polyamides generates viscous particles that can easily stick together. Haferkamp et al. [3] have shown the size of particles generated from laser processing of polymers have a normal distribution on a log-normal scale and that 90% of the particles are smaller than aerodynamic diameter of 1 μm. The particles have a spherical shape and form agglomerates. Mazumder et al. [9] have found that resin aerosol particulates generated by evaporation–condensation process have a mass median aerodynamic diameter (MMAD) of approximately 0.77 μm. The aerosol was generated by treating the composite dust at a temperature above 400 °C. Due to this small size, the particles are highly respirable. The gases and volatile organic compounds generated from laser processing of plastics affect the respiratory tract when inhaled. Most of these gases are allergic toxic or carcinogenic [3]. The TLVs recommended for aerosol particles is the same as that for PNOS ($3\,mg/m^3$ for respirable dust and $10\,mg/m^3$ for inhalable dust). The PELs for the gaseous phases are given by gas species as shown in Table 7.2. The reader is advised to consult NIOSH publication [8] for definitive information and more exhaustive coverage.

Table 7.2 NIOSH recommended exposure limits for hazardous agents [8]

Hazardous agent	NIOSH REL	Health effect
Benzene	Ca; 0.1 ppm ($0.32\,mg/m^3$), 8-h TWA 1 ppm ($3.2\,mg/m^3$) ceiling (15 min)	Cancer (leukemia)
Fibrous glass	3 million fibers/m^3 TWA (fibers $\leq 3.5\,\mu m$ in diameter and $\geq 10\,\mu m$ long); $5\,mg/m^3$ TWA (total fibrous glass)	Eye, skin and respiratory effects
Ethyl benzene	100 ppm ($435\,mg/m^3$) TWA 125 ppm ($545\,mg/m^3$) STEL	Eye, skin, and upper respiratory irritation
Indene	10 ppm ($45\,mg/m^3$) TWA	Mucous membrane and lung irritation; in animals, liver and renal necrosis, spleen injury
Naphthalene	10 ppm ($50\,mg/m^3$) TWA 15 ppm ($75\,mg/m^3$) STEL	Hemolysis and eye irritation that causes cataracts
Phenol	5 ppm ($19\,mg/m^3$) TWA (skin) 15.6 ppm ($60\,mg/m^3$) ceiling (15-m) (skin)	Skin, eye, CNS, liver, and kidney effects
Styrene	50 ppm ($215\,mg/m^3$) TWA 100 ppm ($425\,mg/m^3$) STEL	Nervous system effects, eye and respiratory irritation, reproductive effects
Toluene	100 ppm ($375\,mg/m^3$) TWA 150 ppm ($560\,mg/m^3$) STEL	CNS depression
M, p-Xylene	100 ppm ($435\,mg/m^3$) TWA 150 ppm ($655\,mg/m^3$) STEL	CNS depression, respiratory and eye irritation

Definitions:
Ca Agent recommended by NIOSH to be treated as a potential occupational carcinogen;
Ceiling The exposure that shall not be exceeded during any part of the workday. If instantaneous monitoring is not feasible, the ceiling shall be assessed as a 15-min TWA exposure (unless otherwise specified) that shall not be exceeded at any time during a workday;
CNS Central nervous system;
ppm Parts of contaminant per million parts of air at 25 °C and 1 atm. of pressure;
STEL Short-term exposure limit. Unless otherwise noted, the STEL is the 15-min TWA exposure that shall not be exceeded at any time during a workday;
TWA time-weighted average. Unless otherwise noted, TWA concentrations of a contaminant for up to 10 h/day during a 40-h workweek

7.1.2 Reinforcement Fibers

Carbon fibers which typically have diameters from 6 to 8 μm may splinter lengthwise during machining producing fibrils with diameters less than 6 μm. Therefore a significant fraction of the total dust generated may be respirable. The fiber fragments are irregular in shape and may have sharp ends. Mazumder et al. [9] have shown that mechanical chopping of virgin carbon fibers generates a wide distribution of particulate size with a MMAD of approximately 4.0 μm. Grinding of carbon–epoxy

composite produced aerosol particles consisting of resinous material and fiber fragments with a MMAD of approximately 2.7 μm. The primary health effect of exposure to fiber reinforcement materials, including carbon and glass fibers, is mechanical irritation of the eyes, skin, and upper respiratory tract. Animal and bacterial tests suggest that pitch-based carbon fibers are biologically active, whereas PAN-based fibers produce negative results. The pitch-based carbon fibers may be associated with an increased risk of cancer, although the evidence is weak [10].

Aramid fibers have diameters in the range from 12 to 15 μm, which makes it difficult for the fiber dust to reach deep into the respiratory system. However, aramid fibers are capable of splitting along its axis forming fibrils of diameters in the respirable range. Industrial monitoring shows that airborne respirable fibril levels are low in typical operations. Aramid fibers show no potential skin sensitization and low potential for irritation in animal and human skin tests [10].

The diameter of all glass fibers are larger than 6.0 μm which make them nonrespirable. Continuous filament glass fibers do not possess cleavage planes, which would allow them to split lengthwise to smaller diameter fibrils. Therefore, machining operations break the fibers only in shorter fragments of the same diameter. Like carbon fibers, glass fibers cause mechanical irritations to human organs such as skin, eyes, nose, and throat. Human epidemiology studies have categorized continuous filament glass fibers as noncarcinogenic [11–13].

Moreover, reinforcement fibers are commonly coated with sizing a sizing material to improve handling and enhance properties of the fiber–epoxy composite. This sizing material may be epoxy resins or other organic compounds. These materials may be biologically active and cause irritation or sensitization [14].

7.2 Dust Generation in Dry Machining

The aerodynamic and morphological properties of advanced composites dust have been studied by a few researchers [9, 15, 16]. Mazumdar et al. [9] investigated the morphology of dust particles generated from grinding carbon FRP laminates and chopping virgin carbon fibers. Dust samples examined under scanning electron microscope revealed that it consisted of carbon fibers and resin particles. A significant number of the fiber fragments were found to be of irregular shape, showing sharp ends in a number of fibers. It was also evident that some particles have a diameter that is less than that of the carbon fiber. This is due to the fibers splitting along their axis and forming fibrils. This property is also evident in machining aramid FRPs, but is absent in machining glass FRPs. The aerosol particles have an enormously wide geometric size distribution. The MMAD of the composite aerosol was approximately 2.7 μm. Boatman et al. [15] examined the dust generated from machining different fiber-reinforced epoxies by light and electron microscopy, thermogravimetry (TGA), gas chromatography (GC), and mass spectrometry (MS). It was found that less than 3% of the total mass of bulk samples were respirable dust with particles aerodynamic diameters ranging from 0.8 to 2.0 μm. Microscopic

examination of the bulk particles showed that their size ranged from 7 to 11 µm in diameter, with mean aspect ratios from 4:1 to 8:1.

Milling operations on reinforced thermosetting plastics have been shown to produce mostly coarse (nonrespirable) dust particles [16]. Only up to 1% of total dust is small enough to be considered as respirable. There is less dust formation when thermoplastic FRPs are machined because the fibers are retained in the matrix due to its high fracture strain. The concentration of fine dust was found to depend largely on the cutting tool geometry and the cutting parameters. Increasing the chip per tooth (e.g., reducing the cutting speed while maintaining the feed constant) results in lower concentration of respirable dust. Tool selection is also an important factor. Tools with less number of cutting edges will also produce coarser and less harmful dust particles. This is clearly demonstrated in Fig. 7.1 for the routing of aramid-fiber-reinforced epoxy machined with opposing helix tool and split helix tool. When a split helix tool with larger flutes was used, there was a clear shift in particle size concentration from fine (respirable) to coarse [16].

Investigation of the effect of cutting conditions on total airborne dust emissions in milling medium density fiberboard lead to similar findings [17]. The airborne dust was determined as the fraction of dust where aerodynamic particle size is 100 µm or less. A vertical elutriator was used to separate the airborne dust particles. It was found that the cutting speed is the most influential factor on dust emission. Airborne dust emissions decreased up to 60% when cutting speed decreased from 19 to 8 m/s. Depending upon the tool type and the material to be cut, decreasing of feeding speed caused decreasing of airborne dust emission or did not have any clear effect on airborne dust emission. An apparent relationship exists between the dust emissions and average chip thickness where an increase in the average chip thickness leads

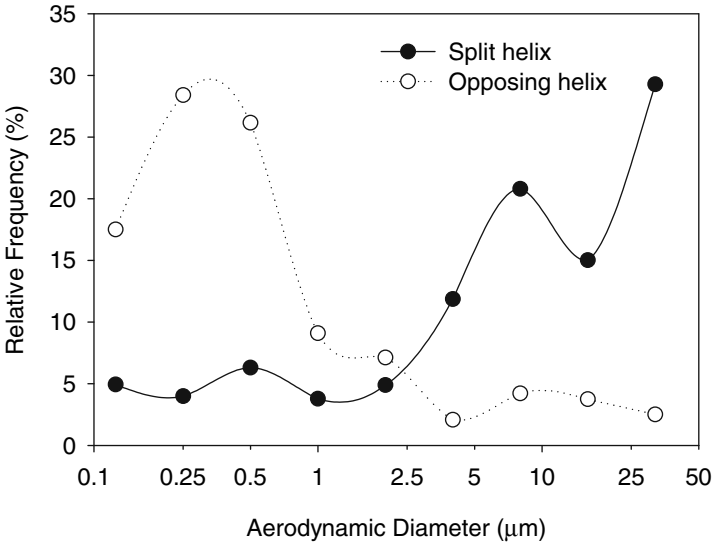

Fig. 7.1 Particle size distribution in milling aramid FRP. $v = 200\,\mathrm{m/min}$, $v_\mathrm{f} = 1\,\mathrm{m/min}$ [16]

to a significant decrease of dust level. Increasing the cutting speed while the feed speed is held constant would lead to an increase of absolute dust emission and in the same way the average chip thickness would be decreased.

7.3 Aerosol Emissions in Laser Machining

Aerosol formation in laser cutting of FRPs results from thermal decomposition of the constituents. Thermal decomposition for epoxy resins takes place at 250–350 °C, for aramid fibers at 550 °C, for glass fibers at 1,300 °C and for carbon fibers at 3,600 °C. Aerosol formation in laser machining of aramid, carbon, and glass FRPs was investigated by [1, 18]. Morphological analysis of the particles obtained from laser cutting of GFRP shows agglomerates of spherical glass beads consisting of primary particles of 1 µm diameter. This agglomeration may have formed from condensation of organic material on the glass beads which helps the glass beads to stick together [3]. Figure 7.2 shows the size distribution of aerosol particles resulting from laser machining of aramid and glass FRPs. It is apparent that the bulk of aerosol particles generated are in the respirable range. It was also shown that the size distribution for aramid FRP exhibited nearly no change when cutting parameters were changed. On the other hand, the size distribution for glass FRP exhibited significant dependence on laser power and cutting speed. The median aerodynamic

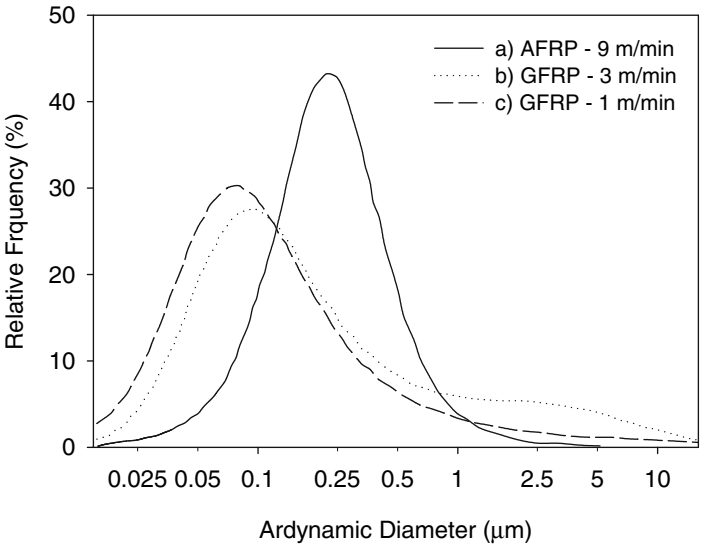

Fig. 7.2 Size distribution of dust emitted by laser beam cutting of aramid fiber epoxy and glass fiber epoxy composites with optimal cutting parameters. (**a**) AFRP: 1,000 W, 9 m/min, 50 l/min nitrogen, (**b**) GFRP: 1,000 W, 3 m/min, 50 l/min, (**c**) 1 m/min, 40 l/min [18]

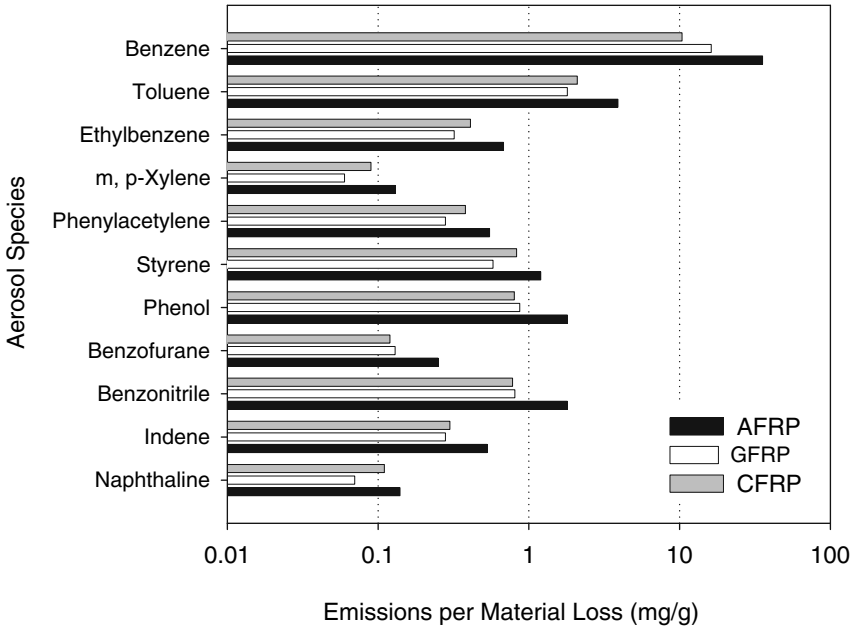

Fig. 7.3 Gaseous organic emissions during laser cutting of fiber-reinforced epoxy resins. Aramid FRP: laser power = 1,000 W, process gas = nitrogen 50 l/min, traverse speed = 8.5 m/min. Glass FRP: laser power = 1,000 W, process gas = nitrogen 50 l/min, traverse speed = 2.5 m/min. Carbon FRP: laser power = 1,250 W, process gas = nitrogen 50 l/min, traverse speed = 1.0 m/min [1]

diameter decreases and the shoulder in size distribution decreases for those cutting conditions which lead to higher temperatures.

Figure 7.3 shows the emission rate of gaseous compounds relative to the weight loss of the material (i.e., in mg/g) in laser cutting of fiber-reinforced epoxy. The gaseous emissions were also recorded when cutting glass-reinforced polyester and glass-reinforced polyamide resins in the same study [1]. These findings reveal that, independent of type of composite, the same gaseous compounds are emitted during the laser cutting process. This suggests that formation of these gaseous compounds is determined by their thermodynamical stability, rather than by the chemical structure of the polymer. A variety of aromatic hydrocarbons are observed in high concentrations dominated by benzene (more than 15 mg/g) and toluene (more than 1 mg/g). Moreover, several alkylbenzenes, phenyl-acetylene, styrene, indene, and naphthalene are formed in substantial amounts. Higher emissions are observed for aramid-reinforced polymer as compared to glass and carbon-fiber-reinforced polymers, which is likely due to the contribution of the fiber decomposition to the overall emissions. The cutting speed was shown to affect the emissions of organic compounds when machining aramid fiber composites, but has no significant influence when machining glass fiber composites. An increase in the emissions by roughly a factor of two occurs when the cutting speed is increased by a factor of

three in the case of aramid FRP. Furthermore, substantial amounts of hydrocyanic acid (HCN) were emitted during laser cutting of aramid-fiber-reinforced epoxy (1.5 mg/g), glass-fiber-reinforced epoxy (0.7 mg/g), carbon-fiber-reinforced epoxy (9.9 mg/g), and aramid-fiber-reinforced phenol (22.2 mg/g). The formation of HCN is believed to be the results of further combustion or break up to smaller units of the organic compounds initially formed by the laser cutting process. The high emissions of HCN for aramid composites is due to the decomposition of the aramid fibers which contain nitrogen. The remarkably high emissions for carbon fiber composites is perhaps due to the reaction of nitrogen in the process gas at the high temperatures required for cutting the carbon fibers. It is noted that for many compounds shown in Fig. 7.3 as well as for HCN there exist PEL and TLV values that must be consulted and compared in order to take the necessary precautions for minimizing exposure.

7.4 Workplace Controls

The health hazards brought about by composite machining are mainly due to inhalation of dust particles that are generally insoluble and gaseous compounds that may be allergic, toxic, or carcinogenic. Skin contact with condensation particles from these emissions may also present dermal hazard. Good work place controls are essential for eliminating possible exposure to these hazards or reducing exposure levels below regulatory limits and as low as reasonably achievable. The various types of workplace controls are generally divided into administrative and engineering controls. These measures aim at reducing overall emissions, containing remaining emissions, and minimizing operator exposure. In addition, personal protective equipment (PPE) may be used in cases when engineering controls are too expensive, impractical, or incapable of reducing and containing emissions.

7.4.1 Administrative Controls

Administrative controls consist of various policies and requirements that are established at an administrative level to promote safety in the workplace. Exposure to work hazards is minimized this way by properly managing the workers interaction with the source of hazard, isolating the hazard, following specific safe handling procedures and proper personal and industrial hygiene. Since this form of control is largely dependent on individual users acting with knowledge and responsibility, it is less satisfactory than engineering controls.Therefore, this form of control should only be used under well-documented conditions and after engineering controls have first been considered or used.

Administrative control of exposure to workplace hazards may include, but not limited to practices such as:

- Ensuring that all workers have been provided with adequate training to enable them to conduct their duties safely
- Properly reviewing MSDS by trained personnel prior to handling materials in question
- Rotation of workers to minimize the length of time a worker is exposed to a certain chemical
- Restricting access to areas in which particularly hazardous chemicals are used
- Posting appropriate signs to identify specific hazards within an area
- Requiring that various standard practices for chemical safety and good housekeeping be observed at all times in the laboratory
- Following adequate personal hygiene program

7.4.2 Engineering Controls

Machining fiber-reinforced composites generates significant amounts of airborne dust and fumes that must be effectively cleared from the workplace in order to reduce exposure. Particles and gases must be removed from the worker's breathing zone, transported by the ventilation system and properly removed by an air cleaning device before venting air to the atmosphere. The most effective engineering control measure is the use of on-tool extraction systems that are attached to a high-vacuum dust collection system. Using this method, aerosols are captured at the generation point, preventing the contaminant from escaping into the air. On-tool extractions systems come in a variety of designs and include shrouds, hoods, suction nozzles (for laser cutting), and sometimes total tool enclosures. The high-vacuum dust collection system creates a negative pressure at the extraction point that is capable of capturing most machining by-products. Due to this powerful vacuum, ventilation efficiency is extremely good and no respiratory protection is therefore necessary. The on-tool extraction system must provide minimum interference with the worker and be easy to use. High-vacuum systems allow the use of smaller diameters extraction hoses that do not restrict the workspace and are lighter and less bulky to handle by the worker.

In a study on the use of shrouded hand tools in grinding and sanding of composites it was shown that the total dust exposure at the worker's breathing zone was significantly reduced to levels below the detection level of the sampling instrument [19]. For laser cutting most of the aerosol emissions occur at the bottom of the workpiece. Applying exhaust air just below the workpiece was shown to capture most of the cutting fumes in machining glass FRP [20]. The captured air was filtered to remove organic gases and then released to the workplace. The average respirable dust concentration was about $0.15\,\mathrm{mg/m^3}$ and the concentration of organic gaseous compounds was below their respective detection limits and far below the threshold level values.

7.4.3 Personal Protective Equipment

Gloves, protective clothing, and eye protection may frequently be required, especially when the engineering controls are not capable of protecting the worker from exposure to hazards. PPE should be used as last resort or temporary solution. The correct approach to safety in the workplace is to reduce or preferably completely eliminate the inherent need for PPE through administrative and engineering control. Nevertheless, when PPE are required, it is necessary that proper equipment is selected according to health authority regulations whenever such regulations are available. The requirements for a respirator program, for example, are described in the OSHA regulation 29 CFR 1910.134 [6]. Similarly, requirements may be described for eye, hearing, and skin protection.

7.4.4 Machine Tool Health

Dust generated from machining FRPs is also harmful to the machine tool. Glass and carbon fibers and particles are highly abrasive. Carbon fibrils are also electrically conductive. Due to the small size of the dust particles and the fibrils, and their ability to become airborne, it is very likely that these particles will penetrate into tight spaces between machine components and into the machine control box. The prolonged contact of the abrasive dust with the moving machine elements such as slideways, ball screws, and bearings may lead to wear. Deposition of the carbon fibrils on printed circuit boards on the machine control will cause short circuits and very expensive damage to the machine tool. It is therefore essential to encapsulate the machine slides with dust covers. Machine enclosure will also help to extract the dust removed and to filter it to protect the operator from dust emissions. The electrical components should be isolated from the machine tool and air-conditioned separately. Figure 7.4 below shows a schematic of a machine tool for machining FRPs with proper components and features installed to meet the demand of this task [16].

7.5 Summary

Traditional machining processes produce dust-like chips that may become airborne. Some of this dust might be small enough to make its way to the lower respiratory tract and hence poses a health hazard. The upper limit to the size of respirable dust particles is 10 μm aerodynamic diameter and only 1% of the particle distribution below this size can make its way into the alveolar region of the lungs. Larger particles that are not respirable, deposit in the head and tracheobronchial airways and can pose a serious nuisance to the eyes, skin, and upper respiratory tract. Laser cutting

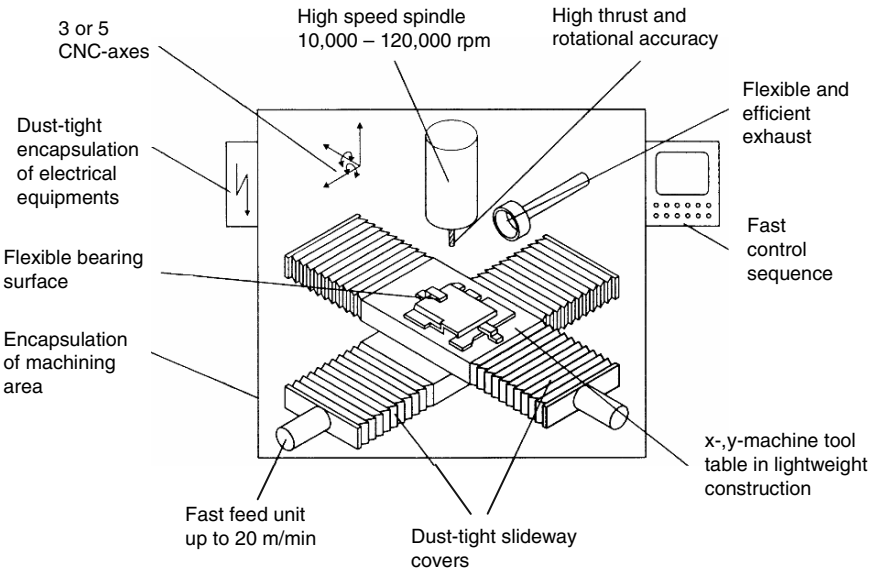

Fig. 7.4 Recommended configuration of milling machine for machining FRPs [16]

on the other hand produces re-solidified particles and gaseous emission that might be toxic, allergic, or carcinogenic.

The common sources of machining aerosols are the mechanical breakage of reinforcement fibers and the chemical breakdown of the polymer matrix and aramid organic fibers due to excessive heating. Carbon fibers are the major source of respirable dust because they may splinter lengthwise during machining producing fibrils of diameters less than 6 μm. Aramid fibers are also capable of splintering, but their emission of respirable fibrils is typically low. Glass fibers on the other hand do not possess the cleavage mechanism that causes splintering and they break perpendicular to the fiber axis into particles of the same order of the fiber diameter. Chemical breakdown of the polymer matrix and aramid fibers occurs in laser machining because of the high temperatures involved. The aerosols generated by vaporization and condensation process contain gaseous organic compounds and solid particles that are generally in the respirable range. A variety of aromatic hydrocarbons are generated in high concentrations, but are dominated by benzene and toluene. Most of these gasses have adverse effects on health after prolonged exposures. Therefore, RELs in the workplace have to be adhered to during machining.

The size distribution of aerosol particles is influenced by machining process parameters. Lower concentrations of respirable dust can be obtained in trimming applications by increasing the chip per tooth (which can be achieved by increasing the feed rate while keeping the spindle speed fixed, by reducing the spindle speed, and by using tools with less cutting teeth). In laser cutting, a decrease in the median aerodynamic diameter is achieved by increasing laser beam power and reducing the

traverse speed. Both conditions are responsible for generating higher temperatures at the cutting front.

There are two main approaches for eliminating exposure to health hazards: administrative and engineering controls. Administrative controls pertain to establishing proper work scheduling, worker training, and policies that will result in minimum workers exposure to hazards. Engineering solutions are those equipments or systems installed at the work place in order to contain and remove hazards. The most effective engineering control of machining dust and fumes is ventilation. In addition, PPE may be used but only as a last resort because priorities should be set on eliminating health hazards or their exposures.

Another key concern in machining FRPs is protecting the machine tool against damage caused by machining byproducts. Two main areas of machine tool system must be properly guarded. One area is the machine electric and electronic control boxes, which have to be isolated and be ventilated separately in order to prevent deposition of the electrically conductive carbon dust on the circuit boards. The second area is the accurate machine slides and ball screws, which have to be protected against abrasive wear of the dust particles.

References

1. Levsen, K., Emmrich, M., Kock, H., Prieß, B., Sollinger, S., Trasser, F.J., Organic emissions during laser cutting of fibre-reinforced plastics. Staub – Reinhaltung der Luft 51, 365–372, 1991.
2. Malkusch, W., Rehn, B., Bruch, J., Medical risk assessment of laser fumes using in vitro test assays. Proceedings of Second EUREKA Industrial Laser Safety Forum, 1993, pp. 78–88.
3. Haferkamp, H., von Alvensleben, F., Seebaum, D., Goede, M., Püster, T., Air contaminants generated during laser processing of organic materials and protective measures. Journal of Applied Laser Applications 10, 109–113, 1998.
4. Hazard Prevention and Control in the Work Environment: Airborne Dust, World Health Organization, WHO/SDE/OEH/99.14, http://www.who.int/occupational_health/publications/en/oehairbornedust3.pdf, cited 26 February 2008.
5. Bourcier, D.R., Exposure evaluation of composite materials with emphasis on cured composite dust. Applied Industrial Hygiene 12, 40–46, 1989.
6. Code of Federal Regulations, Title 29, Part 1910. Occupational safety and health standards, http://www.osha.gov/pls/oshaweb/owastand.display_standard_group?p_toc_level = 1&p_part_number = 1910, cited 26 February 2008.
7. 2008 TLVs®and BEIs®, American Conference of Governmental Industrial Hygienists, Cincinnati, OH, 2008.
8. NIOSH RECOMMENDATIONS FOR OCCUPATIONAL SAFETY AND HEALTH. Compendium of policy documents and statements, 1992, http://www.cdc.gov/niosh/92–100.html, cited 26 February 2008.
9. Mazumder, M.K., Chang, R.J., Bond, R.L., Aerodynamic and morphological properties of carbon-fiber aerosols. Aerosol Science and Technology 1, 427–440, 1982.
10. Polymer Matrix Materials: Advanced Composites, OSHA Technical Manual, Section III: Chapter 1, http://www.osha.gov/dts/osta/otm/otm_iii/otm_iii_1.html, cited on February 22, 2008.
11. Chiazze, L., Watkins, D.K., Fryar, C., Historical cohort mortality study of a continuous filament fiberglass manufacturing plant: I White men. Journal of Occupational and Environmental Medicine 39(5), 432–441, 1997.

12. Chiazze, L., Watkins, D.K., Fryar, C., Historical cohort mortality study of a continuous filament fiberglass manufacturing plant: II Women and minorities. Journal of Occupational and Environmental Medicine 39(6), 548–555, 1997.
13. Marsh, G.M., Stone, R.A., Youk, A.O., Smith, T.J., Rossiter, C.E., Grimm, H.G., Boffetta, P., Saracci, R., Cancer mortality among man-made vitreous fiber production workers. Epidemiology 9, 218–220, 1998.
14. Astrom, B.T., Manufacturing of Polymer Composites, Nelson Thornes, UK, 2002.
15. Boatman, E.S., Covert, D., Kalman, D., Luchtel, D., Omenn, G.S., Physical, morphological, and chemical studies of dusts derived from the machining of composite-epoxy materials. Environmental Research 45, 242–255, 1988.
16. Konig, W., Rummenholler, S. Technological and industrial safety aspects in milling FRPS, Machining of Advanced Composites, ASME, New York, NY, MD-Vol. 45/PED-Vol. 66, 1993.
17. Hemmilä, P., Gottlöber, C., Welling, I., Effect of cutting parameters to dust and noise in wood cutting, laboratory and industrial tests. Proceedings of 13th International Wood Machining Seminar, pp. 375–384, 1997.
18. Busch, H., Hollander, W., Levsen, K., Schilhabel, J., Trasser, F.J., Neder, L., Aerosol formation during laser cutting of fiber reinforced plastics. Journal of Aerosol Science 20, 1473–1476, 1989.
19. Sheehan, J.M., Teitsworth, E.J., The effectiveness of local exhaust- ventilated (shrouded) hand power tools used for grinding/sanding composite materials, American Industrial Hygeine Association Journal 59, 689–693, 1998.
20. Klein, R.M., Dahmen, M., Putz, H., Mohlmann, C., Scholms, R., Zschiesche, W., Workplace exposure during laser machining. Proceedings of the International Laser Safety Conference. ILSC'97, 1997, pp. 252–261.

Index